SHEAR OF SMALL VERTICAL SCALE OBSERVED IN THE PERMANENT OCEANIC THERMOCLINE

by

JOHN CLOUD VAN LEER

B.S., CASE INSTITUTE OF TECHNOLOGY
1962

SUBMITTED IN PARTIAL FULFILLMENT

OF THE REQUIREMENTS FOR THE

DEGREE OF DOCTOR OF SCIENCE

at the

MASSACHUSETTS INSTITUTE OF TECHNOLOGY

and the

WOODS HOLE OCEANOGRAPHIC INSTITUTION

January 1971

Signature of Author.....
Joint Program in Oceanography, Woods Hole Oceanographic Institution and Massachusetts Institute of Technology, Department of Meteorology

Certified by.....
Thesis Supervisor

Accepted by.....
Chairman, Joint Oceanography Committee in the Earth Sciences, Massachusetts Institute of Technology - Woods Hole Oceanographic Institution

SHEAR OF SMALL VERTICAL SCALE OBSERVED IN THE PERMANENT OCEANIC THERMOCLINE

John Cloud Van Leer

Submitted to the Department of Meteorology of the Massachusetts Institute of Technology and to the Woods Hole Oceanographic Institution on January , 1971 in partial fulfillment of the requirement for the degree of Doctor of Science.

ABSTRACT

Two shear experiments performed in the permanent thermocline are described and analyzed in this thesis. The first employed dye streak techniques to gain fractional meter vertical resolution. Shears with small vertical scales with frequent reversals in direction and changes of magnitude were observed in every experiment between 160 and 900 meters depth. The ratio of the standard deviation of shear magnitude to the mean shear magnitude was computed at the depth of each dye experiment. These ratios decreased exponentially with depth suggesting a decay of surface supplied energy. The vertical wave number of the shear is not inconsistent with high mode inertio-gravitational internal waves or interleaving layers or salt-driven convection.

The second experiment used sensor pairs to measure shear, temperature gradient, and salinity gradient with three meter vertical spacing. A weak but significant negative correlation between shear magnitude and density gradient magnitude was found in most of the records whether density gradient was computed from temperature and salinity or estimated from temperature alone. This result disagrees with a simple linear internal wave model developed for a layered medium. The expected positive correlation is strong enough to cause shear instability to occur first in regions of strongest static stability. This prediction again disagrees with observed shear density data in which the smallest Richardson numbers occur in weakly stratified regions. This negative correlation was observed to be strongest in regions of weak static stability.

Perhaps we are observing the results of mixing processes in the main thermocline which cannot be described by the simple linear

equations of motion. Two likely sources for the energy of mixing are suggested. Inertial motions are shown to have sufficient energy at thermocline depth and are known to have high enough vertical wave number to have shears comparable to those observed. Salt fingers are known to be able to release enough energy from an unstable salt buoyancy field to form convective layers under laboratory conditions. Since the temperature and salinity in the main thermocline near Bermuda both decrease with depth and have nearly equal and opposite buoyancy contributions, salt fingers must be considered likely.

In the main oceanic thermocline no single mixing process seems likely to dominate everywhere or perhaps anywhere. The data collected in this thesis and elsewhere are not yet sufficient to define the statistics of these mixing processes or even to uniquely separate one from another at one location. A time series of experiments combining the two techniques developed in this thesis should be able to establish how shears vary in direction with time and vary with density gradient. These questions are at the heart of the thermocline mixing problem.

Thesis Supervisor: Henry M. Stommel
Title: Professor of Oceanography

TABLE OF CONTENTS

LIST OF FIGURES

FIGURES IN TEXT

FIGURES IN APPENDICES

TABLES

PRINTS

ACKNOWLEDGEMENTS

The author wishes to express special thanks to Professor Henry M. Stommel for making this thesis possible through his generous support and helpful suggestions. Further thanks are due to Professor Claes Rooth and also to the Deep Submergence Group at Woods Hole for the chance to participate in a successful dye streak experiment. Appreciation is expressed to Dave Nergaard and the gang at Bendix who built the DCS-100 data sampling system which worked. Thanks are due to Professor Mollo-Christensen for his support and suggestions in the development of the mini-meter current meter. To Captain Hiller and the crew of the Atlantis II the author expresses appreciation for their skillful ship-handling with the difficult scissors experiment. Thanks are also due to Professor Carl Wunsch for the use of his ship time on Atlantis II cruise 47 and his time series programs. The M.I.T. and Woods Hole Information Processing Centers are to be acknowledged for their facilities and programs. The author is grateful to Jim McCullough for his computer interface help and to Bruce M. Gordon for his programming assistance. Gordon Brown is acknowledged for his help with the dye streak reduction and much mechanical help. David Drummond and Valentin Livada were indispensible for their calculation and drafting help. Particular thanks are due Mrs. Karen MacQueen for her very competent and cheerful preparation of a difficult manuscript.

I am grateful to my wife Linda for her patience and sacrifice during my years in graduate school.

This work was done under National Science Foundation Grants GA-1015, GA-1613, GA-12773, GA-21172.

TO LINDA

CHAPTER 1

INTRODUCTION

Global scale thermocline theories

The main thermocline is the transition zone between the warm surface water and the cold main body of the ocean. As an oceanic boundary it is rivaled in importance only by the sea surface and the bottom, yet today little is known about the direct physical processes maintaining the thermocline as it is. These processes appear only as lumped parameters in several world scale oceanic circulation theories by Stommel, Blanford, Munk and others.

Upwelling of approximately one cm/day seems to balance downward diffusion near one cm^2/sec. These numbers raise an interesting question: Where does the energy which mixes the heat downward come from? (of order 10^{-6} ergs/gm second). Munk (1966) discusses four possible sources:

1. Shear mixing due to Richardson type instability of inertio-gravitational internal waves, internal tides or planetary waves.

2. Thermodynamic mixing due to the difference in the molecular diffusion of heat and salt of about 100 - 1. This may give rise to filament (salt-finger) convection (Stern, 1960) or laminar salt-finger layers separated by turbulent mixing layers (Turner and Stommel). Perhaps both filaments and layering act in concert (Turner, 1967).

3. Boundary mixing at surface or lateral boundaries

with communication of properties along constant density surfaces. Here horizontal transport processes may be disguised as vertical eddy diffusion.

4. Biological mixing which Munk discards as at least three orders of magnitude smaller than diffusion computed by T, S, 14C, and O_2 considerations.

He found shear instability of internal tides to be a marginal source of mixing energy.

This thesis is motivated by the desire to understand which of these processes may be important to the physics of the main thermocline.

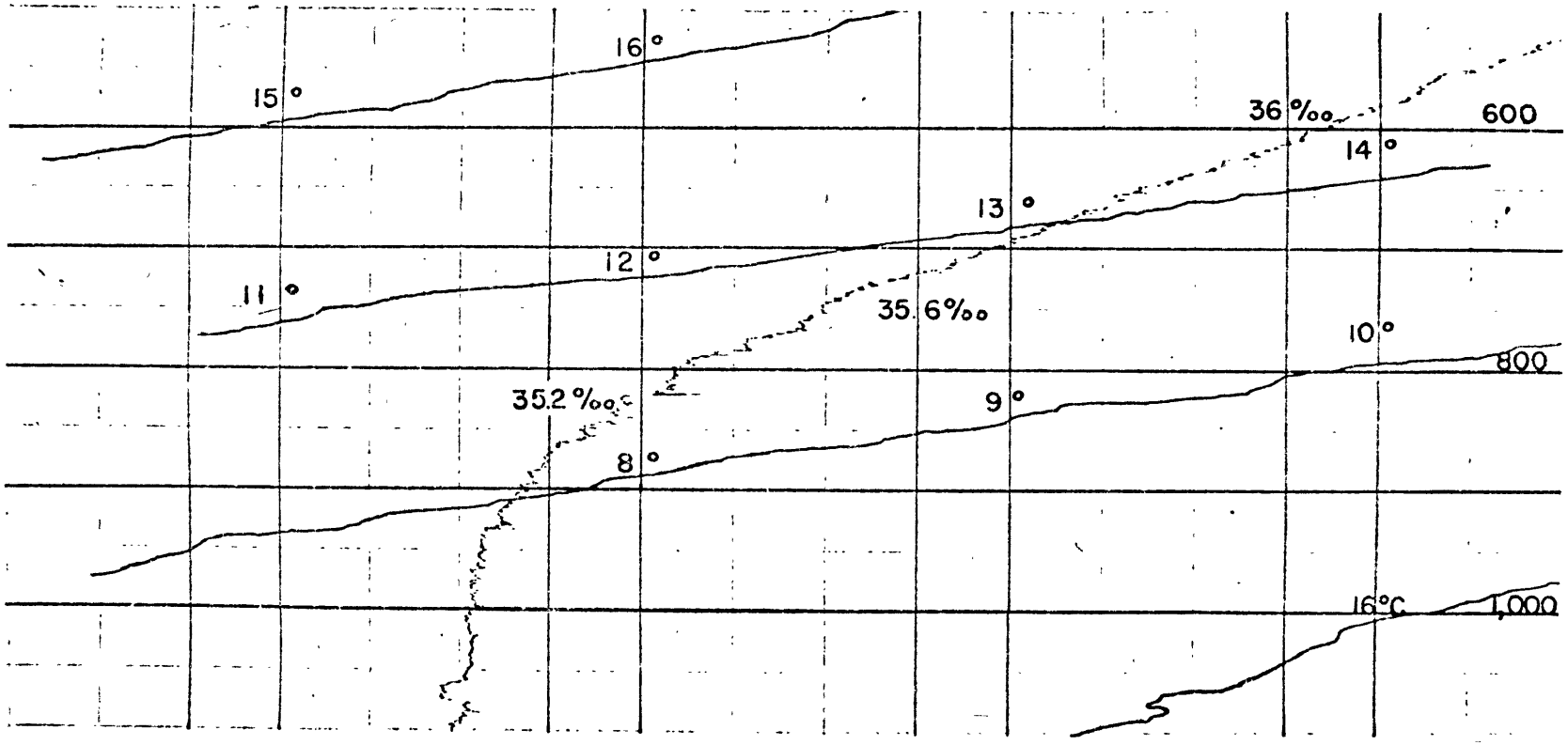

FIG. 1.1: Typical temperature and salinity vs depth data.

Previous work on thermocline micro-structure

Micro-structure observations to date have largely been carried out using Bissett Berman STD systems lowered on cables attached to ships. These continuously recording STD systems have revealed small-scale step-like layers in the main thermocline in many widely scattered areas: near Timor and Mindanao (Stommel and Fedorov, 1966), central South Pacific (Eltanin data, 1967), and Bermuda (Stommel and Cooper, 1967). Vertical temperature gradients between well-mixed layers seem to be at least an order of magnitude greater than the mean gradient for this part of the thermocline (see the typical Bermuda STD cast in figure 1.1). Similar observed structure in salinity may have been badly distorted by ship motion. Tait and Howe (1968) have observed very large (22 meter) step structure in temperature and salinity under the Mediterranean water intrusion in the Northeast Atlantic. These steps are thought to be a possible site for salt finger activity (Turner, 1967). Similar large steps (16 meters) have been observed by Sturges of the University of Rhode Island (personal communication) in the Anegada Passage under a strong subsurface salinity maximum.

Cox et al. (1969) have measured temperature gradients in the Pacific in a region of stabilizing salinity gradients with a free-falling probe. There they find temperature gradients with appreciable energy down to scales of .1 cycles per centimeter. Temperature gradients with sharply decreasing energy are found down to a scale of 1 cycle/cm. Their instrument records the time derivative of temperature as a function of depth with a millimeter scale thermistor. Although

this device reputedly resolves the finest small-scale temperature gradients present it does so at the sacrifice of accuracy in measuring larger vertical scale weak gradients. Perhaps the large-scale weak gradients in the "well-mixed regions" are more important to the thermocline mixing processes. It seems very important to know whether these layers are occasionally statically unstable as they must be in the salt finger model below. If such layers of near-zero or negative gravitational stability exist, they must be unstable to shear induced by wave motion of any frequency, including tidal and inertial where much of the energy exists (see Fofonoff, 1969). Such regions might persist as more or less permanent mixing sites.

Woods (1968) has similarly emphasized the regions of strongest temperature gradient in his beautiful near-surface photographs of shear instability of small single sheet internal gravity waves. Since the regions of strongest temperature gradient suppress turbulence, these waves occur in laminar beautifully-ordered groups which obey the linear shear instability criteria. However Woods does comment that the layers between sharp gradients are weakly turbulent. Therefore these layers must have a lower Richardson number than the laminar sheets and must be the site of most of the mixing.

The experiments reported below were carried out in two locations. The Alvin dye streak experiment (chapter 2) was executed over the continental slope in 2 km deep water. The scissors experiment (chapter 3) was done in the Bermuda area (see figure 1.2). The remaining part of chapter 1 outlines some observational and theoretical ideas which will be used to interpret the experimental results presented in chapters 2 and 3.

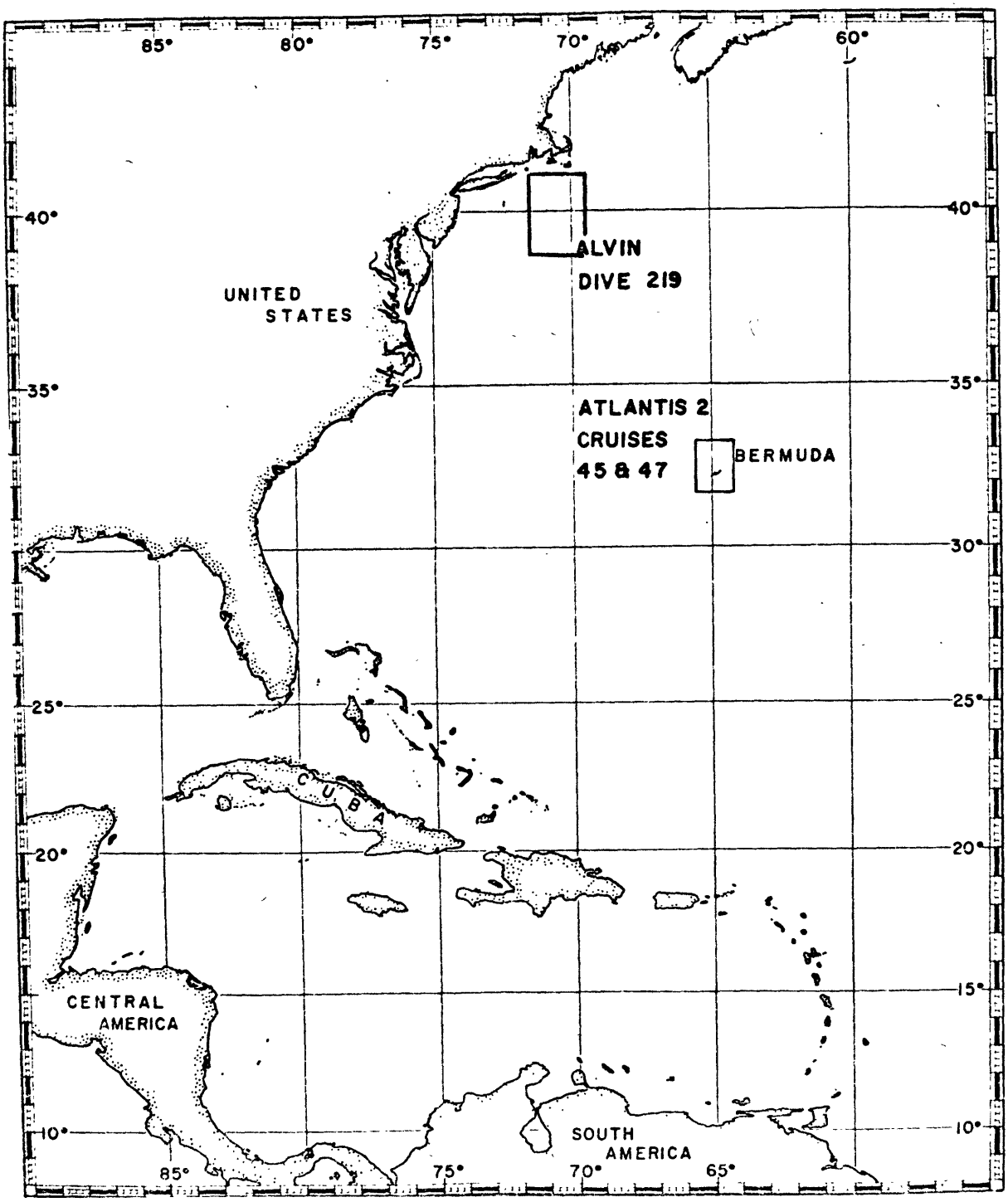

FIG. 1.2: Locations of data areas. The boxed areas are the same size as the borders of the appropriate charts. See figure 2.1 for Alvin dive and figure 3.1 and 3.2 for Bermuda scissors stations.

Shear instability

Since the Austausch coefficient in the main thermocline appears to be one cm^2/sec (far exceeding the corresponding molecular coefficients) the thermocline may be thought of as in a state of turbulent flux. The production of turbulence in a stably stratified fluid is often thought of as associated with shear instability of some sort.

Several theoretical workers (Miles, 1963, Howard, 1963, and others) have found under a variety of conditions that laminar stratified shear flow may be unstable for Richardson number

$$Ri = \frac{\frac{g}{\rho_o}\frac{\partial \rho}{\partial z}}{\left[\frac{\partial u_H}{\partial z}\right]^2} < \frac{1}{4}$$

The assumptions leading to this result may not be valid in the thermocline; for example, small amounts of residual decaying turbulence may affect the critical value. More recent numerical work by Hazen (referred to by Woods (1969)) has shown that if $Ri < 1/4$ most laminar flows are indeed unstable. However, for lack of a more precise criterion, the Richardson number may be used to predict the onset of instability.

Once turbulence has set in at one spot, it extracts further energy from the "mean shear flow". This energy must do work on the gravitationally stable stratification in mixing if the turbulence is to diffuse vertically.

Since no such restriction exists horizontally, this patch-

or-blini of turbulence should assume a strongly oblated shape and continue to grow in volume until the Richardson number exceeds some critical value. When this happens, the turbulence decays and the newly formed mixed layer spreads horizontally due to horizontal pressure forces until balanced geostrophically or frictionally or both, as suggested by Stommel and Fedorov (1966). Woods (1969) suggests that turbulent stratified fluid will not regain its laminar state until about $Ri \approx 1$. This effect is called Richardson number hysterisis because the state of such fluid for $1/4 < Ri < 1$ depends on its recent history.

The above picture of shear instability requires a source of shear that the "production term" can get its teeth into. If horizontal advection in the layered structure of the main thermocline can be shown to be small, a relation between the Richardson number and the variability of vertical fluxes of temperature and salt can be found through successive measurements of a particular set of layers. If one could successfully "tag" one or more layers then detailed repetitive profiles of thickness, temperature, salinity and Richardson number could be found.

Possible sources of shear are internal tides, internal waves, planetary waves and inertial oscillation. With the possible exception of planetary waves, observational evidence suggests that any of the above mechanisms could be present and responsible for the creation of sufficient shears. For example: Webster (1968) and Fofonoff (1969) have found inertial and tidal periods in buoy-mounted,

current meter data which seems to have a high vertical wave number.

Munk (1966) has computed the possible flux of surface tidal energy scattered by irregular bottom topography into high order internal tides to be 4×10^{-6} ergs/gm sec. He points out that this is about 1/6 of the total tidal dissipation on earth and nearly half of this flux is required for mixing. Munk also points out the possible intermittent nature of the mixing processes, whatever they might be.

Inertial motions

Inertial motions have long been known to be intermittent (Webster, 1968). Pollard (1969) has recently given statistics from 29 records from site D as a function of depth which show substantial inertial energy at thermocline depth.

TABLE

Amplitudes of inertial oscillations at each of six depths, compiled from 29 records from moored buoys at site D. Ten per cent of the time the amplitude exceeded the 10% level amplitude at each depth. (Pollard, 1969)

Depth (m)	10	50	100	500	1000	2000
Total duration (days)	219	205	274	124	182	196
Max. amplitude (cm/sec)	49	20	14	13	11	7
10% level amplitude (cm/sec)	23	9	8	9	4	3

If we assume that these motions persist in time only a few days or at most and generally for only a few cycles (Perkins, 1970) then we must conclude that the 10% level amplitude in table must be made up of many individual inertial events, say 10.

We may now inquire at what average rate per gram could energy be dissipated if all the kinetic energy in each event were totally lost between events at each level.

$$Ed = \frac{\frac{1}{2}\,(10\%\ \text{LEVEL})^2\,(\text{EVENTS PER SECOND})}{0.9\,(\text{RECORD DURATION})}$$

Depth (meters)	10	50	100	500	1000	2000
Ed x 10^6 $\frac{erg}{gm \cdot sec}$	310	25.5	1.5	4.8	0.53	0.29

Considering that the 10% level inertial velocities underestimate the average velocity during an event and further that they enter as the square in the dissipation formula above, these numbers compare quite favorably with Munk's 1.8 x 10^{-6} erg/gm sec energy to mix the lower thermocline.

Perkins (1970) has recently examined most of the unpublished records from WHOI buoy mounted current meter data and found "No records separated by more than 100 meters in depth showed significant coherence, a single pair of instruments separated by 80 meters showed moderate coherence (0.6) at inertial period only, while a pair of instruments only 2 meters apart showed almost perfect coherence." So it appears from open ocean measurements that vertically coherent inertial motions have a probable scale of tens of meters (that is, a high vertical wave number). Pollard and Millard (1970), as well as others, have shown that inertial waves at the surface can be generated by rapid fluctuations of the wind direction and/or magnitude. But due to the low horizontal component of the group velocity of such waves they were at a loss to explain their rapid decay except, perhaps, that the wind turned them off. They also could not account for the observed large amplitude of inertial motion at depths well removed from the surface mixed layer and the tidally critical latitudes

of 30 and 73°. Reports of the horizontal coherence distances according to Perkins (1970) are more confusing but are probably the order of 10 km.

The source of inertial waves at depths of hundreds of meters or more which is not clearly explained by wind stress or tidal forcing may have been identified by Frankignol (1969). He found that the action of a constant weak shear on a field of internal gravity waves in a rotating system can rotate the wave number vector transforming these waves into inertial period oscillations. As the wave number vector rotates the vertical scale of the waves diminishes, thereby increasing the vertical gradient of the velocity field. Frankignol further asserts that "Clearly the shear instability will occur very near the inertial frequency". Malone (1968) reports strong inertial motion in Lake Michigan only during the thermocline season and no significant inertial motions otherwise even when meteorological conditions suggest they should exist. Since internal waves are possible only when a thermocline exists Malone's data might be interpreted as support for Frankignol's theory.

Given a near inertial wave, what amplitude should be observed if the vertical wave length λ is order 10 meters and the maximum shear is order 5×10^{-3} sec^{-1}? For a sine wave in z the shear is

$$\frac{dU_H}{dZ} = \frac{2\pi U_{H max}}{\lambda} \cos\left[\frac{2\pi}{\lambda} Z\right]$$

or the maximum shear is

$$\left.\frac{dU_H}{dZ}\right|_{max} = \frac{2\pi U_{H\,max}}{\lambda}$$

so

$$U_{H\,max} \cong 0.8 \text{ cm/sec}$$

This velocity is well within the 10% limits for inertial wave amplitudes observed in the site D data above and is so small that it would likely go unobserved in this buoy data. Thus the Alvin dye streak data presented below will not be found inconsistent with a weak high vertical wave number inertial wave. A similar calculation for typical 10% level = 8 cm/sec from Pollard (1970) and maximum shear amplitude from dye streak and scissors measurements gives a vertical wavelength 50 meters. Again this number is quite compatible with buoy observations at site D.

What form might the result of an inertial wave instability take? After the initial breakdown either due to local shear instability on an interface or elsewhere (or perhaps due to salt convection) a small well-mixed layer might be formed which would then be unstable to any shear. This could be extended horizontally a kilometer or more by inertial shear due in part to the probable horizontal scale of the inertial wave. This is similar to Dr. F. P. Bretherton's idea of clear air turbulence given in a talk at WHOI during the summer of 1970. He also suggested that such instabilities might be responsible for oceanic layer structure as have others.

During a half inertial period such a mixed layer could store considerable vorticity of one sign giving rise to circulation in the layer even when the wave is gone. This stored vorticity might well exceed the vorticity of the original wave motion because it is no longer constrained by wave dynamics. If such instability products were observed with current meters whose spacing was only a little smaller than the layer thickness then the observed shear would be largest in the mixed layers. This picture is not inconsistent with the scissors data whose mean shear is order $5 \times 10^{-3} sec^{-1}$ and whose largest magnitudes most often occur in the more mixed regions. Such mixing could sharpen the embracing interfaces triggering sympathetic salt fingering, thus adding further vorticity to the layer and giving low or even negative Richardson numbers in the layer.

Convective instability of internal waves

Orlanski and Bryan (1969) have suggested a mechanism for the formation of mixed regions in the thermocline. This mechanism is a gravitational "overturning by rotors" associated with a finite amplitude instability of downward propagating internal waves. They further predict for oceanic conditions a most unstable vertical wavelength of 10 to 20 meters. They claim that for a uniformly stratified ocean, gravitational instability occurs before a shear instability in the case of amplifying internal waves. "It is a nonlinear instability which takes place when the partical velocity of the wave motion exceeds the phase velocity of the wave".

This criterion is especially difficult to apply to data gathered in the experiments below because it requires detailed knowledge of the internal wave field. There is no way to know the frequency or horizontal wave length of waves at the site of observation if indeed waves were present at all. However it is interesting to note that the most unstable points coincide with maximum horizontal velocity and minimum shear as well as zero or negative stability. Once formed these rotors might leave well-mixed regions with considerable vorticity and account for the small negative correlation between the magnitude of the shear and the density gradient observed in the Bermuda data below. Their predicted vertical wave length of minimum stability of 10 to 20 meters is also close to the vertical wave length of the shear structure observed in the dye streak data between 400 and 500 meters. The Orlanski-Bryan work unfortunately does not include

rotation or initial step conditions. Since near the inertial frequency, the horizontal phase velocity becomes small, and the observed amplitudes are large, and the observed vertical wave numbers are high, this frequency region should be especially interesting for its convective instability.

The expected correlation between shear and density gradient due to internal waves

This discussion involves only the linear equations of motion and thus will not include the actual mixing process in the thermocline. It is hoped however that these equations will give some insight into what the correlation between shear and density gradient would be in a simple but analytically tractable example of inertio-gravitational waves. The model of the thermocline picked is one of infinite horizontal layers of constant Brunt-Väisälä frequency N. These layers can be thought of as a piece-wise approximation to the actual profile of Brunt frequency with depth. It also can be used to examine the layer-sheet model recently popularized by Woods (1968).

In the layer-sheet model, regions of very high stability (sheets) alternate with regions of lower stability (layers). The critical questions are: What is the expected correlation between shear and the density gradient αN^2 when this structure is undulated by internal waves? And perhaps more important, which layers will be unstable to the wave shear first? Will it be the sheets or the layers?

The basic equations of motion of Perkins (1970) for a rotating, stratified, incompressible, Boussinesq ocean in local Cartesian coordinates are adopted.

$$u_t - f_v + p_x = 0 \qquad (1)$$
$$v_t + f_u + p_y = 0 \qquad (2)$$
$$w_t + N^2\zeta + p_z = 0 \qquad (3)$$
$$\zeta_t - w = 0 \qquad (4)$$
$$u_x + v_y + w_z = 0 \qquad (5)$$

where

$f = 2\Omega\sin\phi$ is the Coriolis frequency,

Ω is the earth's rotation rate,

ϕ, λ, z are latitude, longitude and elevation (measured upwards) respectively,

u, v, w are respectively east-west, north-south, and up-down components of velocity,

p is pressure variation about hydrostatic divided by the mean density,

ζ is vertical particle displacement from equilibrium,

N is the Brunt-Väisälä frequency, defined by $N^2 = -g\rho_z/\rho$.

We assume plane wave solutions in each constant N layer of the form:

$$w(x,y,z,t) = \mathrm{Re}\ (\psi(z)\, e^{i\Phi})$$

and likewise

$$u = \mathrm{Re}\,(U(z)\, e^{i\Phi})$$
$$v = \mathrm{Re}\,(V(z)\, e^{i\Phi})$$
$$p = \mathrm{Re}\,(P(z)\, e^{i\Phi})$$
$$\zeta = \mathrm{Re}\,(H(z)\, e^{i\Phi})$$

where

$$\Phi = kx + ly + \omega t$$

Substituting these solutions into (1) - (5) we have

$$i\omega U - fV + ikP = 0 \qquad (6)$$

$$i\omega V + fU + ilP = 0 \qquad (7)$$

$$i\omega\psi + \frac{dP}{dZ} + N^2H = 0 \qquad (8)$$

$$i\omega H - \psi = 0 \qquad (9)$$

$$ikU + ilV + \frac{d\psi}{dZ} = 0 \qquad (10)$$

Putting (9) into (8) we can eliminate H

$$i\omega\psi + \frac{dP}{dZ} + N^2\frac{\psi}{i\omega} = 0 \qquad (11)$$

Solving (6) and (7) for U and V we have

$$U = +\frac{fV}{i\omega} - \frac{kP}{\omega} \qquad (12)$$

$$V = \frac{-fU}{i\omega} - \frac{kP}{\omega} \qquad (13)$$

Combining (12) and (13) with (11) we get

$$U(z) = \frac{-\omega P(z)\left[k + \frac{fl}{i\omega}\right]}{(\omega^2 - f^2)} \qquad (14)$$

$$V(z) = \frac{\omega P_{(z)}\left[\frac{fk}{i\omega} - l\right]}{(\omega^2 - f^2)} \qquad (15)$$

Putting (14) and (15) into (10)

$$P(z) = \frac{d\psi}{dZ}\left[\frac{\omega^2-f^2}{i\omega k_H^2}\right] \qquad (16)$$

where

$$k_H^2 = l^2 + k^2$$

Substituting this expression for P into (8)

$$\frac{d^2\psi(z)}{d^2Z^2} + k_H^2\left[\frac{N^2(z)-\omega^2}{\omega^2-f^2}\right]\psi(z) = 0 \qquad (17)$$

This is the familiar equation for the vertical displacement given by Cox (1962) in The Sea, and others. This equation with suitable top and bottom boundary conditions constitutes an eigenvalue problem which can be solved numerically for $\psi(z)$ by matching pressure and vertical velocity between the constant N layers at their common interfaces.

Substituting the pressure expression (16) into (14) and (15) respectively and their z derivatives we have

$$\frac{\partial U(z)}{\partial Z} = \left[\frac{fl}{\omega k_H^2} + \frac{ik}{k_H^2}\right]\frac{d^2\psi}{dZ^2} \qquad (18)$$

and

$$\frac{\partial V(z)}{\partial Z} = \left[\frac{-fk}{\omega k_H^2} + \frac{il}{k_H^2} \right] \frac{d^2\psi}{dZ^2} \qquad (19)$$

which, combined with (17) give the shears in terms of $\psi(z)$:

$$\frac{\partial U(z)}{\partial Z} = \psi(z) \left[\frac{N^2-\omega^2}{\omega^2-f^2} \right] \left[\frac{-fl}{\omega} - ik \right] \qquad (20)$$

and

$$\frac{\partial V(z)}{\partial Z} = \psi(z) \left[\frac{N^2-\omega^2}{\omega^2-f^2} \right] \left[\frac{fk}{\omega} - il \right] \qquad (21)$$

The square of the vertical shear in the horizontal velocity is

$$\left[\frac{\partial U_H}{\partial Z} \right]^2 = \left[\frac{\partial u}{\partial Z} \right]^2 + \left[\frac{\partial v}{\partial Z} \right]^2 \qquad (22)$$

or substituting in (20) and (21) we get in each layer

$$\left[\frac{\partial U_H}{\partial Z} \right]^2 = \psi^2(z) \left[\frac{N^2-\omega^2}{\omega^2-f^2} \right]^2 \left[\frac{k_H^2(\omega^2+f^2)}{\omega^2} \right] \qquad (23)$$

For an internal wave of frequency ω and horizontal wave number k_H whose vertical scale is large compared to the individual constant N layers (i.e., low vertical mode) the vertical amplitude $\psi(z)$ changes very little from layer to layer in some small region. So the horizontal velocity shear in each layer is

$$\frac{\partial U_H}{\partial Z} \propto (N^2 - \omega^2) \qquad (24)$$

So for a low frequency wave $N^2 >> \omega^2$ the shear is directly proportional to the density gradient. Or for any given $\omega^2 < N^2$ the shear will be greatest in layers of largest density gradient and least in layers of small density gradient. The next logical question is: which layers will first become unstable to the wave shear?

The Richardson numbers in adjacent strongly stable and weakly stable layers are then proportionate to

$$Ri \propto \frac{N^2}{(N^2 - \omega^2)^2} \qquad (25)$$

In particular if N_w is the Brunt frequency in the weakly stratified layer and N_s is the Brunt frequency in the strongly stratified layer, then we define the stratification ratio as

$$\xi = \frac{N_s}{N_w} \qquad (26)$$

and the ratio of the Richardson number in the N_s layer Ri_s to the Richardson number in the N_w layer Ri_w is:

$$\frac{Ri_s}{Ri_w} = \left[\frac{N_w^2 - \omega^2}{\xi N_w^2 - \frac{\omega^2}{\xi}} \right]^2 \qquad (27)$$

If $N_s > N_w > \omega$ then $\xi N_w^2 > N_w^2$ and $\frac{\omega^2}{\xi} < \omega^2$ so that $\frac{Ri_s}{Ri_w} < 1$. Under these conditions instability always occurs in the strongly stratified layer first if Richardson number is the valid measure of stability for internal wave motions.

A classical transmission reflection problem for inertio-gravitational waves was examined. The same results were found to hold exactly for that system with two semi-infinite layers with different N's with no restriction on the vertical wave number.

So a positive correlation appears to pertain for internal wave motion between the magnitude of the density gradient and the magnitude of the shear for frequencies less than the minimum Brunt-Väisälä and greater than f for both low and high vertical mode structure. These results agree with those of Cox, et al. (1969) and O. M. Phillips (1976). It should be noted that a perfect correlation will not be observed because of the variation of the shear with the phase of the wave motion. This phase effect will produce a scatter of points at each N observed. From the measurements of Cox it is known that the smallest scale vertical temperature gradients exist on vertical scales less than 10 cm and from the dye streak measurements below it seems likely that at least some shear structure on the same small scales exists. It is expected that much of the strong positive correlation which might exist for internal waves trapped on a single sheet of high density gradient will be lost due to the 3 meter vertical sensor spacing, particularly if more than one interface is embraced. But a weak but distinctly positive correlation should be

observed for internal waves which are of large vertical scale compared to 3 meters between shear magnitude and density gradient magnitude even if the layers of high N were of small thickness compared to the scissors spacing of 3 meters. The lowest Richardson numbers should still be expected in regions of greatest density gradient even with some phase related shear scatter.

If the Bermuda shear measurements are correct something is very wrong about our simple linear ideas on the expected density gradient shear correlations and Richardson number predictions. The Bermuda measurements below suggest that at least in some regions the density gradient is negatively correlated with the shear magnitude and thus Richardson number is smallest in regions of weak stability. Woods (1969) provides further evidence that something is wrong. He finds for layers where $N_w \cong \frac{N_s}{3}$ that instabilities at any instant occupy 3 or 4% of the sheet (from heat flux conditions) and that: "A very much less frequent occurance is the breaking of internal, single sheet gravity waves, which was found mainly during the early morning instability of the top sheet of the thermocline". However 10 to 20% of the volume of the N_w layers are filled with mixing element at any time. So evidently the N_w layers have lower (although unmeasured) Richardson number more frequently than do the N_s layers. It also seems rather likely that the Richardson number must sometimes be negative in these regions of mixing because the mixing elements were observed to roll over. This frequency of instabilities in the N_w layers is not very different from the ±23%

probability for $Ri < \frac{1}{4}$ for the temperature derived density gradient or ±30% probability of $Ri < \frac{1}{4}$ for the T-S derived density gradient. The latter included a 13% probability that $Ri < 0$. Woods' results however include no mention of salinity or even the climatic mean direction of the salinity gradient so it is difficult to guess how closely our respective results should agree. The overturning velocities of his mixing elements are given as .1 to .3 cm/sec with diameter of from 20 to 40 cm giving a range of shear between 15 and 3×10^{-3} sec^{-1} which are not greatly different from the sheet (N_s) shears he reported or the Bermuda layer shears reported below. Could the shear in a system with unstable salinity gradients be greater? Perhaps it becomes more organized with rotors filling an entire 3 to 5 meter layer depth as in the salt finger model below. In that event the scissors' 3 meter spacing would measure the full value of the layer shear while underestimating the possibly more intense sheet shear which can occur on a smaller vertical scale (order 10 to 50 cm).

Salt convection

Turner and Stommel (1964) have shown that in the case of a stable density gradient ($\frac{\partial \rho}{\partial z} < 0$ when z is positive upward) there exist two possible convective regimes of oceanographic interest and both are driven by potential energy released by the differing molecular diffusion rates of heat and salt in sea water.

In the first regime, potential energy is released from an unstable salt field ($\frac{\partial S}{\partial z} > 0$) through columnar convection with adjacent rising and sinking filaments exchanging heat through their laminar interface at nearly 100 times the corresponding rate of salt exchange. These "salt fingers" are an extremely efficient counter-flow heat exchanger, allowing salt to drop out of layers above to layers below with a minimum cost in viscous dissipation and dilution due to mixing.

The second regime occurs through release of the potential energy of an unstable temperature field ($\frac{\partial T}{\partial z} < 0$) which causes finite amplitude convective layers to form, separated by very thin laminar interfaces. Here again, the greater thermal diffusivity allows heat to escape through the interface to drive the layer above while holding back the salt.

Although the second regime seems unlikely in the main oceanic thermocline, it does give insight into the form of convection which might be present were the "eddy coefficient" of salt to exceed the "eddy coefficient" of temperature - as suggested by Stommel.

Turner (1967) has shown that in salt finger convection,

buoyancy transport due to salt is about 1.8 times that due to temperature. (This is true over a range of interfacial buoyancy differences due to heat and to salt ($\frac{\alpha \Delta T}{\beta \Delta S}$) from two to ten.) Turner further demonstrates that this is sufficient to drive the Rayleigh type convective layers of the second regime. In the ideal case the permanent thermocline might be thought of as a series of alternate salt finger layers and Rayleigh layers (see figure **3.18**). The scissors data shows a more complicated structure in temperature and salinity than this to pertain in Bermuda but this does not necessarily rule out salt fingers. This layering has been observed (Stern and Turner, 1969) in laboratory experiments using sugar and salt solutions which avoid heat loss problems at the side walls which make experiments with heat difficult near $\frac{\alpha \Delta T}{\beta \Delta S} = 1$.

From a laboratory model with two salt finger layers (one above and one below a convective layer) Turner found measured salt fluxes, F_s, in the Rayleigh layer. These exceed those calculated for solid plane boundaries by f = 12 to 42 times, as the ratio of interfacial buoyancy differences due to temperature to that of salt varied from two to ten.

With this information, the salt flux and the "eddy coefficient" for salt through the convective layer may be calculated according to

$$Fs = F^{*} f \left[\frac{\alpha \Delta T}{\beta \Delta S} , \frac{Ks}{Kt} \right]$$

where $F^* = A(\Delta S)^{4/3}$(reference flux for solid walls) and where

$$A = CKs \left[\frac{g\beta}{\chi_s \nu}\right]^{\frac{1}{3}}$$

and

$C = .085$

K_s = molecular salt diffusivity

K_t = molecular heat diffusivity

$\chi_s = K_s/\rho$

β = salt expansion coefficient

α = heat expansion coefficient

Although no experimental results were obtained where the ratio of buoyancy differences due to salt to that of temperature approached one, Turner believes the ratio of fluxes F_s/F^* may be 50.

Turner (1967) concluded with a computation of downward salt flux under the outflow of the Mediterranean west of Gibraltar where STD soundings indicated a layered structure. In a region with such a large salt excess above and small density gradient ($\frac{d\sigma t}{dz}$ = 2.5×10^{-4}/meter and $\frac{\alpha \Delta T}{\beta \Delta S}$ = 1.15 ±.12) the "eddy coefficient" $K_s = 5$ cm^2/sec seems entirely reasonable. Similar computations on selected layers in the scissors section give $K_s \cong 2$ cm^2/sec and therefore $K_t \cong 1$ cm^2/sec. These numbers seem completely reasonable compared to the global thermocline mean diffusivity given above.

In the upper main thermocline near Bermuda, $\frac{\alpha \Delta T}{\beta \Delta S}$ ranges

between 1.5 and 2 in the interval from 475 to 800 meters (see figure **3.28**). Below 800 meters the curve of $\frac{\alpha \Delta T}{\beta \Delta S}$ vs. depth changes slope abruptly. This might be evidence of different processes at work above and below 800 meters. At the site of the dye streak dive $\frac{\alpha \Delta T}{\beta \Delta S}$ approaches 2 only between 150 and 300 meters. A similar but less pronounced slope change takes place at 300 meters. The regions where $\frac{\alpha \Delta T}{\beta \Delta S}$ is least should be the most likely locations for salt fingers because the least work is required to transport heat against the density gradient. The slope of the deeper curve at both locations appears to be equal on semi-log coordinates, suggesting a similar decay process at both sites. There seems to be significant difference between the character of the shear in the $\frac{\alpha \Delta T}{\beta \Delta S}$ order 2 layers and the layers where $\frac{\alpha \Delta T}{\beta \Delta S}$ is large compared to 2 (see figure **3.29**).

A more extensive discussion of salt fingers related to the scissors and dye streak data is given below.

Horizontal advection

Due to the similarity of micro-structure near land and far from land (Cooper and Stommel, 1968) it appears improbable that lateral advection of properties from oceanic boundaries and islands is responsible for the layered T-S structure observed in the main thermocline, but the possibility cannot be ruled out completely. If these layers were created elsewhere and slid into the thermocline like cards in a deck then the energy of mixing might be quite small in the interior and a series of laminar sliding layers could be observed.

In a recent laboratory experiment Cacchione (1970) showed that progressive internal waves which run up on a sloping bottom can become unstable if the frequency of the input wave exceeds some critical value. This instability has the form of a row of regularly spaced vortices along the slope with short spacing compared to the input wave length. Thin wisps of mixed fluid originating at each vortex penetrate the interior of the fluid. He further shows in a three layer model that the tidal frequency is super critical on the continental slope providing an ample source of mixing energy.

A simple calculation in chapter 2 assuming other advective processes to be absent shows that layers of the sort observed during the dye streak experiment could have propagated the required 20 km only if diffusive processes proceed at near molecular levels.

CHAPTER 2

EVIDENCE OF SHEAR MICROSTRUCTURE IN DYE STREAK DATA

Introduction

As seen in the preceding chapter many observations of salinity and temperature microstructure have been made at sea in the main thermocline. With the exception of Woods' near-surface Malta data there are few records of fine-scale velocity measured in thermocline structure. The data taken with Professor Rooth on Alvin dive #219 on September 10, 1967 are the only known records of shear as a function of depth taken in and below the permanent thermocline in the ocean with fractional meter resolution. The dive took place near the 2,000 meter contour on the continental slope due south of Martha's Vineyard (see figure **2.1**). The data show pronounced shear structure with vertical scales of a meter or less at depths of hundreds of meters. Numerous reversals in the direction of the shear are observed on the same small scale, some of which give the appearance of interleaved sliding layers or inertio-gravitational internal waves of high vertical wave number. The shapes as well as strengths of the observed shear structure have a strong dependence on depth.

Background and technique

Alvin was equipped with stereo cameras, dye dispensing apparatus and a temperature gradient device which malfunctioned (see figure **2.2**). During each experiment a pair of fluorescein dye

pellets were released and allowed to fall, leaving two straight vertical trails separated by about a meter horizontally. Each pellet left a small spiral wake of ring vortices and plumes which grew to about 20 or 30 centimeters diameter as the wake decayed. These vertical streaks would then be distorted according to the time integral of the shear (see figure **2.3**). By using a redundant pellet it was clearly verified that streak shape was not due to any random wake phenomenon. Once several minutes had elapsed the submarine would follow down the trails taking photographs at 6 or 8 second intervals. Of the 400 exposure pairs made, 76 pairs were reduced on a Ballplex Stereo Projector (see figure **2.4**). These were selected for their photographic clarity, continuity from pair to pair, and lack of submarine interference. In all, seven sequences of photographs were reduced between 167 and 905 meters depth covering 9% of this total depth range. A sequence consists of 3 to 20 pairs which could be joined by 3 or more common, distinctly identifiable, small-scale wake features between adjoining pairs.

The shear was computed from discrete data points sampled from a continuous dye streak while it was projected in stereo. Due to the large amount of work connected with data reduction only those points where a change of direction of the streak occurred were sampled. This accounts for the non-uniform thickness of the shear layers shown in figure **2.5** . Each layer represents the average vector shear between two sampled points and includes both magnitude and direction (in local dye streak coordinates). Since no compass was sampled during

these measurements, succeeding sequences cannot be related in direction (except the ones between 418 and 465 meters).

The magnitude information is shown by the solid line with a dot at the center of the averaged interval, while the angle data is dashed with a small vertical rectangle at its center. The error bars were computed assuming a ±5° error in the position of the assumed vertical about both x and y axes. A horizontal rectangle gives the angle error bar so it may be distinghished from the conventional magnitude error bar where they overlap.

Magnitude of the shear

The average magnitude of the shear $\overline{S}$ is generally largest near the surface (about 10^{-2}1/sec at 167 meters) and becomes smaller with increasing greater depth until 450 meters where it settles down to order 10^{-3}1/sec (see figure **2.6**). The weights used in computing the average shear for each sequence are the same layer thicknesses seen in figure **2.5** . The standard deviations about these means are computed with the same weights and decrease more sharply with depth than the mean itself. In fact the ratio $\frac{\overline{\sigma}}{\overline{S}}$ decreases exponentially from .9 in the shallowest sequence to .1 in the deepest (see figure **2.7**). So the shallow shear has small-scale spatial fluctuations in magnitude of the same order as the average shear, while near 900 meters the fluctuations are only a tenth of the average. Woods' Malta data gives $\frac{\overline{\sigma}}{\overline{S}} = 1.28$ at 30 ±10 meters depth in the seasonal thermocline with a mean shear of .011 1/sec, which is

rather close to the mean shear for the uppermost Alvin data.

Direct examination of the magnitude of the shear in figure 2.5 shows that regions of more intense shear tend to be thin compared to the intervening regions in the shallow observations. In deeper measurements these regions have nearly equal thickness. In the terminology of Woods (1968) the thin intense shear regions are called sheets and the thick regions of low shear are called layers. The choice of a figure of merit to describe the presence of intense sheets in thermocline layer structure is somewhat arbitrary. Clearly the frequency distribution of strongly sheeted structure will be skewed heavily toward high shears while more equal thickness of sheet and layers will be more nearly normal. The third moment about the mean shear ν_3 provides a measure of skewness. The shear data divides into two regions. At depths less than 400 meters the third moment is large and positive indicating strong sheets and below this level it becomes small and of mixed sign (see figure 2.8). A more representative figure of merit is the sheet intensity $I = \sqrt{\frac{\nu_3}{S}}$ which compares the third moment about the mean to the mean itself. Both criteria show a rather steady decrease in the intensity of strong sheet structure with depth. The shallow Malta data of Woods is plotted on the same scales for comparison (inverted triangles) based on the Woods (1968) data. It appears more sheetlike than even the shallowest Alvin shear data.

The angle of the shear

The angle of the shear vector changes significantly on the same small scale as its magnitude. Variations of 90 to 180 on vertical scales of a meter or less occur in all dye streak records reduced. The correlation between changes in angle and changes in magnitude as a function of depth does not generally appear strong. The shear angle has higher spatial frequency changes near the surface and more gradual changes at greater depth in a manner similar to the magnitude changes discussed above.

The two longest records occur between 418 and 464 meters (see figure **2.10**) and over all but three meters of this 47 meter interval. The single 3 meter gap in the record represents only a 24 second loss of information. This makes it possible to patch the two angle record together with negligible uncertainty (probably less than $\pm 10°$).

The most striking feature of this angle record is its ten meter scale periodic nature. These angular oscillations are about 180° amplitude with somewhat smaller scale (90° or less) oscillations superimposed. They are also seen in the progressive vector diagrams in figure **2.11** where velocity is plotted as a function of depth. These diagrams have the same shape as the dye streak itself when seen from directly above. The periodic nature of these records might suggest some kind of inertio-gravitational wave with high vertical wavenumber or wavenumbers. Another equally plausible explanation might be sliding layers formed by mixing processes such as breaking

internal waves on the continental slope as proposed by Cacchione (1970). The 180° reversals look quite similar to those shown in his figure 68. Such layers would need to propagate horizontally 20 or more kilometers to reach the slope by the most direct path at 400 to 500 meter depths.

If one assumes that alternate layers in depth (between 425 and 464 meters) are bound toward the slope and away from the slope and that no other advective processes are at work then one can calculate their relative velocities to be of order 1.4 cm/sec between their respective cores. The layers leaving the slope then would have an outward velocity of 0.7 cm/sec or 0.6 km/day. This would require a minimum layer life-time of about a month. Assuming the expression for layer life-time T given by Stommel and Fedorov (1967): $T = \frac{h^2}{2k}$ where h is the half layer thickness and k is the diffusivity one finds for these 10 meter layers of month life-time, $k \leq .01$ cm /sec. That is less than 10 times the molecular coefficient for temperature diffusion.

Relevant temperature, salinity, and density records

Because no useable temperature or salinity data was taken during the actual dives, other sources of data must be used if a comparison with this shear data is desired. STD stations 1 through 10 taken on Professor Wunsch's Atlantis II cruise #47 run down the continental slope past the Alvin dive site and on to site D. These stations were taken in mid-November and are expected to give salinity and temperature information quite similar to that of the Alvin dive

#219 except perhaps in the near surface region. In particular the large salinity-stabilized temperature inversion is seen on most of the slope and shelf stations at about 75 meters ±20 (see figure **2.12**). Below a hundred meters smaller temperature inversions are present which decrease in amplitude and frequency with depth, becoming rare below 300 meters. Similar inversions were noted on the Alvin dive because they interrupted sonic communications with the surface and registered on the sphere temperature indicator. These features are clearly shown in the profiles and T-S diagram from station 8 in figures **2.13** and **2.14** respectively.

Below 150 meters the temperature and salinity gradients are generally in the proper sense for salt fingers to be present. In the region between 150 and 275 meters the average salinity gradient is .003 ‰/meter which is about the same gradient as in the main thermocline near Bermuda at 500 to 700 meters depth. The smallest shear measured was 3×10^{-4} $\pm1\times10^{-4}$(1/sec) at 236.3 meters. This is shown in figure **2.3b** below and to the left of the kink in the center of the pictures. The difference in velocity over this 40 cm layer is 1.2 mm/sec ±.6 mm/sec. There are long laminar looking filaments streaming out of this spot on the left streak. These filaments are clearly sheared even in this weakly sheared layer. These finger-like filaments were doubtless enhanced or triggered by the presence of the fluorescein dye. This structure looks unlike that seen in the other locations with stronger shears present and may give some idea what an actual salt finger layer may look like in nature.

Stability considerations

For the onset of shear instability the critical value of Richardson number $Ri = \frac{N^2}{(SHEAR)^2} = \frac{1}{4}$, then $\frac{N}{SHEAR} = \frac{1}{2}$, or the critical shear $S_{crit} = 2N$ (see Chapter I). It has also been suggested by Paul Linden in a personal communication that salt fingers can exist only for $Ri \gtrsim 10$ or greater in a laminar shear flow. The Brunt-Väisälä frequency N for STD station 8 is plotted in figure **2.15** as a function of depth. The mean Brunt-Väisälä frequency $\overline{N}$ for each depth where dye shear measurements were made is plotted as circles. N was also computed from the slope of the linear least squares fit of density vs. depth in a region ±10 meters from each mean dye experiment depth at stations 7, 8 and 9 for both raising and lowering. $\overline{N}$ is the mean of these N's at each of the above depths. $\overline{N}$ is computed from about 100 individual density observations in each experiment depth with individual N's varying from $\overline{N}$ by 50%. The STD errors make the computation of meter scale statistics of Väisälä frequency practically meaningless (depth ±3 meters, temperature ±.01°C, salinity ±.01 ‰ repeatability).

The mean values of shear $\overline{S}$ from the dye data and Väisälä frequency $\overline{N}$'s from Atlantis II 47 are plotted in figure **2.16** together with dashed lines for Ri = 1/4 and 10. Except for points closest to the surface all the points are well removed from shear instability in the mean. The point at 167 meters may be an artifact caused by autumnal surface cooling or advective processes. These mean data seem to suggest Richardson numbers closer to the value 10 suggested

for salt fingers. Local values of N are likely to vary by a factor of two or more from the $\overline{N}$ at each depth. The standard deviation of the shear varies from $.9\overline{S}$ at 167 meters to $.1\overline{S}$ at 900 meters (see figure **2.7**). So while figure **2.16** gives a suggestion that salt-fingers may be present and shear instability less likely, a more careful study with smaller scale temperature and salinity gradient measurements is called for to match the dye streak resolution and thus determine local Richardson number statistics on a fractional meter scale.

Discussion

If one considers step-like variations in density and velocity with depth to be evidence of some mixing process then variations of their vertical gradients compared to their mean vertical gradient at some location may be a measure of the intensity of this mixing. This same reasoning should hold for the intensity of intermingling of sliding layers. As seen in figure **2.7** the ratio of $\frac{\overline{\sigma}}{\overline{S}}$ appears to decrease exponentially from the surface with a distance constant of 350 meters. This may be evidence that energy for mixing enters through the surface and propagates downward in some manner, decaying as it goes and causing progressively less intense mixing at increased depths.

A semi-log plot of $\frac{\overline{\sigma}}{\overline{S}}$ vs. Väisälä frequency gives a good fit to the dye data below 400 meters (see figure **2.17**). The mean data taken by Woods (1968) also seems to fall on this line.

The shallower dye data departs somewhat, perhaps due to changing surface conditions between cruises or real variations. The scissors shear data also departs from this curve in the same manner, which may be evidence of the influence of a different mixing process like salt fingers. These data may also be direct evidence of the mixing processes and are easier to compare with data from other locations, being independent of the depth and shape of the thermocline.

Spatial fluctuations in shear, such as those observed at 170 meters, moved by an internal wave of small vertical wave number (i.e. the main thermocline moving as a whole) could reduce the high frequency coherence between even closely-spaced moored current meters. Such low coherence at higher frequencies has been reported by Siedler (1970) from site D data. Siedler's interpretation of internal wave motion of high wave number may be equally valid.

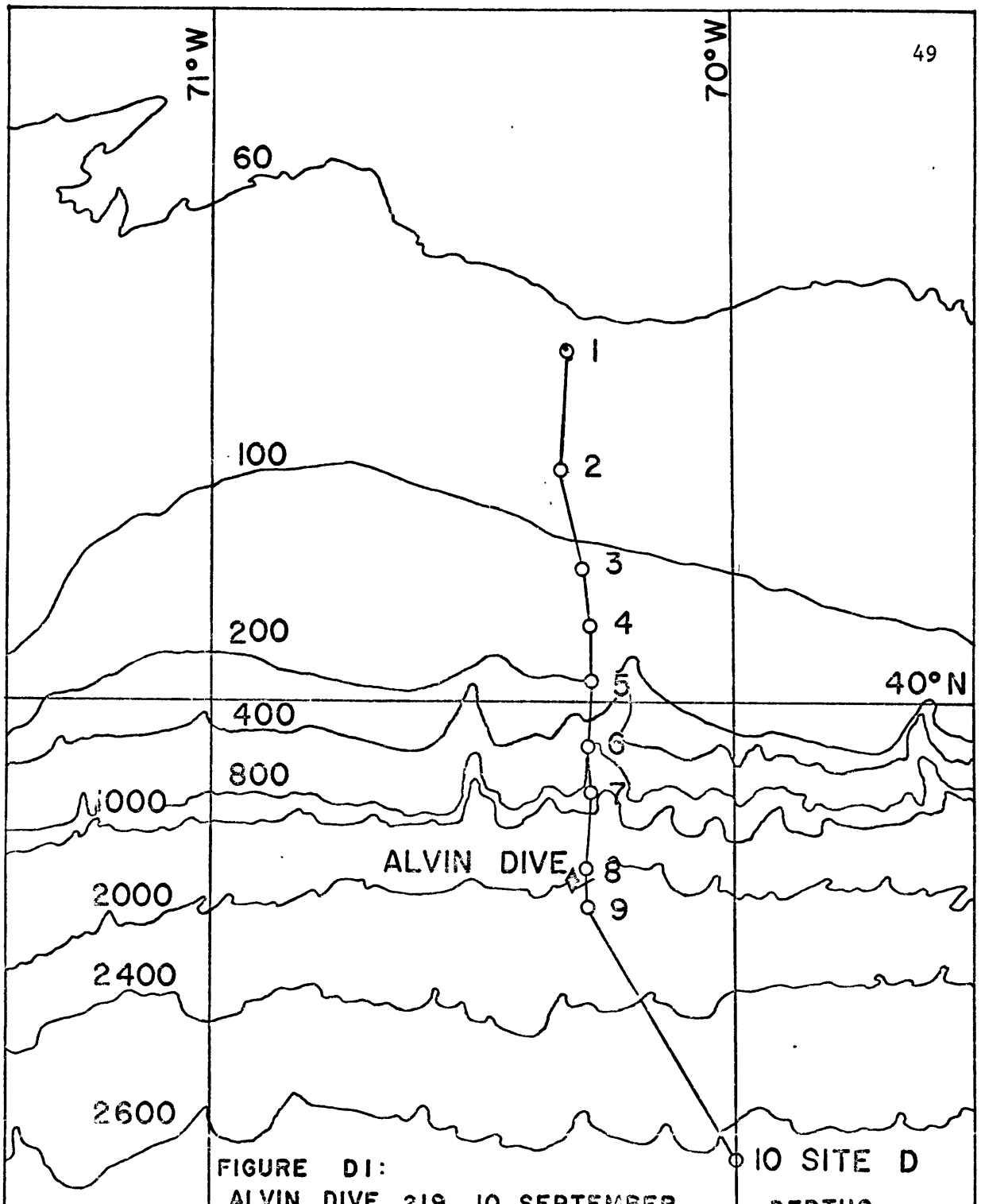

FIGURE D1:
ALVIN DIVE 219, 10 SEPTEMBER 1967. THE OPEN CIRCLES LOCATE ATLANTIS II CRUISE 47 STD STATIONS 1 THROUGH 10 OCCUPIED ON 16 OCTOBER 1968

DEPTHS CONTOURED IN METERS

FIG. 2.1

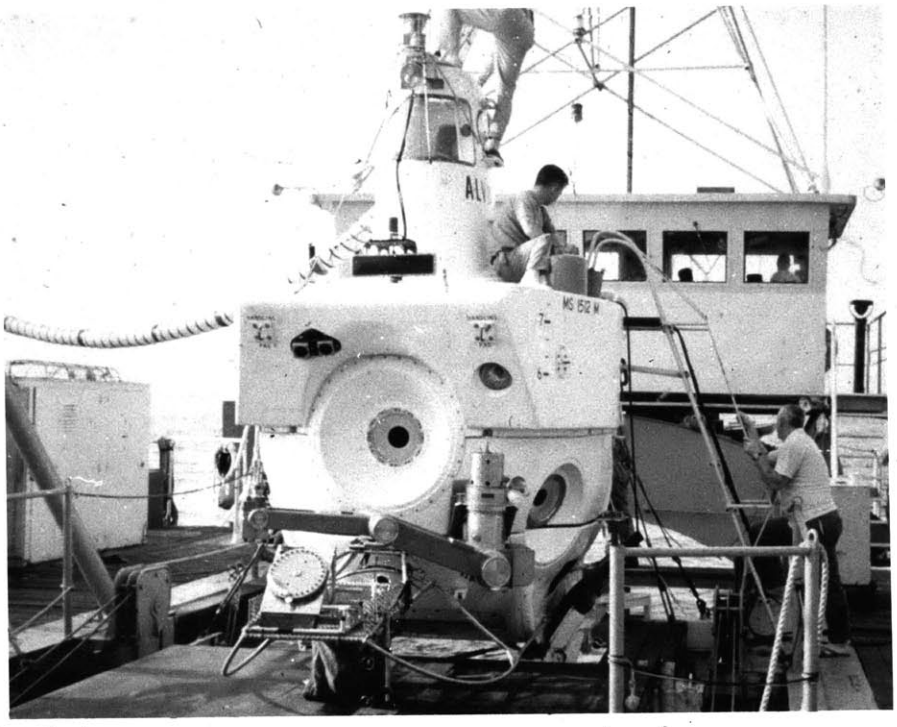

Submersible Alvin ready for dye streak dive. Note stereo cameras (upper left) and flash (upper right),

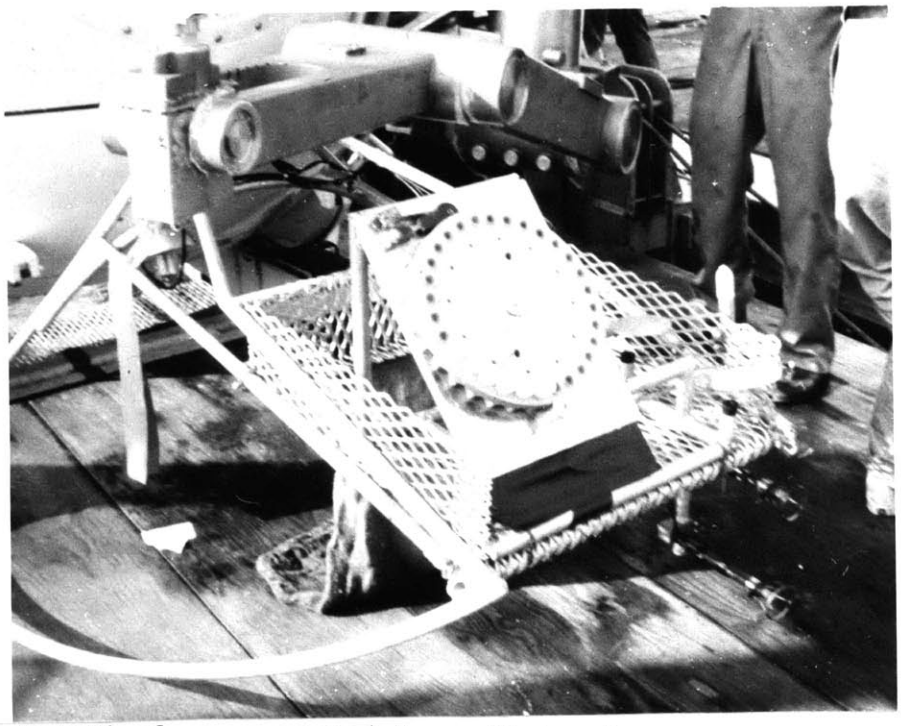

Detail of arm operated dye pellet releaser.

FIG. 2.2

FIG. 2.3: Stereo dye streak photos

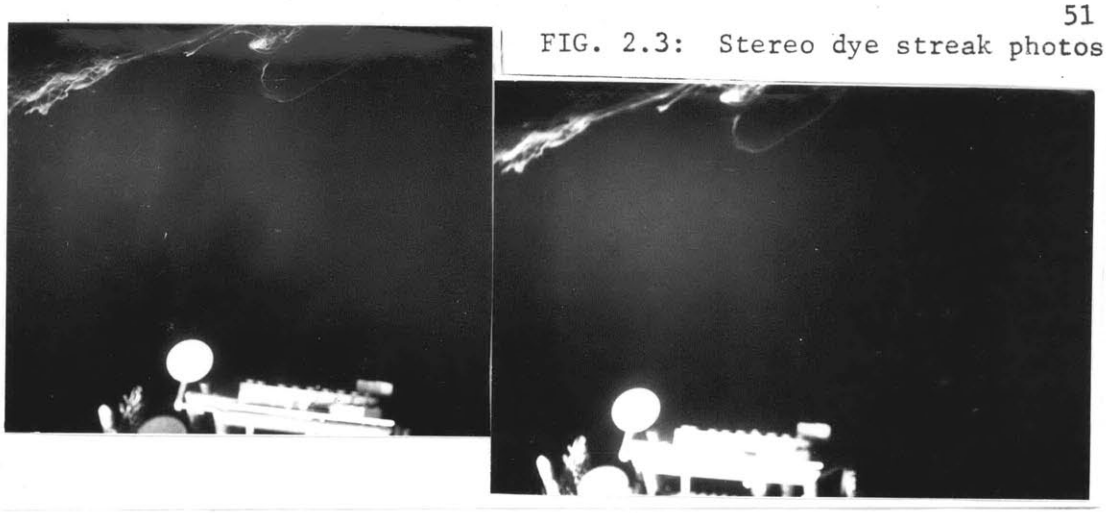

a) Depth 230 m, E. T. = 14 min. Example of high shear with a laminar looking core region similar to those reported by Woods (1968).

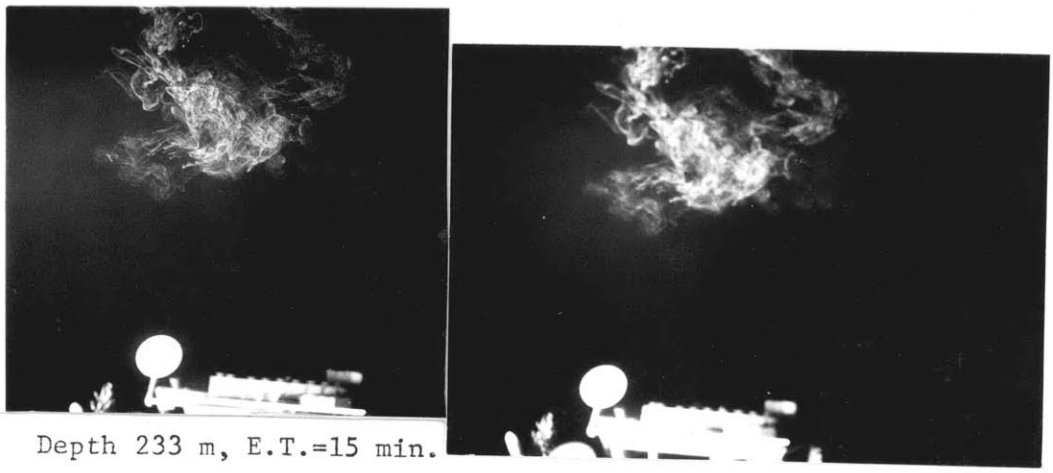

Depth 233 m, E.T.=15 min.

b) Note how both dye streaks contort together. Also note the streamers issuing from the left side of the left streak below the strong kink. The region with streamers contains the lowest shears measured.

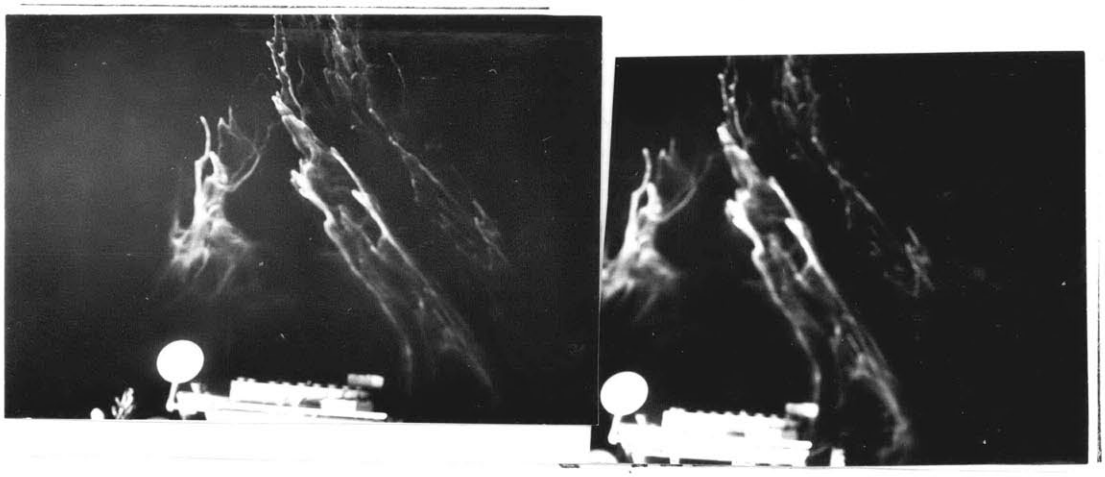

c) Case of submarine interfering with dye streak shape.

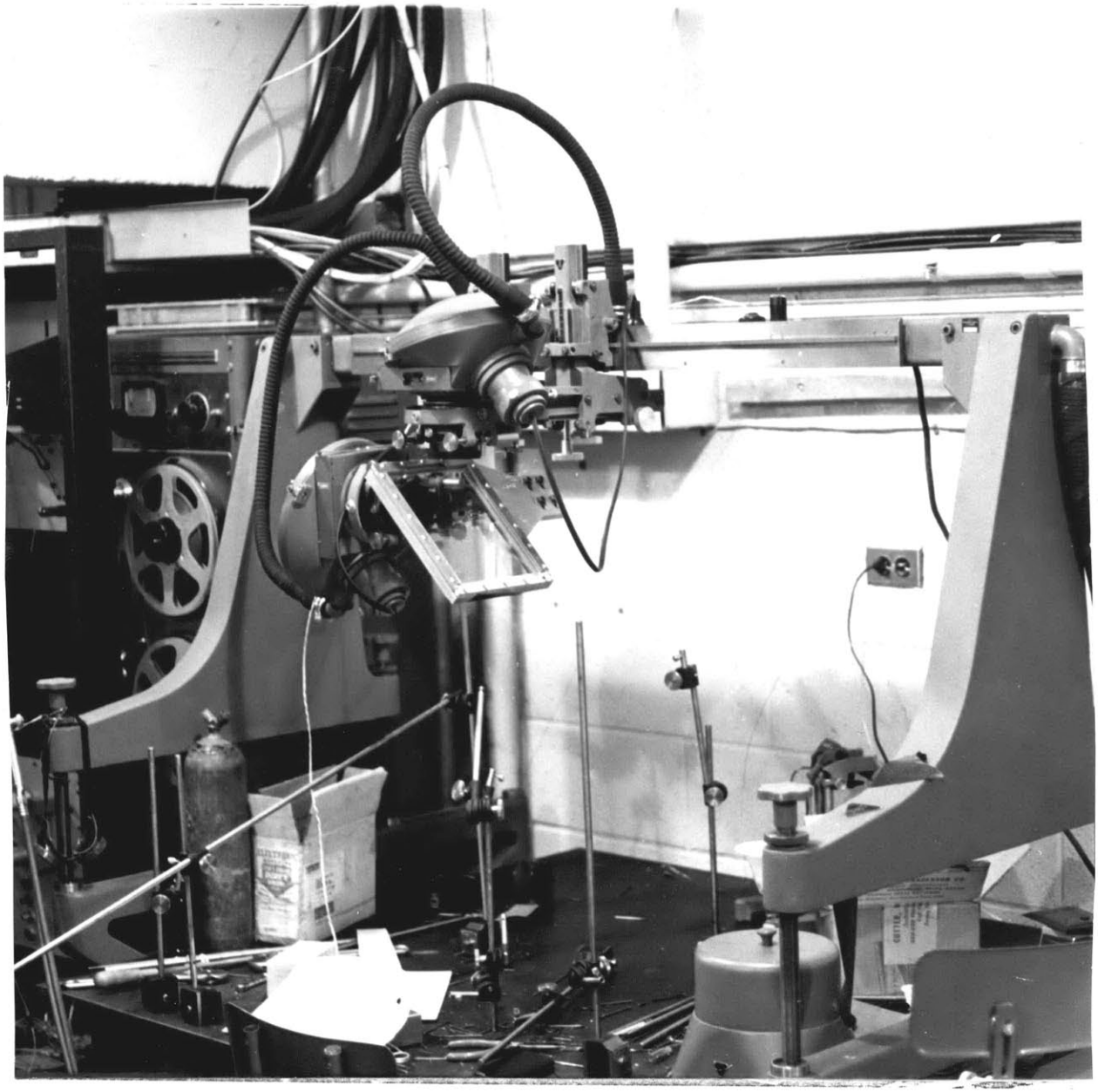

FIG. 2.4 Modified ballplex stereo projector

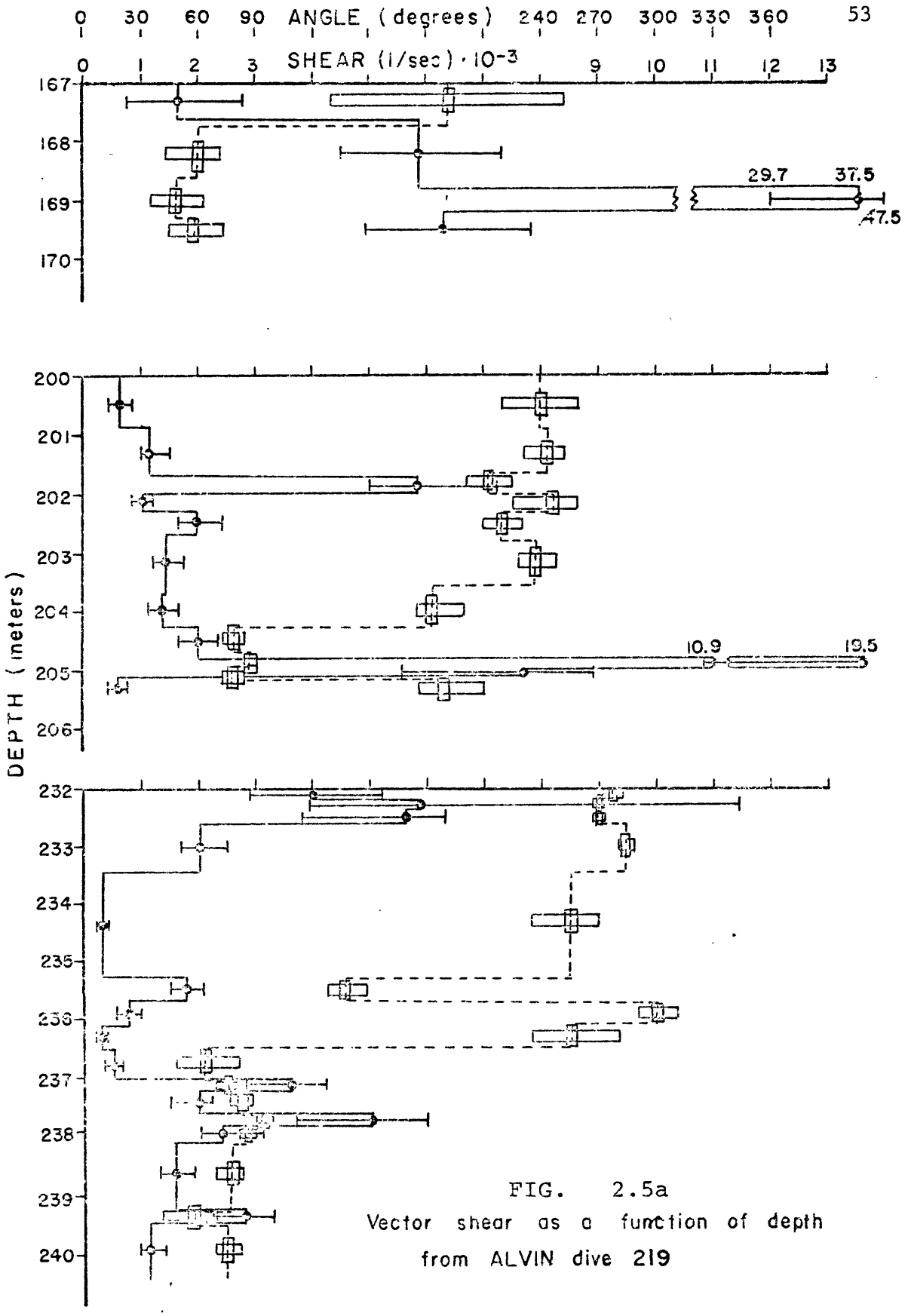

FIG. 2.5a
Vector shear as a function of depth from ALVIN dive 219

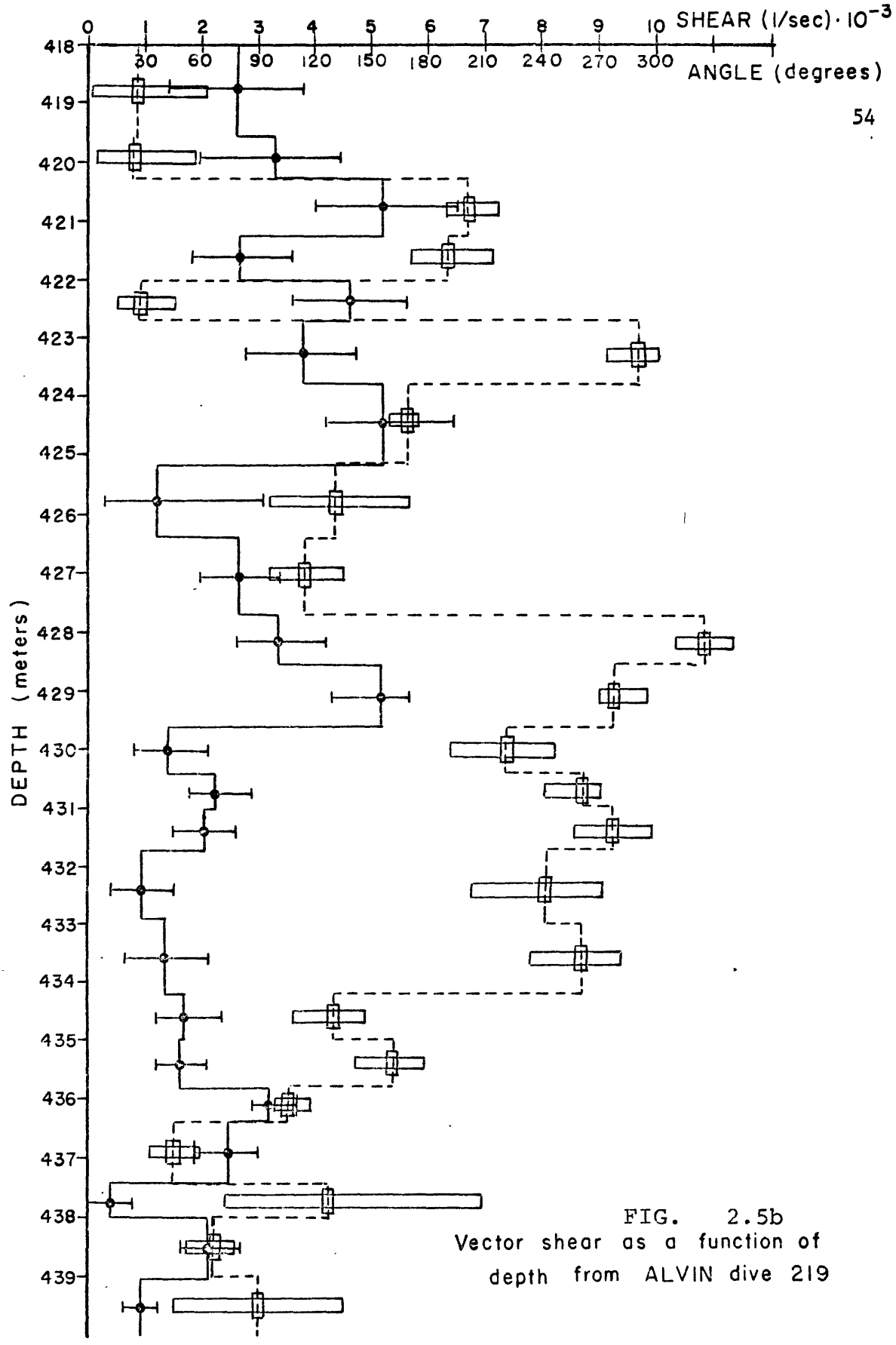

FIG. 2.5b
Vector shear as a function of depth from ALVIN dive 219

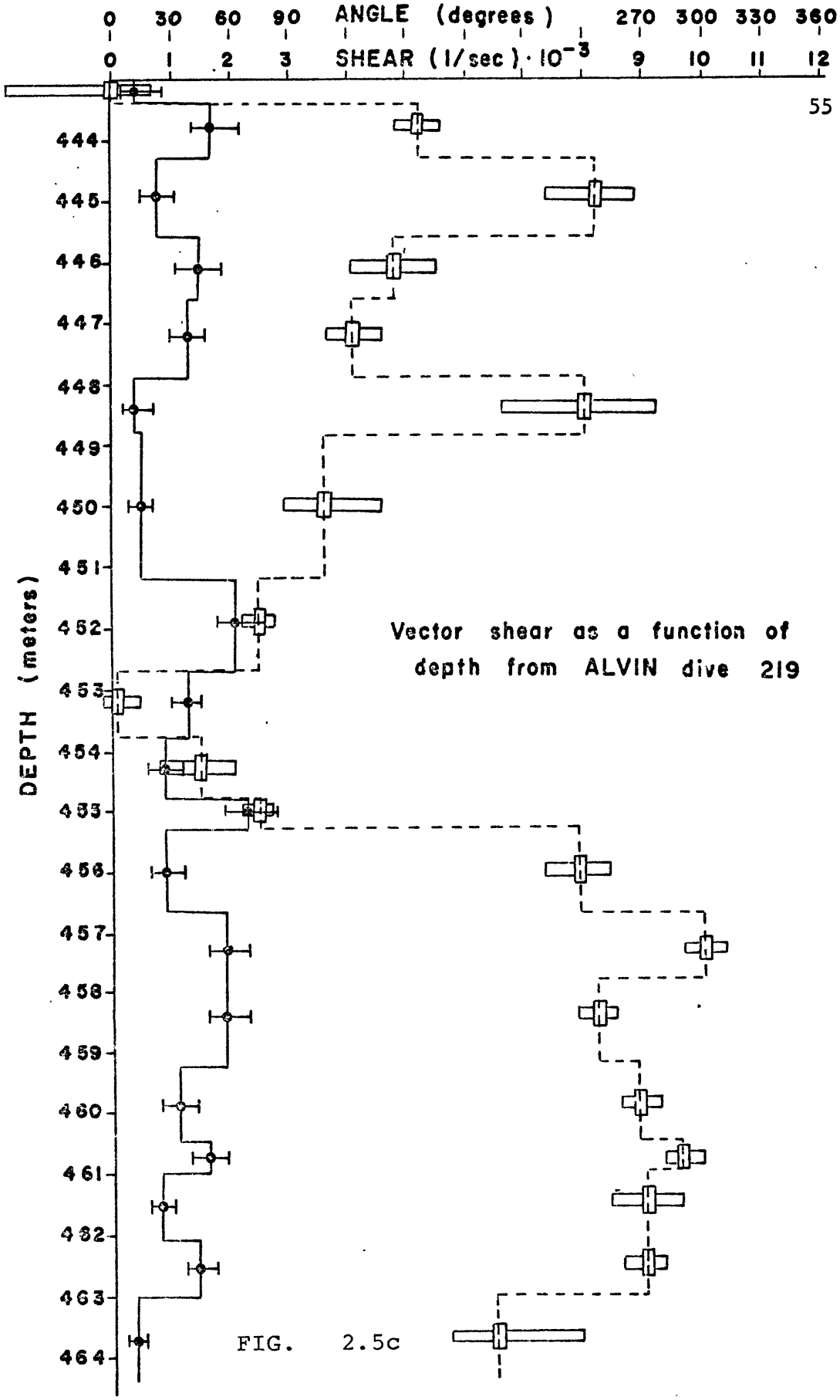
0 30 60 90 ANGLE (degrees) 270 300 330 360
0 1 2 3 SHEAR (1/sec)·10⁻³ 9 10 11 12
DEPTH (meters)
444
445
446
447
448
449
450
451
452
453
454
455
456
457
458
459
460
461
462
463
464
Vector shear as a function of depth from ALVIN dive 219

FIG. 2.5c

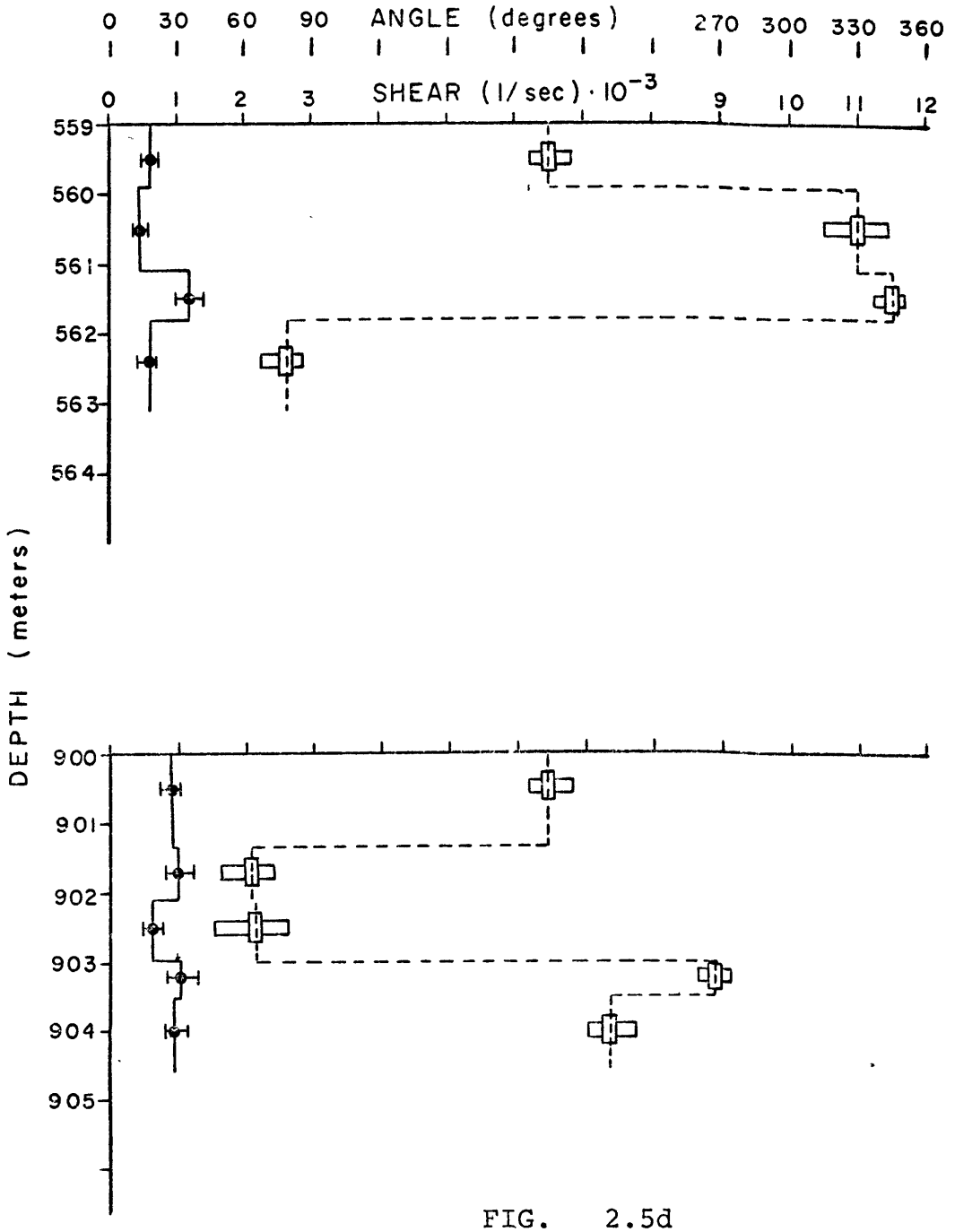

FIG. 2.5d
Vector shear as a function of depth from ALVIN dive 219

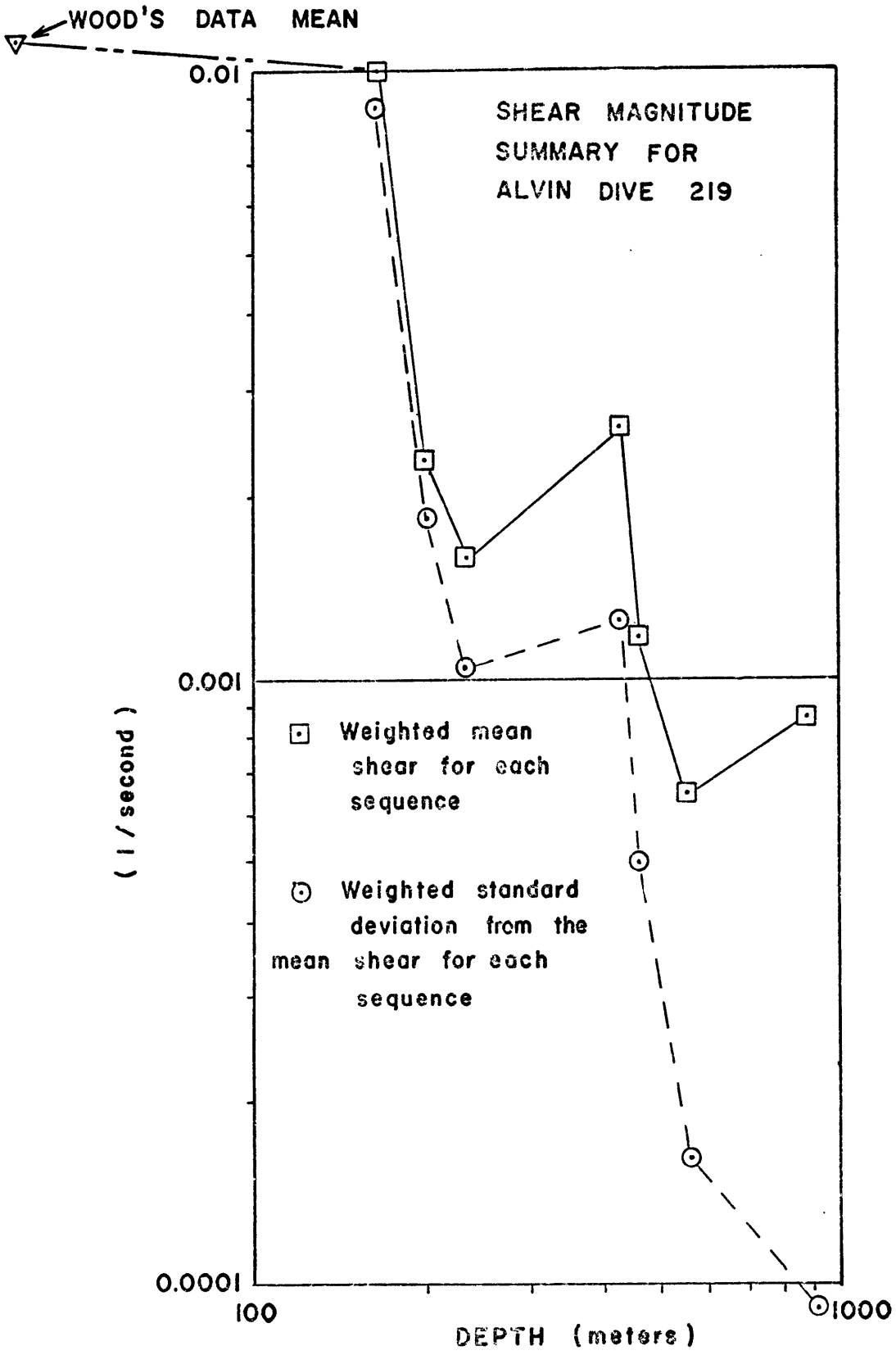
WOOD'S DATA MEAN
0.01
0.001
0.0001
SHEAR MAGNITUDE
SUMMARY FOR
ALVIN DIVE 219
Weighted mean
shear for each
sequence
Weighted standard
deviation from the
mean shear for each
sequence
(1 / second)
100
1000
DEPTH (meters)

FIG. 2.6

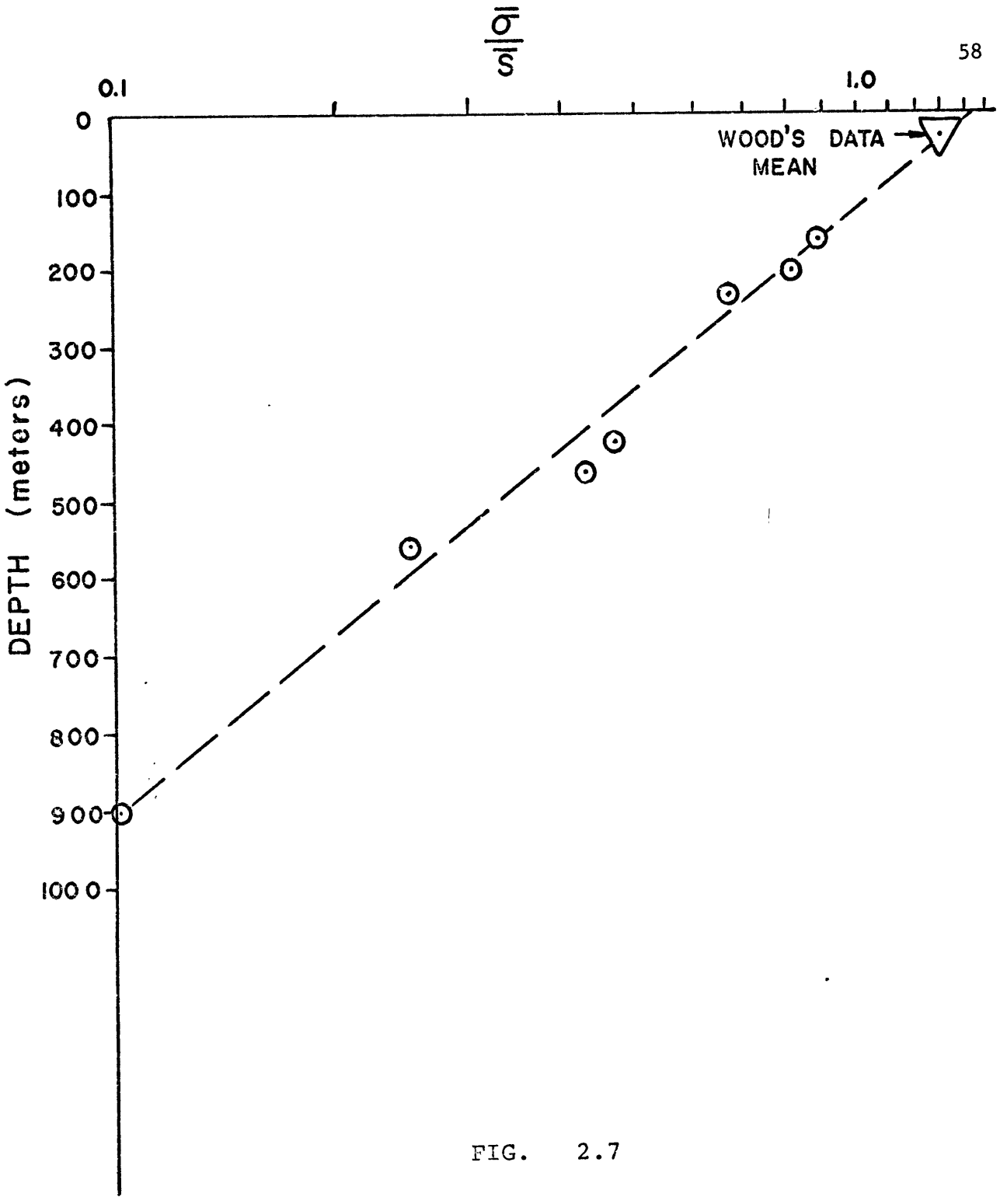
$\frac{\sigma_l}{\sigma_s}$
0.1
1.0
0
100
200
300
400
500
600
700
800
900
1000
DEPTH (meters)
WOOD'S DATA
MEAN

FIG. 2.7

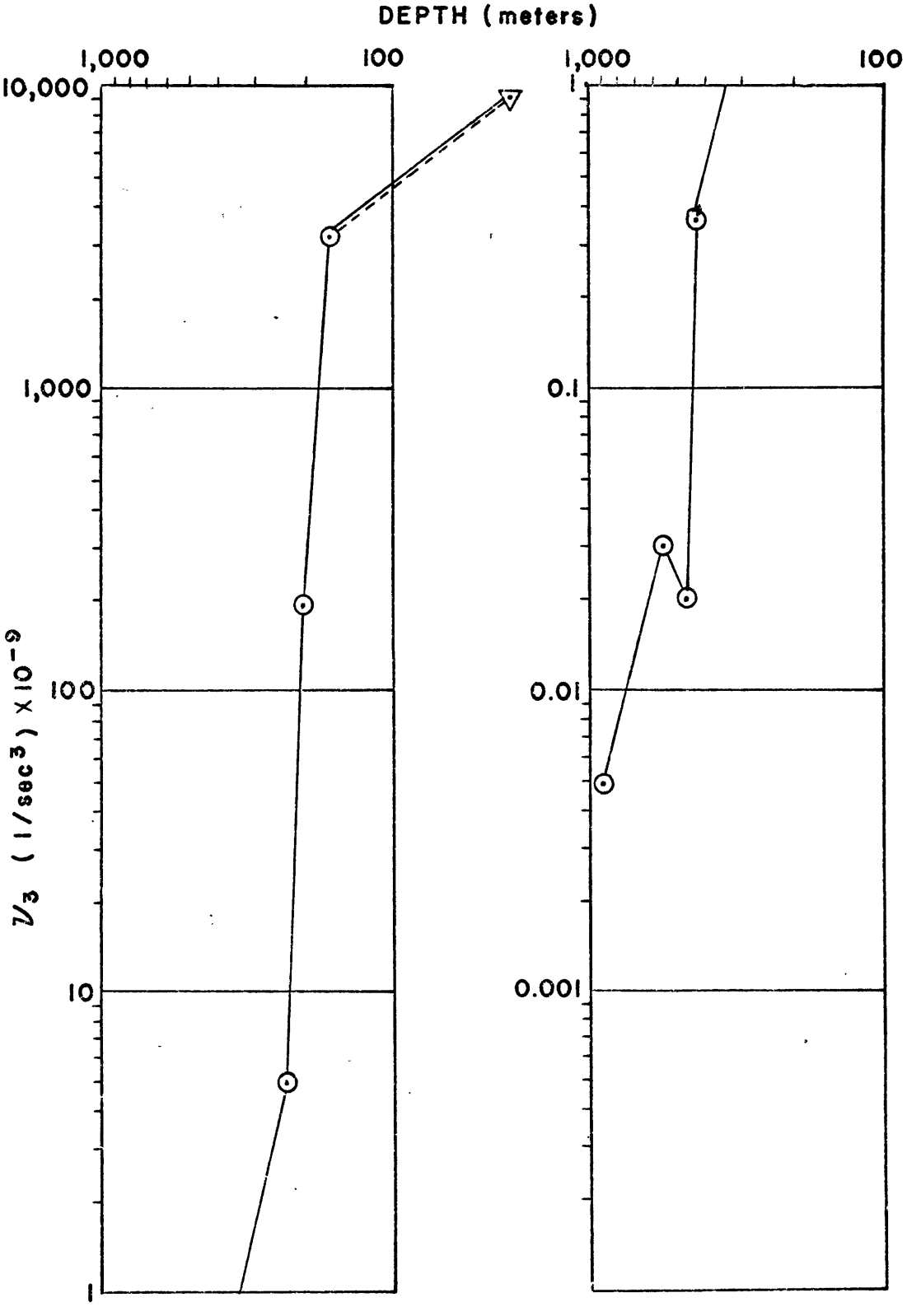
DEPTH (meters)
1,000
100
1,000
100
10,000
1,000
100
10
1
0.1
0.01
0.001
γ_3 (1/sec^3) X 10^{-6}

FIG. 2.8

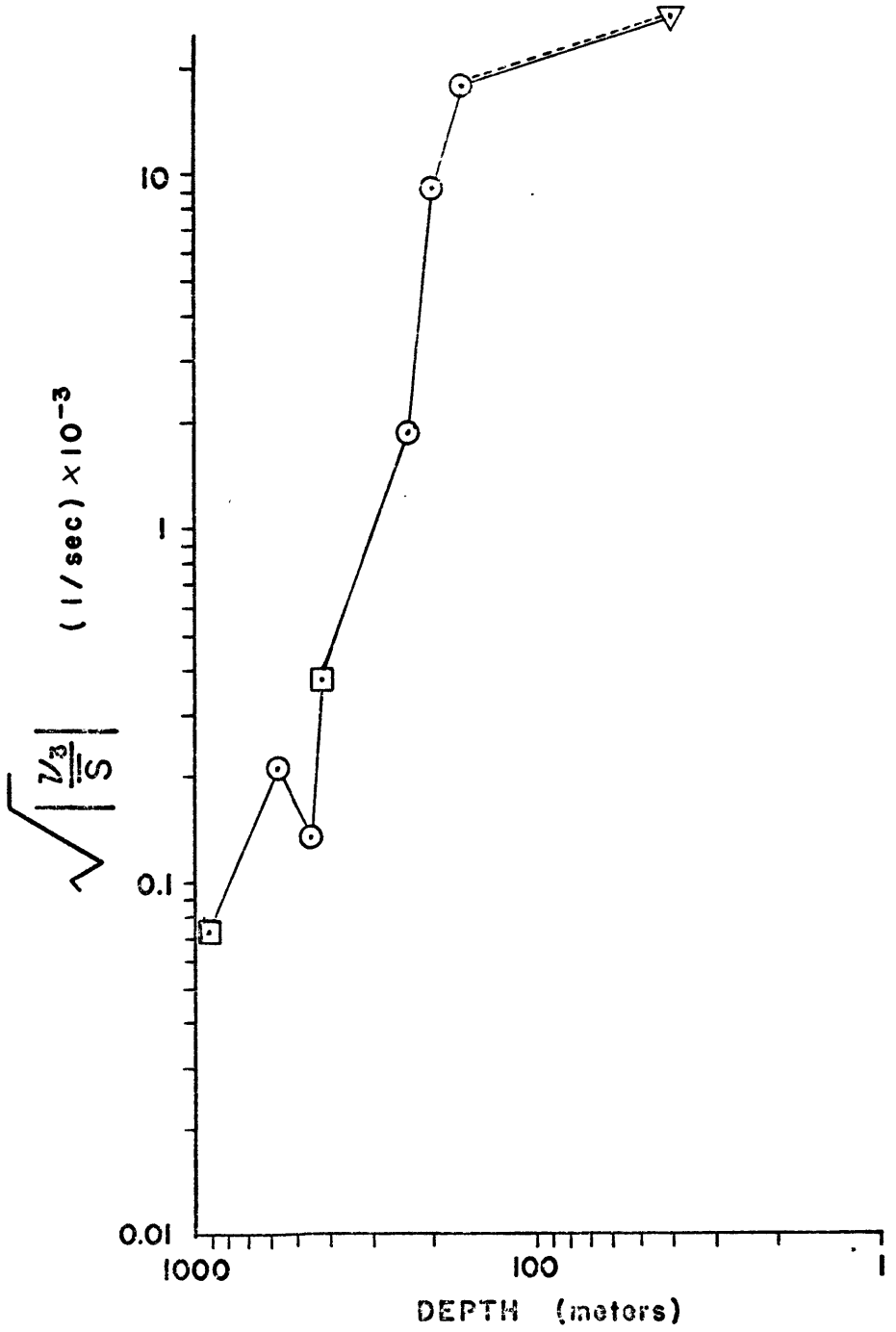

FIG. 2.9 Sheet intensity as a function of depth.

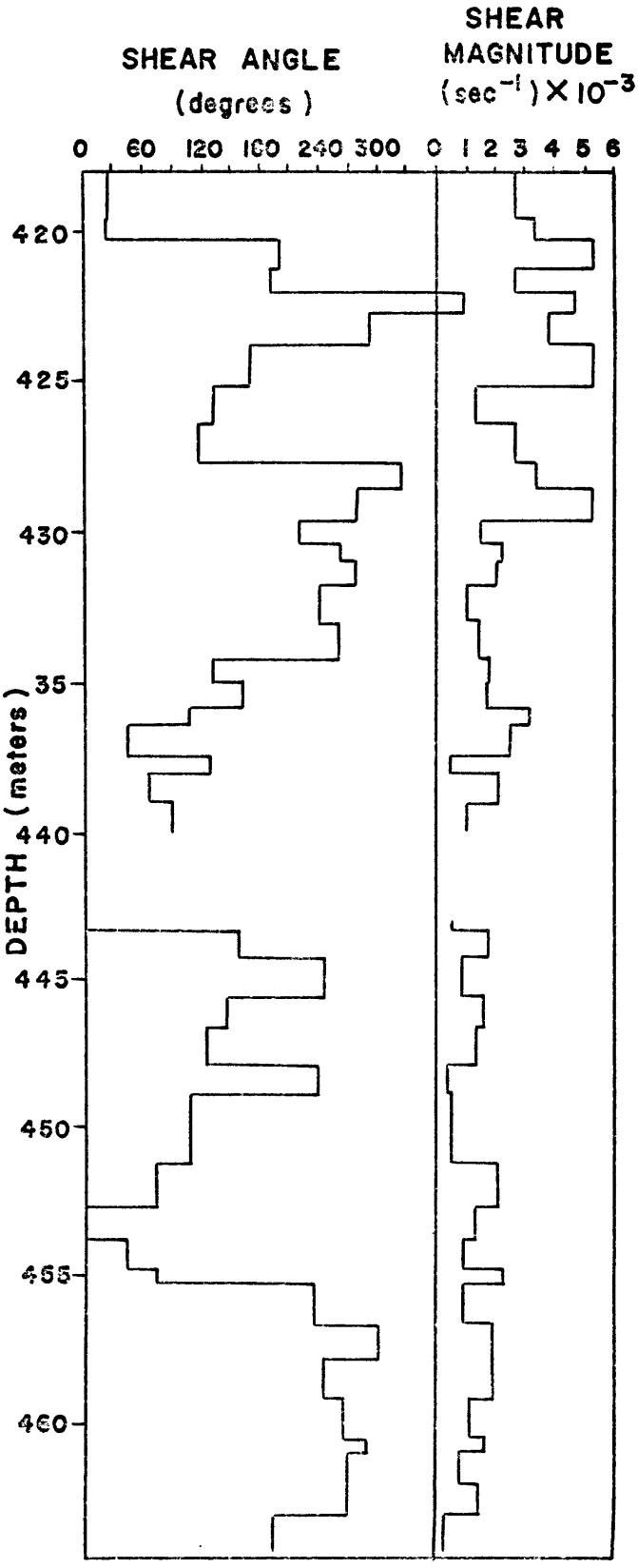
SHEAR ANGLE
(degrees)
SHEAR MAGNITUDE
(sec⁻¹) X 10⁻³
0 60 120 180 240 300
0 1 2 3 4 5 6
420
425
430
435
440
445
450
455
460
DEPTH (meters)

FIG. 2.10

Progressive vector diagrams of Velocity vs. Depth

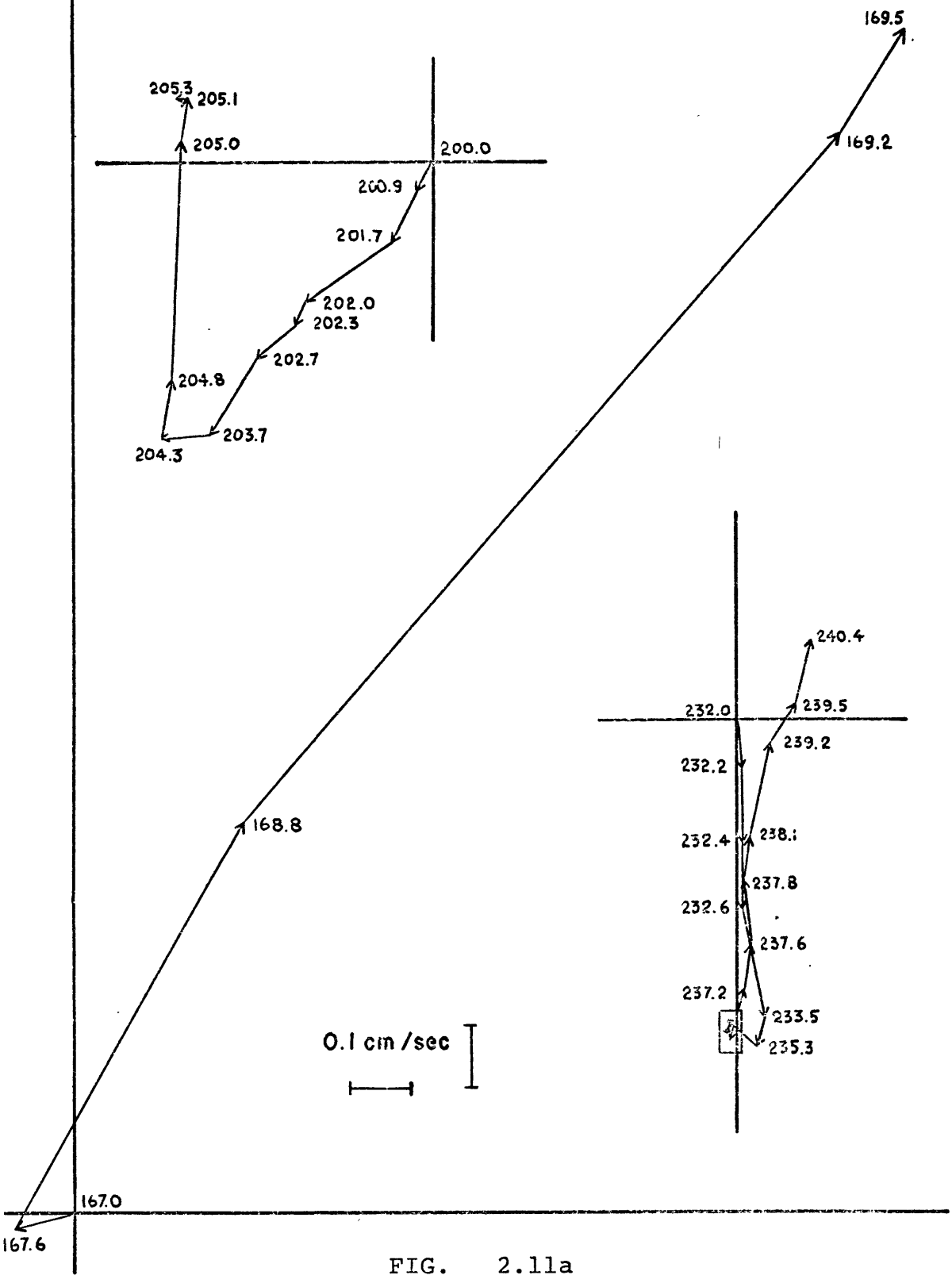

FIG. 2.11a

Progressive vector diagrams of Velocity vs. Depth

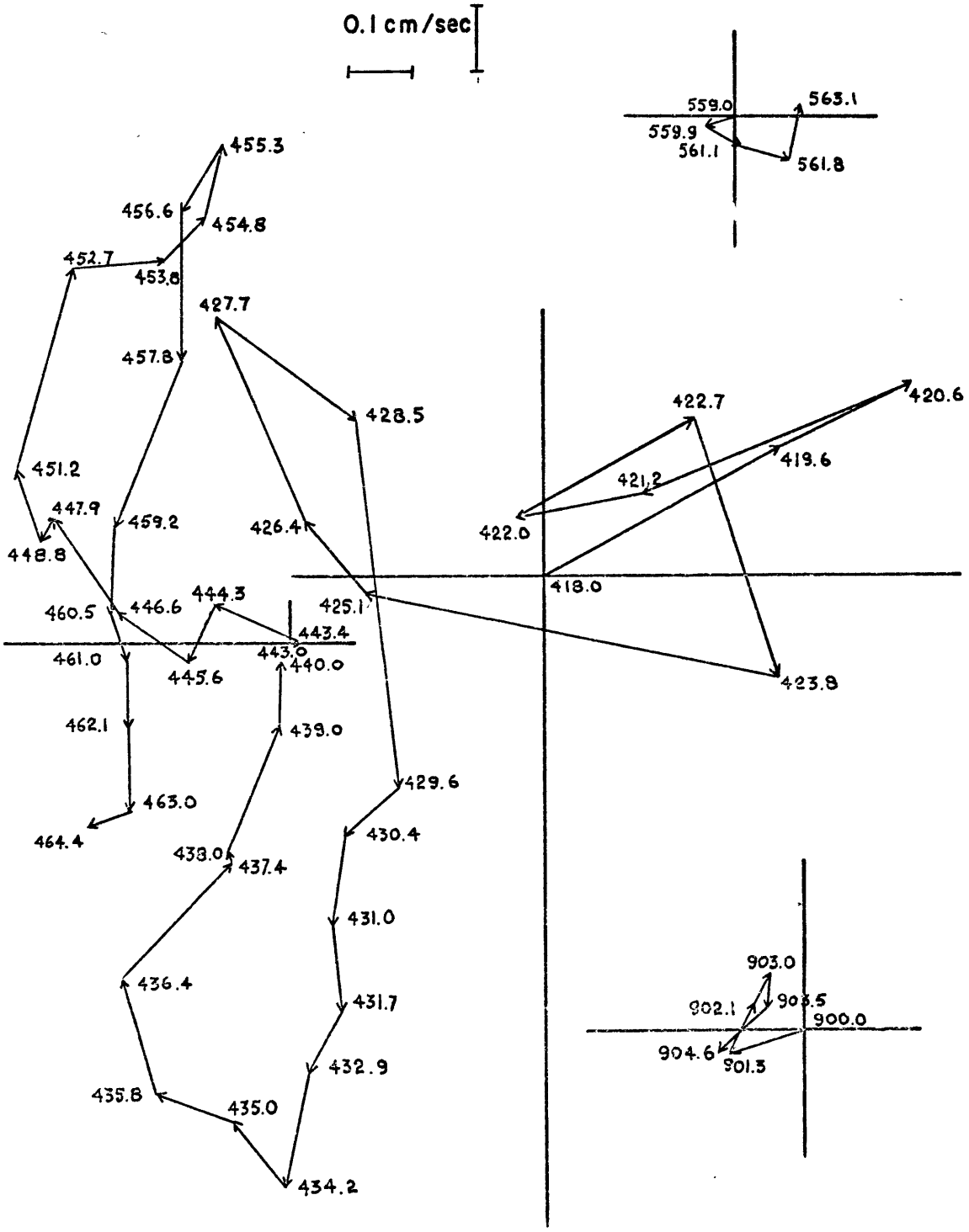

FIG. 2.11b

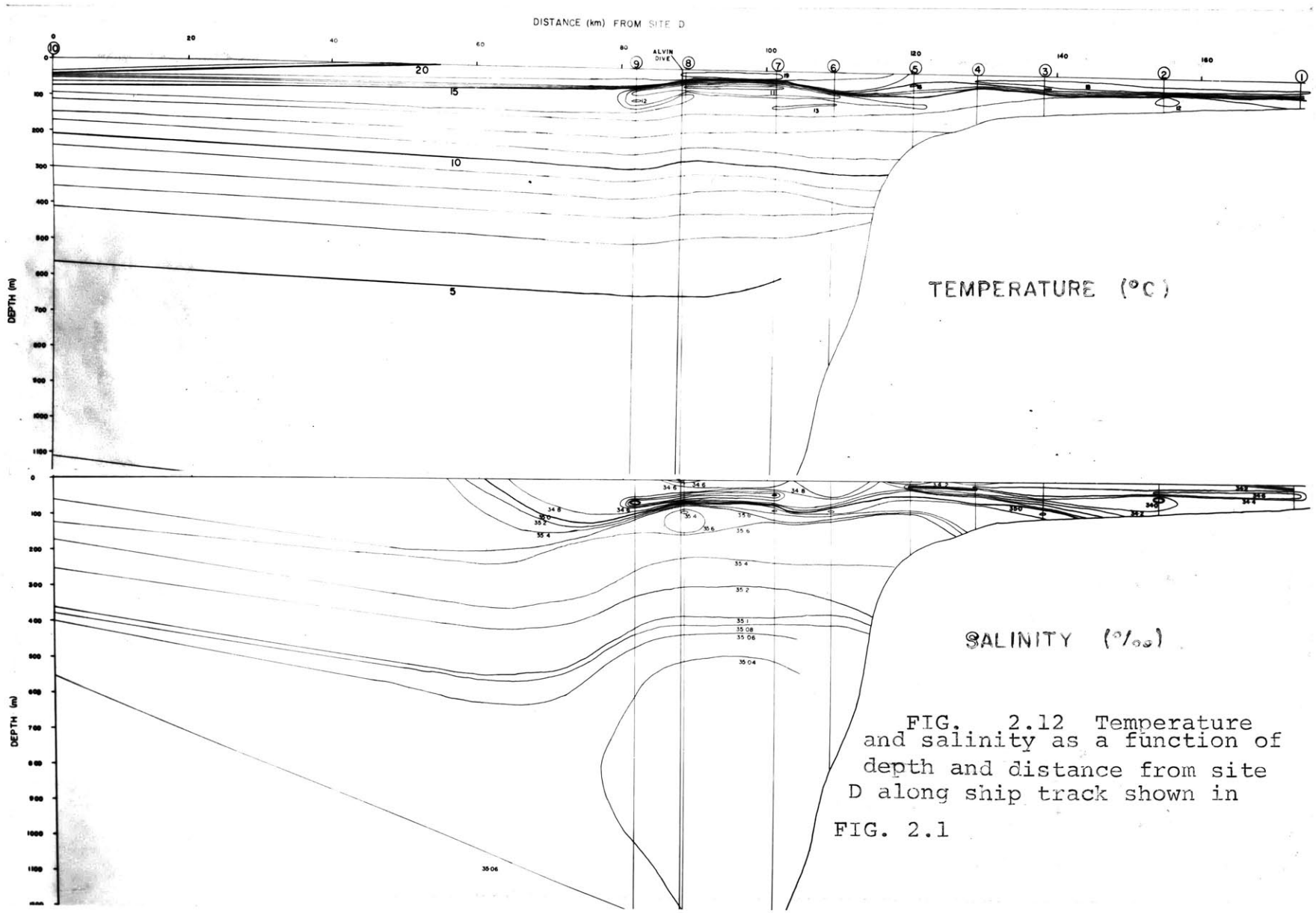

FIG. 2.12 Temperature and salinity as a function of depth and distance from site D along ship track shown in FIG. 2.1

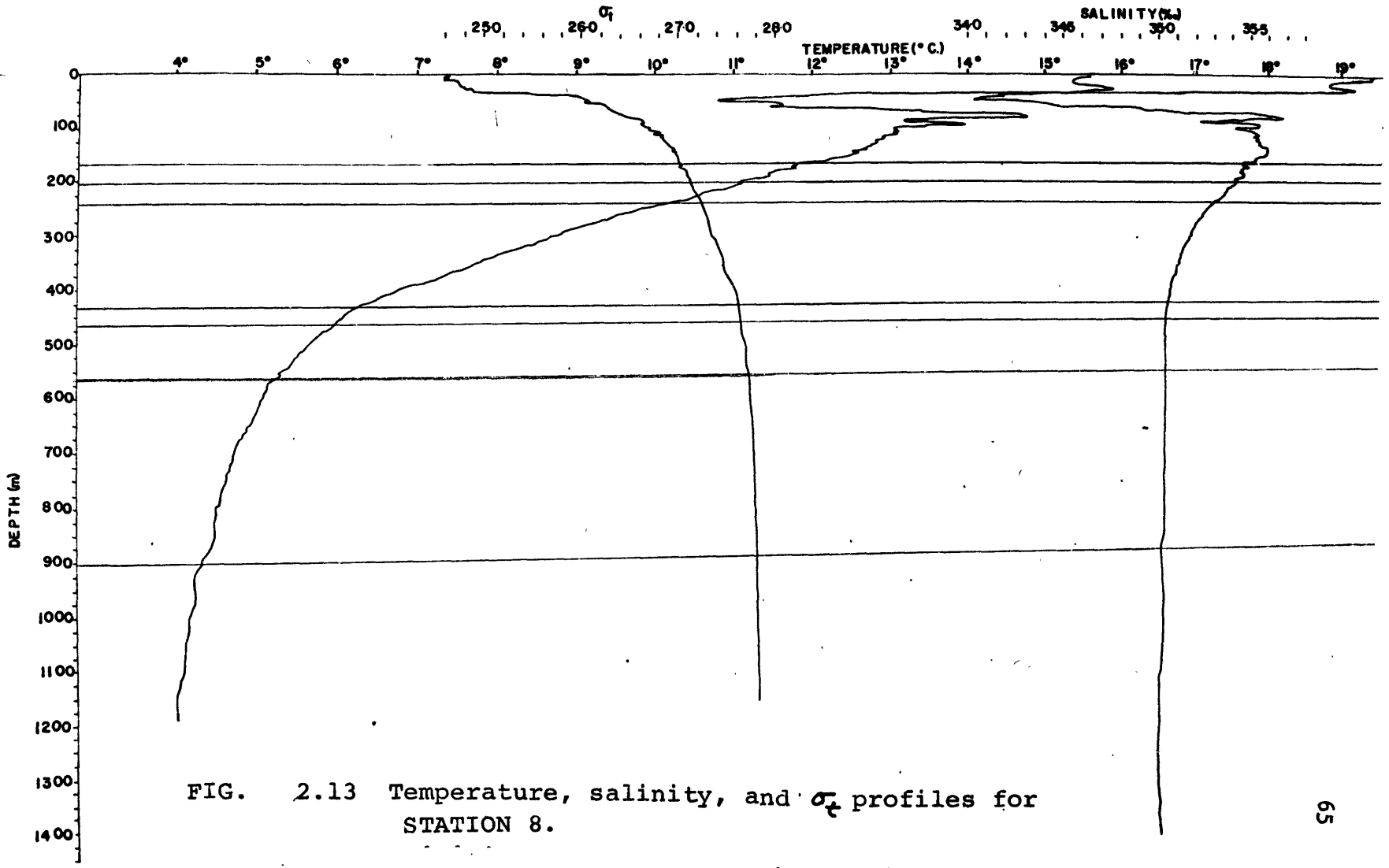

FIG. 2.13 Temperature, salinity, and σ_t profiles for STATION 8.

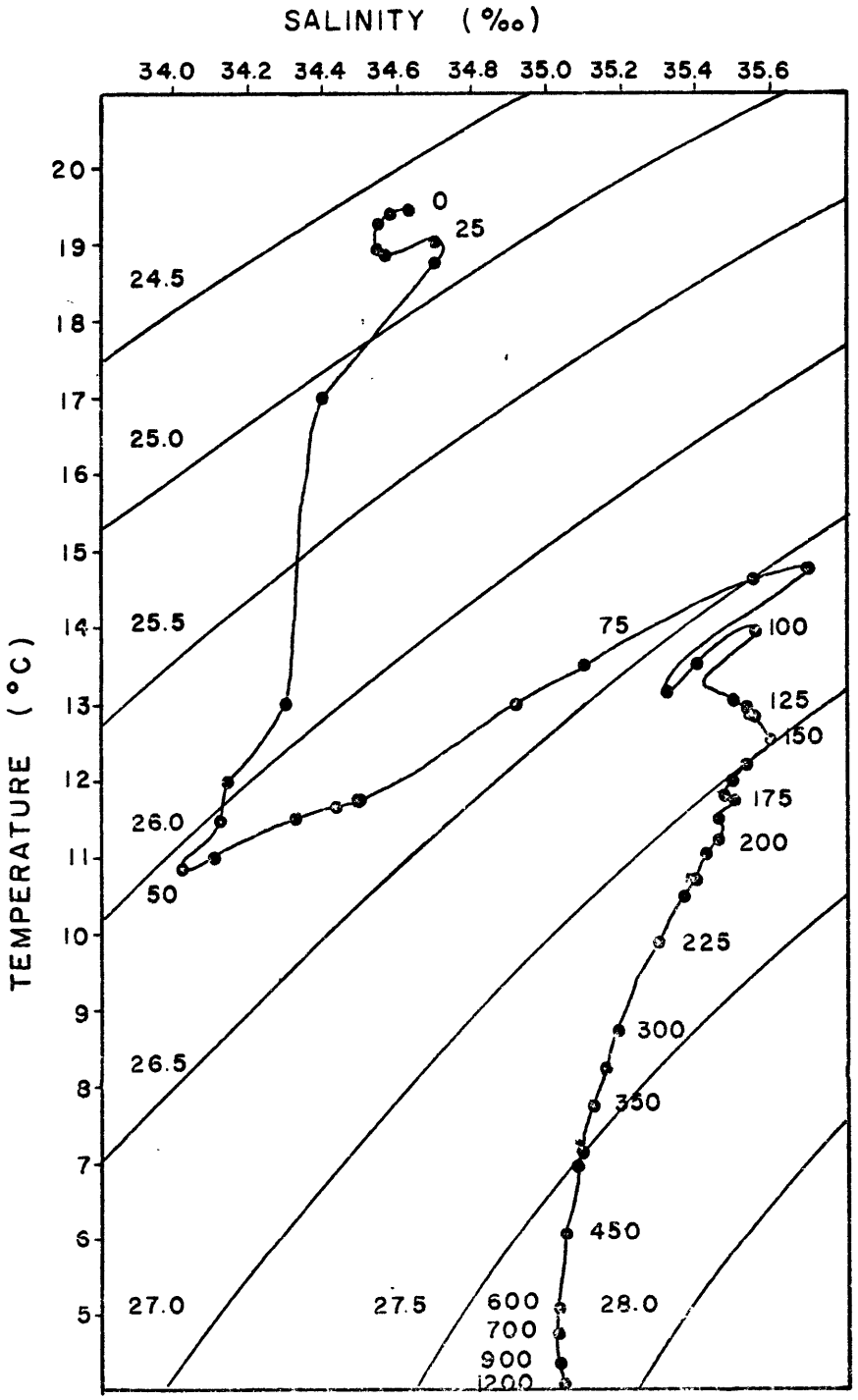

FIGURE 2.14
T-S DIAGRAM FOR STD STATION 8. THE NUMBERED DOTS ARE THE DEPTHS SAMPLED AND THE SLOPING LABELEDLINES ARE OF EQUAL σ_t.

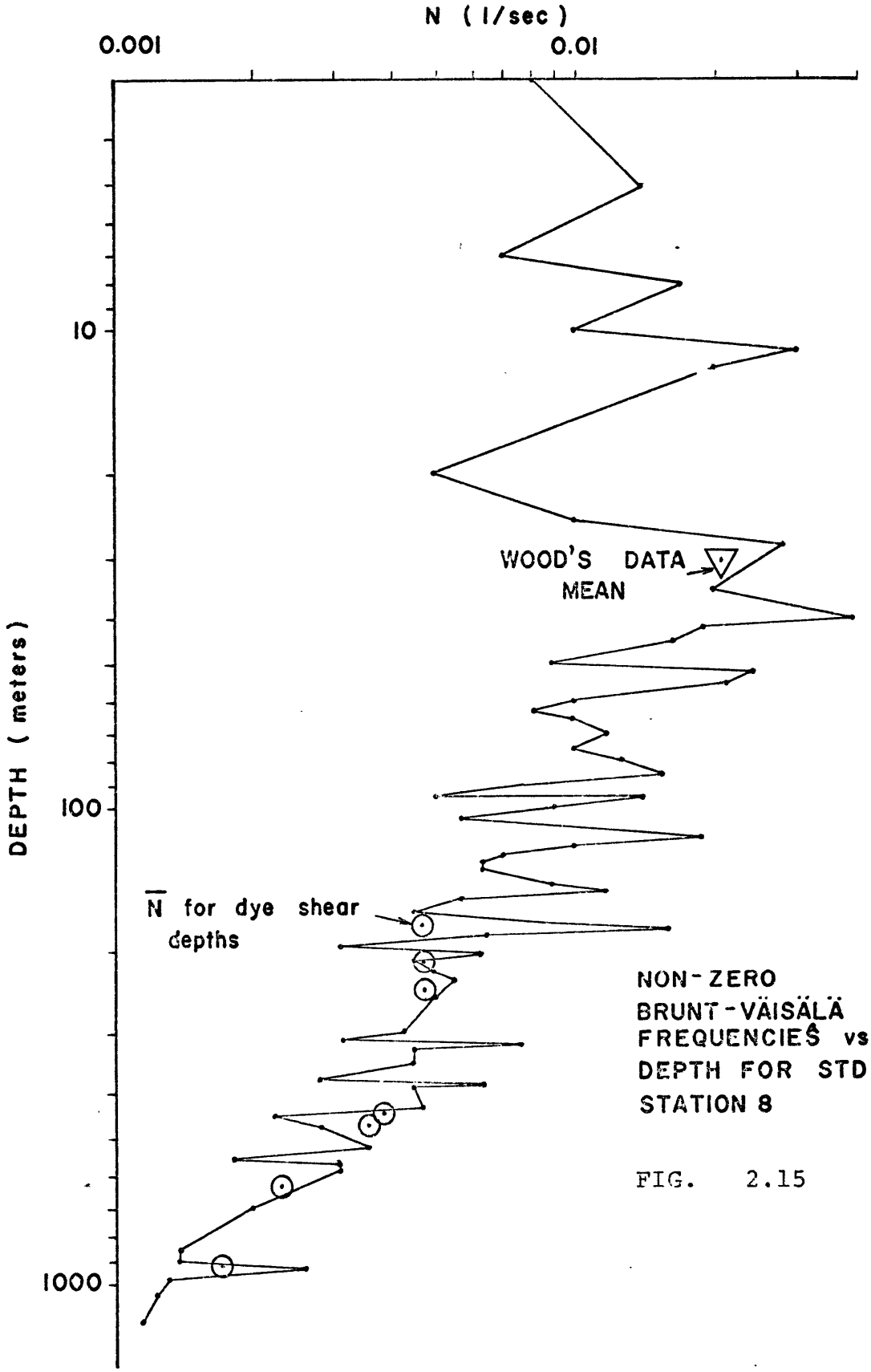

NON-ZERO BRUNT-VÄISÄLÄ FREQUENCIES vs DEPTH FOR STD STATION 8

FIG. 2.15

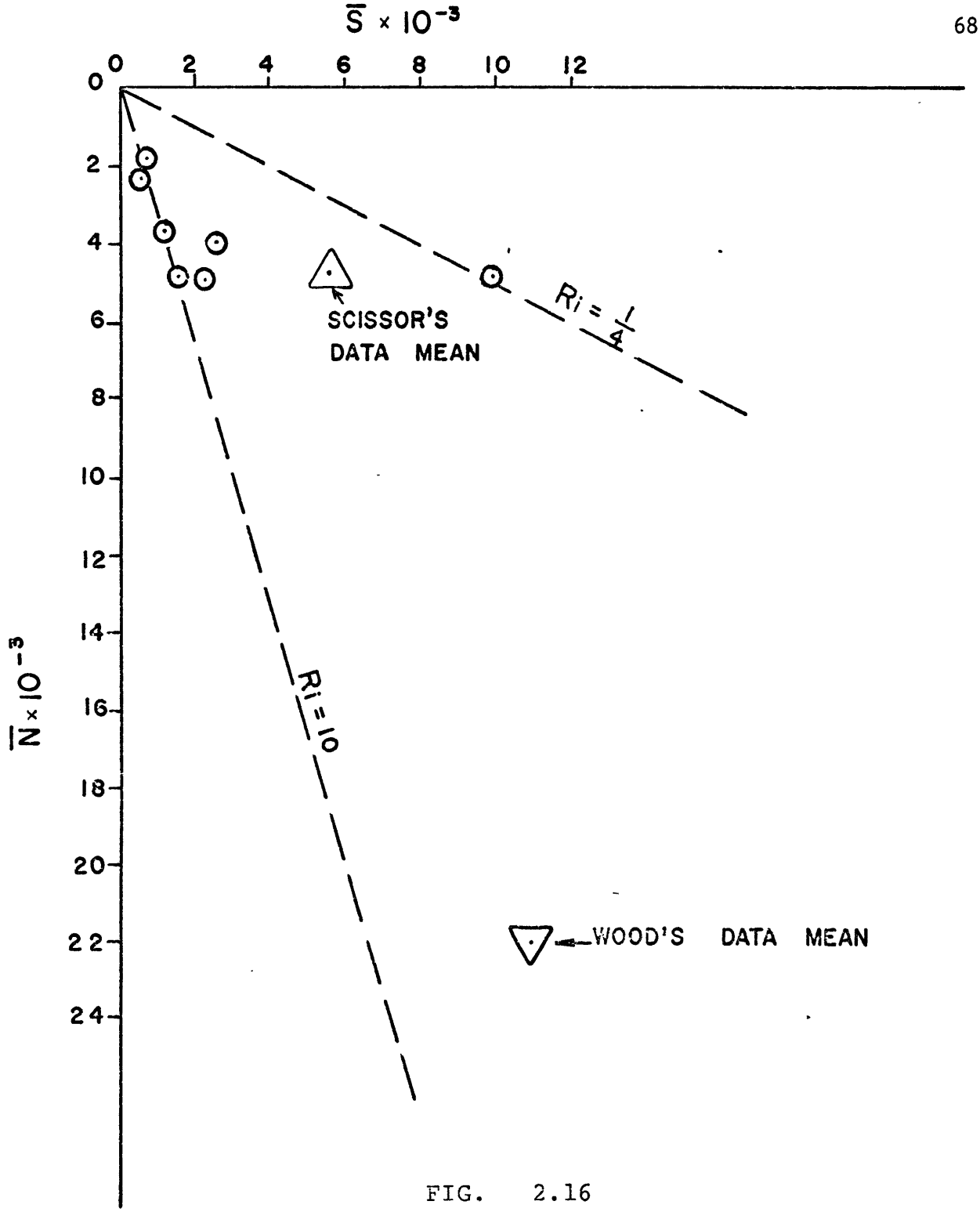
$\bar{S} \times 10^{-3}$
0
2
4
6
8
10
12
$\bar{N} \times 10^{-3}$
0
2
4
6
8
10
12
14
16
18
20
22
24
$Ri = \frac{1}{4}$
$Ri = 10$
SCISSOR'S
DATA MEAN
WOOD'S DATA MEAN

FIG. 2.16

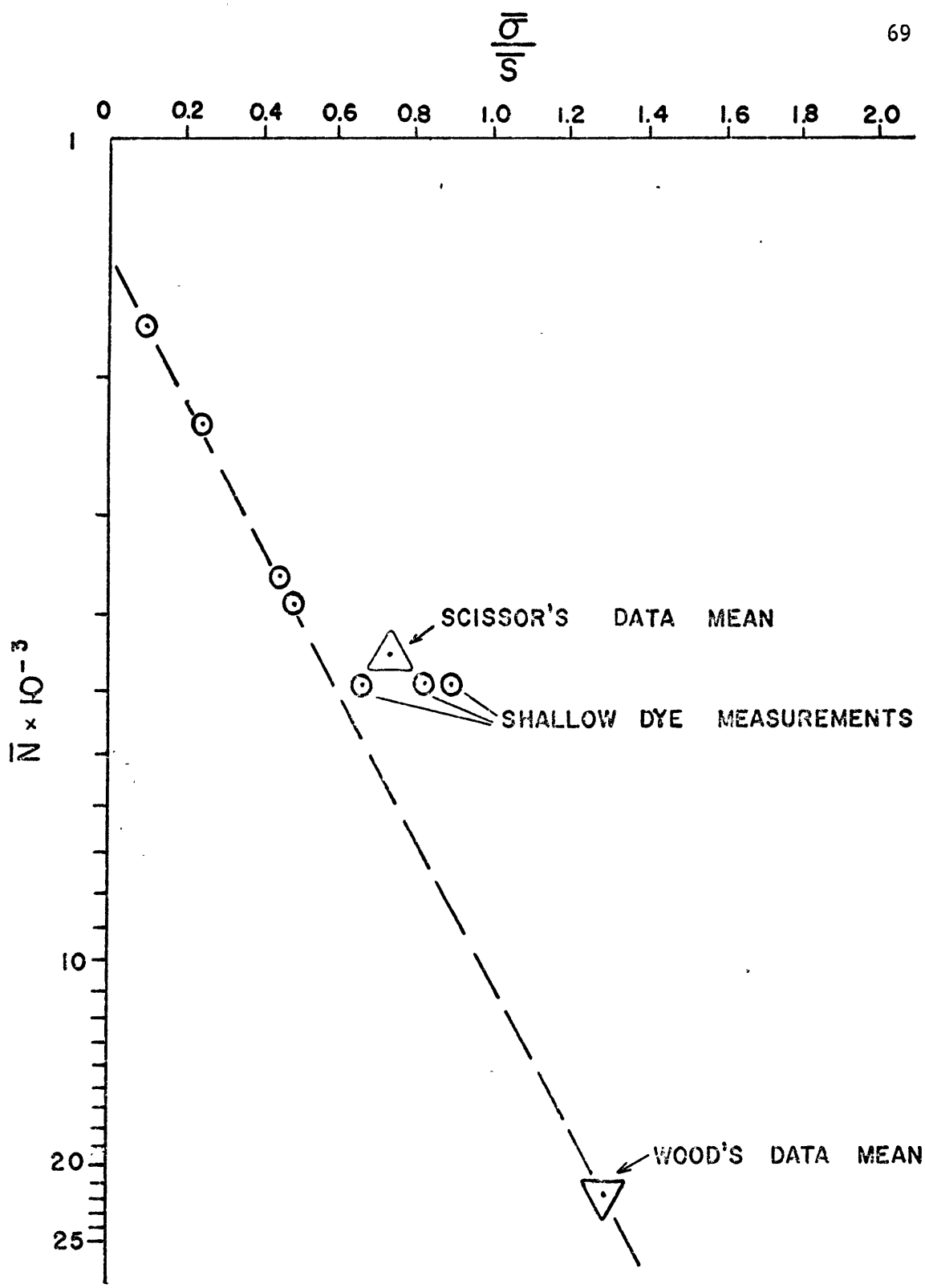
σ/S
0
0.2
0.4
0.6
0.8
1.0
1.2
1.4
1.6
1.8
2.0
1
10
20
25
N̄ x 10⁻³
SCISSOR'S DATA MEAN
SHALLOW DYE MEASUREMENTS
WOOD'S DATA MEAN

FIG. 2.17

CHAPTER 3

THE SHEAR DENSITY GRADIENT CORRELATION MEASUREMENT NEAR BERMUDA

Introduction

With the possible exception of the shallow measurements of Siedler (1970), the observations of shear reported here are the only known ones of such small vertical scale made in the main thermocline. The shear data are supported with synchronous measurements of temperature and salinity gradient as well as depth established by a new type of precision pressure sensor. These supporting measurements allow the density gradient to be calculated, thus giving some of the first estimates of static and shear stability in deep thermocline microstructure.

The most striking result of the scissors data is a small (-.13), but statistically significant (at the 99% confidence level), negative correlation between the magnitude of the shear and the density gradient. This means that the stronger shears are more often associated with weak density gradient and weaker shears most often appear in strong density gradients. These observations are at variance with the expected positive correlation for a large class of flows and wave motions. In particular a multilayered inviscid analytic internal wave model with layers of alternately greater and lesser stability shows the strongest shears associated with the layers of strongest stability in the frequency range between the local Väisälä

frequency and the local Coriolis frequency for both high and low vertical mode structure. This expected positive correlation for internal waves agrees with that predicted by Phillips (1971) and Cox, et al. (1969) and Woods (1968). In fact the predicted shear on the more strongly stable layers is large enough that instability of the Richardson type is preferred there rather than in the weakly stratified layers. A similar positive correlation was found for geostrophically balanced sliding layers of alternate stratification while these layers sliding in a uniformly viscous medium produced no clear-cut negative correlation.

What possible conclusions are left? Perhaps we are looking directly at the results of the mixing process. The layers which are more mixed in temperature and have the strongest shear may be rotors left by some shear instability or by the release of salt into the convecting layers as in Stern and Turner (1969) and as originally proposed by Stommel.

These observations were made on Atlantis II Cruises 45 and 47. The times and locations are given in figures 3.1 and 3.2 together with Table 3.1 .

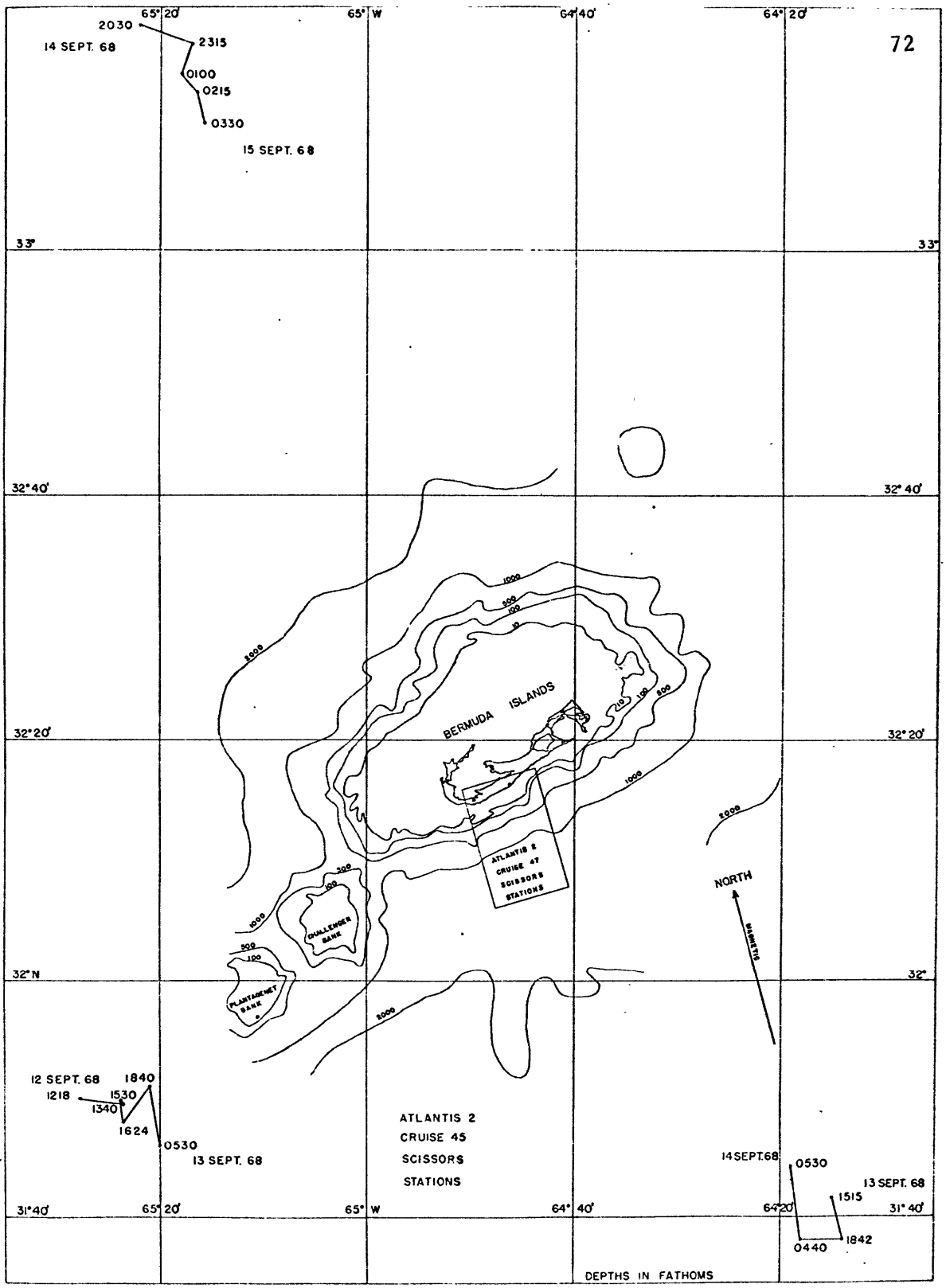
65° 20'
65° W
64° 40'
64° 20'
2030
14 SEPT. 68
2315
0100
0215
0330
15 SEPT. 68
33°
32° 40'
32° 20'
32° N
32°
31° 40'
BERMUDA ISLANDS
1000
500
100
0
2000
200
ATLANTIS 2
CRUISE 47
SCISSORS
STATIONS
CHALLENGER BANK
PLANTAGENET BANK
NORTH
MAGNETIC
12 SEPT. 68
1840
1218
1530
1340
1624
0530
13 SEPT. 68
ATLANTIS 2
CRUISE 45
SCISSORS
STATIONS
14 SEPT. 68
0530
13 SEPT. 68
1515
1842
0440
DEPTHS IN FATHOMS

FIG. 3.1

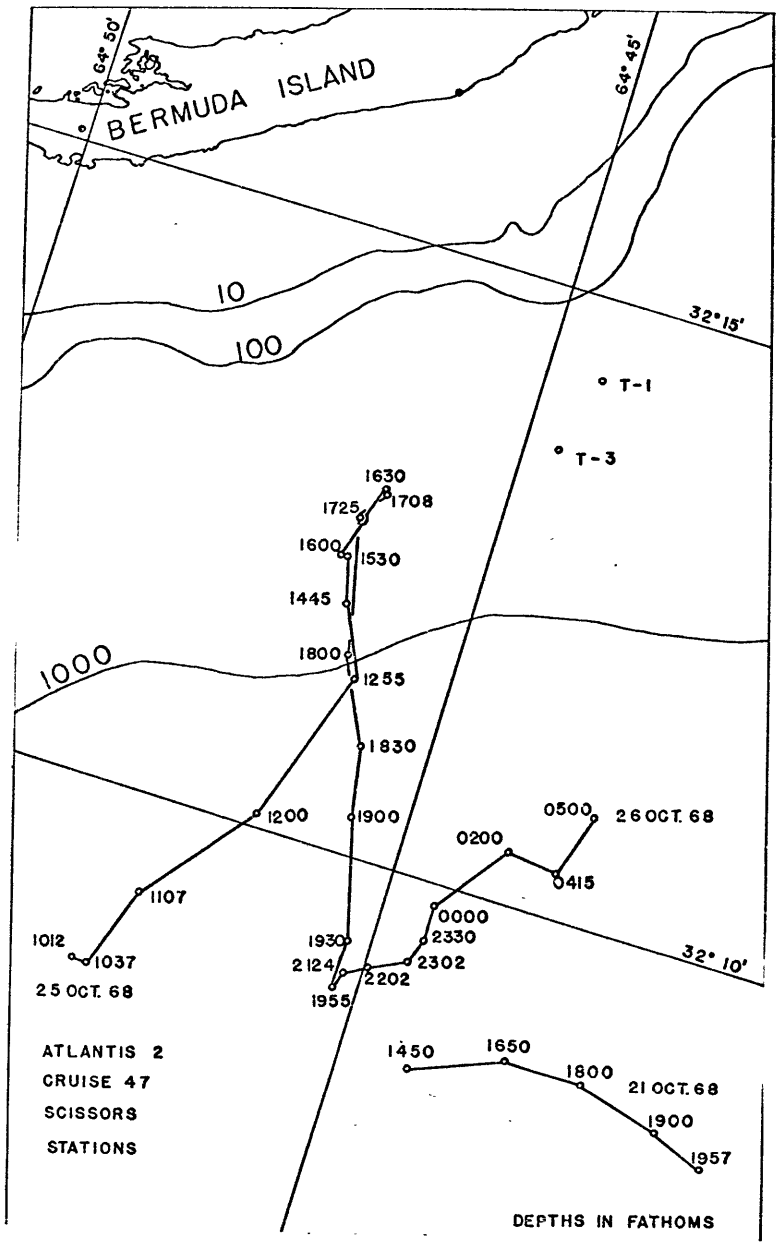
64° 50'
BERMUDA ISLAND
64° 45'
10
100
1000
32° 15'
32° 10'
T-1
T-3
1630
1725
1708
1600
1530
1445
1800
1255
1830
1200
1900
0500
26 OCT. 68
0200
0415
1107
0000
2330
1012
1037
25 OCT. 68
1930
2124
2202
2302
1955
ATLANTIS 2
CRUISE 47
SCISSORS
STATIONS
1450
1650
1800
21 OCT. 68
1900
1957
DEPTHS IN FATHOMS

FIG. 3.2

TABLE 3.1

SET NO.	DATA TYPE	COMMENT	STARTING TIME	(MAX)	(MIN)	(MAX)	(MIN)	(MAX)	(MIN)	(MAX)	(MIN)	DATE
1 1/2/t	Lowering	No cur-	1400	2020	21	25.0	15.9	36.6	35.8	0	0	9/12
2 1/1	L & hold	rent met-	1508	2000	11	16.0	12.8	36.1	35.5	40	0	9/12
3 2/1	Hold	ers.	1620	1980	5	14.0	13.2	35.8	35.5	31	21	9/12
4 2/2	Hold		1740	1980	11	13.5	13.0	35.7	35.5	52	38	9/12
5 3/2	2 Up-downs		1949	1921	11	14.8	11.9	35.8	35.3	82	0	9/12
6 4/1	2.5 Up-downs		2059	2230	11	15.4	12.4	36.0	35.4	75	0	9/12
7 4/2	1.5 Up-downs	Temp. bad	2202	1396	11	14.6	12.0	35.9	35.3	78	0	9/12
8 5/1	Lower,down,step	5	0200	2060	11	20.5	11.2	36.6	35.3	72	0	9/14
9 5/2	Step, 3 meters		0308	2021	0	13.8	12.2	35.8	35.4	52	0	9/14
10 6/1	To surface		0415	535	31	24.9	16.9	36.6	35.2	0	0	9/14
11 7/1	Lower, steps	1	2137	2017	11	22.5	14.1	36.7	35.7	33	0	9/14
12 7/2	Step, 3 meters		2244	2035	11	14.1	13.0	35.8	35.5	78	35	9/14
13 8/1	Step, 3 meters		2357	2037	11	15.6	14.0	36.0	35.6	40	0	9/14,15
14 8/2	Steps, sawtooth		0118	2037	4	14.9	14.2	35.9	35.7	36	21	9/15
15 9/2	To surface		0248	1784	431	27.1	15.5	36.7	35.9	0	0	9/15
16 10/2	L & hold		1530	1960	68	26.1	11.3	36.6	35.2	36	0	10/21
17 10/1	Hold		1635	1940	11	11.6	9.8	35.4	35.1	76	33	10/21
18 11/2	To surface	Current	1748	1190	11	17.0	10.2	36.4	35.1	68	0	10/21
19 12/1	Lower	meter dies	1110	1420	11	14.7	12.8	35.8	35.4	0	0	10/25
20 12/2	Lower		1217	1946	13	22.0	14.7	36.5	35.7	0	0	10/25
21 13/1	Hold & drift		1507	1850	11	16.7	14.5	36.3	35.7	0	0	10/25
22 13/2	Tow		1620	1922	3	17.9	14.9	36.4	35.8	0	0	10/25
23 14/1	Tow		1745	1788	13	17.8	17.3	36.4	36.2	0	0	10/25
24 14/2	Tow		1858	1620	21	17.8	14.6	36.4	35.7	0	0	10/25
25 15/1	Hold & raise	On hose	2223	2005	21	13.0	11.9	35.6	35.3	25	4	10/25
26 15/2	Come on scale	On hose	2115	1860	11	15.3	11.9	35.9	35.3	20	0	10/25
27 16/1	Hold	On hose	2333	1940	11	12.7	12.1	35.6	35.4	25	12	10/25
28 16/2	Hold	On hose	0040	1917	11	12.7	12.7	35.6	35.3	25	15	10/26
29 17/1	Hold & raise	On hose	0153	1730	23	14.6	12.4	35.8	35.4	25	0	10/26
30 17/2	Raise, lower	And break	0259	1955	21	13.5	9.4	35.7	35.1	80	0	10/26

Scissors sensor array layout

The scissors sensor array includes ten individual sensors mounted on a tubular stainless steel space frame along with suitable electronics to supply power and code and transmit data (see figures **3.4** and **3.6**). Two identical sets of sensors are held in horizontal planes spaced apart vertically by 300 cm. All ten variables are sampled during every 2 second sampling period and transmitted to the surface for recording on magnetic tape. An unscrambling system allows any (or all) variables to be sampled during the data taking process. A crystal clock gates frequencies proportional to temperature, salinity and depth for precise 0.2 second periods and up-down counters store current speed component pulses for 2.0 second periods.

Both the upper and lower sensor locations contain the following instruments: (see figure **3.5**)

1) 1 Bendix platinum resistance temperature probe,

2) 1 Bisset-Berman temperature and pressure compensated induction conductivity head and "Paraloc" Oscillator,

3) 2 mini-meter current meters arranged at right angles to each other and the vertical.

The timing diagram (see appendix **E**) shows that upper and lower temperature, and also salinity, are synchronous to 0.2 seconds each and so computed density is synchronous to 0.4 seconds as are the upper and lower velocities. The worst case will give synchronism within 2.0 seconds. This rapid sampling sequence makes computed 3 meter vertical gradients accurate within the time response and accuracy of available sensors.

With such a sensor pair arrangement with rapid sampling,

common mode errors tend to cancel. For example:

a) The ship drift appears in both the upper and lower current meters. When these two measured currents are subtracted to compute velocity shear the ship drift cancels out. Effects due to current meter tilt out of the horizontal plane or vertical motion similarly cancel to first order. Clearly, since the instrument spacing may be measured to better than one percent, the ultimate accuracy of shear measurements depends on the quality of the current meters themselves.

b) Errors in the computed temperature and salinity gradient due to uncertainty in depth or internal wave motion of the gradients will greatly be reduced by reading two sensors at the same time with a precisely fixed vertical separation. Again, common mode sensor errors due to pressure, temperature and depth cancel to first order.

An uncomplicated motion isolation system was used to isolate the sensors from ship and sea surface motion. All but about 14 lbs of a half ton submerged system was balanced out with buoyancy modules which were located below the zone of surface wave influence. The remaining buoyancy was gained by displacing water in a neutrally buoyant fire hose with constant pressure compressed air supplied from the ship. The arrangement acted as a mechanical low pass filter which rejected most of the wave heave. Figure 3.7 shows a power density spectrum of the scissors vertical velocity computed from the rate of change of pressure for constant depth runs with and without motion isolation. Notice the order of magnitude decrease in the power density for the data taken with the fire-hose motion isolation. A similar decrease in ship drift velocity was realized when the floating umbilical was kept slack.

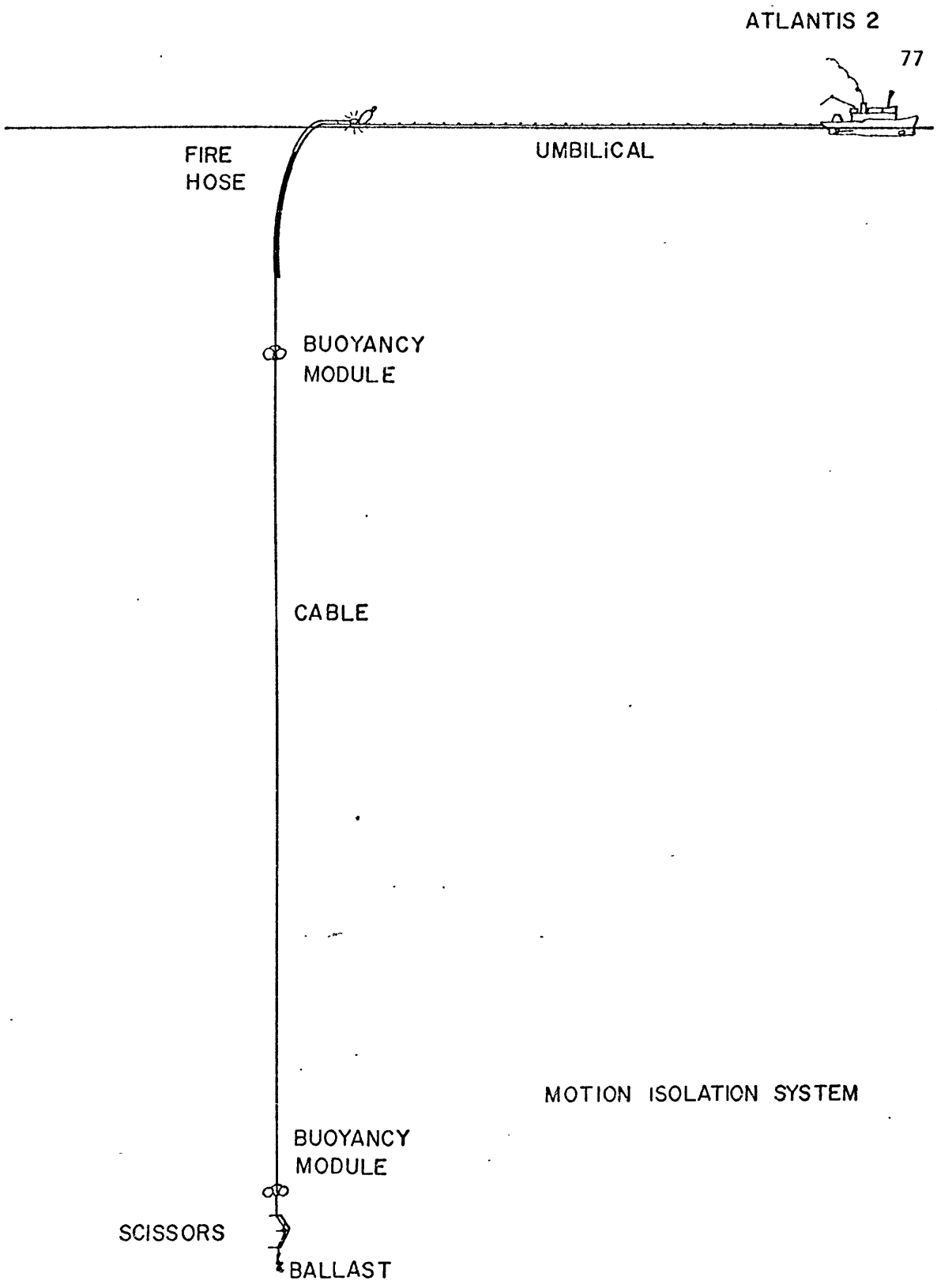
ATLANTIS 2
77
FIRE
HOSE
UMBILICAL
BUOYANCY
MODULE
CABLE
MOTION ISOLATION SYSTEM
BUOYANCY
MODULE
SCISSORS
BALLAST

FIG. 3.3

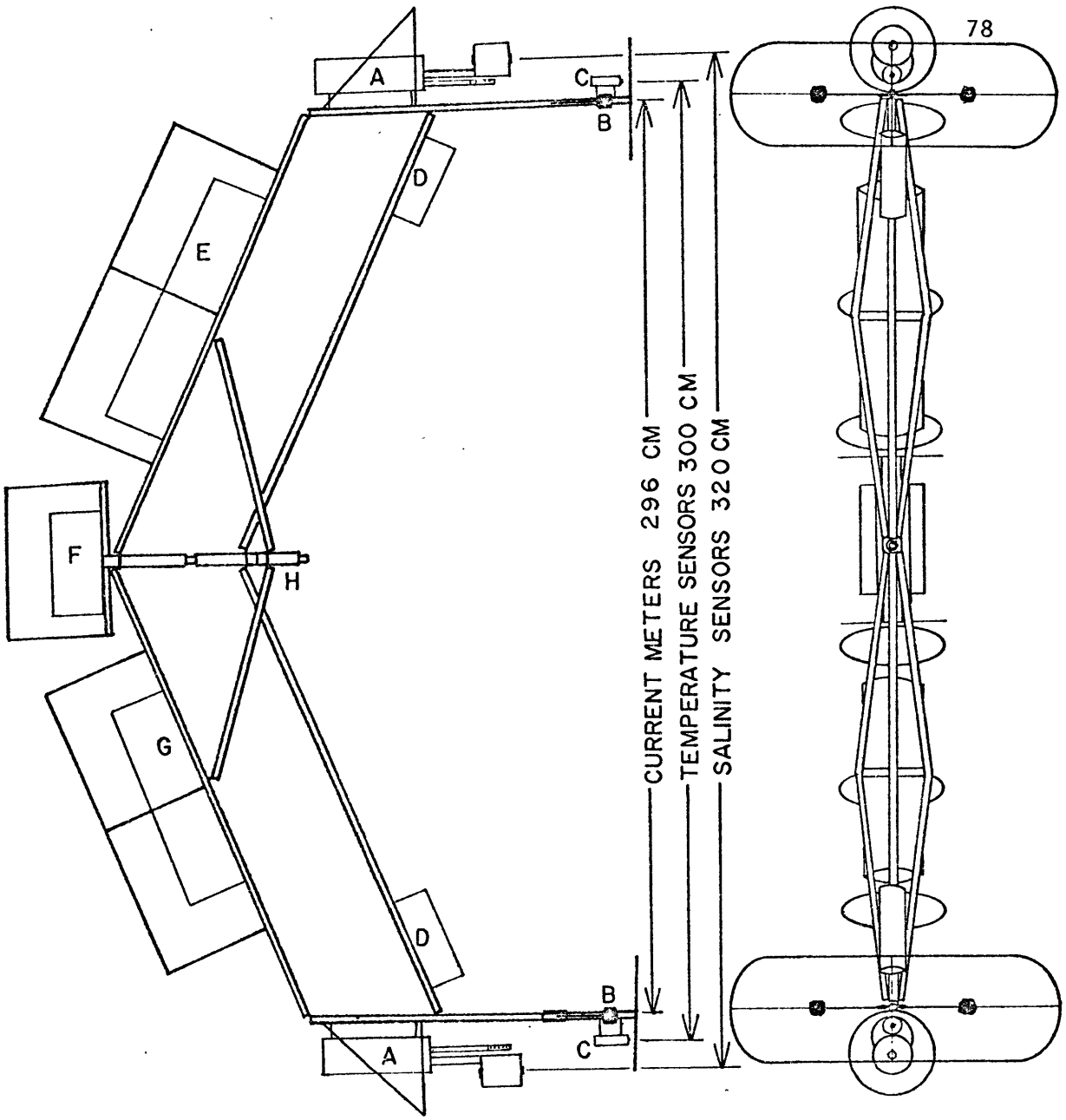

FIG. 3.4: Scissors Sensor Array Schematic Diagram

A) 2 Model 6007 Bissett Berman in situ salinometers
B) 4 Mini-meter current meters
C) 2 Bendix temperature sensors
D) 2 Mini-meter electronics housings
E) 1 Precision pressure sensor and cable end power supplies
F) 1 Geodyne compass
G) 1 Bendix DCS-100 Mark II data collection system
H) Scissors spacing adjustment sleeve

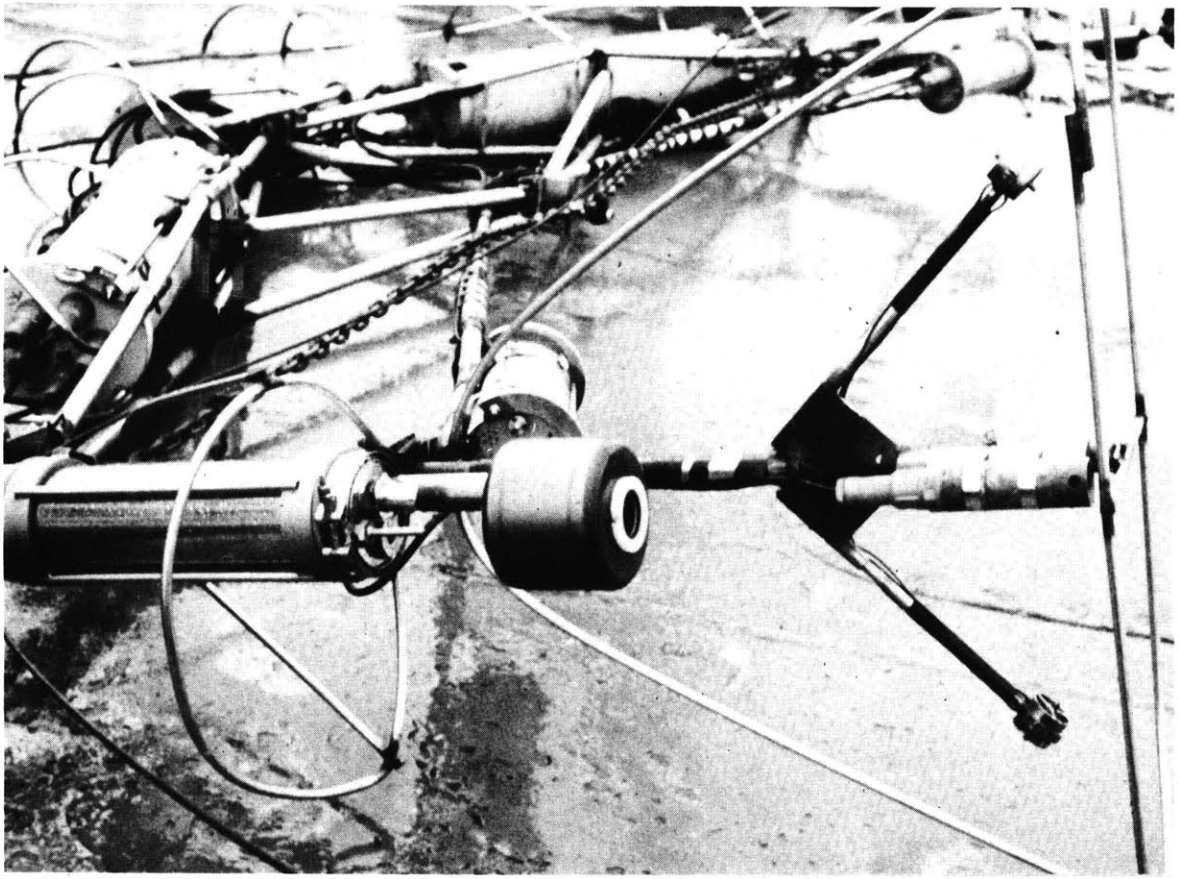

Figure 3.5: Detail of sensor layout. Note that the small ducted current meters are arranged at ±45° angles to the scissors frame axis. The lower temperature sensor is on the right side of the picture in the center while the lower salinity sensor head is directly in the center.

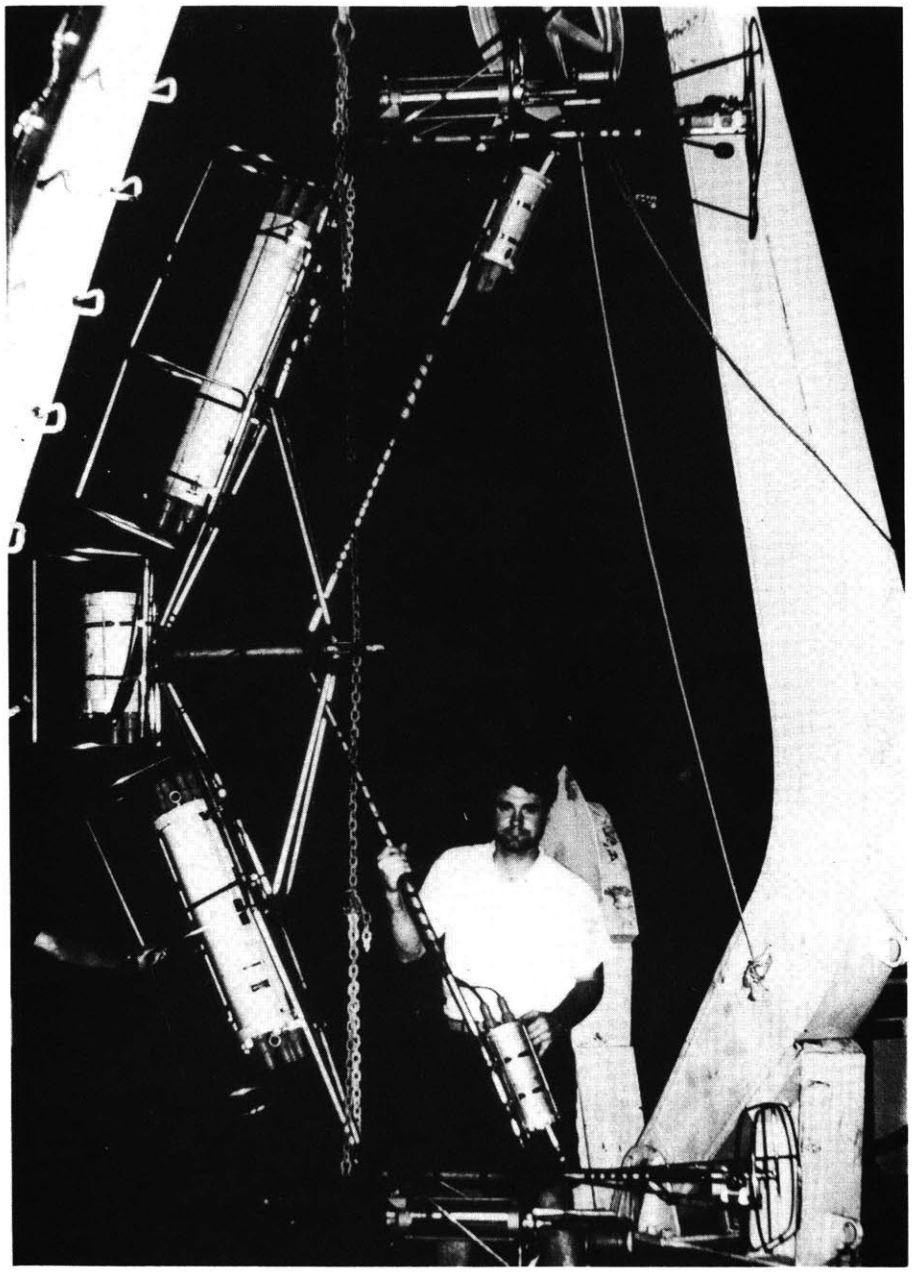

Figure 3.6: Complete "Scissors Sensor Array" ready to be launched on Atlantis II Cruise #47. Temperature and salinity sensors and current meters are located at the top and bottom of the array.

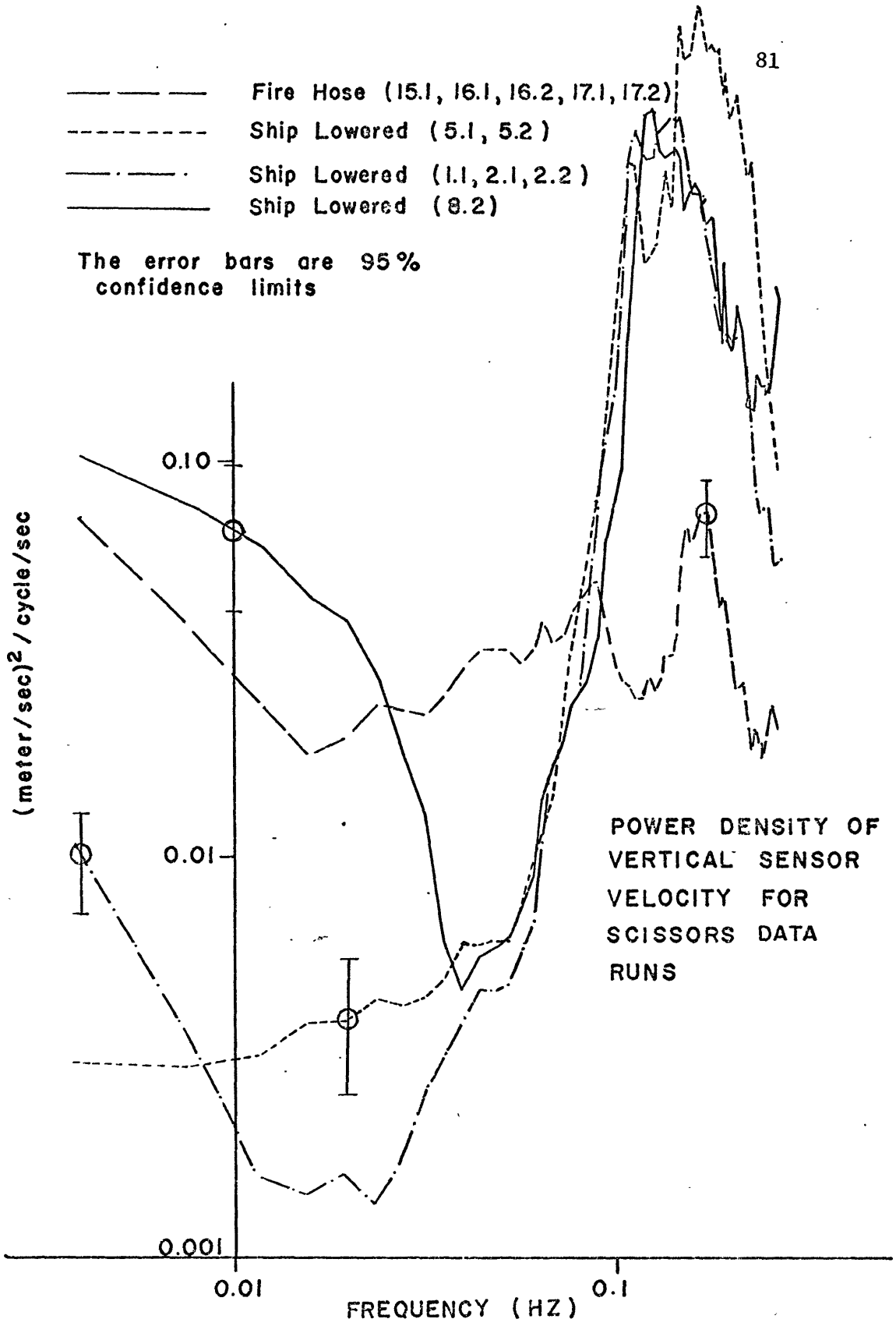
Fire Hose (15.1, 16.1, 16.2, 17.1, 17.2)
Ship Lowered (5.1, 5.2)
Ship Lowered (1.1, 2.1, 2.2)
Ship Lowered (8.2)
The error bars are 95% confidence limits
0.10
0.01
0.001
(meter/sec)² / cycle/sec
0.01
0.1
FREQUENCY (HZ)
POWER DENSITY OF VERTICAL SENSOR VELOCITY FOR SCISSORS DATA RUNS

FIG. 3.7

Background of Bermuda current meter shear measurements

The shear measurements described in this section were all made on Atlantis II Cruise 47 during a 5 hour period near Bermuda on the only occasion when the fire-hose motion isolation system was successfully deployed. A total of 7,200 shear measurements were made with scissors maintained at a nearly constant depth while traversing horizontally about 1.8 kilometers of microstructure. During this period between 2200 hours 25 October and 0300 hours 26 October 1968 the ship was hove to with occasional jogging to keep a slack on the umbilical cord. The depth of water there was greater than 2 km (see figure **3.2**).

The shear was measured between small ducted orthogonal pairs of current meters separated vertically by 3 meters. These current meters are described in detail in the appendix and their relative position to the other sensors is found above in the section on the physical description of the scissors. The component velocities are individually counted during each entire 2 second data cycle giving 2 second vector averages. The counters can count both up and down from their initial zero setting which allows them to average out oscillations of the supporting structure even if they occur at zero velocity. It should also be noted that least count error in the usual sense is absent because no current meter pulses are lost except during the 1/100 second transmission period which represents about 1/2% of the data cycle. At typical speeds of 10 cm/sec this means an average loss of only one pulse in ten recording periods. This

allows accurate vector averages over periods greater than the 2 second data cycle provided that the scissors heading remains constant over the averaging period. During the two hours when the Geodyne Compass was working the heading was constant within ±4° magnetic and it is assumed that similarly constant headings pertain during the other three hours of fire hose data.

During the fire hose lowerings the upper right component current meter became stuck from time to time. It was decided to reject this upper right component in all the data due to its poor reliability. In order to calibrate the upper left current meter it was assumed that the missing upper right current meter output was equal to the lower right current meter output. This is justified on three grounds. First since the shears are small (order 1.5 cm/sec in 3 meters) compared to the average speed through the water of about 10 cm/sec, the position of the left upper meter output in calibration space will be good to about ±15%. Second, the sensitivity of the magnitude of the right meter to angle is minimum at the average true angle near 215° in calibration space. Last, at this position in the calibration region the two left speed components track each other within about ±1/4 cm/sec or closer at equal true speeds and angles. These combined possible errors should be less than ±1/2 cm/sec or order 10^{-3} 1/sec in the left component of shear if the calibration remained stable. In the calculations and discussion that follow, only the magnitude of the left component of the vector shear is reported. This will be referred to as the $|y|$ shear.

Magnitude of the shear

For the shear measurements made near Bermuda the grand mean magnitude was $(8.5\pm7.2)\times10^{-3}sec^{-1}$ for the raw unfiltered data. When the calibrated current meter data has been digitally filtered with a moving weighted vector average the grand mean becomes $(5.5\pm4.1)\times10^{-3}sec^{-1}$ (see appendix for filter details). The reduction in magnitude of the filtered mean reflects the smoothing of wave heave, quantization effects and current meter periodicity due to rotor unbalance which otherwise become rectified thus increasing the apparent absolute magnitude of the shear.

The magnitude of the shear reported here is comparable to the magnitude of the shear observed in Alvin dye streak data taken between 200 and 400 meters depth. The ratio of the standard deviation about the grand mean to the mean itself ($\frac{s}{|\bar{q}|}$ = .74 for the filtered scissors shear) falls on the curve in figure 2.7 at 230 meters depth. This is not surprising since the mean temperature and salinity gradients at these depths on the continental slope were found nearly equal to those at 650 meters depth near Bermuda. This mean Bermuda shear is about half that reported by Wood (1968) of about $11\times10^{-3}sec^{-1}$ and a quarter of the 20×10^{-3} maximum reported by Stommel and Fedorov (1967). Both of these observations were made nearer the surface ($\sim$30 and $\sim$80 meters respectively) and were taken in regions of greater stability. The Bermuda observations seem to agree reasonably well at least in the mean with the few available comparable observations.

The shear magnitude data is summarized in figure 3.8 . The raw data is shown with a dashed line and the vector averaged data is shown with a solid line.

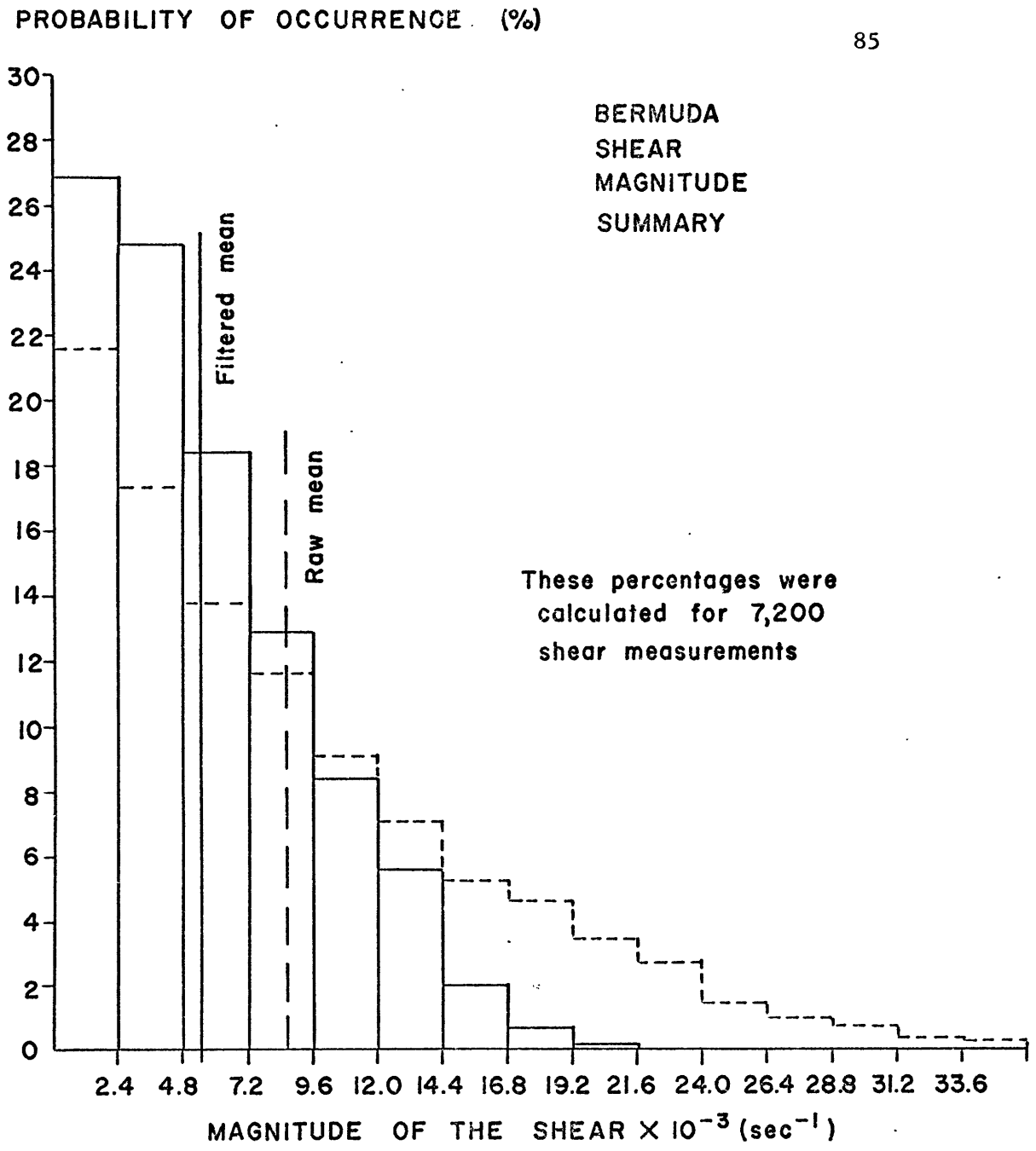
PROBABILITY OF OCCURRENCE (%)
30
28
26
24
22
20
18
16
14
12
10
8
6
4
2
0
BERMUDA
SHEAR
MAGNITUDE
SUMMARY
Filtered mean
Raw mean
These percentages were calculated for 7,200 shear measurements
2.4 4.8 7.2 9.6 12.0 14.4 16.8 19.2 21.6 24.0 26.4 28.8 31.2 33.6
MAGNITUDE OF THE SHEAR X 10^{-3} (sec^{-1})

FIG. 3.8

The observed shear-density gradient correlation

It is of considerable theoretical interest to know what the correlation is between shear and density gradient in the permanent thermocline. Several workers (Cox et al., 1969 and O. M. Phillips, 1970) have suggested that for internal wave motion the correlation should be positive. Other processes are also discussed later in detail, where a positive correlation means large shears are associated with large stable density gradients and small shears with density gradients of small static stability. Note that either T or S gradients are considered positive respectively when T or S increases upward, which is opposite to this density gradient convention. Further note that the confidence intervals quoted refer to instrumental confidence, not confidence that these coefficients represent the thermocline as a whole.

The density gradient shear correlation was first computed on 7,200 raw temperature, salinity and shear data taken during the fire hose constant depth runs. This gave a correlation of $r = -.019$ which is not significantly different from zero at the 95% confidence level of $\pm.023$. This confidence level and those that follow are calculated on the assumption of a jointly normal process. With this assumption the change of variable $W = \frac{1}{2} \ln \left[\frac{1+r}{1-r}\right]$ is permitted (see Hoel, 1966). For such a stationary process with population correlation p, individual realizations of w are normally distributed about the mean $\mu W = \frac{1}{2} \log \left[\frac{1+p}{1-p}\right]$ with standard deviation $\sigma_W = \frac{1}{\sqrt{N-3}}$ where N

is the sample size.

These data were then smoothed digitally as described in the shear section and a new linear density gradient shear correlation coefficient was computed. This gave a value of r = -0.13 which is significant at the 99% level of confidence (see figure 3.9). Since the sign of this correlation was opposite to the expected sign a considerable search for systematic errors was undertaken.

The salinity sensors were considered a possible cause of systematic error to be investigated because they contribute heavily to the density gradient (see the salinity gradient section). For this purpose it was assumed that the salinity gradient was directly proportional to the temperature gradient. The constant of proportionality $\frac{\overline{\nabla_z S}}{\overline{\nabla_z T}} = \frac{0.00325\,‰\,m^{-1}}{0.0237\,°C\,m^{-1}} = .142\,‰/°C$ was computed form STD temperature and salinity data. The density gradient was then computed using WHOI subroutine DSIGMAT. The resulting correlation is r = -.041 which is significantly different from zero at the 99% confidence level. Furthermore if these data are digitally smoothed the negative correlation increases to r = -.12 (see figure 3.10).

Next the question of persistence in time of this negative correlation was addressed. The correlation between temperature derived density gradient and shear was computed for each of the five separate data runs. These results are shown in table 3.2 . There appear to be three negative and one positive correlations which are significantly different from zero at the 95% confidence level and one

Run Number	Number of Points	Linear Correlation Coefficient	Level of 95% Confidence
15.1	1776	+.063	.046
16.1	1794	+.0005	.047
16.2	1639	-.133	.049
17.1	882	-.219	.066
17.2	1120	-.065	.059

TABLE 3.2

negligibly small correlation. So at least in this series of measurements the negative correlation seems to occur more than twice as frequently as the positive correlation.

Finally the filtered temperature gradient, salinity gradient, and shear data were sorted into 9 equal intervals of salinity gradient and the temperature gradient shear correlation was computed for each salinity gradient. These results are shown in figure . This negative correlation is strongest in the salinity gradient interval centered on zero where r = -.21 and gradually declines in strength, becoming non-significant when the salinity gradient exceeds +.005 ‰/ meter or is less than zero (i.e., stabilizing).

So evidently most of the observed negative correlation between temperature gradient and shear occurs in regions of small

destabilizing salinity gradient. Due to the temperature salinity correlation these are also regions of smallest stabilizing temperature gradient. This means that the regions of lowest static stability are the greatest contributors to the negative density gradient-shear correlation.

It must be realized that these data represent only a small sample of layer structure. This time series is far from stationary and many more realizations would be needed to have a truly strong case for the negative correlation between shear magnitude and density gradient. Perhaps these layers are different from the general case and the positive correlation observed during the first hour pertains in most cases.

The data do show for the first time (at least in one local region near Bermuda) that the magnitude of the shear and the density gradient are correlated in thermocline microstructure above the level of instrumental noise. To be truly convincing such shear measurements would need to be made with the dye streak technique used in the last chapter, where the shear is sampled from a complete record in depth rather than at some fixed interval.

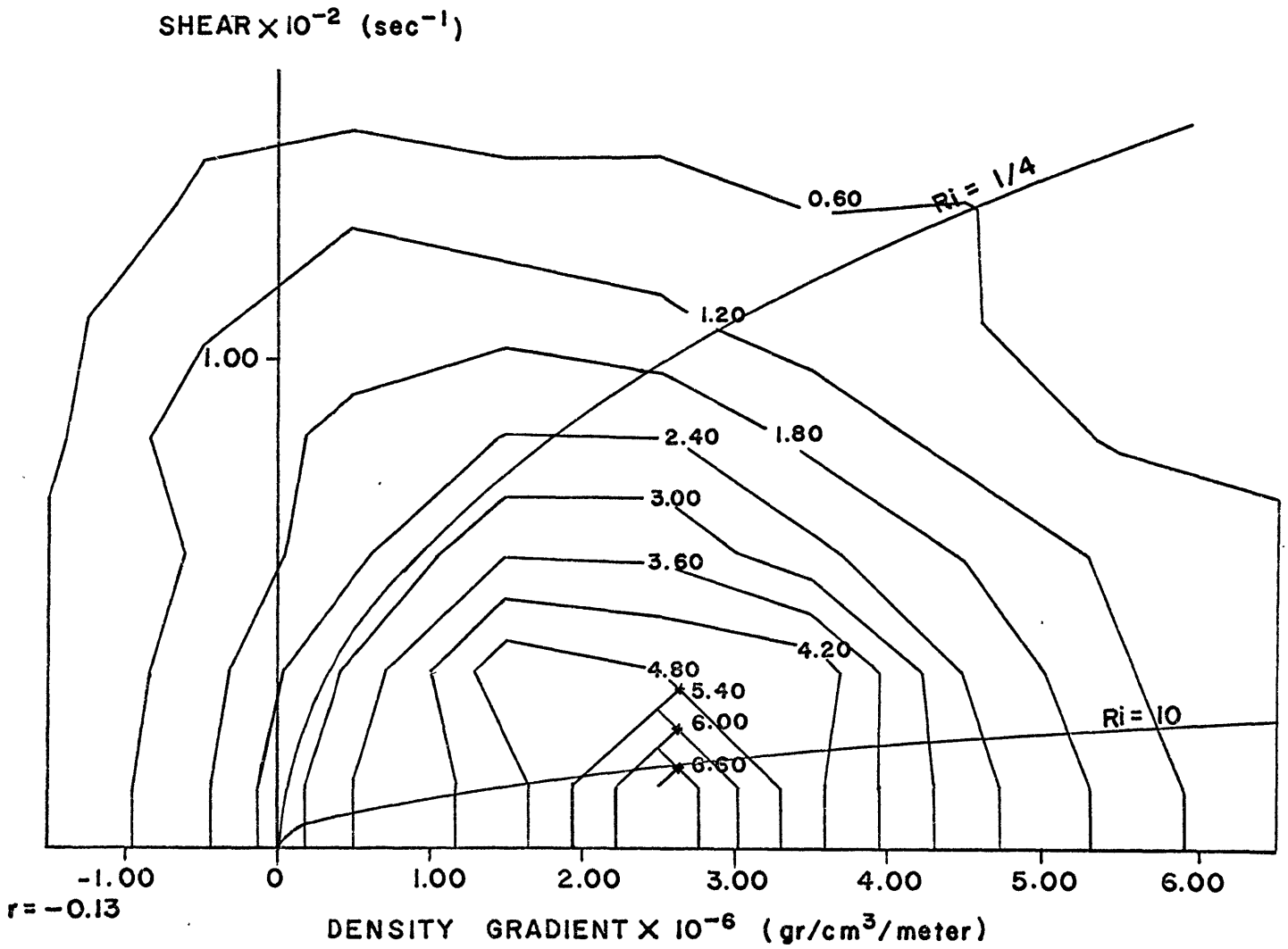
SHEAR X 10⁻² (sec⁻¹)
0.60
Ri = 1/4
1.20
1.00
1.80
2.40
3.00
3.60
4.20
4.80
5.40
6.00
6.60
Ri = 10
-1.00
0
1.00
2.00
3.00
4.00
5.00
6.00
r = -0.13
DENSITY GRADIENT X 10⁻⁶ (gr/cm³/meter)

FIG. 3.9

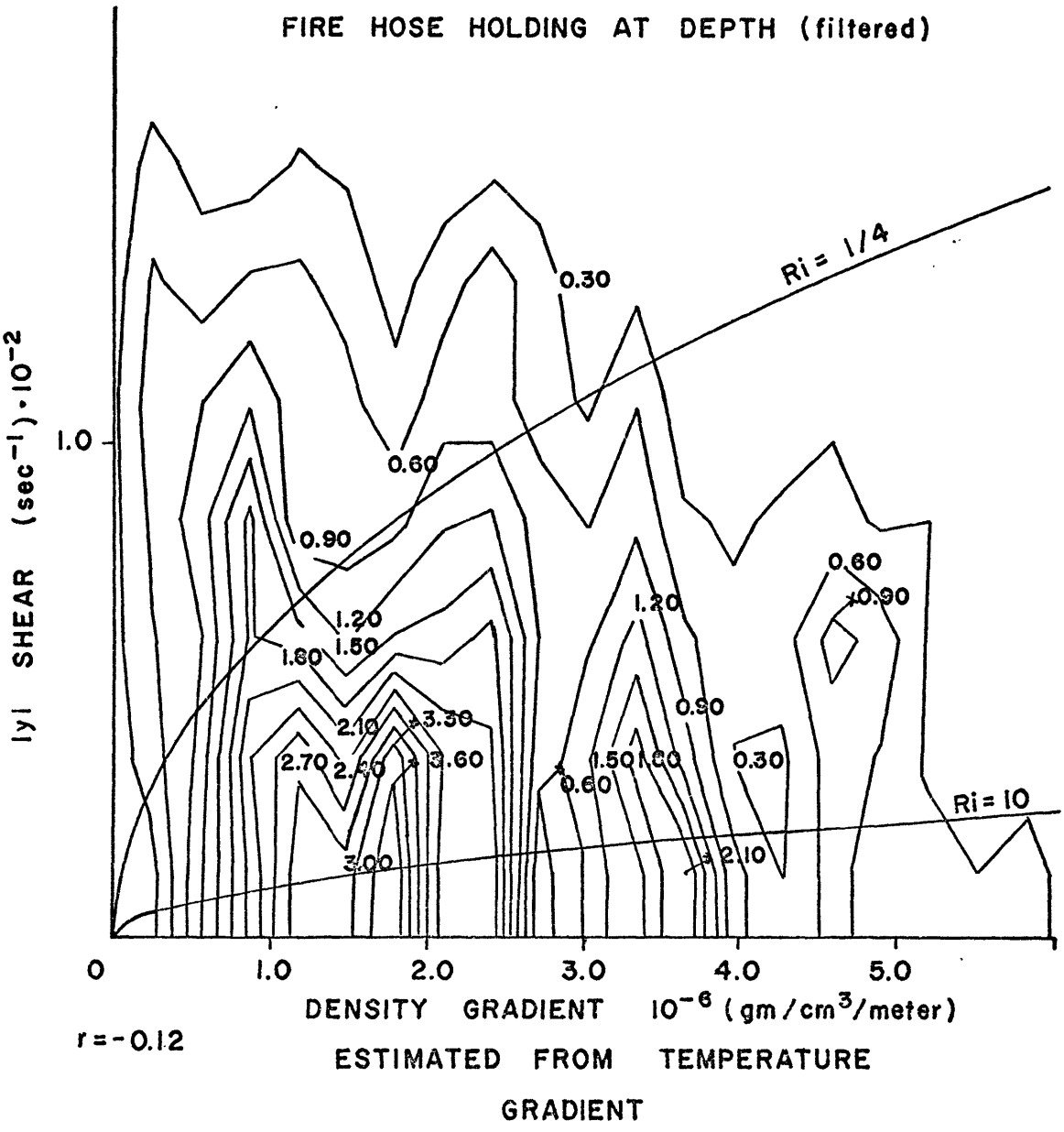
FIRE HOSE HOLDING AT DEPTH (filtered)
|y| SHEAR (sec⁻¹)·10⁻²
1.0
Ri = 1/4
Ri = 10
0.30
0.60
0.90
1.20
1.50
1.80
2.10
2.40
2.70
3.00
3.30
3.60
0
1.0
2.0
3.0
4.0
5.0
DENSITY GRADIENT 10⁻⁶ (gm/cm³/meter)
r = -0.12
ESTIMATED FROM TEMPERATURE GRADIENT

FIG. 3.10

CORRELATION BETWEEN THE SHEAR MAGNITUDE AND THE TEMPERATURE GRADIENT AS A FUNCTION OF SALINITY GRADIENT

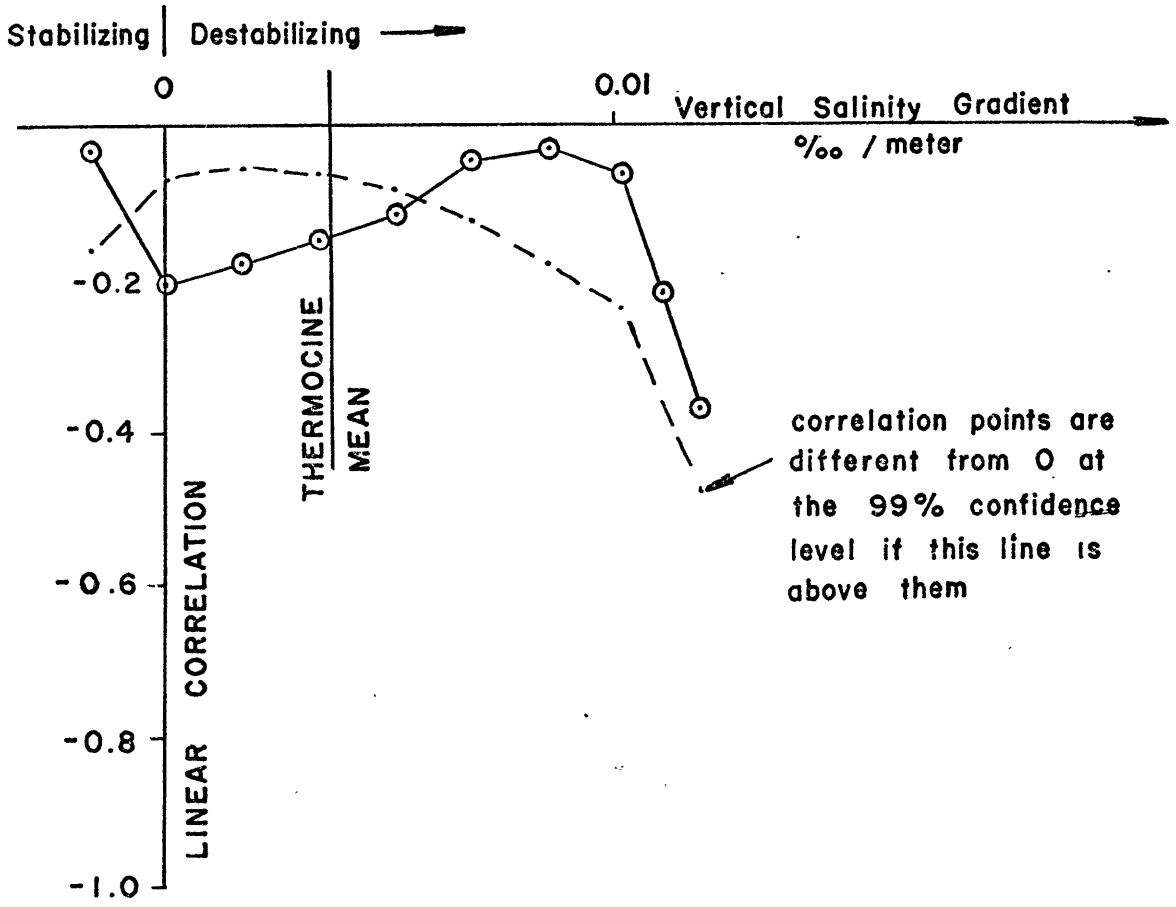

FIG. 3.11

Richardson number calculations

The Richardson number has been identified by several workers to be the correct stability parameter for density stratified shear flows. In particular Miles and Howard have shown for steady inviscid shear flow that if $\frac{\frac{g}{\rho_0}\frac{\partial \rho}{\partial z}}{\left[\frac{\partial U_H}{\partial z}\right]^2} > \frac{1}{4}$ everywhere the flow will be stable. More recent numerical work by Hazel (DAMTP, Cambridge), reported by Woods (1969), shows that most flows of Ri < 1/4 are in fact unstable. Paul Linden of the same department has suggested in a personal communication that salt fingers may exist only for Ri> 10 for laminar shear flows and Ri > 1000 for turbulent flows. These tentative results were found from his laboratory experiment with Turner.

The central question in computing Richardson numbers is what to do about data where density gradient is apparently unstable due primarily to destabilizing salinity gradients (see figure 3.12). One possible viewpoint is to assume they don't exist and are an artifact of the salinity sensors. The density gradient can then be derived from the temperature gradient as is done above. The other possibility is to assume that they are real as is suggested by the mean salinity gradient computed below in regions of near-zero temperature gradient. Since it is impossible to settle this question definitively with the present data, both results are presented. These cumulative frequency curves (see figure 3.13) are based on filtered data and both show that 50% or more of the data lies in a region 1/4 < Ri < 10. The major difference lies in the region of Ri < 1/4

which includes almost twice as much data for T-S computed density curve with 13.5% having negative Richardson numbers. Both curves have significant amounts of data in the potential salt finger region.

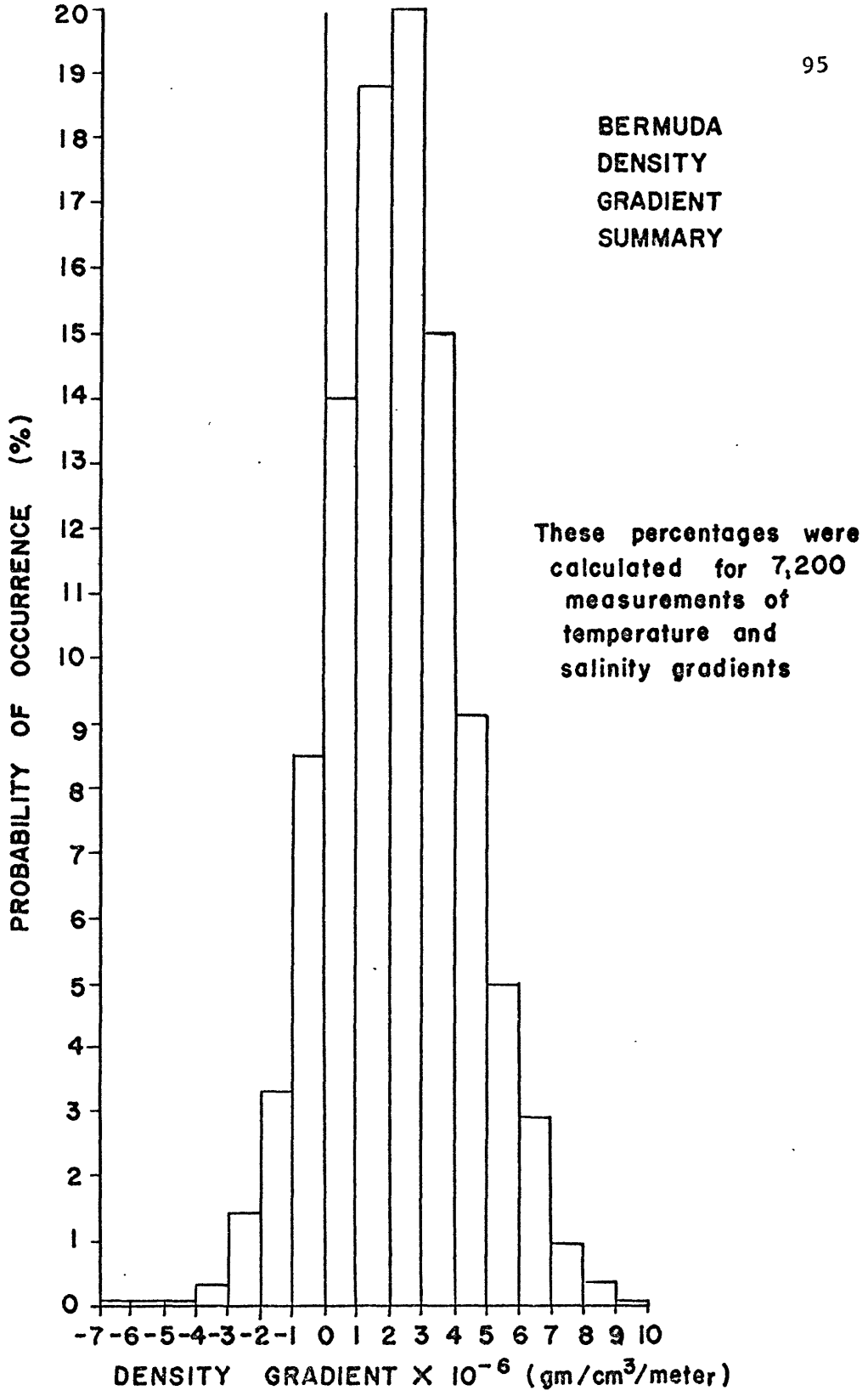
BERMUDA
DENSITY
GRADIENT
SUMMARY
These percentages were calculated for 7,200 measurements of temperature and salinity gradients
PROBABILITY OF OCCURRENCE (%)
0
1
2
3
4
5
6
7
8
9
10
11
12
13
14
15
16
17
18
19
20
-7 -6 -5 -4 -3 -2 -1 0 1 2 3 4 5 6 7 8 9 10
DENSITY GRADIENT X 10^{-6} (gm/cm^3/meter)

FIG. 3.12

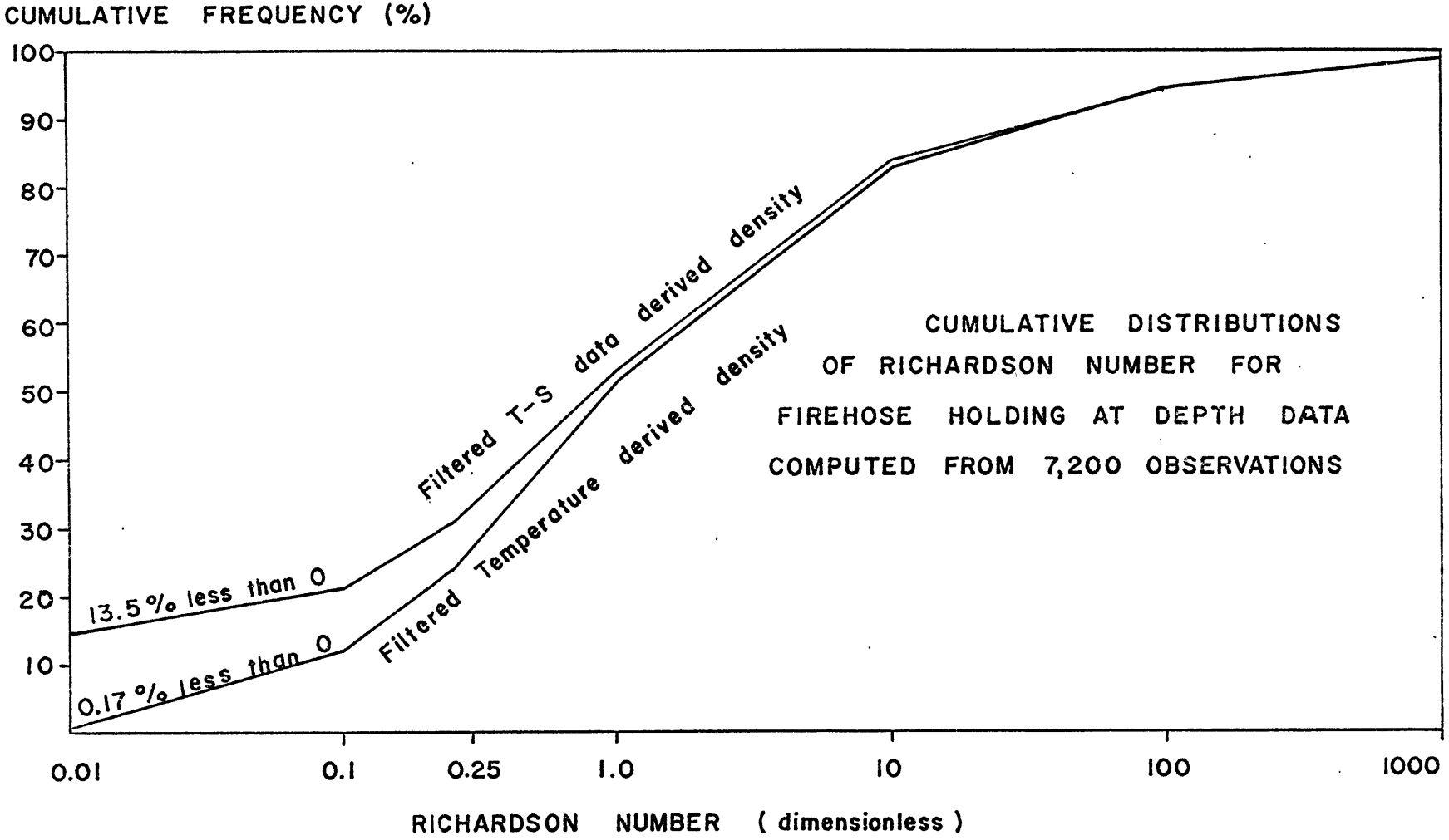
CUMULATIVE FREQUENCY (%)
100
90
80
70
60
50
40
30
20
10
Filtered T-S data derived density
Filtered Temperature derived density
13.5 % less than 0
0.17 % less than 0
CUMULATIVE DISTRIBUTIONS
OF RICHARDSON NUMBER FOR
FIREHOSE HOLDING AT DEPTH DATA
COMPUTED FROM 7,200 OBSERVATIONS
0.01
0.1
0.25
1.0
10
100
1000
RICHARDSON NUMBER (dimensionless)

FIG. 3.13

Salinity gradients in well-mixed temperature regions

Before the salinity gradient results can be sensibly interpreted, it is necessary to review briefly what is known about the Bissett Berman Model 6007 in-situ salinometer, two of which were used to determine the salinity gradient. This sensor actually measures the electrical conductivity of a closed loop of sea water by induction techniques. However to reduce the telemetry accuracy requirements (by a factor of ten) only that portion of the conductivity variation related to changes in salinity is transmitted. The portion of the actual conductivity change which is due to temperature change is computed in-situ to third order and together with a smaller first order pressure correction is subtracted from the output signal before transmission to the surface. The critical question is how accurate is the sensor and in which circumstances is this accuracy most open to question?

Pingree (1970) in a very careful study concludes that the standard deviation for this salinity sensor is ±.005% when calibrated in-situ with respect to water bottles and an Autolab laboratory salinometer which have a standard deviation of ±.003% together. These comparison results were obtained over several days and a salinity range of .8% within selected homogeneous layers and they suggest that this salinity sensor is probably as accurate as the traditional water bottle measurements in homogeneous regions. Jaeger (1969) of Bissett Berman states that the largest salinity errors are associated with largest temperature gradients. He asserts that these errors are due to "the poor time response of the oscillator and automatic gain

control circuits as well as the difference in time constants between the conductivity head and the temperature probe". He further states that "a significant change in temperature with resultant change in conductivity causes these oscillators to go into nonlinear operation". All of these effects are most pronounced when the temperature gradient is greatest and the speed of penetration of this gradient is greatest.

Since the scissors measures both the temperature gradient and the salinity gradient, a comparison of the scatter of salinity gradients as a function of the temperature gradient can be made. The data selected for this comparison were the firehose constant depth data. The salinity spiking due to fast penetration of sharp temperature gradients should be minimum due to the ship heave suppressing of the firehose. For this comparison these temperature and salinity data were digitally smoothed with a running weighted average to average out salinity spikes and least count jitter (see appendix for weighting function). Next the smoothed data were sorted in temperature and salinity gradient intervals. The standard deviation due to quanitization error is $\sigma = \sqrt{\frac{1}{12}}$ (least count) = .29 (least count) according to Bendat and Piersol (1966). Accordingly, to gain the greatest possible resolution in salinity gradient the filtered salinity gradient values were sorted at the 1/3 least count level. To give reasonably large sample sizes for each temperature gradient interval, twice the least count in temperature gradient was selected. Finally mean temperature and salinity gradients over the depth interval from

625 to 762 meters were computed from 6 Atlantis II 47 STD lowerings (see figures 3.12, 3.13). They are $\overline{\frac{dT}{dz}}$ = .0237 ±.0020 °C/meter and $\overline{\frac{dS}{dz}}$ = .00325 ±.00035 °/oo /meter respectively. It was assumed, for the computations that follow, that these average temperature and salinity gradients computed on the 100 meter scale are equal to the average temperature and salinity gradients observed on the 3 meter scale by the scissors.

The mean salinity gradient and the standard deviation of the salinity gradient for each of eleven temperature gradient intervals was computed (see figure 3.16). The standard deviation shown by the dashed line for the smaller temperature gradients is about .005°/oo / meter becoming more than half again this large for larger temperature gradients. This larger scatter in the salinity gradient at higher temperature gradients would be expected on the instrumental grounds outlined above even if the actual temperature-salinity correlation were perfect. The mean salinity gradient for each temperature gradient interval is also plotted in figure 3.16 as the heavy unbroken line. Assuming each mean is single realization from a normal process the standard deviation of each mean is given approximately by $\sigma_m = \frac{\sigma}{\sqrt{N}}$ where N is the number of observations and σ is the estimate of the process standard deviation. Ninety-five per cent confidence intervals for each mean may then be calculated for each mean and are given by $\pm 1.96\sigma_m$. These confidence intervals are plotted in the same figure as the light unbroken lines embracing the mean line.

The most striking result of these computations is that the

mean salinity gradient for near zero temperature gradient is statically unstable at the 95% confidence level if the above assumptions are valid. Is this apparently unstable salinity gradient great enough for Rayleigh convection to set in? Chandrasekhar (1961) gives critical Rayleigh numbers as a function of Taylor numbers in a rotating thermally stratified system. The Taylor number $T = \frac{4\Omega^2 d^4}{\nu^2}$ where Ω is the vertical component of the earth angular velocity, d is the layer thickness and ν is the kinematic viscosity. For a layer 3 meters thick at the latitude of Bermuda the Taylor number is about 3×10^5 which corresponds to a critical Rayleigh number of 4.26×10^4 for a Schmidt number of order 10^3. For near zero temperature gradient we then compute a haline Rayleigh number $R = \frac{g\beta\frac{\partial s}{\partial z} d^2}{Ks\,\nu}$ where Ks is the salt diffusivity, β is the salt expansion coefficient, $\frac{\partial s}{\partial z}$ is the vertical salinity gradient and g is gravity. Using the above critical Rayleigh number the critical salt gradient for a 3 meter layer is $\frac{\partial s}{\partial z_{crit}} \geq 2\times10^{-10}$ ‰/meter.

Clearly if the mean salinity gradient is order 10^{-3} ‰/meter in the near zero temperature gradient regions, these regions will be strongly unstable. Even though the foregoing linear stability analysis is open to question in nature some form of convection almost surely would dominate. A contour plot of the probability of occurance of temperature and salinity gradients is seen in figure 3.17. Such regions could correspond to the convecting layers in the salt finger model of Turner (1968). If this is true then such layers are intermittent (occurring on the 3 meter scale in about 4 percent of this data) rather than continuous in time or space as Turner's simple

steady state model suggests.

The above salinity gradient calculations are open to question on several grounds. First one might reasonably ask if these salinity sensors are mutually stable to ±.002 ‰ over the 5 hour period of the fire hose measurements. Long term tests on a similar Bissett Berman salinometer in sea water by Brown et al. (1966) showed that salinity output variations were +.002 ‰ over a 12 day period and -.005 ‰ over a 44 day period. Although the above stability requirements are not unreasonable in view of the Bissett Berman results this point cannot be considered settled. A further uncertainty is whether enough data were taken so that the average temperature and salinity gradient on the 3 meter scale is in fact equal to the average temperature and salinity gradient on a 100 meter scale. Deviations from these assumed equalities would shift the origin of the above T-S gradient plot. We can only estimate the stability of the STD means. The standard deviation of the 100 meter mean temperature gradient is $\sigma_{mT} = \frac{\sigma_s}{\sqrt{6}}$ = .00082 °C/meter and of the salinity gradient is $\sigma_{mS} = \frac{\sigma_s}{\sqrt{6}}$ = .00014 ‰ /meter. These expected deviations are not large enough to shift the above origin significantly enough in either T or S to stabilize the mean .001 ‰ /meter salinity gradient at zero temperature gradient.

A more definitive future experiment is planned where temperature and conductivity gradients will be measured directly with a least count resolution of $\pm 2.5 \times 10^{-4}$ °C/meter and $\pm 1 \times 10^{-4}$ milli mho/cm/meter which gives about ±.001 ‰ /meter on a 30 cm vertical scale. More

importantly these gradient sensors will be inverted periodically to check the location of zero gradient. Furthermore electrical conductivity gradient will be measured directly so no unpredictable temperature compensation circuit will be required. It is hoped that these future measurements will resolve the important question: are the regions of near zero temperature gradient statically unstable or not? The present observations suggest that they might be.

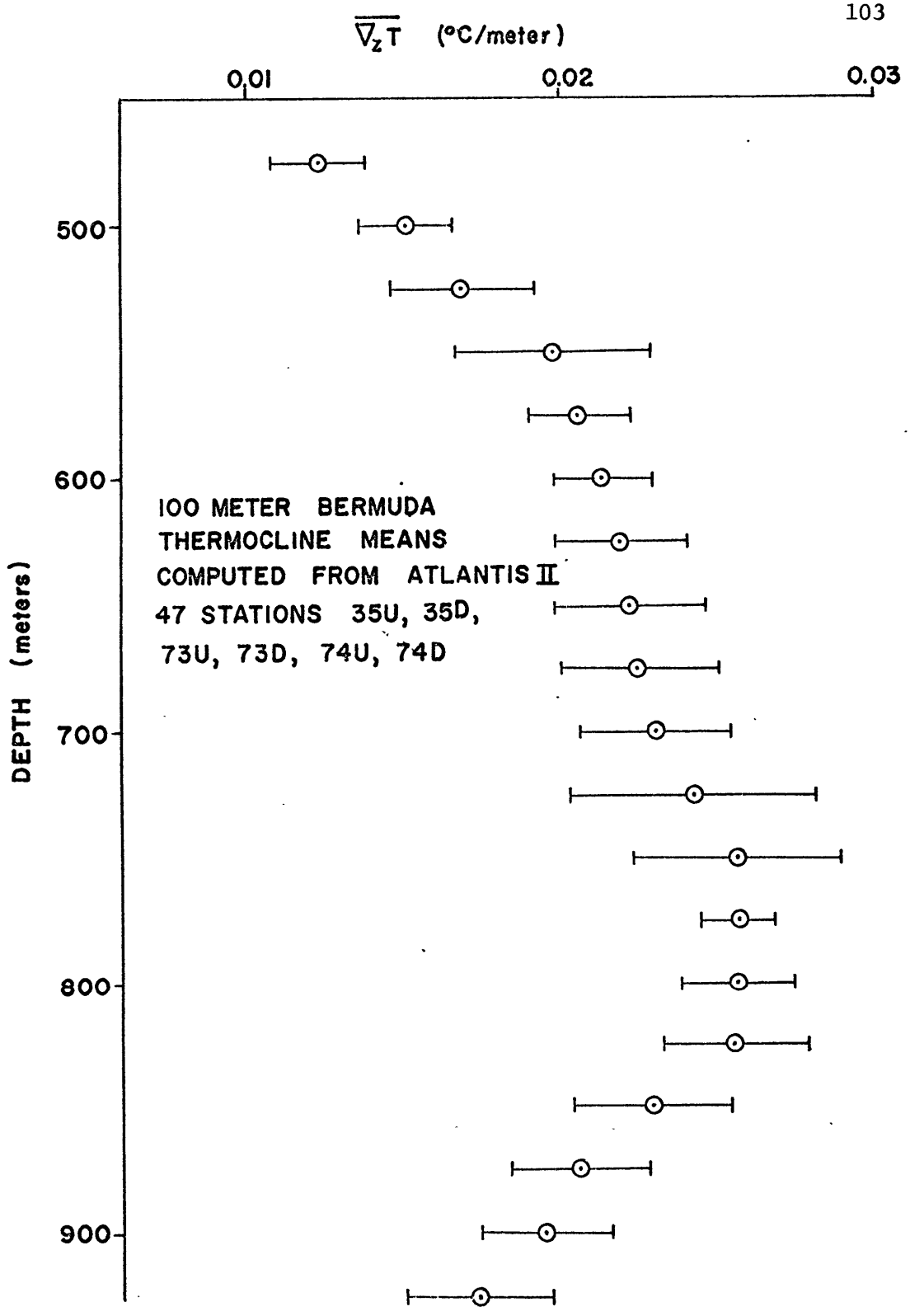
$\overline{\nabla_z T}$ (°C/meter)
0.01
0.02
0.03
500
600
700
800
900
DEPTH (meters)
100 METER BERMUDA
THERMOCLINE MEANS
COMPUTED FROM ATLANTIS II
47 STATIONS 35U, 35D,
73U, 73D, 74U, 74D

FIG. 3.14

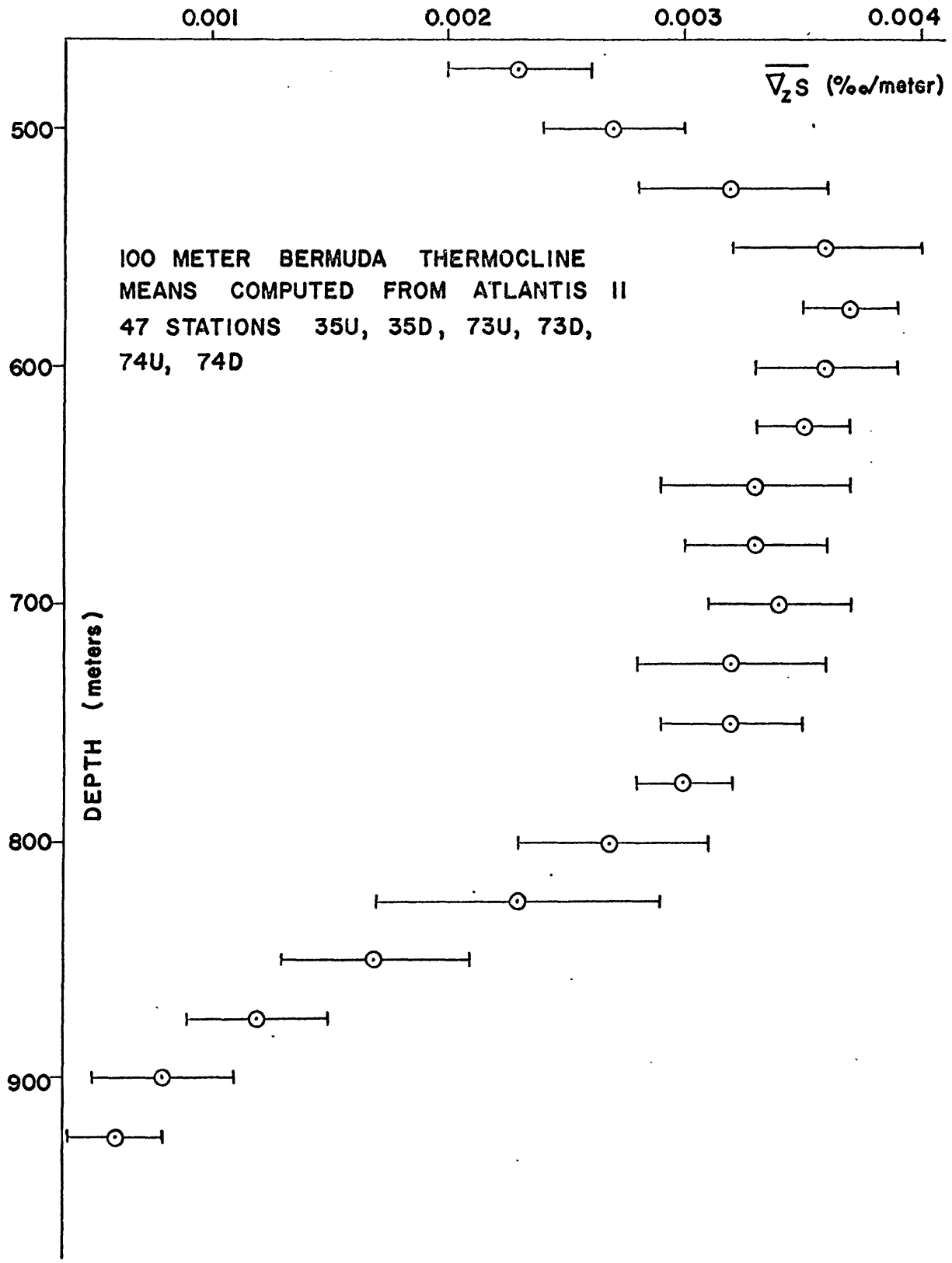
0.001
0.002
0.003
0.004
$\overline{\nabla_z S}$ (‰/meter)
100 METER BERMUDA THERMOCLINE
MEANS COMPUTED FROM ATLANTIS II
47 STATIONS 35U, 35D, 73U, 73D,
74U, 74D
500
600
700
800
900
DEPTH (meters)

FIG. 3.15

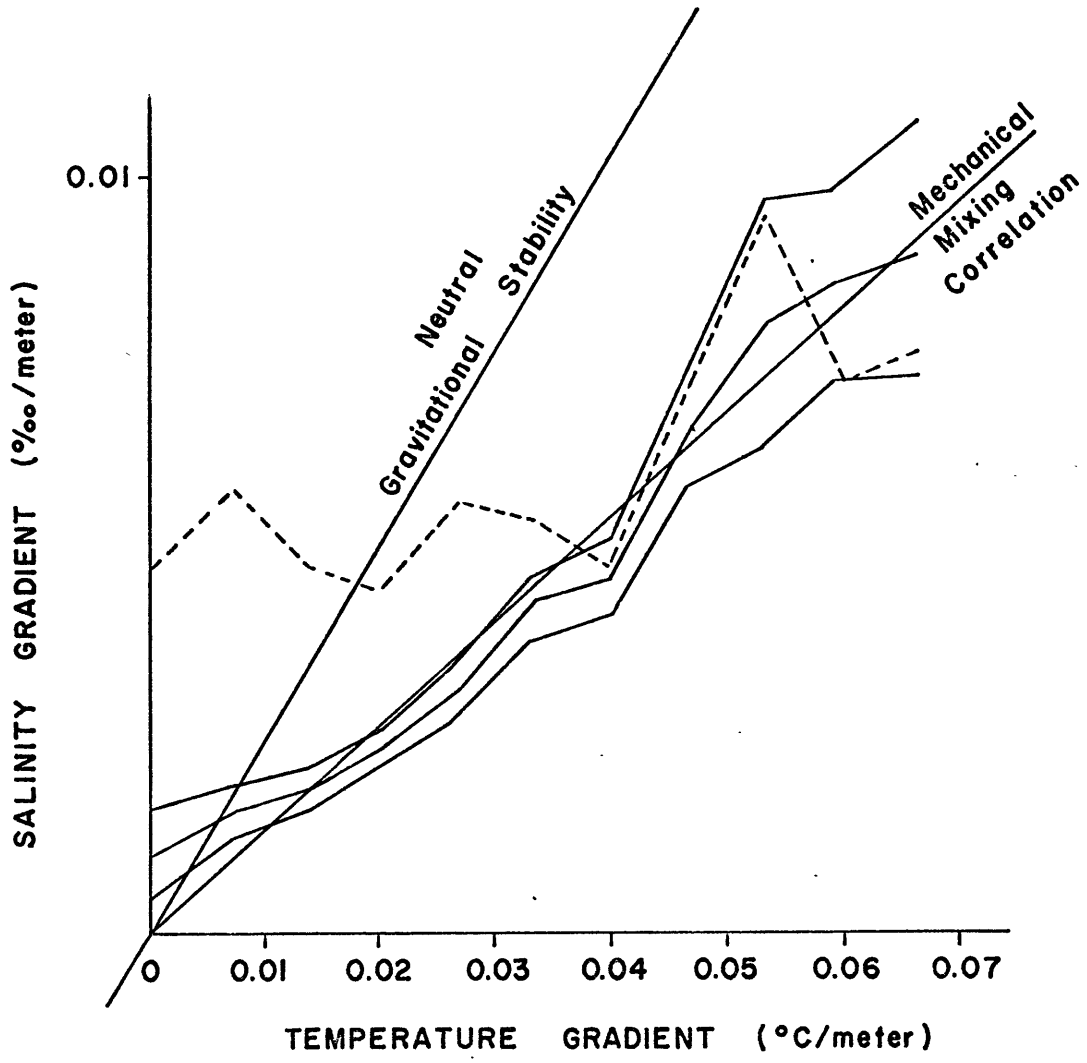
0.01
SALINITY GRADIENT (‰/meter)
Neutral Stability
Gravitational
Mechanical Mixing Correlation
0
0.01
0.02
0.03
0.04
0.05
0.06
0.07
TEMPERATURE GRADIENT (°C/meter)

FIG. 3.16

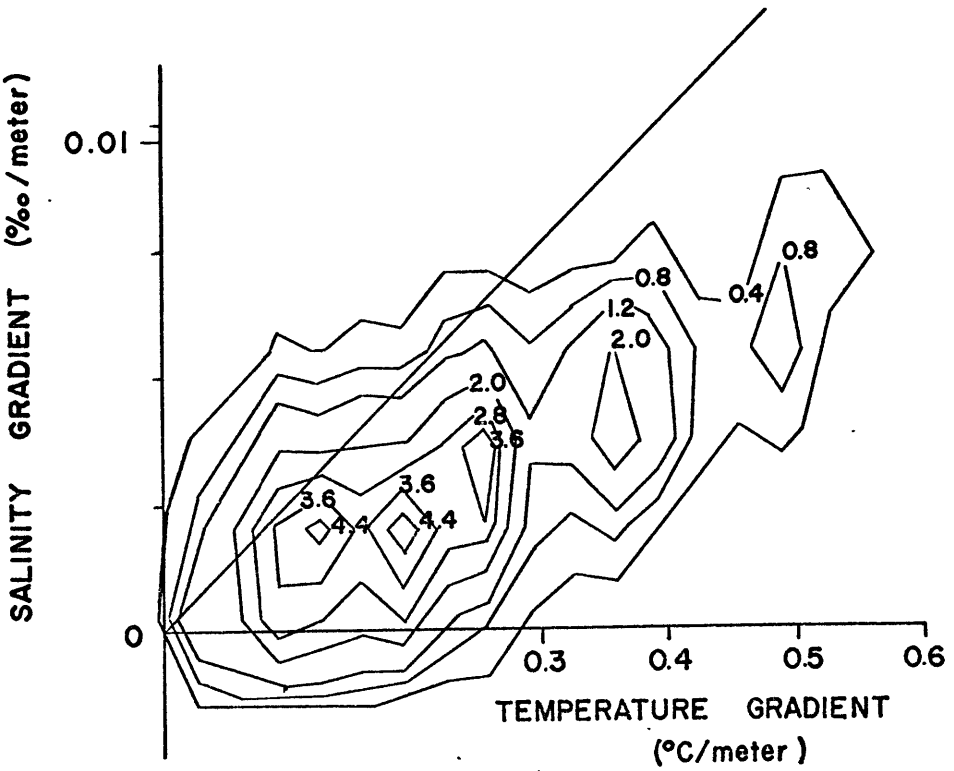
SALINITY GRADIENT (‰/meter)
0.01
0
0.3
0.4
0.5
0.6
TEMPERATURE GRADIENT
(°C/meter)
0.8
0.4
0.8
1.2
2.0
2.0
2.8
3.6
3.6
3.6
4.4
4.4

FIG. 3.17

The salt finger mechanism of mixing in the ocean is unique because it alone distinguishes between temperature and salinity, at least on the small scale. The diameter of the individual salt fingers L is estimated by Stern (1969) to be of order $L = \left[\frac{g\alpha}{K_t \nu}\left[\frac{\partial T}{\partial z}\right]\right]^{-\frac{1}{4}}$ 0.6 cm @ .05°C/meter and 1.0 cm @ .01°C/meter, so that individual salt fingers will not be directly observed with the larger (5 to 10 cm diameter) sensors which were used. It may still be possible to look for indirect evidence of salt fingering (see also appendix G) in the temperature-salinity gradient correlation and in the density shear correlation if one considers the temperature and salinity and their gradients to be distributed as in figure 3.18 discussed by Stern. Here in salt finger layers (thickness = h) the horizontally averaged salinity gradient is small while the corresponding temperature gradient is maximum. Between pairs of active salt finger layers Stern and Turner have shown convective layers to be present in the laboratory as Stommel had suggested. These convective layers shear off the ends of the fingers. This shearing process limits the growth in thickness of the embracing salt finger layers and forms some sort of boundary layer between the convecting layers and the salt finger layers where the vertical salinity gradient is maximum. From time lapse movies of Turner and also Lambert (or URI) it was seen that motion in adjacent convective layers frequently was in the same direction on both sides of the salt finger layer. This appeared to be caused by strong plumes separating from both sides of the salt finger

layer at the same horizontal position. The shear in the salt finger layers was evidently small because the salt fingers remained vertical. Such motions could give rise to the negative correlation between shear and density gradient observed in my data (see figures 3.9 and 3.18).

Although it is relatively easy to show the existence of salt fingers in the laboratory with large temperature and salinity gradients, experiments with the two orders of magnitude smaller oceanic size gradients and larger physical dimensions are quite difficult to set up due to heat leakage at the side walls. Accordingly Stern and Turner (1969) have investigated a system of alternating salt finger layers and convecting layers using a sugar-salt rather than heat-salt system. They have found a series of formulas for computing dimensions and fluxes in a sugar-salt system which contain several "constants" which depend in an unknown fashion upon the molecular properties of the solutes used. However from Turner's previous temperature-salt work they give the salt finger layer thickness as:

$$h \propto \frac{\nu}{c\,(\beta \Delta s)^{1/3}}$$

where

ν = kinematic viscosity (cm^2/sec)

β = coefficient of salt expansion ($1/‰$)

ΔS = salinity difference across the salt finger layer($‰$)

$c \cong .1$ cm/sec when $10 \geq \frac{\alpha \Delta T}{\beta \Delta s} \geq 1.8$

For any given temperature and salinity this relation becomes

$$h\,(\Delta S)^{1/3} = \text{constant}$$

From Turner (1967) page 605 we can find from his figure $h \cong 2\,cm$ when $\Delta T = 15°C$ $10 \geq \frac{\alpha \Delta T}{\beta \Delta S} \geq 2$ for all his experiments so $0.4 \leq \Delta S \leq 2‰$ so for the ocean

$$2 \times \left[\frac{0.4‰}{\Delta S \text{ observed}}\right]^{1/3} \leq h \leq 2 \times \left[\frac{2‰}{\Delta S \text{ observed}}\right]^{1/3}$$

From his discussion it is most likely that the maximum value of $2‰$ applies so that the maximum thickness relation is used to estimate the layer thickness (see figure 3.19).

If the Stern and Turner formula for computing the thickness of a salt fingering layer is correct the salinity difference must be very small for thick salt finger layers. From figure 3.19 it is clear that if the gradients of temperature and salinity are measured on a 3 meter scale then the salinity gradient will be less than the least count noise of the salinity sensors for thick salt finger layers. The temperature gradient might still be large enough to measure. But if the salt finger layers are small in thickness compared to the scissors spacing (as expected 10 cm) then these salinity differences should be observed.

What might the observed temperature gradient - salinity gradient correlation for a region of the ocean which contains salt fingers and convecting layers be expected to look like? The convecting layers must be represented by points of low temperature and

salinity gradients which lie on the unstable side of the neutral gravitational stability curve due to an excess of destabilizing salinity gradient. The size of this excess will be the order of the average salinity (.0032 °/oo /meter or less). Since the destabilizing salt gradient must exceed neutral stability it seems unlikely that much convection will occur at temperature gradients much greater than the intersection of the neutral stability curve with the average salinity gradient. For the Bermuda data this limit would be about .013°C/meter. If the thermocline average temperature and salinity gradients are to be preserved, these convective points of excess salinity gradient at low temperature gradient must be balanced by a salinity gradient deficit at some larger temperature gradients. (See figure 3.20). This contrasts with the expected linear temperature-salinity gradient correlation for a purely mechanically mixed thermocline. In that case the temperature and salinity gradients should appear locally in a constant ratio. For a salt finger thermocline, points in the convection region should scatter significantly above this mechanical mixing curve. For greater temperature gradients the mean salinity gradients should lie significantly below this mechanical mixing line (see figure 3.20). These ideas appear to agree with the position of the mean salinity gradient as a function of temperature gradient displayed above in figure 3.16.

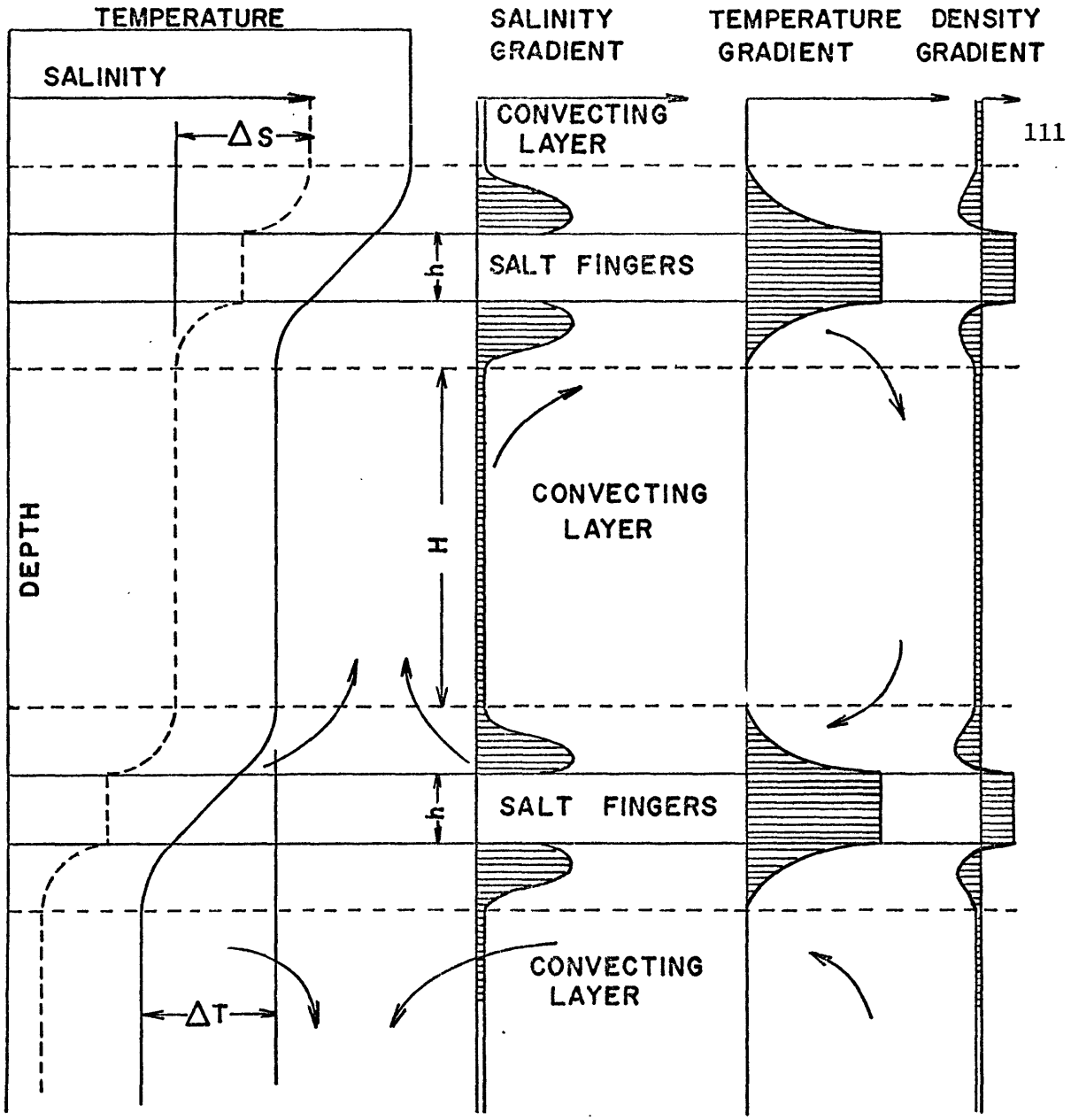

SALT FINGER SCHEMATIC AFTER TURNER AND STERN THE GRADIENTS SHOWN ARE HORIZONTALLY AVERAGED VERTICAL GRADIENTS (Negative density gradients are exagerated for clarity.)

FIG. 3.18

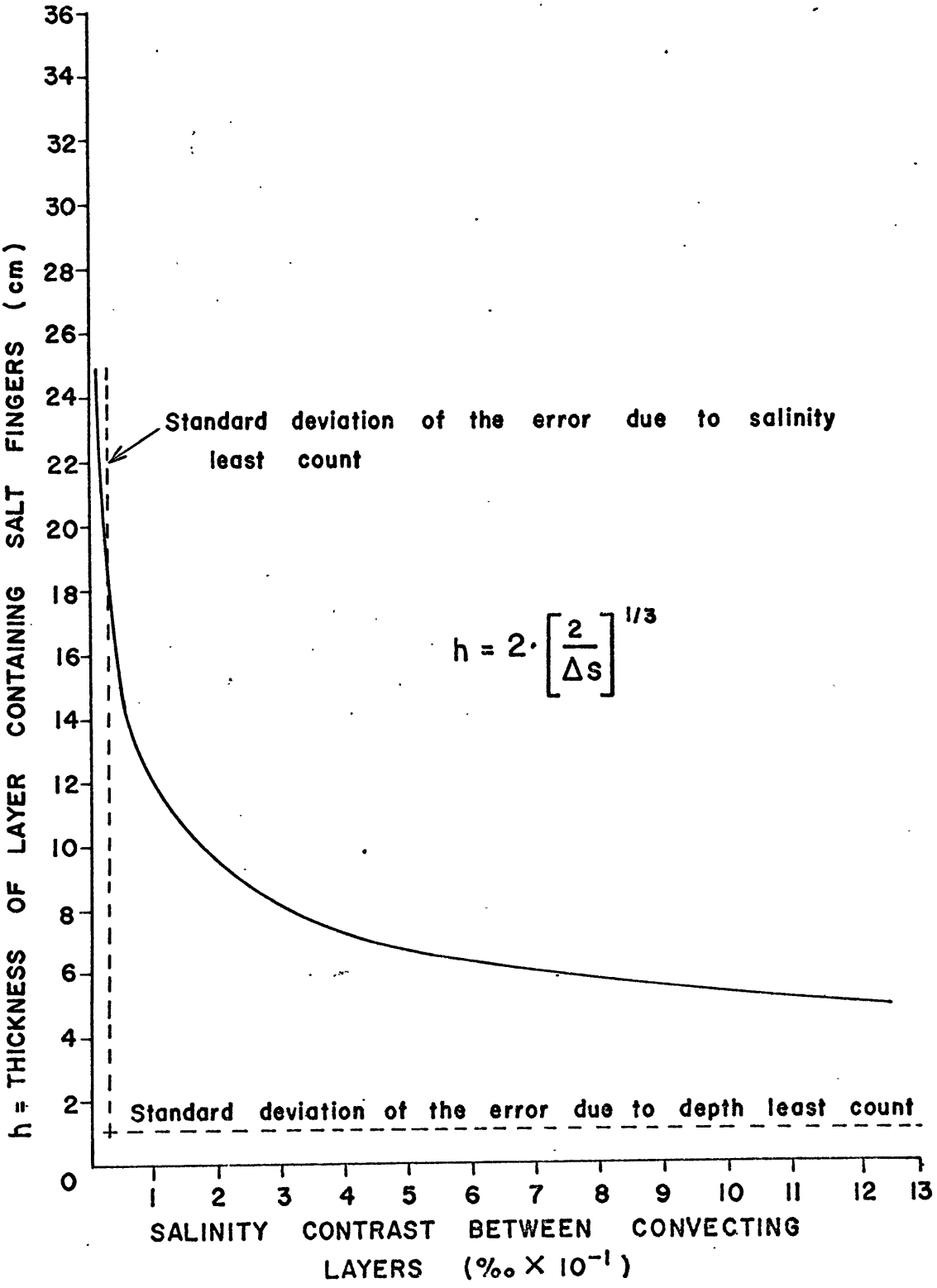
h = THICKNESS OF LAYER CONTAINING SALT FINGERS (cm)
36
34
32
30
28
26
24
22
20
18
16
14
12
10
8
6
4
2
0
Standard deviation of the error due to salinity least count
$h = 2 \cdot \left[\frac{2}{\Delta s}\right]^{1/3}$
Standard deviation of the error due to depth least count
1 2 3 4 5 6 7 8 9 10 11 12 13
SALINITY CONTRAST BETWEEN CONVECTING LAYERS (‰ × 10^{-1})

FIG. 3.19

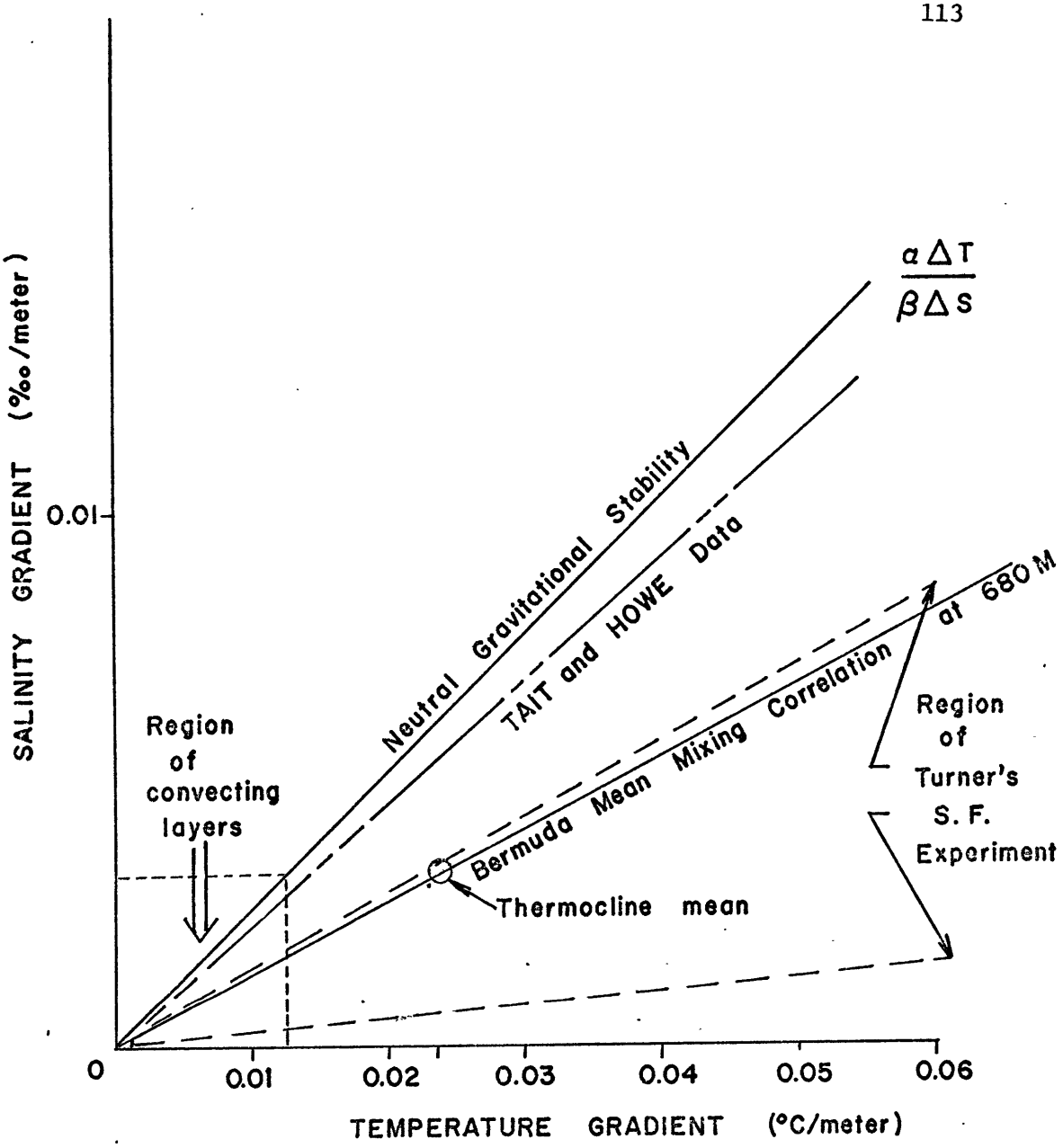
SALINITY GRADIENT (‰/meter)
0.01
0
0.01
0.02
0.03
0.04
0.05
0.06
TEMPERATURE GRADIENT (°C/meter)
$\frac{\alpha \Delta T}{\beta \Delta S}$
Neutral Gravitational Stability
TAIT and HOWE Data
Bermuda Mean Mixing Correlation at 680 M
Region of convecting layers
Region of Turner's S. F. Experiment
Thermocline mean

FIG. 3.20

Bermuda temperature and salinity gradients

The temperature and salinity gradients discussed above were computed by direct sensor subtraction with fixed 3 meter spacing. These above data were recorded while holding the scissors at a nominally constant depth from the fire hose so the data could be filtered. The temperature gradient appears to have a well-defined modal structure whereas in the salinity data this structure does not appear well defined. (See figures 3.17, 3.21, and 3.22.) Such modal distributions would be expected in sharply layered T-S microstructure but the 3 meter interval will blur such structure of a scale small compared to 3 meters. From the work of Cox it is evident that these small scales can occur. Two examples of ship-lowered gradient sections are shown in figure 3.23 from two widely spearated locations (the lower left and lower right of figure 3.1 respectively) on the same day. These results as well as results from other locations appear much the same on a 3 meter scale. It is particularly hard to pick a dominant vertical scale because all measurable scales appear to be present. The results of multiple temperature lowerings can be seen in figure 3.24. These ship lowerings were taken as the ship drifted, making a 70 meter peak to peak saw tooth depth time chart whose tooth spacing is $\sim$1/3 kilometer. It can be seen that strong gradients frequently persist from trace to trace suggesting that their horizontal extent agrees with Cooper and Stommel's (1968) estimates of 400 to 1000 meters. Note that the same temperature gradient and depth scales are used as in figure 3.23. It is more interesting to note that clearly recognizable features do not vary significantly in

depth from trace to trace suggesting that internal wave motion is either not present, is of very low frequency, and/or is horizontal (as in inertial motion). The same temperature gradient lowerings are replotted against temperature in figure 3.25.

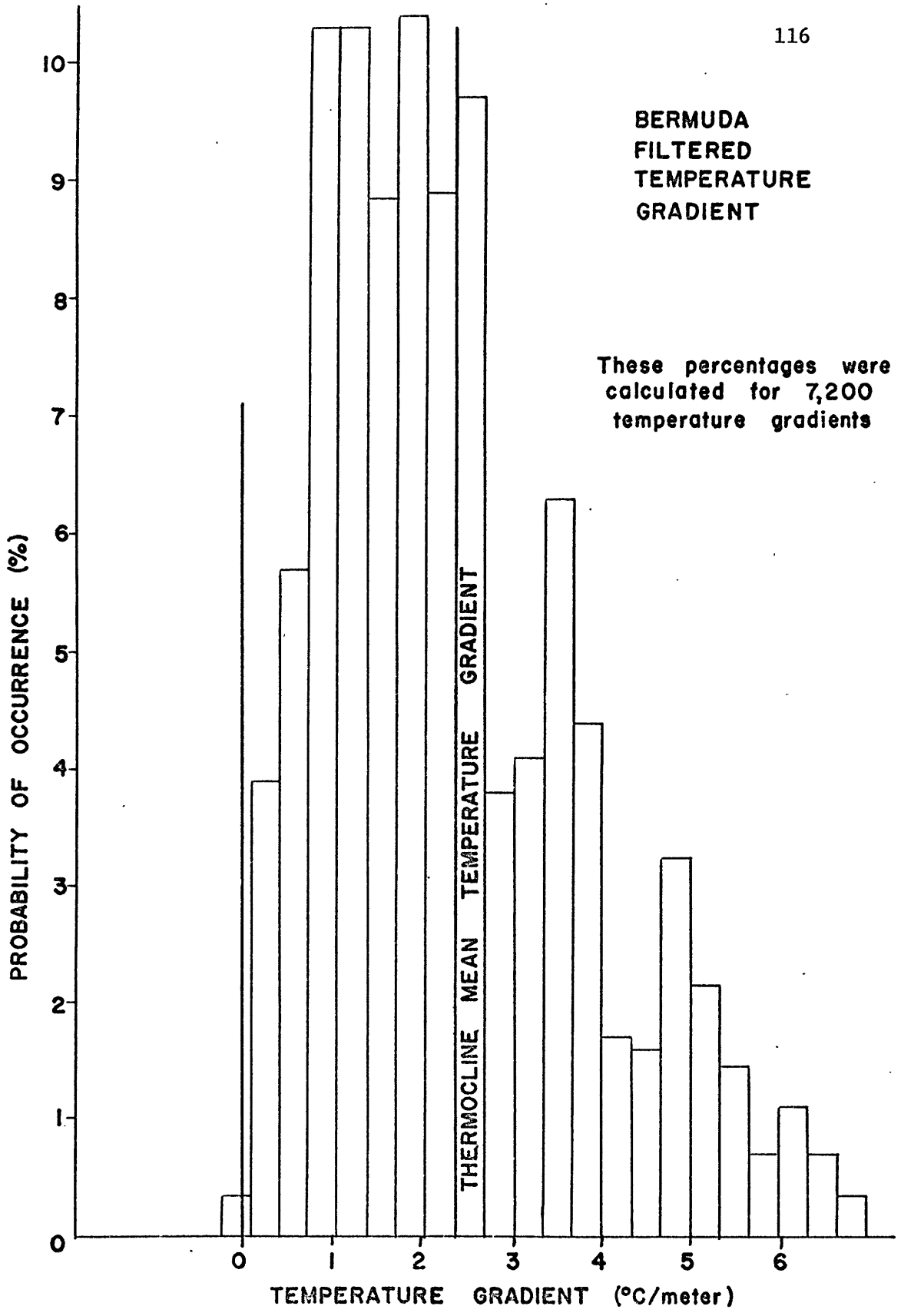
BERMUDA
FILTERED
TEMPERATURE
GRADIENT
These percentages were calculated for 7,200 temperature gradients
THERMOCLINE MEAN TEMPERATURE GRADIENT
PROBABILITY OF OCCURRENCE (%)
TEMPERATURE GRADIENT (°C/meter)
0
1
2
3
4
5
6
7
8
9
10

FIG. 3.21

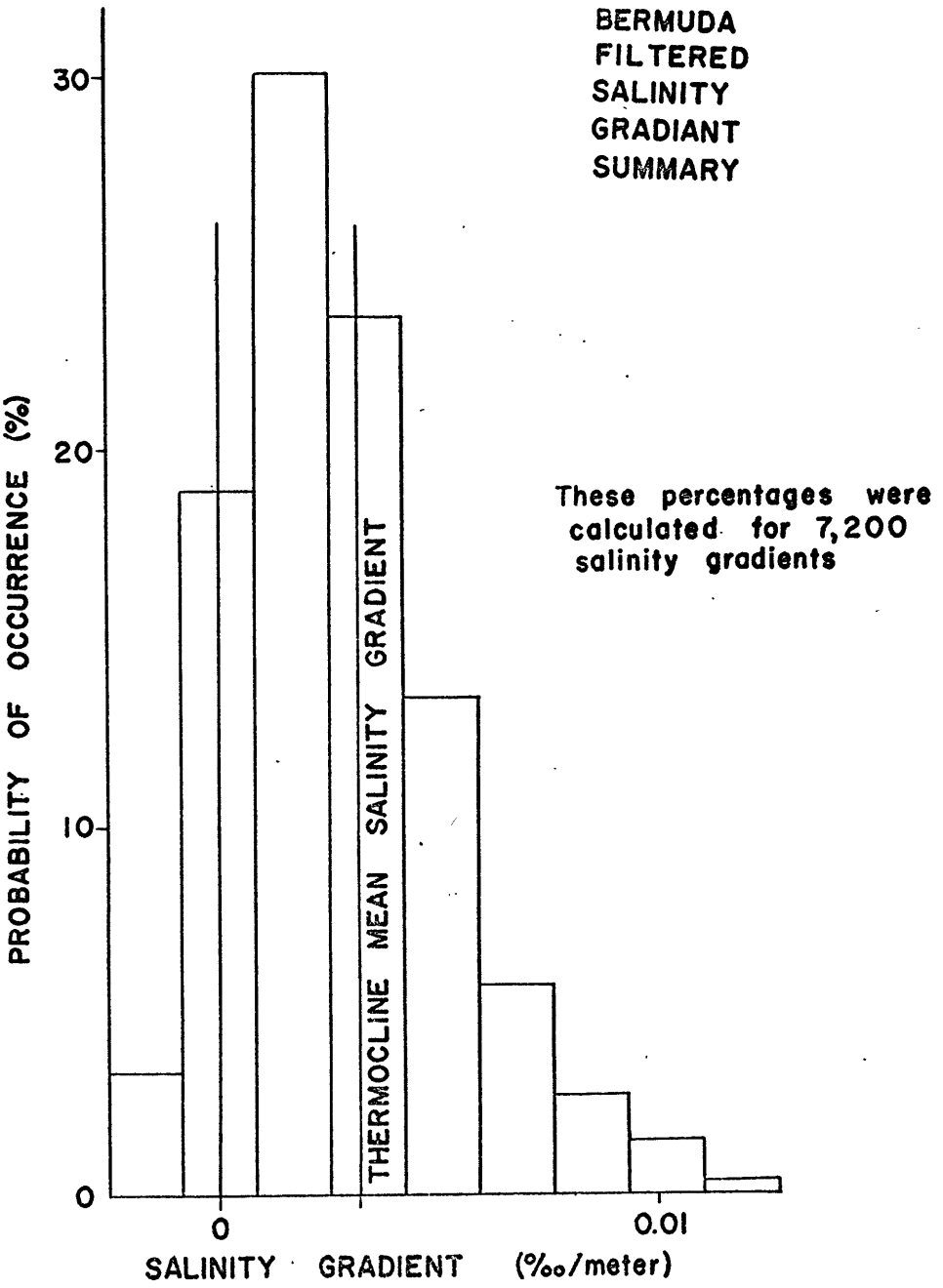
BERMUDA
FILTERED
SALINITY
GRADIANT
SUMMARY
These percentages were calculated for 7,200 salinity gradients
PROBABILITY OF OCCURRENCE (%)
30
20
10
0
THERMOCLINE MEAN SALINITY GRADIENT
0
0.01
SALINITY GRADIENT (‰/meter)

FIG. 3.22

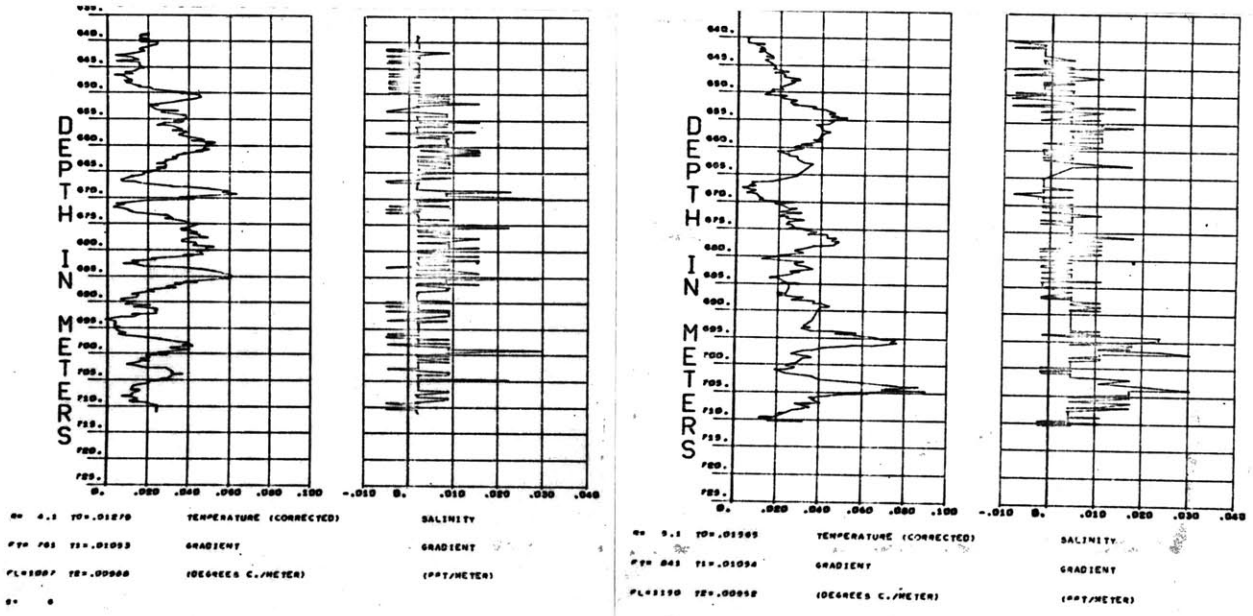
DEPTH IN METERS
TEMPERATURE (CORRECTED)
GRADIENT
(DEGREES C./METER)
SALINITY
GRADIENT
(PPT/METER)
DEPTH IN METERS
TEMPERATURE (CORRECTED)
GRADIENT
(DEGREES C./METER)
SALINITY
GRADIENT
(PPT/METER)

FIG. 3.23

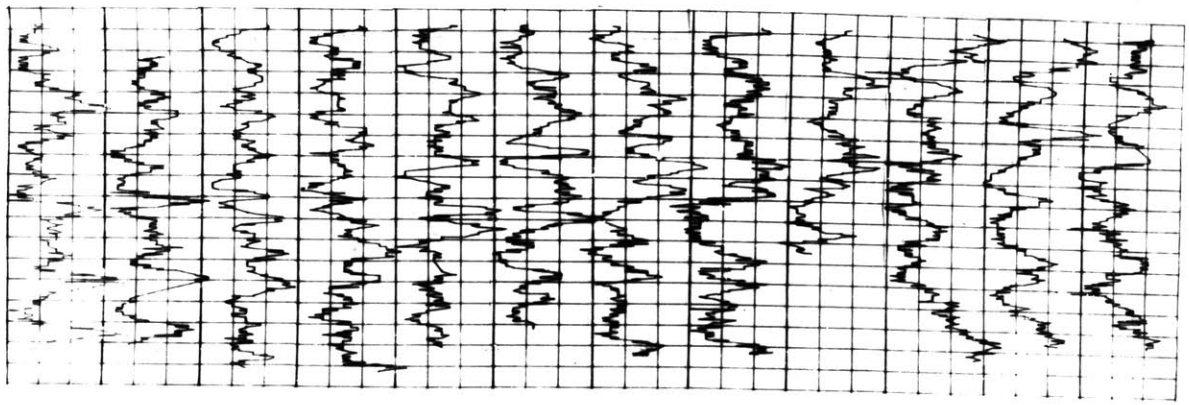

FIG. 3.24

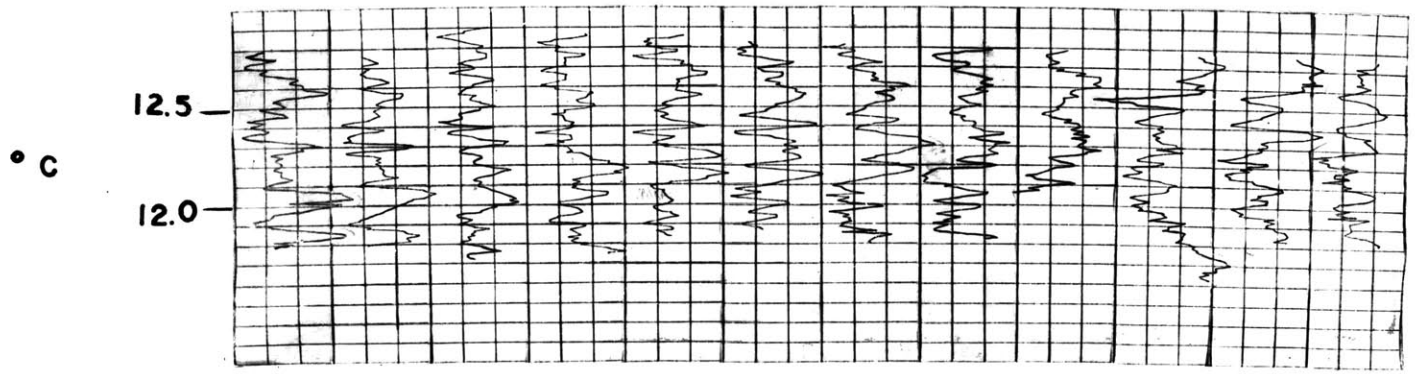

FIG. 3.25

Individual temperature and salinity records

Figures 3.26 and 3.27 show the individual temperatures and salinities vs. depth. From these it can be seen that temperature and salinity gradients of less than a meter in vertical extent are reasonably common. Several two to five meter thick well-mixed regions are also seen.

Measurements of temperature microstructure have been made (Stommel and Cooper; Cox et al.) with a single temperature sensor whose accuracy could only be estimated from laboratory calibrations. The measurements reported here were made with two identical platinum resistance thermometers spaced vertically approximately 3 meters apart. During raisings and lowerings, then, the outputs as a function of depth from the individual sensors could be compared by simply displacing one temperature vs. depth trace with respect to the other by a depth increment equal to the sensor spacing. If both sensors measured the water temperature as a function of depth with infinite resolution and complete accuracy and if the true water temperature as a function of depth remained unchanged during the passage of both sensors then the above comparison would yield a difference of zero at all depths of comparison. In practice the measurements are discrete digital sample points so some interpolation errors and quantization errors enter the comparison. This comparison gives an in-situ estimate of the temperature offset between the sensors for each depth of comparison. We may then compute a mean offset for each lowering. The standard deviation of this mean offset also places an upper bound on the errors of the individual measurements including mixing effects,

time lag errors and sensor drift. In addition this standard deviation is inflated by interpolation errors and real changes between the water masses each sensor is exposed to during the time between their individual passages. The above statement is particularly true for the ship-lowered measurements where wave heave motions tend to randomize common mode errors.

With a means of establishing an upper bound on the individual measurement errors it becomes possible to reduce systematic errors by minimizing standard deviation of the offset. The first systematic error checked for was the tilt of the scissors frame from the vertical for ship-lowered runs where no buoyancy modules or ballast were used. This was done by finding the depth offset which minimized the standard deviation of the comparison. For the ship-lowered measurements the best offset was about 2.28 $\pm$.097 meters or an equivalent average tilt of 40° $\pm$3° from vertical. This correction reduces the standard deviation about 30% from the 3 meter separation value.

The second systematic error to be investigated is the time lag error encountered by a sensor moving quickly through a steep temperature gradient. With the high resolution depth sensor an accurate 2 second averaged vertical velocity of the scissors synchronous in time with the temperature measurements can be had. Knowing the vertical speed of a temperature sensor and a crude estimate of the temperature gradient from adjacent temperatures one can estimate the lag error independently for each sensor. The resulting corrected

traces could then be compared as above and a new standard deviation computed. This process when repeated three times reduced comparison error 20 to 50% on most ship lowerings coming down to order ±.01°C. Similar attempts to reduce salinity sensor temperature-induced lag errors were fruitless. In all cases the salinity comparison errors grew. Raw temperature lag errors also did not correlate with the salinity comparison errors. These two facts lead the author to conclude that salinity errors are not simple temperature lag type but rather the nonlinear ringing type described in the salinity gradient section above.

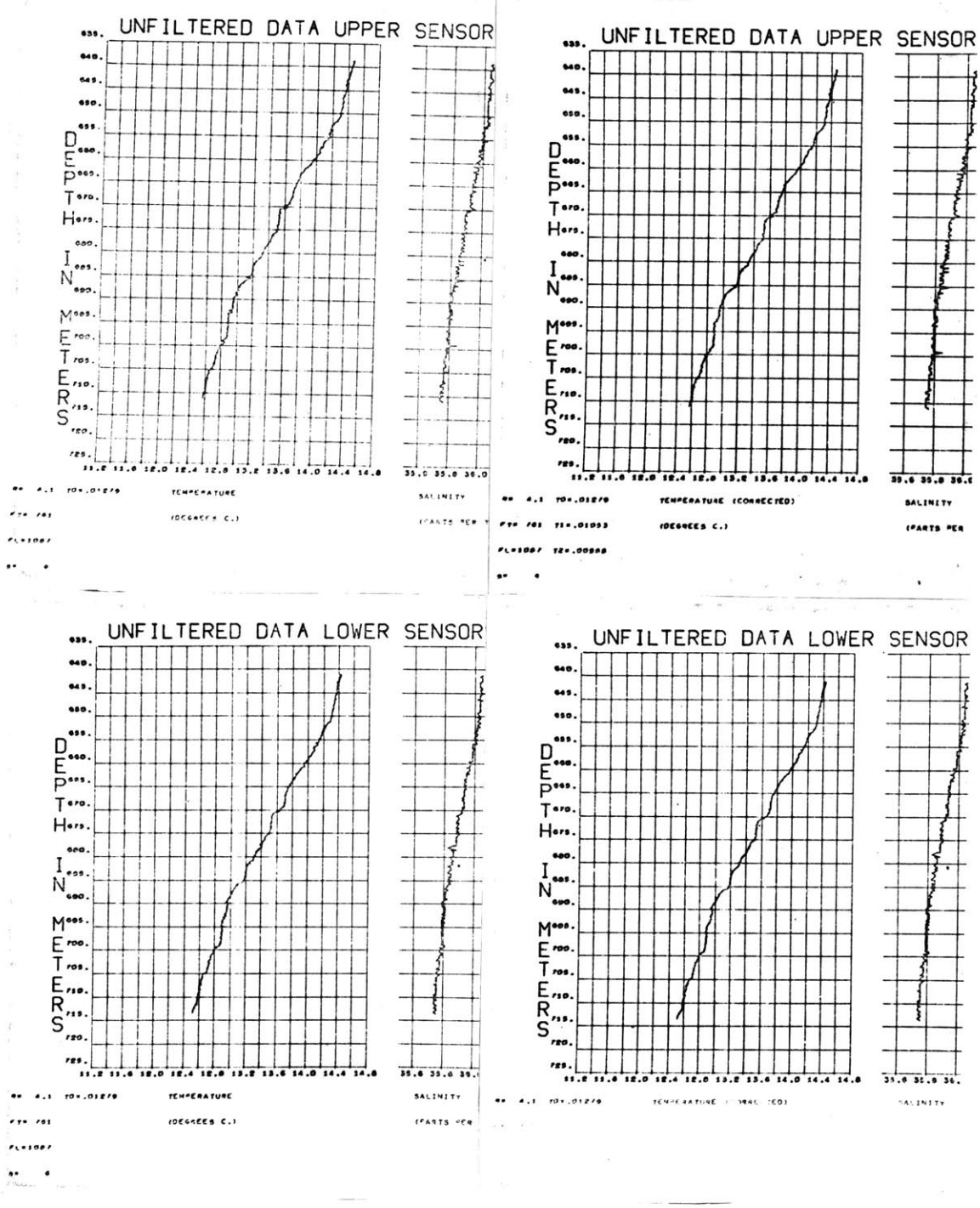
UNFILTERED DATA UPPER SENSOR
DEPTH IN METERS
TEMPERATURE (DEGREES C.)
SALINITY (PARTS PER
UNFILTERED DATA UPPER SENSOR
DEPTH IN METERS
TEMPERATURE (CORRECTED) (DEGREES C.)
SALINITY (PARTS PER
UNFILTERED DATA LOWER SENSOR
DEPTH IN METERS
TEMPERATURE (DEGREES C.)
SALINITY
UNFILTERED DATA LOWER SENSOR
DEPTH IN METERS
SALINITY

FIG. 3.26

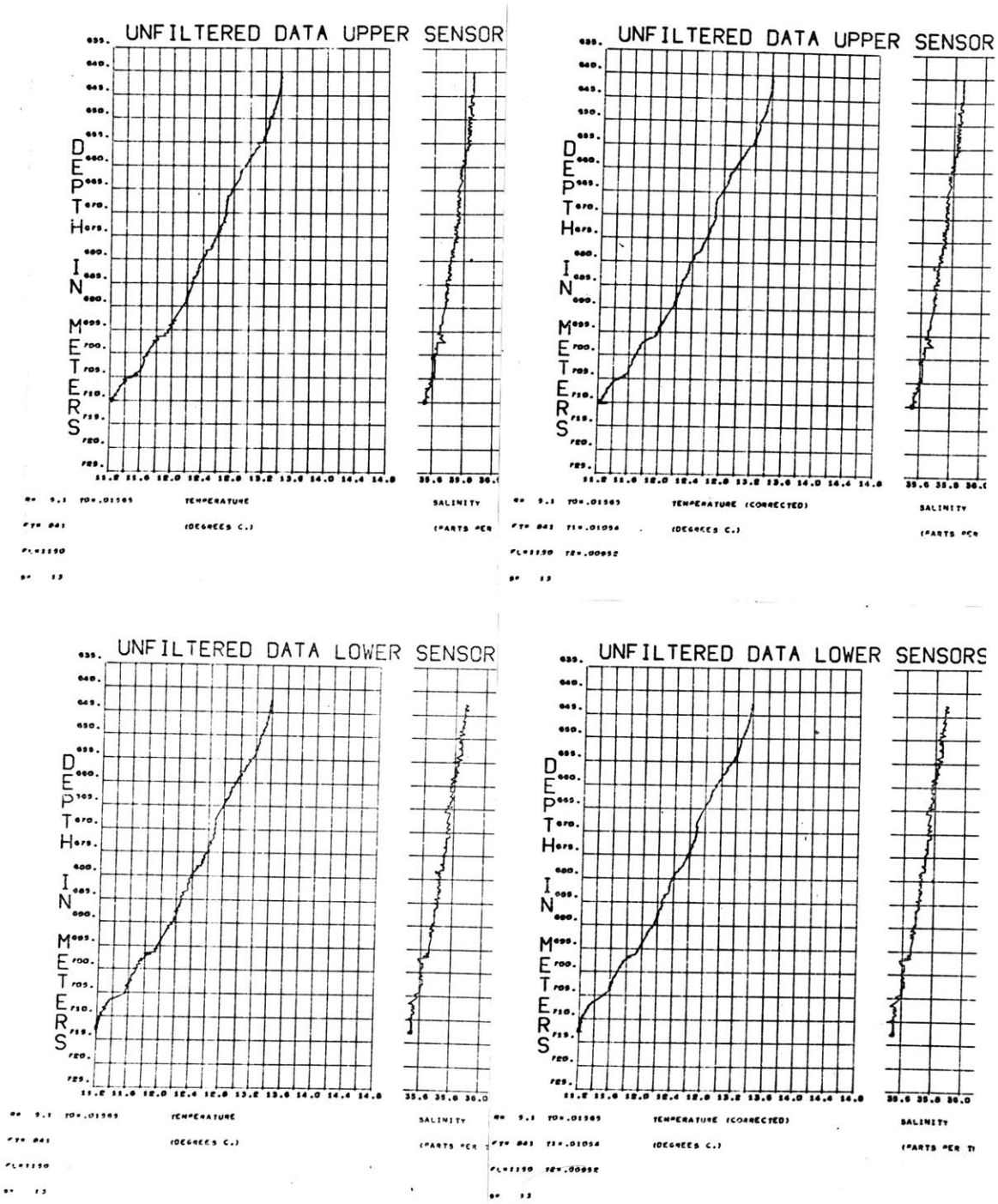
UNFILTERED DATA UPPER SENSOR
DEPTH IN METERS
TEMPERATURE
(DEGREES C.)
SALINITY
UNFILTERED DATA UPPER SENSOR
DEPTH IN METERS
TEMPERATURE (CORRECTED)
(DEGREES C.)
SALINITY
UNFILTERED DATA LOWER SENSOR
DEPTH IN METERS
TEMPERATURE
(DEGREES C.)
SALINITY
UNFILTERED DATA LOWER SENSORS
DEPTH IN METERS
TEMPERATURE (CORRECTED)
(DEGREES C.)
SALINITY

FIG. 3.27

Further indirect evidence of salt convection

Figure 3.28 shows the variation of $\frac{\alpha \nabla_z T}{\beta \nabla_z S}$ as a function of depth. This parameter compares the stabilizing influence of the temperature gradient to the destabilizing effect of the salinity gradient. As it approaches 1 from large values salt fingers become increasingly likely because the energy released by the salt field needs to do progressively less work against the density gradient to transport heat. It seems interesting that this buoyancy ratio groups scissors mean with the shallow dye shear measurements when plotted against $\frac{\overline{\sigma}}{\overline{S}}$ (see figure 3.29). A similar effect is noticed when the buoyancy ratio is divided by $\frac{\overline{\sigma}}{\overline{S}}$ and is plotted vs. the Vaisala frequency. These results suggest that the shear may be coupled to salt-driven convection in some way.

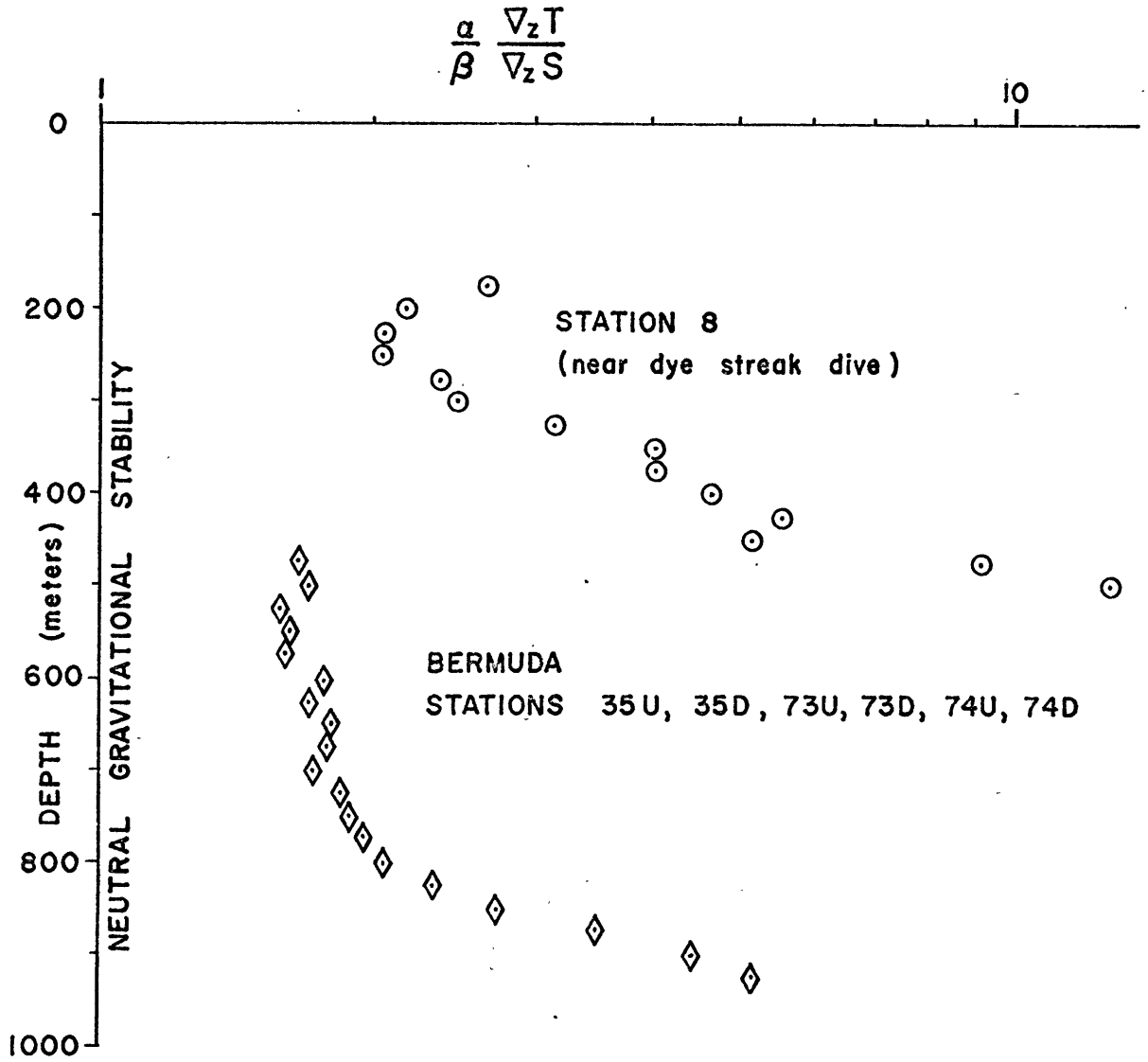

100 METER THERMOCLINE MEANS COMPUTED FROM ATLANTIS II CRUISE 47 STD STATIONS

FIG. 3.28

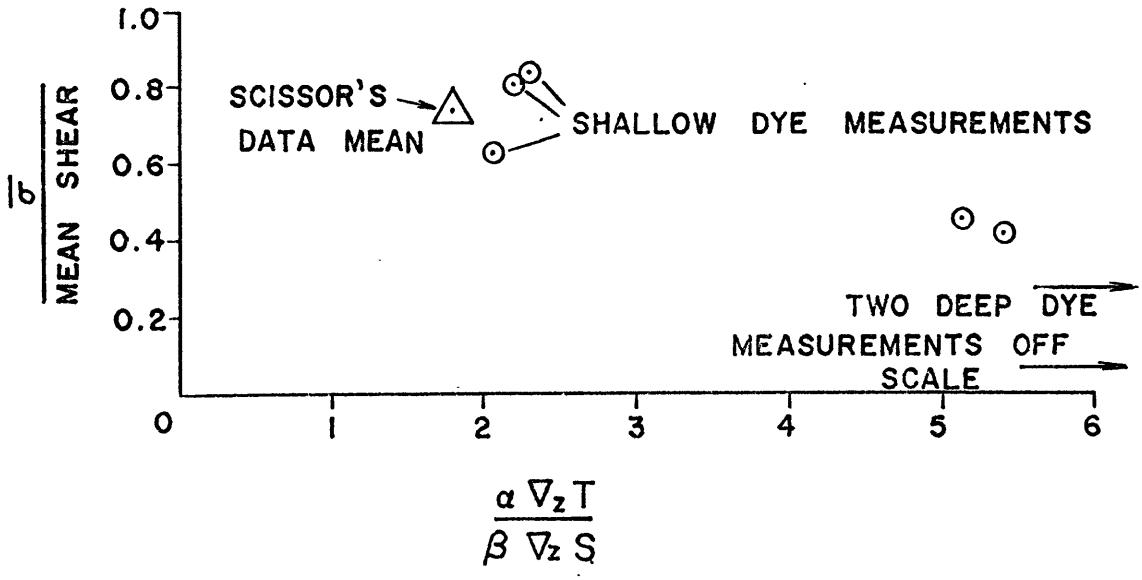
1.0
0.8
0.6
0.4
0.2
0
1
2
3
4
5
6
MEAN SHEAR
SCISSOR'S DATA MEAN
SHALLOW DYE MEASUREMENTS
TWO DEEP DYE MEASUREMENTS OFF SCALE
α ∇z T / β ∇z S

FIG. 3.29

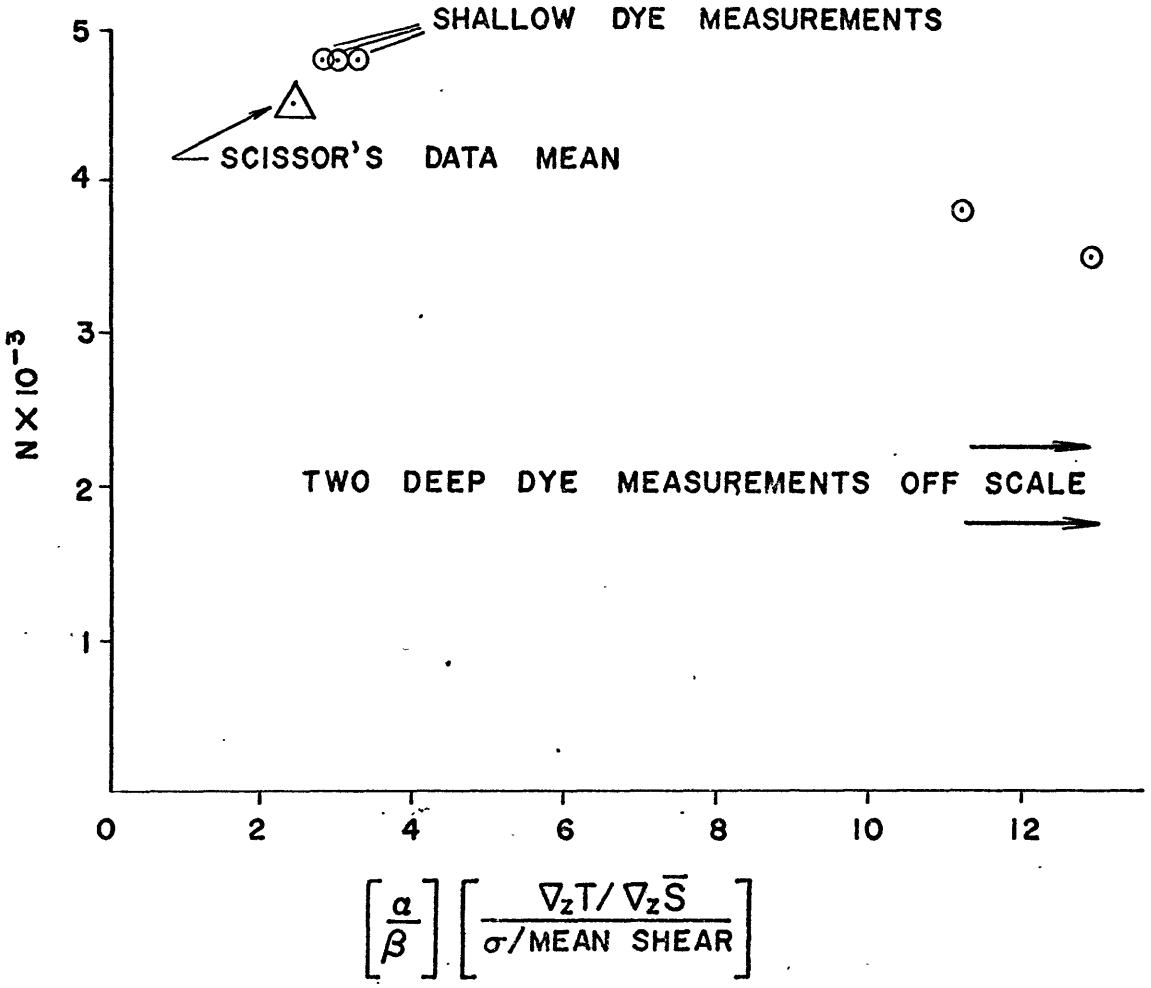
SHALLOW DYE MEASUREMENTS
SCISSOR'S DATA MEAN
TWO DEEP DYE MEASUREMENTS OFF SCALE
N X 10⁻³
5
4
3
2
1
0
2
4
6
8
10
12
[α/β] [∇zT/∇zS̄ / σ/MEAN SHEAR]

FIG. 3.30

BIBLIOGRAPHY

von Arx, W. S., 1962: An Introduction to Physical Oceanography. Addison-Wesley Publishing Company, Inc., Reading Mass.

Bendat, J. S., and A. G. Piersol, 1966: Measurement and Analysis of Random Data. John Wiley & Sons, Inc., New York.

Birchfield, G. E., 1969: Response of a circular model Great Lake to a suddenly imposed wind stress. J. Geophys. Res., 74, 23, 5547-5554.

Blanford, R., 1965: Notes on the theory of the thermocline. J. Marine Res., 23, 1, 18-29.

Cacchione, D. A., 1970: Experimental study of internal gravity waves over a slope. Ph.D. Thesis, M.I.T. and W.H.O.I.

Cairns, J. L., and E. C. LaFond, 1966: Periodic motions of the seasonal thermocline along the southern California coast. J. Geophys. Res., 71, 16, 3903-3915.

Cooper, J. W., and H. Stommel, 1968: Regularly spaced steps in the main thermocline near Bermuda. J. Geophys. Res., 73, 18, 5849-5854.

Cox, C., Y, Nagata, and T. Osborn, 1969: Oceanic fine structure and internal waves. Bull. of the Japanese Society of Fisheries Oceanography, special number (Professor Uda's Commemorative Papers), 67-71.

Cox, C. S., 1962: Internal waves. In The Sea, ed. M. N. Hill, vol. 1, chapt. 22, part II, 752-763. Interscience Publishers, London.

Csanady, G. T., 1968: Motions in a model Great Lake due to a suddenly imposed wind. J. Geophys. Res., 73, 20, 6435-6447.

Ellison, T. H., and J. S. Turner, 1959: Turbulent entrainment in stratified flows, J. Fluid Mech., 6, 423-448.

Fofonoff, N. P., 1969: Spectral characteristics of internal waves in the ocean, Deep-sea Res., 16 supplement, 58-71.

Frankignoul, C. J., 1970: The effect of weak shear and rotation on internal waves. Tellus, 22, 2, 194-203.

Grigg, H. R., and R. W. Stewart, 1963: Turbulent diffusion in a stratified fluid. J. Fluid Mech., 15, 174-186.

Groves, G. W., 1959: Flow estimate for the perpetual salt fountain. Deep-sea Res., 5, 209-214.

Halpern, D., 1967: On the generation of short period internal waves in Massachusetts Bay. Thesis proposal, Department of Meteorology, M.I.T.

Haltiner, G. J., 1958: The diurnal temperature wave with a coefficient of diffusivity which varies periodically with time and exponentially with height. J. Meteorology, 15, 3, 317-323.

Hodgman, C. D., ed, 1957: Handbook of Chemistry and Physics. Chemical Rubber Publishing Co., Cleveland, Ohio.

Hoel, P. G., 1966: Elementary Statistics, 2nd. edition. John Wiley & Sons, Inc., New York.

Howard, L., 1961: Note on a paper of John W. Miles. J. Fluid Mech., 10, 4, 509-512.

Howard, L., 1963: Neutral curves and stability boundaries in stratified flow. J. Fluid Mech., 16, 3, 333-342.

Johns, B., and M. J. Cross, 1969: The decay of internal wave modes in a multi-layered system. Deep-sea Res., 16, 185-195.

Johns, B., and M. J. Cross, 1970: The decay and stability of internal wave modes in a multisheeted thermocline. J. Marine Res., 28, 2, 215-224.

Kinsman, B., 1965: Wind Waves: Their Generation and Propagation on the Ocean Surface. Prentice-Hall, Inc., Englewood Cliffs, New Jersey.

Kitaigorodsky, S. A., 1960: On the computation of the thickness of the wind-mixing layer in the ocean. Izv. Geophys. Ser., 425-431.

Kraus, E. B., and C. Rooth, 1961: Temperature and steady state vertical heat flux in the ocean surface layers. Tellus, 13, 231-238.

LaFond, E. C., 1961: Internal wave motion and its geological significance. Mahadevan Volume, 6 May, 67-71.

Long, R. R., 1970: A theory of turbulence in stratified fluids. J. Fluid Mech., 42, 2, 349-365.

Malone, F. D., 1968: An analysis of current measurements in Lake Michigan. J. Geophys. Res., 73, 22, 7065-7081.

Miles, J., 1961: On the stability of heterogeneous shear flows. J. Fluid Mech., 10, 496-508.

Miles, J., 1963: On the stability of heterogeneous shear flows, part II. J. Fluid Mech., 16, 2, 209-227.

Munk, W. H., 1966: Abyssal recipes. Deep-sea Res., 13, 707-730.

Munk, W. H., and E. R. Anderson, 1948: Notes on a theory of the thermocline. J. Marine Res., 7, 3, 276-295.

Munk, W. H., and N. A. Phillips, 1968: Coherence and band structure of inertial motion in the sea. Revs. Geophysics, 6, 4, 447-472.

Neumann, G., and W. J. Pierson, Jr., 1966: Principles of Physical Oceanography. Prentice-Hall, Inc., Englewood Cliffs, New Jersey.

Nield, D. A., 1967: The thermohaline Rayleigh-Jeffreys problem. J. Fluid Mech., 29, 3, 545-558.

Orlanski, I., and K. Bryan, 1969: The formation of the thermocline step structure by large amplitude internal gravity waves. J. Geophys. Res., 74, 28, 6975-6983.

Phillips, O. M., 1966: The Dynamics of the Upper Ocean. University Press, Cambridge.

Phillips, O. M., 1971: On spectra measured in an undulating layered medium. J. Physical Oceanography, 1, 1, 1-6.

Pingree, R. D., 1970: In situ measurements of salinity, conductivity and temperature. Deep-sea Res., 17, 603-610.

Pollard, R. T., 1970: On the generation by winds of inertial waves in the ocean. Deep-sea Res., 17, 795-812.

Pollard, R. T., and R. C. Millard, Jr., 1970: Comparison between observed and simulated wind-generated inertial oscillations. Deep-sea Res., 17, 813-821.

Richardson, L. F., 1926: Atmospheric diffusion shown on a distance-neighbour graph. Proc. Roy. Soc. A., 110, 709-737.

Robinson, A., and H. Stommel, 1959: The oceanic thermocline and the associated thermohaline circulation. Tellus, 11, 3, 295-308.

Rooth, C., and W. Düing, 1971: On the detection of 'inertial' waves with pycnocline followers. J. Physical Oceanography, 1, 1, 12-16.

Schroeder, E., and H. Stommel, 1969: How representative is the series of PANULIRUS stations of monthly mean conditions off Bermuda? Progress in Oceanography, 5, ed. Mary Sears. Pergamon Press, Oxford and New York. 31-40.

Shonting, D. H., 1964: Some observations of short-term heat transfer through the surface layers of the ocean. Limnology and Oceanography, 9, 4, 576-588.

Shonting, D. H., 1967: Measurements of particle motions in ocean waves. J. Marine Res., 25, 2, 162-181.

Shonting, D. H., 1968: Autospectra of observed particle motions in wind waves. J. Marine Res., 26, 1, 43-65.

Siedler, G., 1970: Vertical coherence of short-periodic current variations. Contribution no. 2 4 6 7 from the Woods Hole Oceanographic Institution.

Stern, M. E., 1960: The 'salt fountain' and thermohaline convection., Tellus, 12, 2, 172-175.

Stern, M. E., 1968: T-S gradients on the micro-scale. Deep-sea Res., 15, 245-250.

Stern, M. E., 1969: Collective instability of salt fingers. J. Fluid Mech., 35, 2, 209-218.

Stern, M. E., and J. S. Turner, 1969: Salt fingers and convecting layers. Deep-sea Res., 16, 497-511.

Stommel, H., 1961: Thermohaline convection with two stable regimes of flow. Tellus, 13, 2, 224-230.

Stommel, H., 1962: On the cause of the temperature-salinity curve in the ocean. Proc. National Acad. Sciences, 48, 5, 764-766.

Stommel, H., A. B. Arons, and D. Blanchard, 1956: An oceanographic curiosity: the perpetual salt fountain. Deep-sea Res., 3, 152-153.

Stommel, H., and J. Cooper, 1967: Regularly-spaced steps in the main thermocline near Bermuda. J. Geophys. Res., 73, 18, 5849-5854.

Stommel, H., and K. N. Fedorov, 1967: Small scale structure in temperature and salinity near Timor and Mindanao. Tellus, 19, 306-325.

Stommel, H., K. Saunders, W. Simmons, and J. Copper, 1969: Observations of the diurnal thermocline. Deep-sea Res., 16 supplement, 269-284.

Stommel, H., and J. Webster, 1962: Some properties of thermocline equations in a subtropical gyre. J. Marine Res., 20, 1, 42-56.

Sverdrup, H. U., M. W. Johnson, and R. H. Fleming, 1942: The Oceans: Their Physics, Chemistry, and General Biology. Prentice-Hall, Inc., Englewood Cliffs, New Jersey.

Tabata, S., N. E. J. Boston, and F. M. Boyce, 1965: The relation between wind speed and summer isothermal surface layer of water at ocean station P in the Eastern Subarctic Pacific Ocean. J. Geophys. Res., 70, 16, 3867-3878.

Tait, R. I., and M. R. Howe, 1968: Some observations of thermohaline stratification in the deep ocean. Deep-sea Res., 15, 275-280.

Tukey, J. W., 1965: Data analysis and the frontiers of geophysics. Science, 148, 3675, 1283-1289.

Turner, J. S., 1965: The coupled turbulent transports of salt and heat across a sharp density interface. Int. J. Heat Mass Transfer, 8, 759-767.

Turner, J. S., 1967: Salt fingers across a density interface. Deep-sea Res., 14, 599-611.

Turner, J. S., 1969: A note on wind mixing at the seasonal thermocline. Deep-sea Res., 16 supplement, 297-300.

Turner, J. S. and H. Stommel, 1964: A new case of convection in the presence of combined vertical salinity and temperature gradients. Proc. National Acad. Sciences, 52, 49-53.

Webster, F., 1968: Observations of inertial-period motions in the deep sea. Revs. Geophysics, 6, 4, 473-490.

Wilson, W., and D. Bradley, 1968: Specific volume of sea water as a function of temperature, pressure and salinity. Deep-sea Res., 15, 355-363.

Woods, J. D., 1968: Wave-induced shear instability in the summer thermocline. J. Fluid Mech., 32, 4, 791-800.

Woods, J. D., 1968a: An investigation of some physical processes associated with the vertical flow of heat through the upper ocean. Meteorological Magazine, 97, 65-72.

Woods, J. D., 1969: Introduction to turbulence in stratified flow. Micro-oceanographical work off Malta. Turbulence and the transition from laminar to turbulent flow in stratified fluids. Clear air turbulence and its relations to turbulence in the sea. Cahiers de mecanique mathematique, 39-75. Conference on Hydrodynamics of the Ocean, held at the University of Liege, 20 - 24 May, 1969.

Woods, J. D., and G. G. Fosberry, 1966-67: The structure of the thermocline. Underwater Association Report, 5-18.

Worthington, L. V., and W. G. Metcalf, 1961: The relationship between potential temperature and salinity in deep Atlantic water. Rapp. et Proc.-Verb., 149, 122-128.

Wunsch, C., 1969: Progressive internal waves on slopes. J. Fluid Mech., 35, 131-145.

Wunsch, C., 1970: On oceanic boundary mixing. Deep-sea Res., 17, 293-301.

Wunsch, C., 1970: Temperature microstructure on the Bermuda slope, with application to the mean flow. To be published.

Wunsch, C., and J. Dahlen, 1970: Preliminary results of internal wave measurements in the main thermocline at Bermuda. J. Geophys. Res., 75, 30, 5899-5908.

BIOGRAPHY

The author was born February 14, 1940 in Washington, D.C. and grew up in nearby Chevy Chase, Maryland. He went to Maryland public schools and in 1958 entered Case Institute of Technology in Cleveland, Ohio, where he received a B. S. Degree in 1962.

In June, 1962 he married Linda Boynton of Westmoreland Hills, Maryland and came to live in Cambridge, Massachusetts, where he commenced work for the Instrumentation Laboratory at the Massachusetts Institute of Technology. His work dealt with designing and testing inertial guidance systems.

In 1965 he left the Instrumentation Laboratory (now the Draper Laboratory) to enter M.I.T. as a doctoral candidate in Physical Oceanography.

John Van Leer is the father of three children: Robert Benson Van Leer, age 7; Samuel Boynton Van Leer, age 5; and Louisa Birchard Van Leer, age 2; and resides in Nahant, Massachusetts.

The author is a member of the Society of Sigma Xi and serves on the board of the Nahant Conservation Commission.

APPENDIX A

CURRENT METER DESIGN, CONSTRUCTION AND CALIBRATION

The sensors for temperature, salinity and pressure used on the scissors are capable of resolving structure of the order of 5 centimeters thick. Clearly then a current meter which could resolve the same scales would be desirable. Several types of current meters were considered for the scissors. Hot film or hot wire type sensors were examined but appeared at the time to be too delicate and leak-prone for extended use in salt water at 600 to 800 meters depth. Further their nonlinear character along with sensitivity to surface contamination would make a pair of hot film sensors drift relative to each other and would thus be impractical for shear measurements. Savonious rotor meters with vanes for direction had the advantage of availability. Present units of this type were considered to be too large, particularly since the scissors could be adjusted to 50 centimeter sensor spacing. Further difficulties were the differing response times of the rotor and vane as well as their vertical offset of about 20 centimeters and rectification of wave heave noise.

After considerable searching we found a small plastic propellor type rotor made by a French firm, Neyrpic, Inc. These propellors are 3.5 cm O.D. and 2 cm long and rotate approximately once for every 10 cm of water passing through them.

Due to time limitations it was decided to build orthogonal

pairs of current meters rather than vane mounted units which would require mechanical design of the vane as well as an electrical angle read-out device. Although the pair of current meters is more easily built, it requires a very low threshold meter for good angle resolution at low speeds and a complicated calibration procedure. It further requires a repeatable monotonically decreasing output for a constant speed input as the angle between sensitive axis of the meter and current vector goes from 0 to ±90°. It finally requires that the direction of flow through each current meter be known. If the above requirements are met a unique calibration relationship can exist.

Threshold and running friction requirements

In rotor type current meters the water flow through the meter provides the energy for rotation of the rotor which must work against bearing friction and drag. Since the amount of energy available for these purposes depends directly on the mass of water flowing through the meter, this energy decreases as the square of the diameter. Clearly, bearing friction and signal pickoff torque must be minimized. Jewel bearings which have been widely used on large current meters were found to have large starting friction when operated as a horizontal pair. On the other hand, small stainless steel ball pivot bearings (type S3PR made by Miniature Precision Bearings, Inc., Keene, New Hampshire) have a starting torque of <1 dyne cm at light

preloads. Although these pivot bearings give an order of magnitude lower starting and running torque they must be replaced after each data run because they corrode and fill with small salt crystals as they dry after submersion.

For any given set of preloaded bearings the friction torque depends directly on the load, so a neutrally buoyant rotor would give the lowest threshold. The plastic Neyrpic propellors with shaft and light chopper that were used have a weight of 5.4 grams and a specific gravity of 1.4, which compares very favorably with metal units. Sytachic foams could be used for future propellors to attain very nearly neutrally buoyant rotors.

A further possible source of interfering torque is the rotation pickoff. The magnetic reed switch type pickoff provides positive counting but has far too high interference torque for a 3.5 cm diameter rotor. Magnetic induction coils which can have low enough interfering torque are seriously prone to radiated electrical noise which the Bendix digital data acquisition system provides in quantity. Furthermore, magnetically induced voltage signals vary proportionally with the speed of rotation making direction determination difficult. Photo optical systems provide no interfering torque and a constant amplitude signal which is easily processed by a digital system. The limiting factor in starting threshold and low speed running was imperfect rotational balance in water which proved far larger than bearing friction in the operational current meter.

With a propellor and bearing combination selected, the rest of the mechanical design remained. During the spring of 1968 Professor Mollo-Christensen was also interested in developing a small-scale current meter and agreed to support machining and towing tests of prototype current meters. His 10 cm diameter in-house propellor current meter with an exposed propellor was tested with a variety of shroud configurations as well as bare. These tests were carried out in the M.I.T. towing tank, which has a minimum synchronously controlled carriage speed of .6 knots and a useful length of about 50 feet. The purpose of these tests was to find the design which gives the monotonic relationship between output speed and the off axis angle which approximates a cosine response most closely, where the off axis angle is the angle formed by the axis of propellor rotation and the input current vector.

The types of current meter ducts were 7 cm long cylindrical, 20 cm long cylindrical with and without aluminum honeycomb, 20 cm long cylindrical duct through a 22 cm diameter sphere with and without honeycomb. The bare propellor was also towed. All tests consisted of constant .6 knot towing carriage speeds 0±90° in 10° steps and all ducts were 10 cm I.D. The tests with the honeycomb showed multiple maxima both to the right and left of 0° as did the ducted sphere. The long duct without honeycomb gave a double maximum of 20% greater than the carriage speed at ±30° off axis angle. The bare propellor had an asymmetrical output with a single maximum

at its lead angle of 25°.

Only the type with a short duct gave a monotonically decreasing output for increasing off axis angle. This unit was further tested in 5° steps for the complete 360° and found to have a nearly flat response ±20° from both 0° and 180° with a steeper than cosine decrease to zero near ±90°. The most sensitive positions for angular change were ±45° and ±135°. The mini-meters were then built in pairs with a scaled down short duct and mounted at ±45° on the scissors frame to best take advantage of their maximum angle sensitivity.

One basic component of the mini-meter design is the plastic fiber optics suggested by Professor Mollo-Christensen. These are sold by Edmund Scientific Co., Barrington, New Jersey, under the Dupont trade name Crofon and consist of a bundle of 16 .010" O.D. Lucite fibers each coated with a layer of high index of refraction polymer. Each bundle is covered with a black polyethylene jacket and loses 9% of its light per foot of transmission in the wave length range of 400 to 1100 millimicrons. They permit the bulky electronics package to be removed from the near flow field. A 1250 foot-candle Tung-sol brand miniature light bulb inside the electronics housing shines through a conical window (see figure #1-A). Butted end-on to this window are the 3 foot long fiber optics which carry the light to the current meter. There the light beam is interrupted by a light chopper carried on the outside of the propellor ten times for each revolution. The interrupted light signal returns through another bundle of fibers through another window to a Texas Instrument LS-400

photo diode. Most of the light losses occur in the windows and the water gap rather than the fibers. The fiber bundles were free flooding and worked well for extended periods at pressures of 1000 PSI. However the water forced between the fibers remains trapped and in two months clouds the fiber cores so that about half as much light is transmitted compared to new units. The rest of the mechanical details should be clear from the mechanical drawings included (prints 1-A through 4-A and 6-A ; see also figure #1-A and #2-A).

Electronics for the current meter

The design goals for the electronic mini-meter read-out were that it function from 0 to 10 meters per second and be able to detect the direction of revolution. Further that it should be compatible with the Bendix DCS-100 data acquisition system which can store up to ±64 pulses/2 second sampling period. Since the high speed bit rate exceeds the storage capacity it was further desirable to divide the output rate by 1, 2, 5, or 10 depending on the current speeds expected.

The high speed LS-400 photo diode will satisfy both the zero speed and the 1 KHz requirement provided that care is taken in finishing and positioning the ends of the fiber optic bundles. Since this diode has a "dark" impedance of several Megohms it must be monitored with a field effect transistor (FET) such as the MPF105 used to avoid loading. Each current meter has two signal optical paths and two photo cells. The light chopper has wide enough spaces and

teeth so that both signal bundles can be covered or uncovered at the same time, thus giving a two bit Grey Code with only one bit changing at any one time. Each photo diode FET combination is followed by an operational amplifier with a diode clipped input driven in positive feedback into positive or negative saturation as the photo diode turns on and off. These two amplifiers feed the appropriate integrated circuit logic which decides which direction the rotor is turning and feeds an output pulse onto either the clockwise or counterclockwise output terminal. Either output can be fed through a decade divider to divide by 1, 2, 5, or 10 according to the pattern of jumper wires on the small interval patch panel (see schematic diagram print **5-A** and printed circuit layout figure **#3-A**).

Towing tests at WHOI

Both orthogonal pairs of mini-meters were simultaneously towed from the carriage in the Woods Hole towing tank in the early spring of 1969. The current meters were attached to a vertical strut which was bolted to a machinist's rotary table such that precise angular position could be established easily (see figure **#4-A**). The towing carriage was fitted with a light chopper which fed the prototype current meter circuit to give one pulse per centimeter of carriage travel. This circuit's output was then plugged into the compass input of the Bendix recording system and hence the carriage motion could be recorded synchronously with the current meter calibration data (see figure **#5-A**). The towing carriage is driven by a synchronous electric

motor through a variable speed drive, gear belt and pinion gear which is engaged in a rack gear that runs the entire length of the tank.

By using the above calibration method, many two-second averaged current meter outputs can be recorded for each true towing speed and angle down the tank. Four nominal calibration speeds (5, 10, 20, 50 cm/sec) and 36 equally spaced calibration angles were used. During each constant speed and angle traverse between 6 and 72, two-second averages of all four current meters and the carriage speed were recorded. All the two-second samples were averaged for each traverse and normalized to the four nominal speeds and the standard deviation SIGMA computed. Table # 1-A presents these results where the column on the right is the number of samples used in each average and each current meter and the normalized towing speed is printed together with its standard deviation. Even though the towing carriage drags a heavy cable it maintains its speed with a standard deviation of about 1/2 cm per 2 seconds or ±1/4 cm/sec. The standard deviations for the current meters average about 1 cm/2 sec or ±1/2 cm/sec with maximums near 0°, 90°, 180°, and 270°, where one of each pair of meters stalls. The meter standard deviations also increase slightly with increasing towing speed.

Figures # 6-A and # 7-A are plots of the averaged number of pulses per sample from the upper and lower pair of mini-meters (see table # 1-A for data). Points of equal towing speed are connected by straight lines in both figures. The outer ring of points is for 50 cm/sec and the inner ring is for 5 cm/sec. Figures # 8-A and

#9-A are the same, except that points of constant angle are connected with straight lines (one line for each of the 36 towing angles). Note how these lines of constant angle bunch together at angles where a meter approaches its stall speed (0°, 90°, 180°, 270°).

A Fortran IV program was written which interpolates linearly in polar coordinates in angle and speed between the 144 known calibration points for any pair of input data points to find the true input current vector. This program was coded in part by Sally Kelly of the M.I.T. Information Processing Center staff.

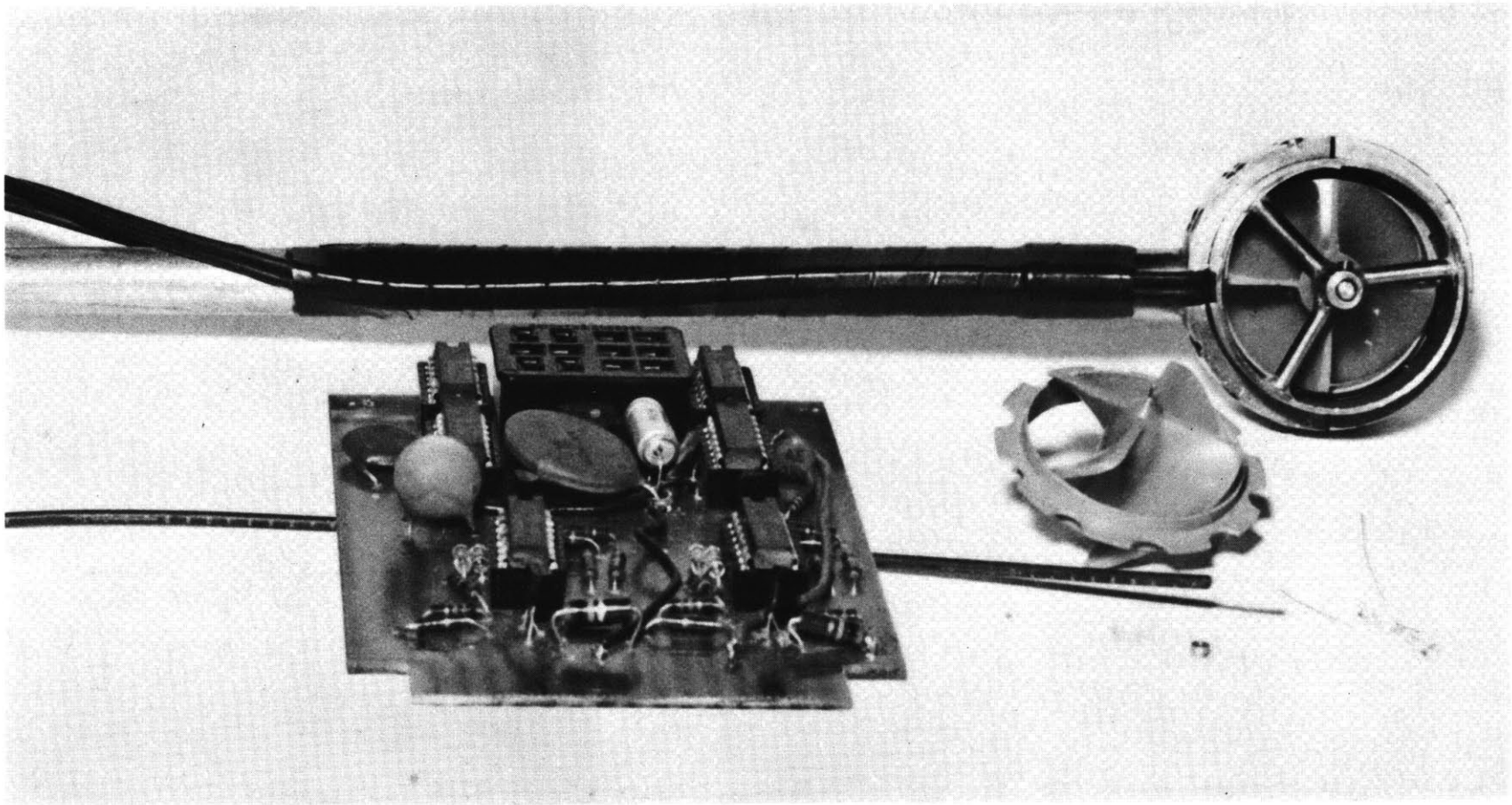

FIG. #1-A Complete mini-meter together with electronics, fiber optics, light bulb, bearing, propellor, and light pressure windows.

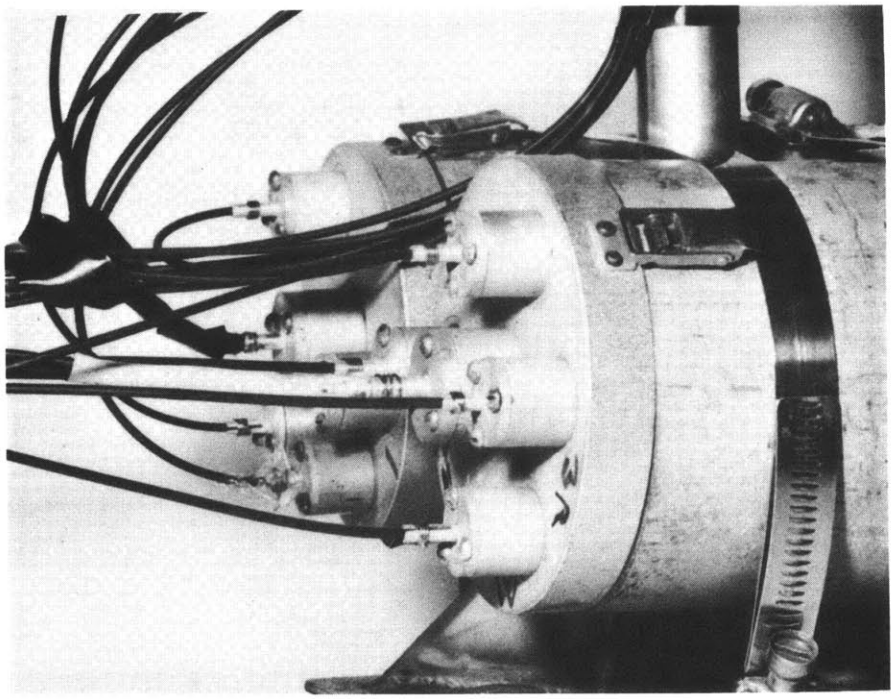

FIG. #2-A Detail of high pressure windows and fiber optics.

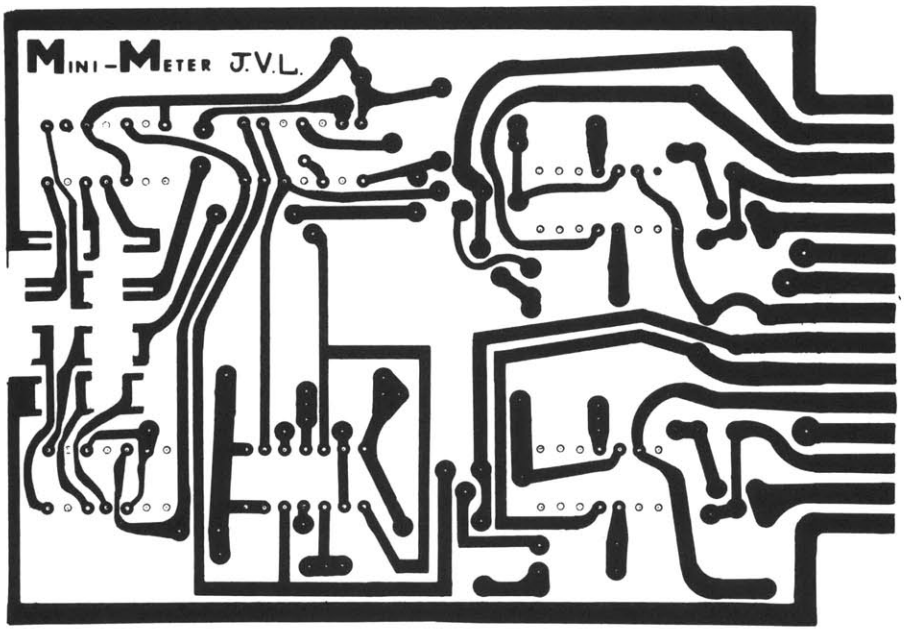

FIG. #3-A Printed circuit board for the mini-meter electronics.

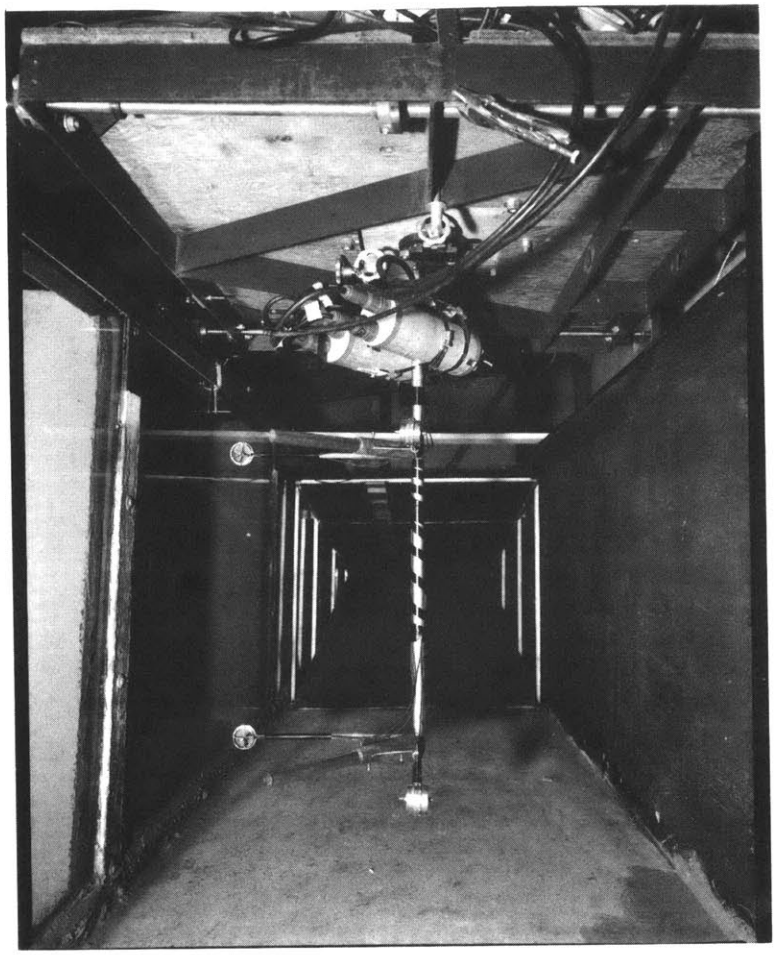

FIG. #4-A Both pairs of mini-meters mounted on a rotary table in towing tank at WHOI.

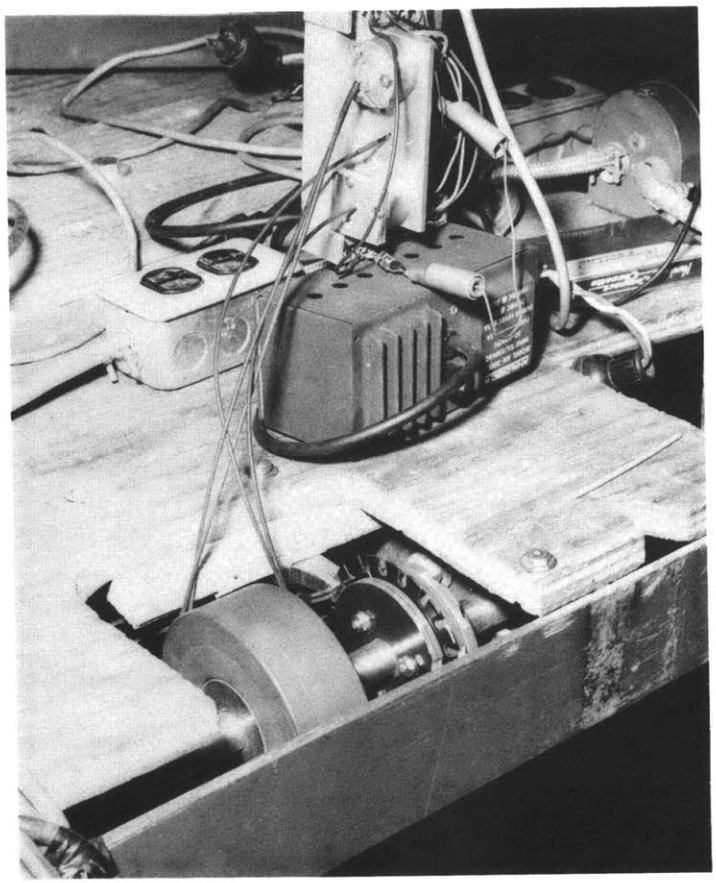

FIG. #5-A Optical towing carriage readout.

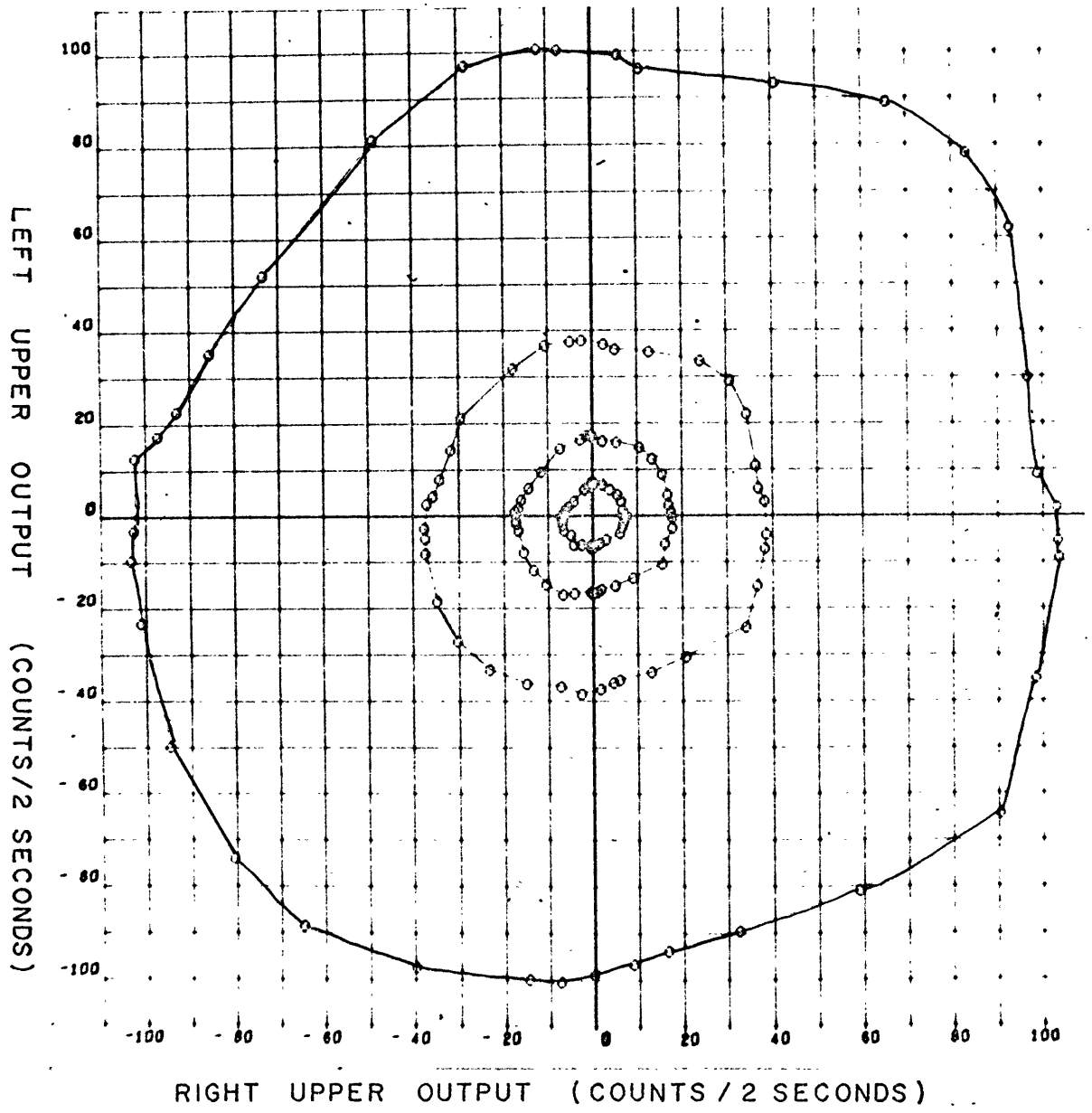

FIG. #6-A Calibration data for the upper pair of mini-meters with points of equal towing speed connected.

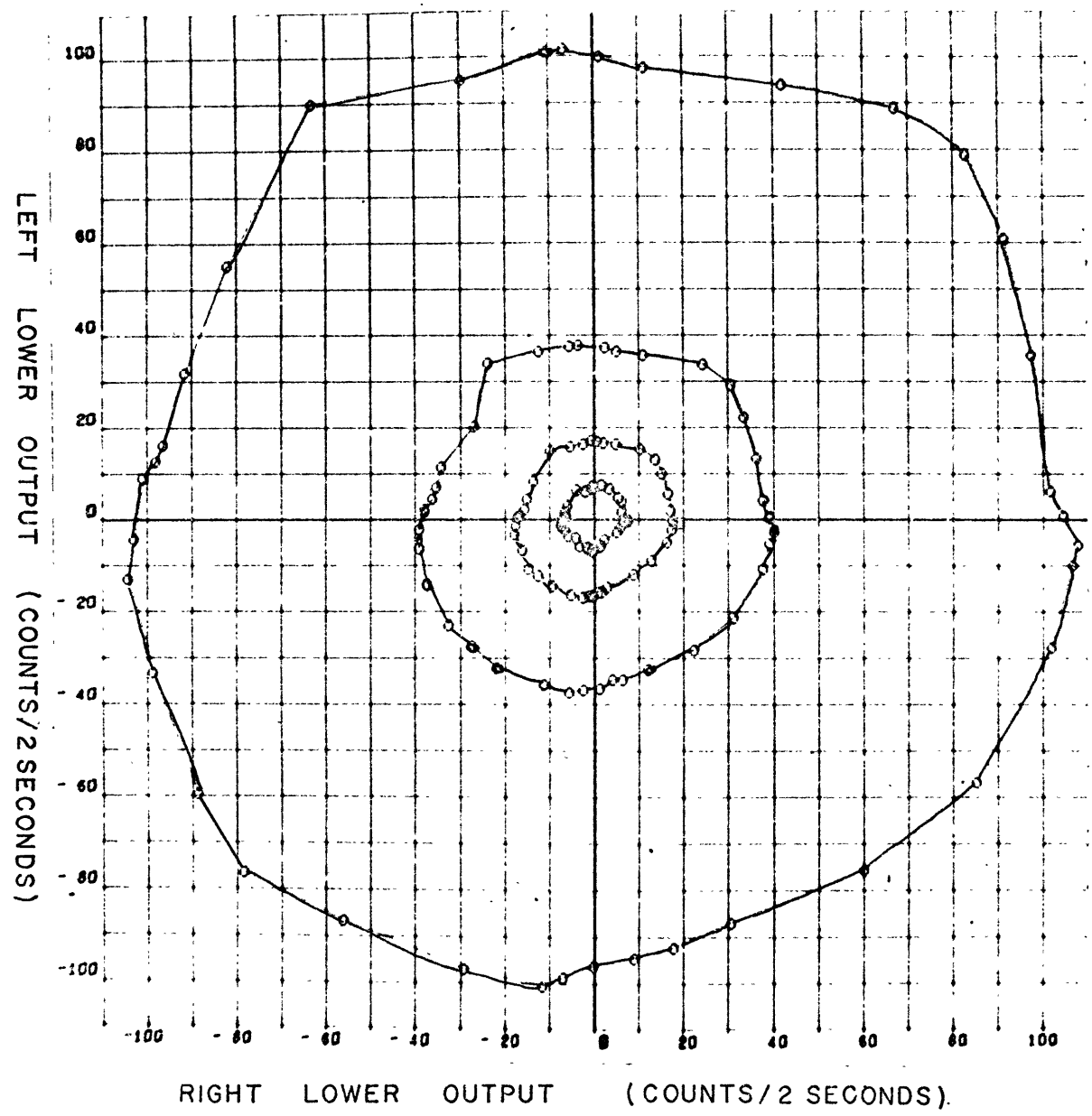

FIG. #7-A Calibration data for the lower pair of minimeters with points of equal towing speed connected.

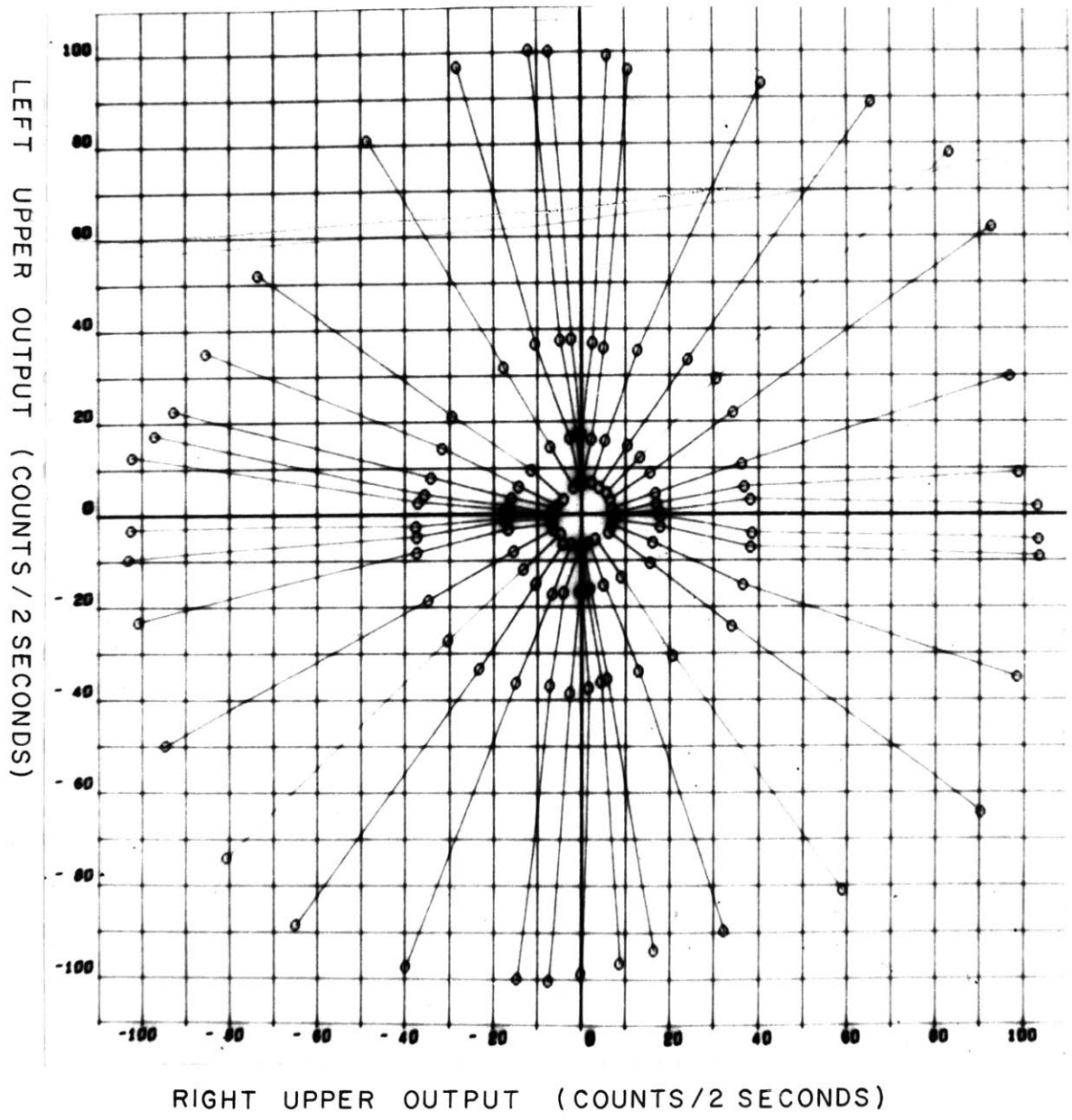

FIG. #8-A Calibration data for the upper pair of mini-meters with points of equal towing angle connected.

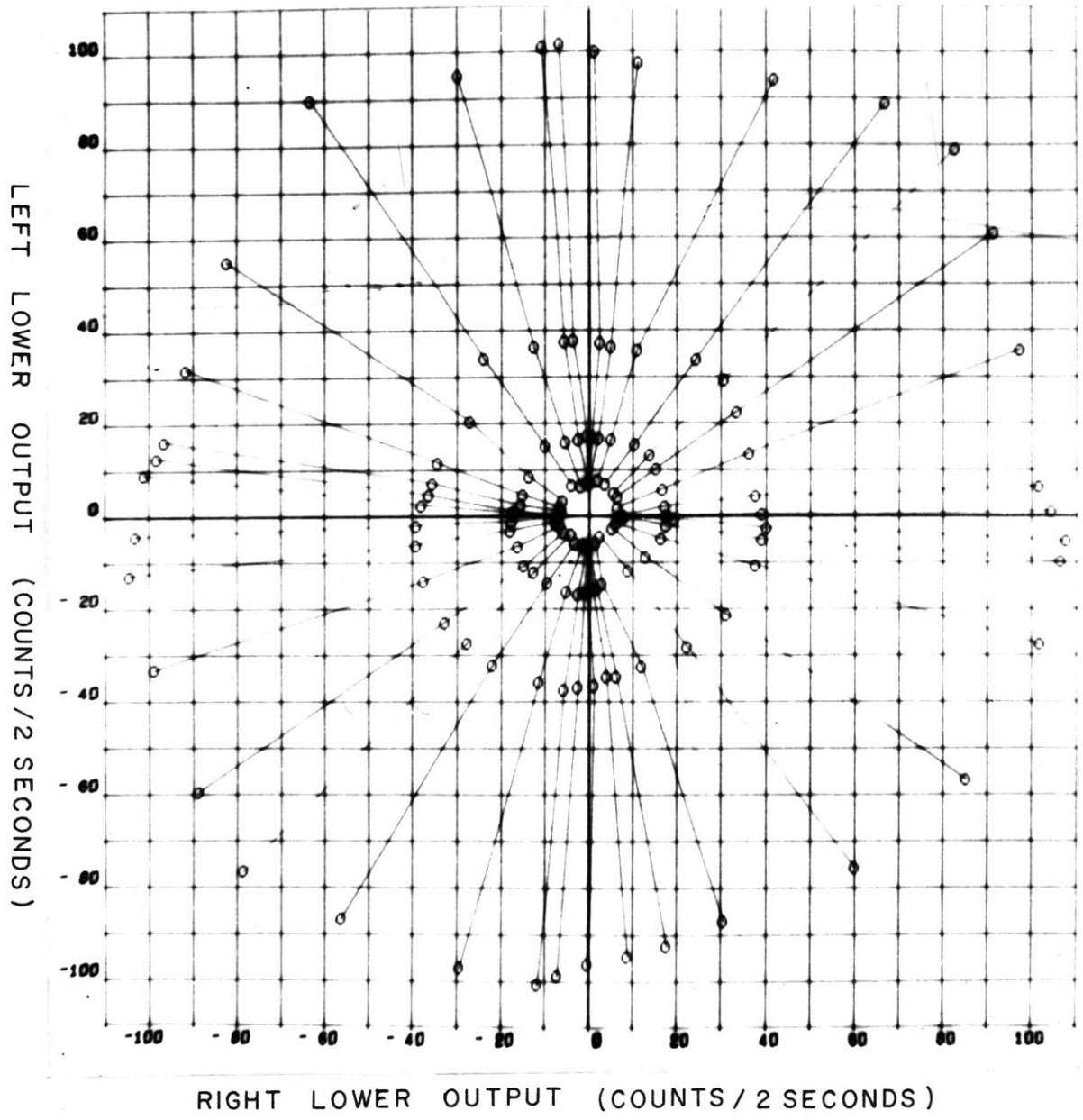

FIG. #9-A Calibration data for the lower pair of mini-meters with points of equal towing angle connected.

TABLE 1-A CURRENT METER CALIBRATION RESULTS

TRUE ANGLE	TRUE SPEED CM./SEC.		RIGHT UPPER COUNTS	SIGMA	LEFT UPPER COUNTS	SIGMA	RIGHT LOWER COUNTS	SIGMA	LEFT LOWER COUNTS	SIGMA	NO# AVR
5.	5.00	0.5	7.79	0.5	0.01	1.3	7.68	0.5	0.01	0.0	24
15.	5.00	0.4	7.71	0.8	0.33	1.6	6.94	0.8	0.11	0.0	38
25.	5.00	0.2	6.95	0.8	1.52	0.8	6.62	0.5	1.95	0.2	19
35.	5.00	0.4	6.60	0.7	3.21	0.5	6.44	0.7	4.19	0.7	42
45.	5.00	0.4	5.72	0.8	4.74	0.5	5.59	0.9	5.13	0.7	22
55.	5.00	0.7	4.05	0.9	5.91	0.8	3.80	1.1	6.95	0.8	45
65.	5.00	0.3	2.19	0.7	7.06	0.5	2.09	0.6	7.71	0.7	34
75.	5.00	0.3	0.11	0.0	7.16	1.0	0.11	0.0	7.36	0.7	32
85.	5.00	0.3	0.01	1.6	6.95	0.9	0.01	0.9	7.50	0.8	36
95.	5.00	0.8	-0.01	2.7	7.12	1.0	-0.01	0.9	7.27	0.9	48
105.	5.00	0.5	-0.11	1.8	7.28	0.6	-0.11	0.3	7.15	0.5	38
115.	5.00	0.4	-0.30	1.2	6.69	0.5	-1.70	1.0	6.32	0.6	32
125.	5.00	0.4	-1.83	1.3	5.94	0.6	-3.65	0.8	6.56	0.5	30
135.	5.00	0.4	-3.91	1.4	3.35	0.8	-5.58	1.2	3.33	1.7	47
145.	5.00	0.4	-5.39	0.7	1.81	0.8	-6.35	0.9	2.07	1.1	35
155.	5.00	0.3	-6.10	1.0	1.43	1.3	-5.90	1.4	1.01	0.4	72
165.	5.00	0.4	-6.36	0.6	0.01	1.6	-6.54	0.7	0.11	0.2	39
175.	5.00	0.5	-6.85	0.5	0.01	2.8	-6.79	0.6	0.01	0.0	48
185.	5.00	0.5	-6.47	0.6	-0.01	2.6	-6.79	0.8	-0.01	0.5	21
195.	5.00	0.5	-6.61	0.4	-0.97	2.1	-7.14	0.5	-1.00	0.0	45
205.	5.00	0.0	-6.45	0.9	-1.94	0.8	-6.36	0.6	-2.04	1.1	34
215.	5.00	0.4	-6.34	0.5	-2.99	0.5	-5.34	0.6	-3.41	0.7	26
225.	5.00	0.2	-4.53	0.8	-3.87	0.5	-3.61	1.7	-3.72	1.0	37
235.	5.00	0.5	-4.00	0.8	-6.17	0.4	-2.80	1.2	-5.49	0.6	14
245.	5.00	0.4	-2.17	1.8	-6.12	0.5	-1.20	0.0	-5.89	0.6	38
255.	5.00	0.4	-0.12	1.6	-6.32	0.6	-0.31	0.8	-6.50	1.4	61
265.	5.00	0.3	-0.01	1.5	-6.29	0.4	-0.05	0.2	-6.35	0.4	49
275.	5.00	0.5	0.01	1.3	-6.85	0.5	0.01	0.0	-6.06	0.5	10
285.	5.00	0.5	0.11	1.0	-6.49	0.5	0.05	0.0	-6.07	0.6	43

TABLE NUMBER 1-A CONTINUED

TRUE ANGLE	TRUE SPEED CM./SEC.		RIGHT UPPER COUNTS	SIGMA	LEFT UPPER COUNTS	SIGMA	RIGHT LOWER COUNTS	SIGMA	LEFT LOWER COUNTS	SIGMA	NO# AVR
295.	5.00	0.5	0.42	2.0	-6.32	0.5	0.10	0.5	-6.46	0.6	46
305.	5.00	0.5	1.81	1.3	-5.96	0.5	1.59	2.0	-5.70	0.6	40
315.	5.00	0.5	3.18	1.3	-5.00	0.5	2.70	2.0	-4.20	1.2	25
325.	5.00	0.6	6.35	0.6	-3.57	0.8	5.42	0.7	-2.46	1.8	33
335.	5.00	0.4	6.72	0.5	-2.10	0.7	6.13	0.9	-1.51	2.0	34
345.	5.00	0.3	7.06	0.5	-1.10	2.2	7.25	0.5	-0.11	0.0	10
355.	5.00	0.5	7.32	0.5	-0.01	3.1	7.84	0.6	-0.01	1.1	20
5.	10.00	0.3	17.69	0.5	0.92	1.7	17.85	0.5	0.01	0.0	40
15.	10.00	0.5	17.16	0.5	2.60	0.8	17.32	0.6	2.30	1.1	36
25.	10.00	0.4	16.72	0.6	4.60	0.6	16.72	0.5	5.97	0.9	41
35.	10.00	0.5	15.79	0.5	9.19	0.6	15.39	0.5	10.31	0.5	39
45.	10.00	0.5	13.50	0.4	12.40	1.4	13.89	0.5	13.37	0.5	39
55.	10.00	0.4	10.52	0.5	15.05	0.5	10.64	0.8	15.68	0.6	24
65.	10.00	0.5	5.54	0.8	16.00	0.5	5.01	0.8	16.72	0.5	40
75.	10.00	0.5	2.15	2.2	16.46	0.6	2.16	1.0	16.95	0.6	41
85.	10.00	0.5	0.04	2.3	17.44	0.7	0.98	1.6	17.37	0.6	26
95.	10.00	0.5	-0.19	2.4	17.39	0.4	-0.28	1.3	17.42	0.6	31
105.	10.00	0.5	-1.00	1.6	17.41	0.5	-2.30	1.0	16.70	0.4	29
115.	10.00	0.5	-2.53	1.1	16.76	0.6	-5.13	0.6	16.13	0.5	38
125.	10.00	0.4	-7.01	0.4	14.63	0.8	-9.56	0.5	15.35	0.5	26
135.	10.00	0.5	-11.43	0.5	9.63	0.9	-13.43	0.6	8.69	0.9	33
145.	10.00	0.4	-14.35	0.6	6.19	1.5	-14.70	0.6	4.85	1.4	36
155.	10.00	0.5	-15.88	0.5	3.74	0.9	-15.32	0.6	2.53	1.5	24
165.	10.00	0.5	-16.52	0.5	1.98	0.9	-16.42	0.7	1.07	0.4	29
175.	10.00	1.8	-17.24	1.7	1.07	1.8	-17.12	1.8	0.70	1.4	35
185.	10.00	0.4	-17.12	0.5	-0.90	0.8	-17.48	0.5	-1.17	1.8	36
195.	10.00	0.5	-17.20	0.4	-1.34	0.8	-17.52	0.6	-2.96	0.7	18
205.	10.00	0.5	-16.64	0.5	-3.14	0.6	-15.85	0.5	-6.32	0.6	26
215.	10.00	0.4	-15.41	0.6	-7.88	0.5	-14.64	0.8	-10.45	0.5	30

TABLE NUMBER 1-A CONTINUED

TRUE ANGLE	TRUE SPEED CM./SEC.		RIGHT UPPER COUNTS	SIGMA	LEFT UPPER COUNTS	SIGMA	RIGHT LOWER COUNTS	SIGMA	LEFT LOWER COUNTS	SIGMA	NO# AVR
225.	10.00	0.4	-13.14	0.5	-11.68	0.7	-12.18	0.5	-12.06	0.5	31
235.	10.00	0.3	-10.22	0.5	-14.86	0.5	-9.09	0.5	-14.13	0.3	30
245.	10.00	0.4	-6.44	0.5	-17.04	0.5	-4.81	1.2	-16.03	0.3	26
255.	10.00	0.5	-3.89	1.0	-16.56	0.4	-2.40	2.0	-16.77	0.6	35
265.	10.00	0.2	-0.39	1.9	-16.51	0.5	-0.73	1.6	-16.38	0.6	32
275.	10.00	0.5	0.01	1.3	-16.79	0.5	0.12	0.9	-16.36	0.3	16
285.	10.00	0.3	1.21	1.5	-16.52	0.5	1.16	1.2	-15.57	0.6	37
295.	10.00	0.5	2.06	1.7	-15.92	0.5	2.02	1.2	-15.71	0.4	42
305.	10.00	0.5	5.08	1.4	-15.08	0.5	3.16	2.2	-14.41	0.4	36
315.	10.00	0.4	9.15	0.9	-13.28	0.4	9.15	0.9	-11.73	0.6	34
325.	10.00	0.5	15.59	0.6	-10.41	0.6	13.00	1.1	-8.76	0.6	34
335.	10.00	0.4	16.35	0.5	-5.93	0.6	16.56	0.6	-4.86	0.4	19
345.	10.00	0.4	17.93	0.5	-2.63	2.0	17.64	0.6	-2.05	2.4	18
355.	10.00	0.3	17.80	0.4	-0.41	1.4	19.36	0.5	-0.58	1.0	28
5.	20.00	0.6	38.45	0.7	3.35	0.9	39.18	0.6	0.44	1.3	31
15.	20.00	0.5	36.93	0.5	6.19	0.9	37.79	0.5	4.54	2.0	32
25.	20.00	0.5	36.34	0.6	11.13	0.5	36.48	0.5	13.50	0.5	29
35.	20.00	0.3	34.45	0.6	22.14	0.6	33.59	2.1	22.46	0.6	33
45.	20.00	0.4	30.77	0.7	29.44	0.6	30.77	0.5	29.57	0.6	14
55.	20.00	0.4	24.06	0.5	33.76	0.7	24.60	0.7	33.98	0.6	31
65.	20.00	0.4	12.76	0.5	35.51	0.6	11.05	0.7	35.93	0.7	21
75.	20.00	0.4	5.01	0.9	36.27	0.7	5.00	1.7	36.80	0.6	31
85.	20.00	0.4	2.60	1.1	37.40	0.7	2.53	1.2	37.47	0.7	31
95.	20.00	0.5	-2.38	1.5	38.00	0.6	-3.39	1.0	38.07	0.9	28
105.	20.00	0.5	-4.80	0.8	37.84	0.8	-5.50	0.7	37.91	0.5	26
115.	20.00	0.9	-10.40	0.6	36.99	1.1	-12.35	0.9	36.72	0.7	33
125.	20.00	0.3	-17.68	0.7	31.99	1.4	-23.55	0.9	34.14	0.9	16
135.	20.00	0.4	-29.27	0.6	21.46	1.8	-26.83	0.8	20.49	1.2	19
145.	20.00	0.5	-31.69	0.7	14.36	2.7	-34.17	0.7	11.70	2.4	28

TABLE NUMBER 1-A CONTINUED

TRUE ANGLE	TRUE SPEED CM./SEC.		RIGHT UPPER COUNTS	SIGMA	LEFT UPPER COUNTS	SIGMA	RIGHT LOWER COUNTS	SIGMA	LEFT LOWER COUNTS	SIGMA	NO. AVR
155.	20.00	0.5	-34.22	0.6	8.12	1.2	-35.42	0.7	7.33	1.7	33
165.	20.00	0.5	-35.59	0.5	4.56	0.9	-36.24	0.8	4.82	1.4	33
175.	20.00	0.3	-37.07	0.6	2.75	1.1	-37.76	0.5	2.60	1.6	32
185.	20.00	0.4	-37.47	0.6	-2.51	0.6	-38.87	0.6	-2.07	1.9	33
195.	20.00	0.5	-37.38	0.6	-4.81	0.8	-39.05	0.7	-6.25	0.8	33
205.	20.00	0.4	-37.16	0.6	-8.17	0.5	-37.19	0.8	-14.03	0.8	34
215.	20.00	0.3	-34.72	0.7	-18.32	0.5	-32.38	0.6	-22.74	0.5	33
225.	20.00	0.5	-30.07	0.5	-26.95	0.5	-27.25	0.5	-27.19	0.5	28
235.	20.00	0.5	-22.97	0.5	-33.15	0.6	-21.53	0.9	-32.01	0.5	26
245.	20.00	0.5	-14.66	0.6	-36.23	0.6	-11.03	0.4	-35.53	0.6	14
255.	20.00	0.5	-6.98	1.2	-36.82	0.9	-5.44	1.1	-37.37	0.7	29
265.	20.00	0.9	-2.53	1.1	-38.33	0.7	-2.22	1.2	-36.66	0.7	25
275.	20.00	0.4	1.71	0.9	-37.18	0.5	1.38	1.2	-36.33	0.5	22
285.	20.00	0.5	4.49	1.0	-35.78	0.5	4.31	1.3	-34.45	0.6	28
295.	20.00	0.5	6.11	1.2	-35.30	0.6	6.42	1.4	-34.49	0.5	32
305.	20.00	0.4	12.98	2.2	-33.68	0.5	12.14	3.0	-32.31	0.5	30
315.	20.00	1.6	20.90	1.6	-30.30	0.6	22.39	1.3	-28.19	0.8	32
325.	20.00	0.5	34.25	0.8	-23.96	0.6	31.27	1.3	-21.05	0.7	32
335.	20.00	0.8	36.82	0.8	-14.88	0.5	37.95	0.8	-10.45	0.6	26
345.	20.00	0.4	38.48	0.6	-6.93	1.3	39.38	1.0	-5.14	1.1	16
355.	20.00	0.4	38.80	0.7	-3.83	2.5	40.47	0.6	-2.53	1.6	27
5.	50.00	0.3	102.91	0.6	1.97	1.2	104.43	0.9	1.01	1.0	8
15.	50.00	0.4	98.84	0.8	9.22	1.1	101.64	1.5	6.42	1.6	6
25.	50.00	0.3	96.71	0.6	29.92	0.9	97.24	0.6	35.89	0.5	11
35.	50.00	0.5	92.69	0.9	62.34	0.5	91.38	1.4	61.25	0.8	12
45.	50.00	0.3	83.44	0.7	78.54	0.7	82.91	0.5	79.17	0.6	11
55.	50.00	0.4	65.87	0.5	89.35	0.7	67.18	0.8	89.24	0.4	9
65.	50.00	0.6	41.10	0.9	93.44	0.7	42.07	1.3	94.42	0.5	12
75.	50.00	0.3	10.92	1.1	96.61	0.7	11.28	2.2	97.82	0.4	13

TABLE NUMBER 1-A CONTINUED

TRUE ANGLE	TRUE SPEED CM./SEC.		RIGHT UPPER COUNTS	SIGMA	LEFT UPPER COUNTS	SIGMA	RIGHT LOWER COUNTS	SIGMA	LEFT LOWER COUNTS	SIGMA	NO. AVR
85.	50.00	0.7	5.99	1.3	99.51	1.0	1.39	1.9	100.33	0.6	12
95.	50.00	0.5	-7.27	1.8	100.75	0.8	-6.64	1.2	102.06	0.5	9
105.	50.00	0.0	-12.03	2.2	100.98	1.0	-10.62	0.4	101.64	0.5	6
115.	50.00	0.0	-28.30	0.8	97.23	1.1	-29.74	0.5	95.26	0.7	6
125.	50.00	0.4	-48.78	1.3	81.51	1.5	-63.17	0.5	90.35	0.8	6
135.	50.00	0.4	-73.38	0.5	52.40	2.0	-82.08	0.7	55.35	1.5	7
145.	50.00	0.0	-85.51	0.9	35.19	3.1	-91.28	0.6	32.03	3.7	9
155.	50.00	0.4	-92.83	0.5	22.89	2.5	-96.07	0.4	16.50	1.9	10
165.	50.00	0.4	-96.98	0.9	17.59	1.9	-97.99	0.9	12.86	1.6	11
175.	50.00	0.5	-102.08	0.6	12.83	1.5	-100.74	1.1	9.12	1.3	13
185.	50.00	0.6	-102.60	0.8	-3.01	0.5	-102.76	0.9	-4.26	1.4	15
195.	50.00	0.5	-103.00	1.0	-9.43	0.6	-104.15	0.6	-12.93	1.2	12
205.	50.00	0.5	-100.61	1.1	-23.06	0.8	-98.54	2.1	-33.05	1.2	13
215.	50.00	0.4	-94.38	1.0	-49.69	0.7	-88.38	1.3	-59.58	0.8	17
225.	50.00	0.4	-80.51	0.8	-74.02	0.5	-78.40	0.5	-76.42	0.5	6
235.	50.00	0.4	-64.93	0.4	-88.49	0.6	-55.96	0.5	-86.68	0.4	7
245.	50.00	0.5	-39.73	0.6	-97.35	1.0	-28.96	0.8	-97.04	0.5	13
255.	50.00	0.4	-14.54	0.4	-99.80	1.4	-11.39	0.5	-100.79	0.5	5
265.	50.00	0.4	-7.36	0.9	-100.32	0.8	-6.85	3.1	-98.85	0.6	6
275.	50.00	0.5	0.01	1.1	-98.86	0.4	0.01	1.4	-96.21	0.4	7
285.	50.00	0.5	8.87	1.2	-96.55	0.0	9.00	3.2	-94.58	0.0	4
295.	50.00	0.4	16.62	2.3	-93.62	0.8	18.00	2.8	-92.39	0.5	12
305.	50.00	0.5	32.38	5.5	-89.60	0.7	30.85	2.1	-87.09	0.4	9
315.	50.00	0.0	59.31	2.0	-80.88	0.5	60.29	1.4	-75.66	1.1	6
325.	50.00	0.3	90.45	1.1	-64.24	0.6	85.47	2.1	-56.65	0.8	12
335.	50.00	1.0	98.46	1.2	-35.11	0.6	101.82	0.8	-27.41	0.8	7
345.	50.00	0.4	103.71	0.7	-8.84	3.3	106.33	0.9	-9.66	1.5	8
355.	50.00	0.5	103.38	0.3	-5.35	1.4	107.53	0.5	-5.28	1.0	9

MINI - METER ASSEMBLY 26 MAY 68 J.C.V.L.

MATERIAL →

ALL 304-316 STAINLESS EXCEPT PROP

SCALE → X4

PRINT I-A

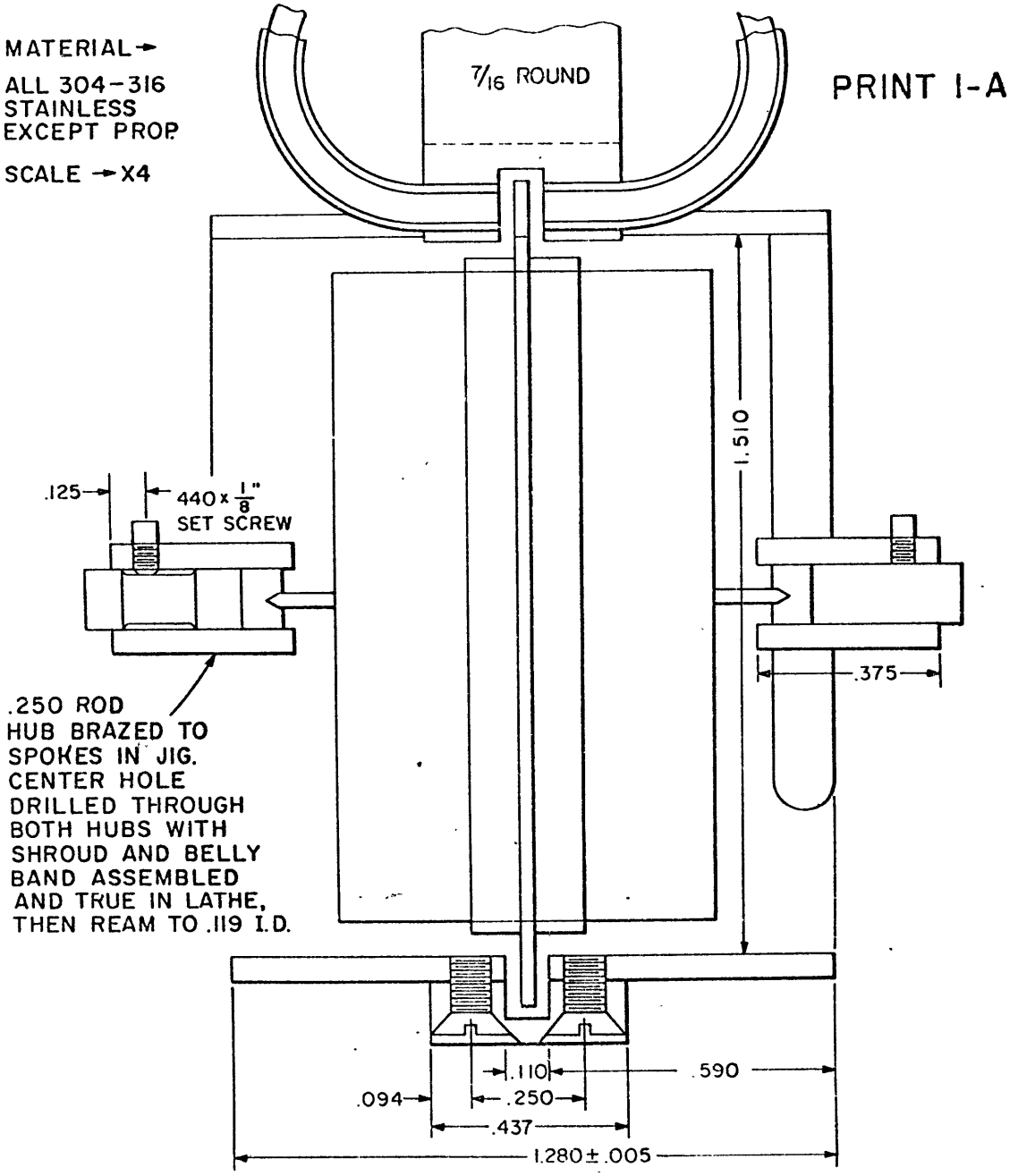

MINI-METER LIGHT CHOPPER 26 MAY 68 J.C.V.L.

MATERIAL → PVC

SCALE → X4

10 SLOTS EQUALLY SPACED WITH INDEXING HEAD 36° APART (COULD BE CUT WITH 1/4" END MILL

PRINT 2-A

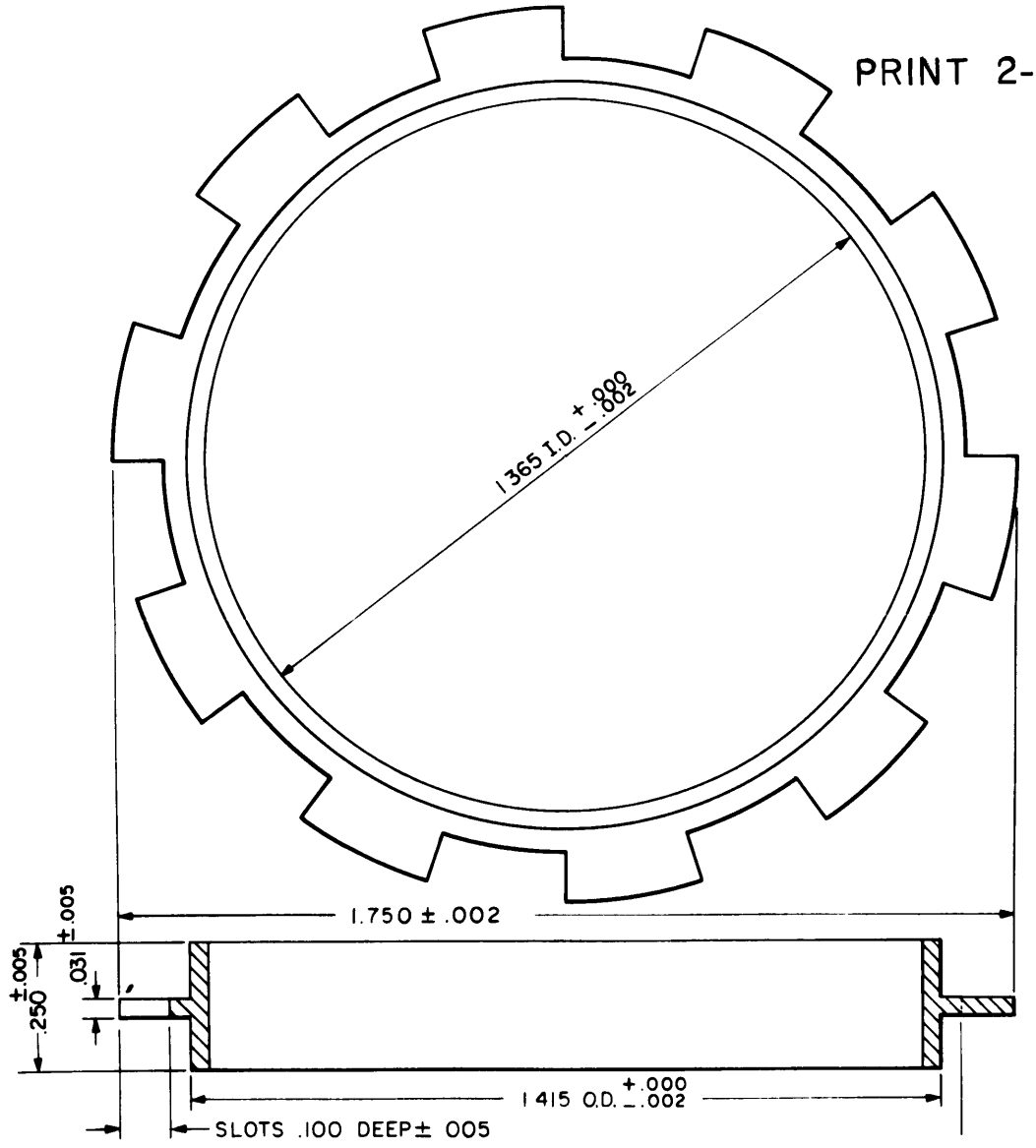

MINI-METER 26 MAY 68 J.C.V.L.

BEARING SLUG

BOTH ENDS TURNED WITH VERY FINE FINISH AND FLATNESS.

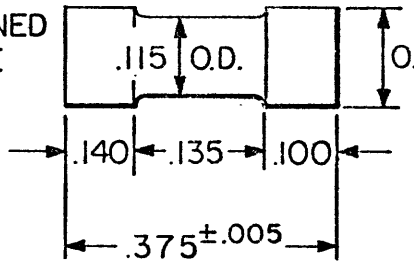

161

PRINT 3-A

LIGHT PIPE ROD

SIDE

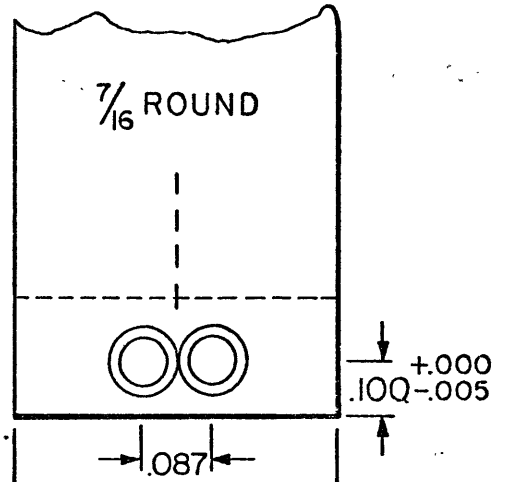

BOTTOM

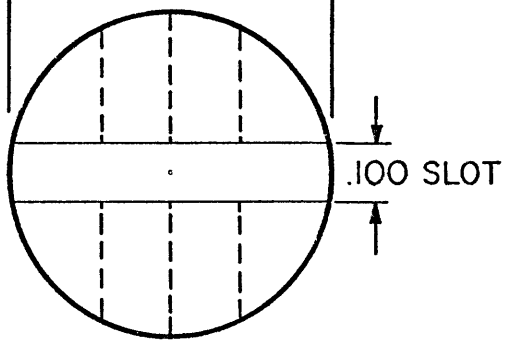

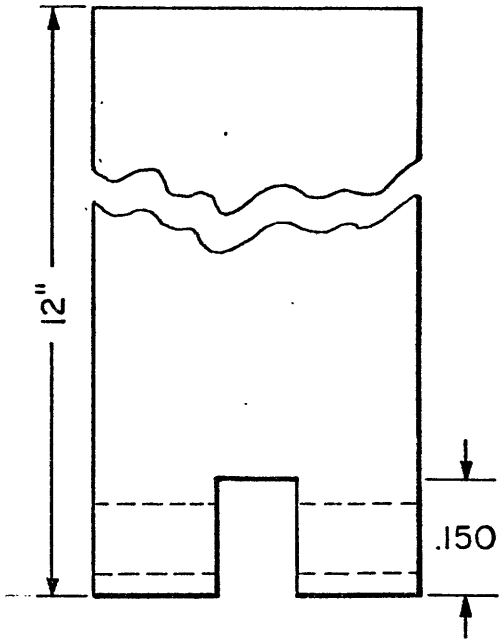

BOTH HOLES DRILLED THROUGH BOTH SIDES WITH No. 44 DRILL .086

MINI-METER 26 MAY 68 J.C.V.L.

PRINT 4-A

SHIM DETAIL

1

STAINLESS

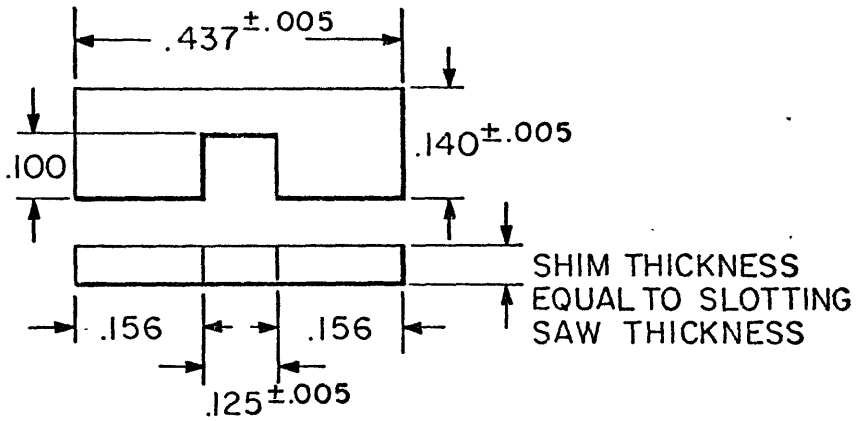

MAKE 2 SHIMS PER CURRENT METER AND SILVER SOLDER 1 TO EACH HALF OF BELLY BAND AFTER SLOTTING.

SHAFT DETAIL

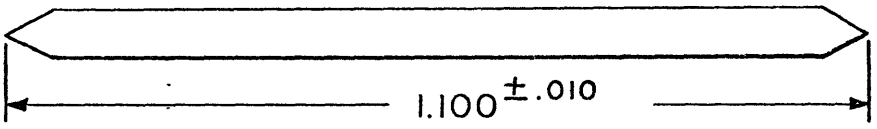

ENDS GROUND TO 60° CONES

SHAFT DIAMETER = .0625

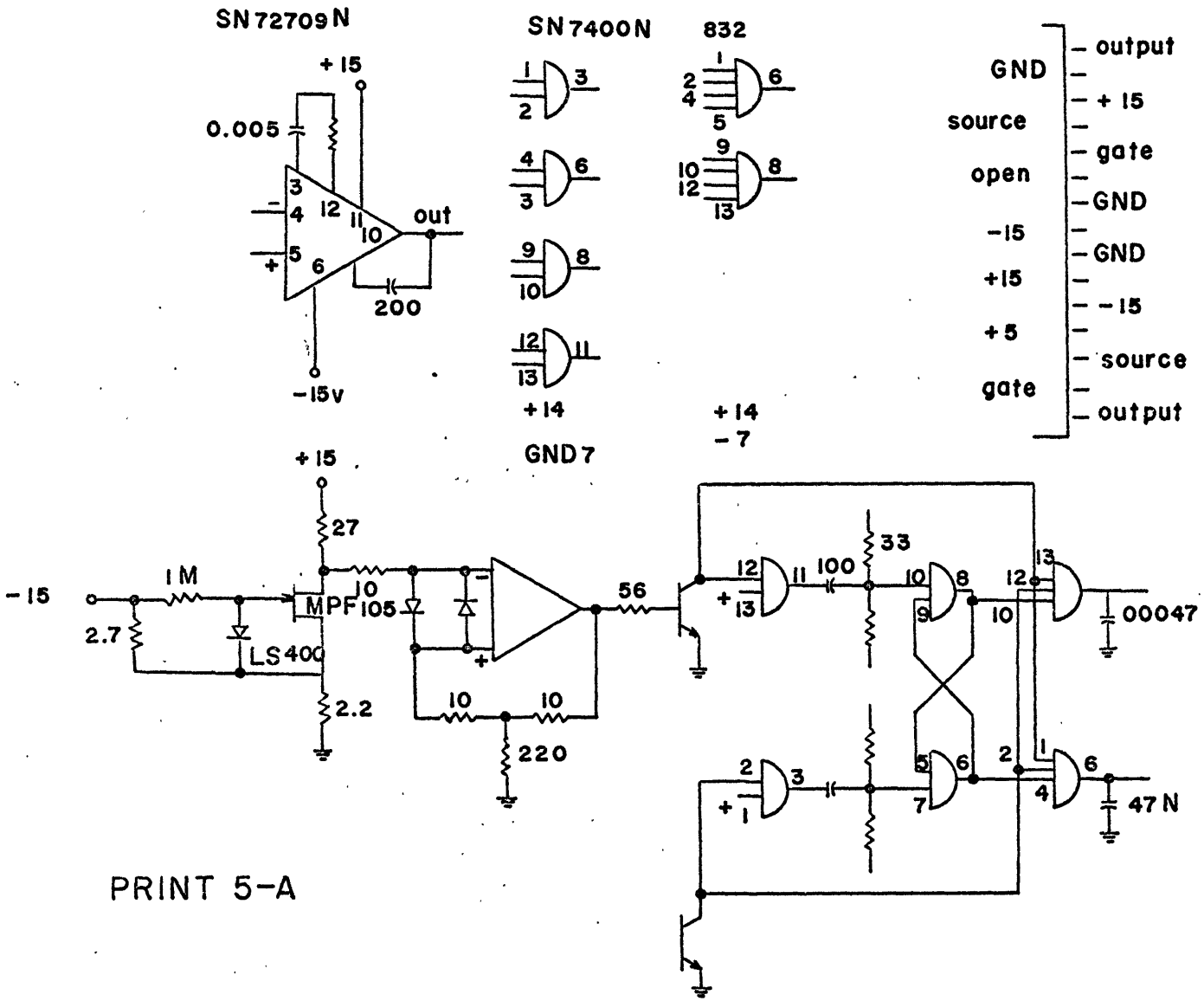
SN72709N
+15
0.005
3
4
5
6
12
11
10
out
200
-15v
SN7400N
1
2
3
4
6
9
8
10
12
13
11
+14
GND 7
832
1
2
4
5
6
9
10
12
13
8
+14
-7
GND
source
open
-15
+15
+5
gate
output
+15
gate
GND
GND
-15
source
output
-15
1M
2.7
LS400
27
MPF105
10
2.2
10
10
220
56
33
100
00047
47N

PRINT 5-A

MINI - METER (SHROUD AND BELLY BAND) 26 MAY 68 J.C.V.L.

MATERIAL

SHROUD → 1 5/8" TUBE

B & W GAGE 18 { O.D. ⇒ 1.625 / I.D. ⇒ 1.525

BELLY BAND → 1 1/2" SCHEDULE 40 PIPE ⇒ O.D. ⇒ 1.900 MACHINE I.D. TO FIT SHROUD O.D.

7/16 ROUND

.125" DIA x .630 SPOKES SILVER SOLDERED TO HUBS AND SHROUDS

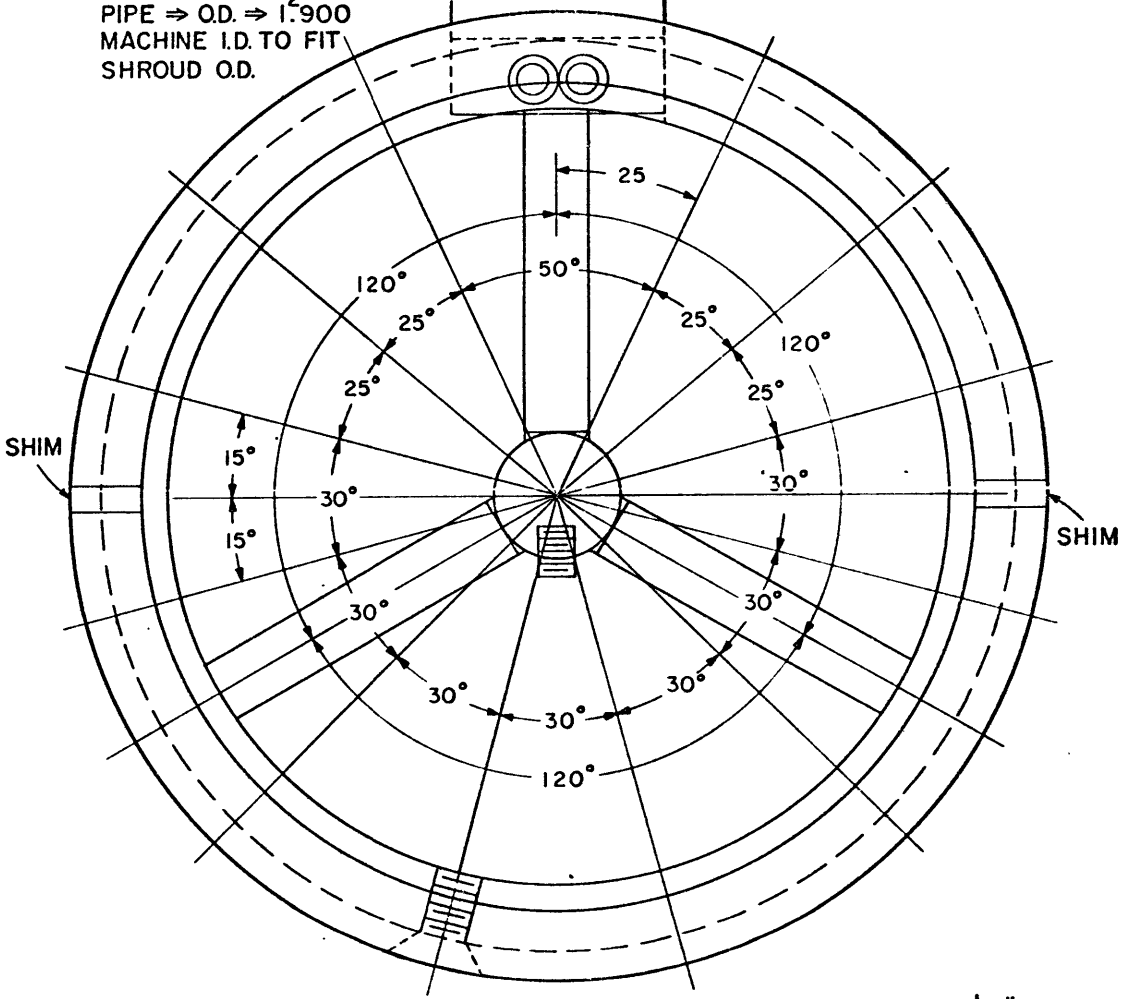

BORE AND REAM .437 HOLE THROUGH BELLY BAND AND SHROUD ASSEMBLY WHILE MOUNTED IN INDEX HEAD

24 NO 2-56 x 1/8" BOLT SPACED AROUND BELLY BAND AT ANGLES SHOWN

PRINT 6-A

APPENDIX B

PRECISION PRESSURE SENSOR

One of the greatest drawbacks of most STD systems used for microstructure work is their lack of depth resolution. This is primarily due to the large full scale (0-1500 meter typically) with a hysterisis which probably exceeds ±1 meter. Bissett-Berman gives their absolute accuracy to be ±1/4% or about ±4 meters, some significant part of which is hysterisis. For a microstructure experiment it is desirable to resolve depth to the scale size of the sensors. Accordingly a PB1400 Winsco data sensor 100 psid differential pressure sensor was selected with a resolution and hysterisis of ±.07% or ±.07 psid. This sensor should then resolve changes in pressure relative to its standard of ±1 cm of water.

The pressure standard then becomes the controlling factor in the system accuracy. Since for a two phase equilibrium gas-liquid system the absolute pressure is a well-known function of the temperature alone, such a system was selected for the pressure standard (see figure # 1-B). A two phase standard using 6 cubic inches of carbon dioxide varies in pressure about 15.5 meters of water per degree centigrade change in temperature and thus should give an accuracy of ±1.5 cm of water per ±.001°C which was the design goal. Toward this end a two stage temperature controller was used. The outside layer of control had a thermal gain of about 16 which for the fire hose constant depth data gives ±1/64°C and used two thermoelectric

heat pumps and thus could run when the outside temperature is above or below the set point. This allowed the system to attain thermal equilibrium on deck before launching. The inner stage of control was an Oven Industries proportional controller with a thermal gain of 100 capable of ±.002°C control for short periods like a day. The outer stage is insulated with a large Dewar flask while the inner stage has a jacket of polyurathane foam. This gives a thermal time constant of 1.5 hours for the inner member. Since the inner stage of temperature control failed to work the depth was probably only accurate to ±1/4 meter referred to absolute. However due to the long thermal time constant, short term (or say a minute) pressure comparisons are probably the order of the least count in pressure of 3.5 cm of water.

This type of pressure gauge can take a 10 times full scale overload without damage. Its time response is very fast and its construction is rugged, making it ideal for microstructure work. The main drawbacks to this system are high power consumption, limited full scale range and large size. A more detailed report will be soon forthcoming in an M.I.T. patent application.

The following factors affect the accuracy and repeatability of the depth sensing instrument to <.05% accuracy except the over pressure zero shift which is order ±.5%.

1) Change in volume and pressure of pressure standard due to
    a) movement of diaphragm
    b) temperature fluctuations of chamber

c) pressure effects on chamber

2) Hysterisis

3) Nonlinearity

4) Temperature coefficient of the gauge and electronics

a) zero shift

b) sensitivity

5) Over pressure

a) zero shift

b) sensitivity

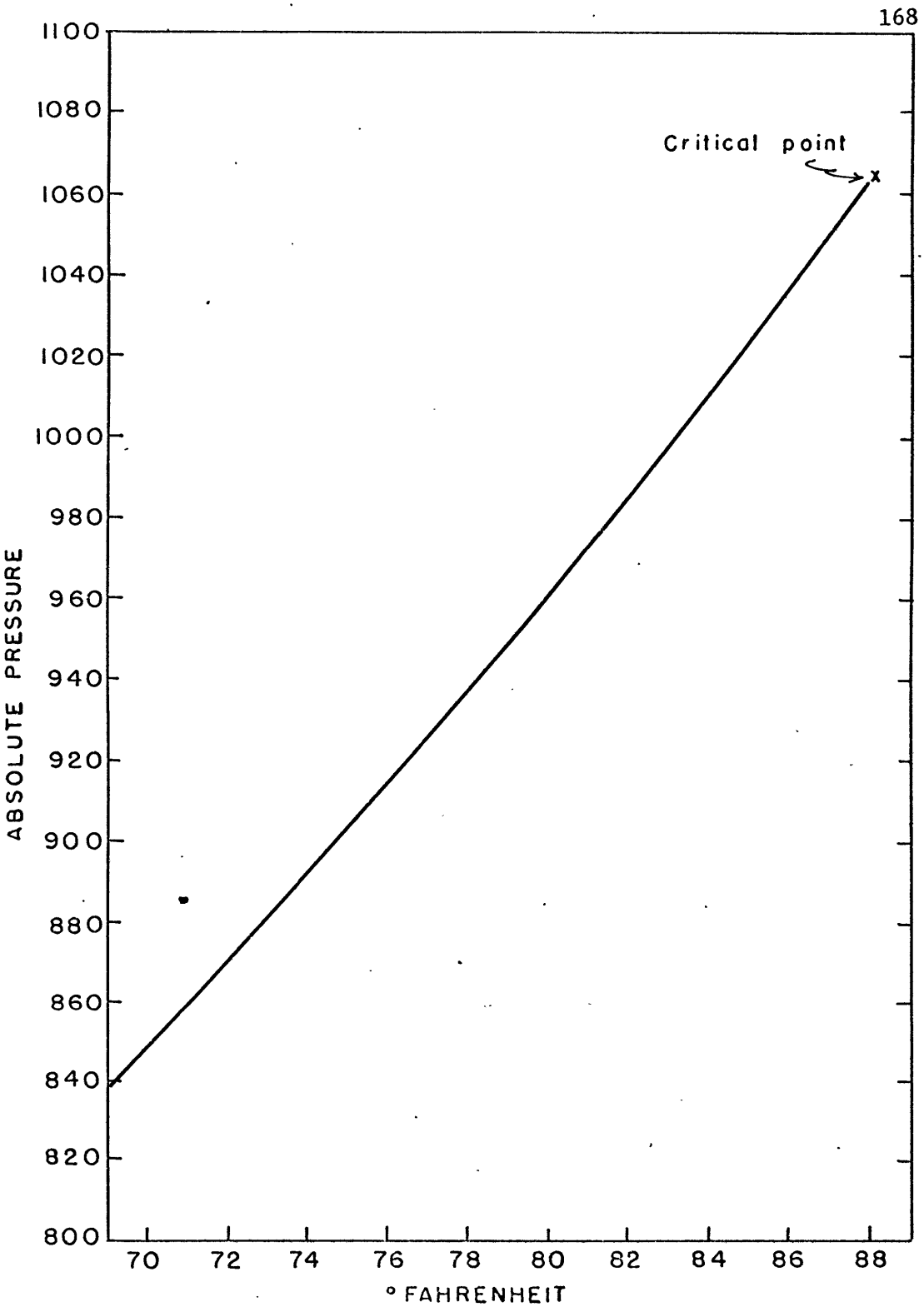

CARBON DIOXIDE EQUILIBRIUM PRESSURE TEMPERATURE CURVE
(The Handbook of Chemistry and Physics)

FIG. # 1-B

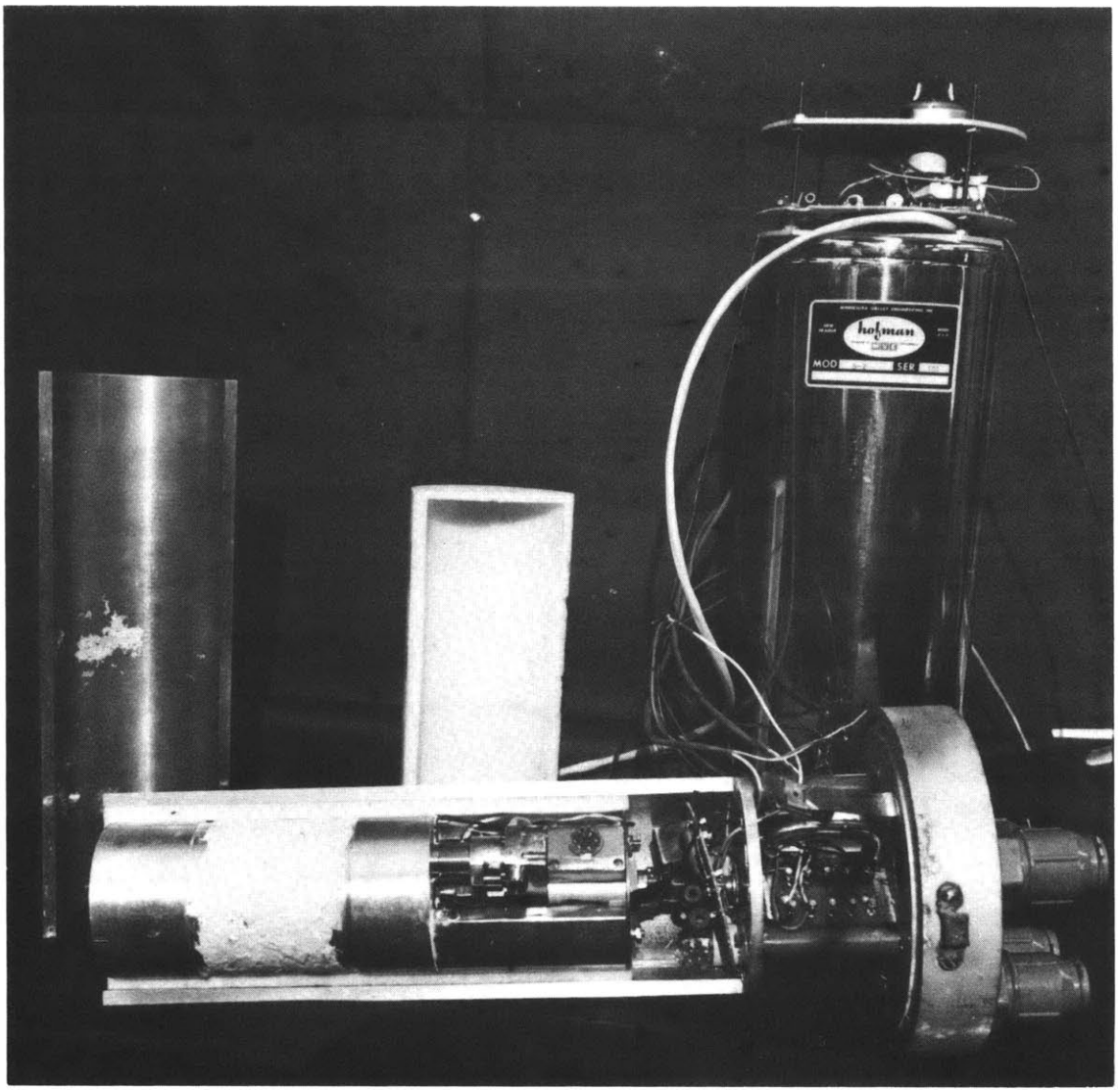

FIG. # 2-B. Precision pressure sensor components.

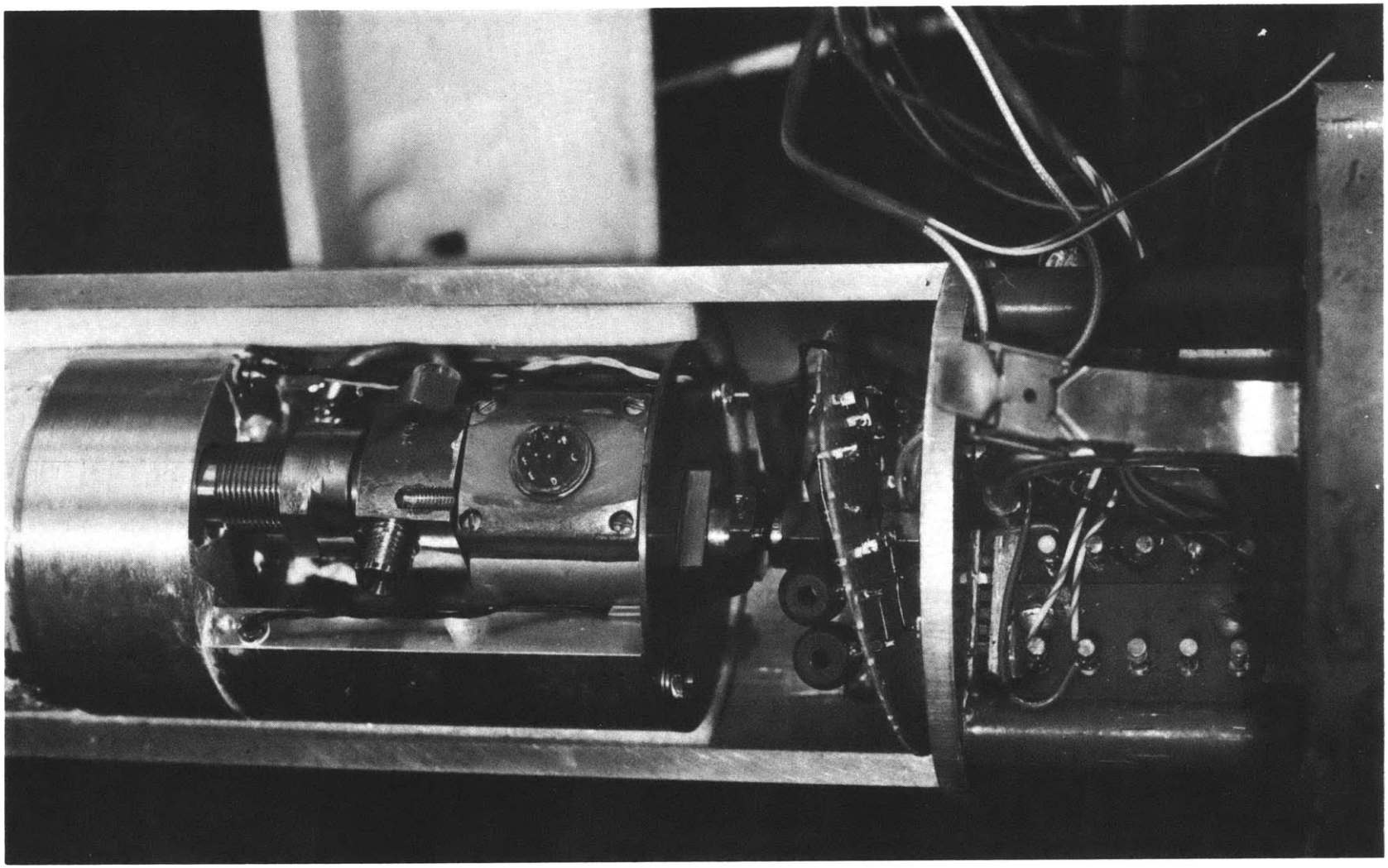

FIG. # 3-B. Pressure sensor detail.

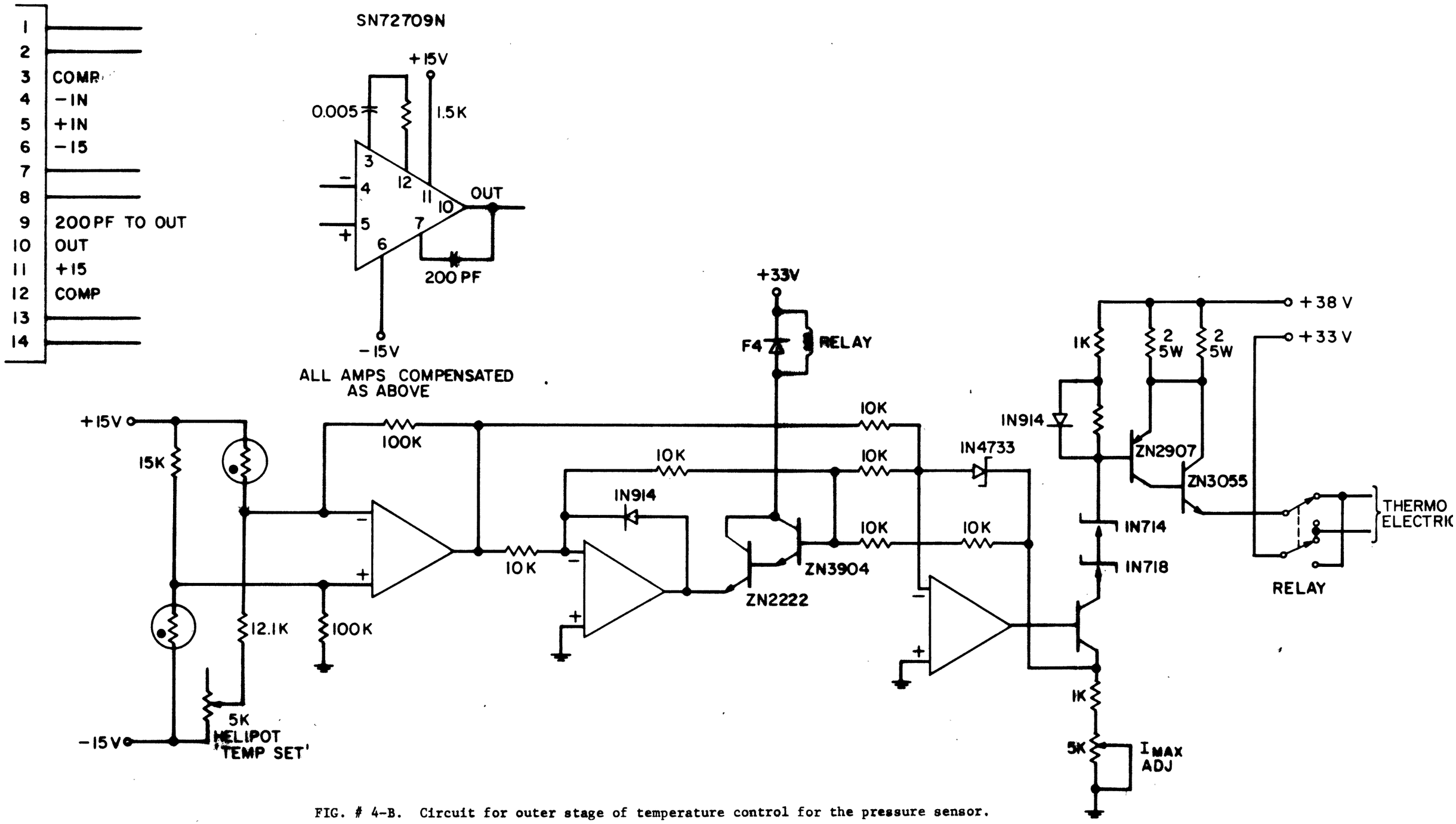

FIG. # 4-B. Circuit for outer stage of temperature control for the pressure sensor.

APPENDIX C

MOTION ISOLATION SYSTEM

One of the most pressing problems encountered in microstructure measurements is noise introduced by ship-coupled motion of the sensors relative to the water. This takes two principal forms - wave heave noise, which is mainly vertical, and ship drift, which moves the sensors horizontally. Typical values of heave in good weather are one-half meter rms amplitude with a period near six seconds. The ship drift is typically a knot or two with a strong dependence on wind speed.

There are several techniques for isolating the sensors from ship motion. One is to use a free-falling vehicle. This technique has been used successfully by Professor Charles Cox (1969) and his research team at Scripps to measure vertical temperature gradient. Professor Delbar Kelly at M.I.T. has also been working on a free-fall probe for oceanographic purposes. Another alternative is an instrumented swallow float or an independently controllable vehicle like the "Auto Probe" developed at W.H.O.I. by Ken Bert, Doug Webb and others. All of the above methods require a complex telemetry system or an expensive internal recorder together with a battery pack for self-contained power.

A further technique is to use a manned submarine such as Professor Claes Rooth and I did in the Alvin dye experiment.

The method of reducing sensor motion chosen for the scissors

experiment reduces both wave heave and ship drift an order of magnitude while at the same time providing a means of raising and lowering the scissors slowly and smoothly through a 100 meter depth interval. This method also provides a hard wire connection to the data sampling system which makes data transmission reliable and recording cheap. Because power is transmitted down the cable and data recordings are made on deck, the duration of data taking is limited only by system reliability and weather conditions, and the data may be reduced with an on-board computer in real time allowing scientific feed-back in the experiment.

To reduce the wave heave effect the mass of the submerged part of the system was made large (58 slugs) while the force to excite vertical motion was made small. This was done by reducing the total submerged weight to 15 lbs by using two buoyancy modules with 445 lbs lift each. These consisted of three each two-foot diameter half-inch wall thickness aluminum spheres held in nets and then clamped to the cable (see figure #2-D). These 6 balls were loaned by the Deep Submergence group at W.H.O.I., and have been tested to 4,500 PSI. These balls together with a pressure release provide an emergency retrieval system (see table 1C).

The remaining 15 lbs of wet weight were trimmed out with a partly inflated 400 foot length of 1 1/2" fire hose clamped to the steel cable. The hose was open to the sea on the bottom and connected to an air supply at the top. By letting air into the fire hose the scissors could be raised, or by letting air out of the hose it could

be lowered.

Since time limitations precluded the design and construction of a servo to control the fire hose pressure, it was necessary to make it stable at any degree of inflation. To that end the fire hose was fitted with internal flotation tubes so it would be neutrally buoyant when flooded. Thus the fire hose could be operated at nearly constant pressure (about 15 PSI) and variable volume. The rate of air leakage into or out of the fire hose was controlled by a ten-turn needle valve and thus could be set to an arbitrarily slow repeatable rate.

The fire hose develops 0.44 pounds of buoyancy per foot of length submerged and inflated. So a wave with 10 foot amplitude momentarily submerging the upper floating end of the hose would develop only 4.4 pounds of lift compared to a ship, which would develop many tons of lift for the same wave. If the system is viewed as a spring mass system then the undamped natural period of resonance is $T = 2\pi\sqrt{\frac{M}{k}}$. M is the mass of 58 slugs and K is the spring constant of .44 lbs force per foot displacement. The resulting natural period of 72 seconds together with substantial damping makes the system run very smoothly even in rough weather.

The second component of sensor motion is ship drift. This problem was reduced through the action of a 1,000 foot floating umbilical cord which connects the fire hose and the underwater system with the ship. The entire system, including the umbilical cord, was launched while the ship fell off down wind, streaming the scissor gear from the starboard side abaft the beam. Once the launching is

complete the ship may either turn and back into the wind or, if the ship has a bow thruster like the Atlantis II did, she may head up into the wind. By either of these actions a large bight is left down wind between the ship and the floating end of the fire hose, with ample slack so that the ship can jog with wind and sea variations without taking a strain on the umbilical cord. The Atlantis could keep headed up into a 35 knot wind although the pounding and cavitation of the bow thruster annoyed many in the ship's company. The end of the fire hose was clearly marked by a strobe flash at night and a large orange tuna float by day. The umbilical was made visible by the white foam plastic "handy floats" which married the steel cable to the orange garden hose that supplied ship's air to the fire hose.

The entire system took about 4 hours to launch and an hour to retrieve under less than ideal conditions. The operations took a high degree of skill and constant attention from the mate on watch from launch to retrieval. In one instance the fire hose was fouled in the starboard screw but was freed in a half hour with no significant damage. It would not be wise to use such a floating umbilical from a ship which had neither a bow thruster nor twin screws.

Due to the large submerged mass of the system and the 4,000 lb breaking strength of the U.S.S. .219" steel armored cable, extreme care in launch and retrieval was required to avoid snapping the cable. An accumulator was rigged with 24 two foot strands of 1/2" diameter bungy cord fixed to a pulley on one end and to the deck on the other. The steel cable then passed from the small deck-mounted winch (see figure #I-D) to the pulley two feet above the deck and thence up and

through the meter wheel 15 feet above the deck and then over the starboard side. As the strain in the cable increased, the shock cord stretched, lifting the pulley farther and farther from the deck. As the cable between the winch and meter wheel approaches the straight condition the strain grows without limit. The resulting non-linear spring characteristic will give four meters of wire for a peak load of 1,500 lbs in response to ship heave.

This accumulator proved necessary to prevent cable breakage during retrieval due to heavy dynamic loads. About 2,000 lbs maximum loads were experienced, which is perilously close to the 4,000 lb breaking strength quoted by the manufacturer.

TABLE 1-C

	Weight in pounds		
	dry	wet	
scissors frame	80	68	
2 current meters	14	5	
1 pressure sensor and power supply	79	26	
1 pelican hook pressure release	5	4	
1 Bendix sampling system	50	8	
2 salinity sensors	92	66	
1 compass housing	20	10	
2 temperature sensors	8	5	
1 chain 1/4" x 30'	37	30	
external wiring	17	10	
TOTAL SCISSORS WEIGHT	402	232	
buoyancy module	374	445	buoyant
600 meters of cable	190	165	
excess buoyancy if cable failed		48	
second buoyancy module	374	445	buoyant
expendable ballast	538	478	
TOTAL WEIGHT OF SYSTEM		15	
TOTAL DRY WEIGHT	1,878		

APPENDIX D

SEA CABLE SYSTEM

The underwater cable used was both a strength member to support the scissors and a coaxial electrical cable with the outer conducting galvanized steel armor immersed in sea water and a rubber insulated copper inner conductor. The armor was prestressed at the factory by U.S. Steel in two reversed layers of 15 wires each to give torsional balance under all load conditions. The 5,000 foot piece of cable used was surplus WHOI property and has the following properties per 1,000 feet:

1) 87 lb
2) 10.7 Ω
3) breaking strength 4,000
4) capacitance .001 μf @ 1 KHZ
5) minimum sheave diameter 14".

The cable was terminated with a Bissett Berman split brass clamping block which crushes the cable with six 1/4-28 bolts and holds the splayed armor ends under two concentric brass washers. The center conductor was spliced to a single conductor mecca connector as was the armor ground.

The deck end of the cable was wound on a temporary winch on the fan tail (see figure I-D). This winch was made at WHOI and had a four speed gear box and a reversible electric motor. The slowest speed of nearly 6 meters/minute was used almost exclusively to reduce cable strain. The cable was led from the winch to the accumulator

through a meter wheel mounted atop an "A-frame" and over the side. The 15 foot tall "A-frame" was large enough that the complete scissors could be launched in its erect position by hydraulically leaning the "A-frame" over the side.

The deck-mounted winch was fitted with a set of 6 slip rings so the flow of signals and power would be uninterrupted when the winch drum was turning (see figure# 1-E). Since slip ring transients could interfere with the constant current (2 amperes) power supply, the required current regulation was carried out on the cable side of the slip rings. A pair of large capacitors stores the charge required to continue constant current supply for momentary open circuits of the power supply slip ring. The remaining slip rings are used for signals from the submerged unit and sensing wires from the power supply. The slip rings, current regulator, signal separator and storage capacitors are housed in a military surplus Atlas missile guidance enclosure which is sealed with O-rings against sea spray.

Wiring between pressure housing was made of four and six conductor cables fitted with Mecca brand 10 K series field installable plastic connectors and bulkhead feed-throughs. The current meters passed their signals to their electronics housings through Corfon brand fiber optics and 1/16" thick plexiglass windows. There are about 200 water tight seals in the scissor array in all.

A chain bridle transmits the tension between the buoyancy balls and the ballast release without straining the scissors frame. The chain's 12,000 lb breaking strength insures that the buoyancy

module (see figure# 2-D) will remain married to the scissors if the coaxial cable to the surface should break. The Benthos brand pressure release shears calibrated pins at 1,120 ±100 meters depth releasing a pelican hook holding 470 wet lbs of ballast (see figure# 1-D).

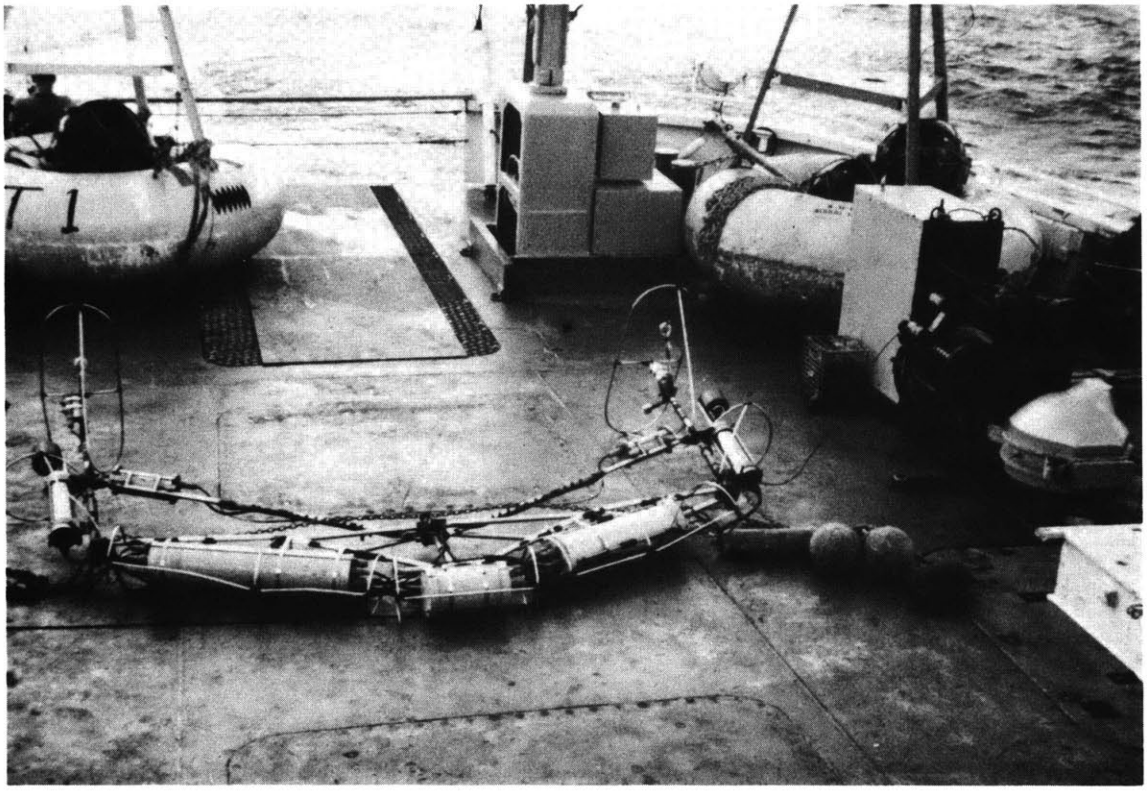

FIG. # 1-D: Deck layout including portable winch and slip ring housing. Note the expendable ballast fastened to the scissor. The "A-frame" is just out of the picture on the left side.

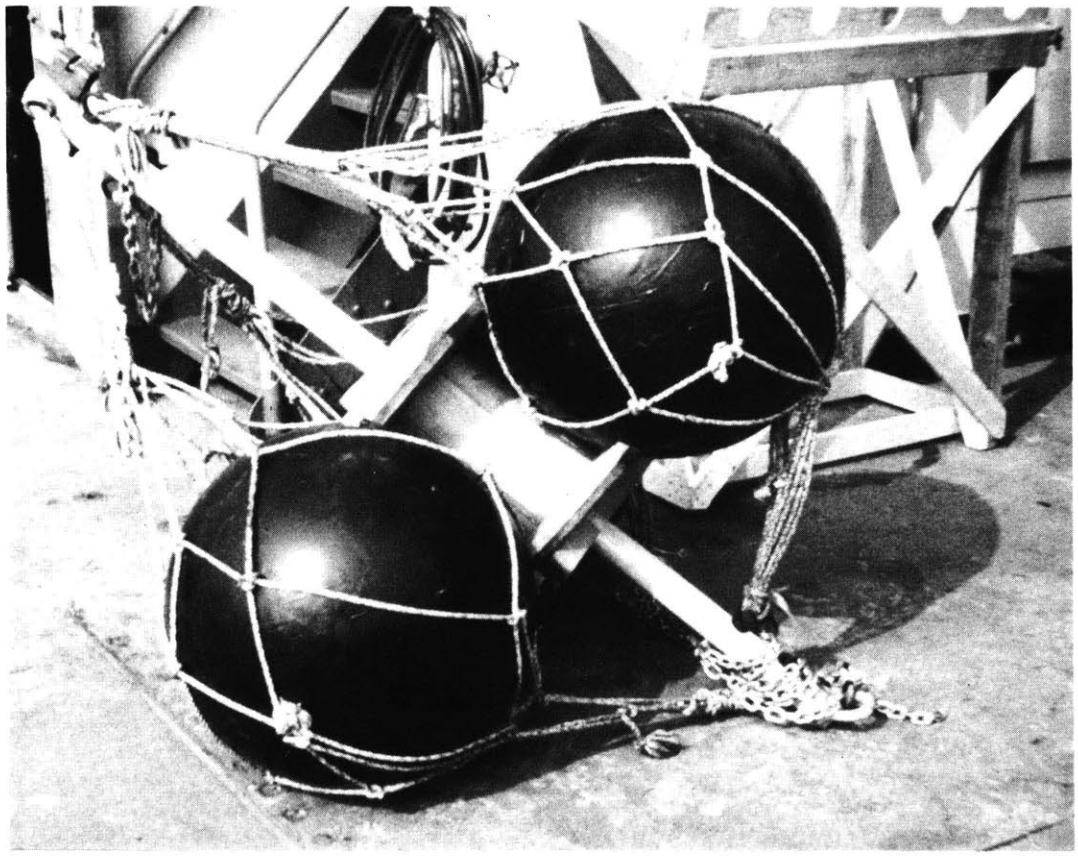

Figure #2-D. One of two buoyancy modules located below the surface mixed layer. This one is chained to the top of the scissors and has sufficient lift to float the scissors if the cable breaks and the pressure activated release drops the 500 lb. balast. The other buoyancy module supports the cable weight and all but 20 lbs. of the balast.

APPENDIX E

DESCRIPTION OF THE ELECTRONIC SYSTEM

The heart of the electronic system is the Bendix DCS-100 Mark II data collection cylinder (see figure # 1-E). It is presently set up to sample 10 variables of three different kinds (see figure # 2-E). Low level D.C. voltages 0-100 m volts are handled by an internal voltage-to-frequency converter which is switched from channel to channel with low noise FET transistors and generates 0 to 2,000 pulses during each 0.2 second sampling period. Since only one amplifier and voltage-to-frequency converter is used for all analog channels, slow drift in this unit appears equally in both temperature channels and cancels out in the temperature differences. The second type of signal is a frequency output such as the Bisset-Berman salinity sensors. Any frequency from 0 to 10,000 Hz could be sampled equally well. The upper limit in frequency is imposed by the cable impedence and the Sony tape recorder used. The final type of signal is a slow pulse train of 5 volt integrated circuit pulses. The pulses are counted and stored during the 2 second frame period in five up-down counters which transmit them in short bursts of 0 to 128 pulses at a 10 K Hz pulse rate. Each up-down counter receives input pulses on two wires depending on whether it is to count up or down from 64, which was chosen arbitrarily to be zero.

This type of data is generated by the mini-meters which give pulses on the count up wire when water flows through the duct in the

positive direction and give pulses on the count down wire when the flow is in the negative direction. The Geodyne compass also feeds an up-down counter on frame pulse command. If the data pulse rate exceeds ±64 pulses per 2 seconds the most significant bit is lost and the counter starts at 64 again.

All timing in the Bendix system is controlled by a crystal clock which is counted down from 100 K Hz to generate frame and line pulses. For each analog or frequency channel the sampling time occurs during a period of 199,912.70 ±.05 μ sec between two 250 μ sec blanking pulses. The line pulse occurs in the middle of each blanking pulse and provides the reference trigger pulse for the read-out counter. The number of (50 μ sec) data pulses recorded between each pair of line pulses is then proportional to the variable and is not influenced by fluctuations in recorder speed. The sampled signals are sent from output multiplexer to the signal driver and thence up the cable. At the ship end of the cable the signals go through a blocking capacitor and separate signal slip rings to the unscrambler and a Sony two track tape recorder. The unscrambler separates data pulses from frame and line pulses so they may be recorded on separate tracks. It further separates all ten variables onto individual terminals so they may be monitored by a counter and oscilloscope in the field in real time as well as during play back.

All system power is fed through a Sola 60 Hz constant voltage transformer to suppress voltage transients. The surface units have individual power supplies whereas the scissors power comes from

the Gates power supply. This supply feeds a constant current of 2 amperes through the slip rings and down the sea cable. At the sea end a group of inverters is hung on a 33 volt zener diode which provides rough regulation for all the different voltages required. Fine power regulation for sensor bridges and other applications together with over voltage protection and fuzzing is found on the submerged power supply (see figure # 4-E). Figure # 3-E is an electrical block diagram of the entire system. For more complete detail refer to the Operating Manual of the DCS-100 Mark II, written by its designer David K. Nergaard, or to the other parts of the Appendix of this thesis for the MIT supplied units.

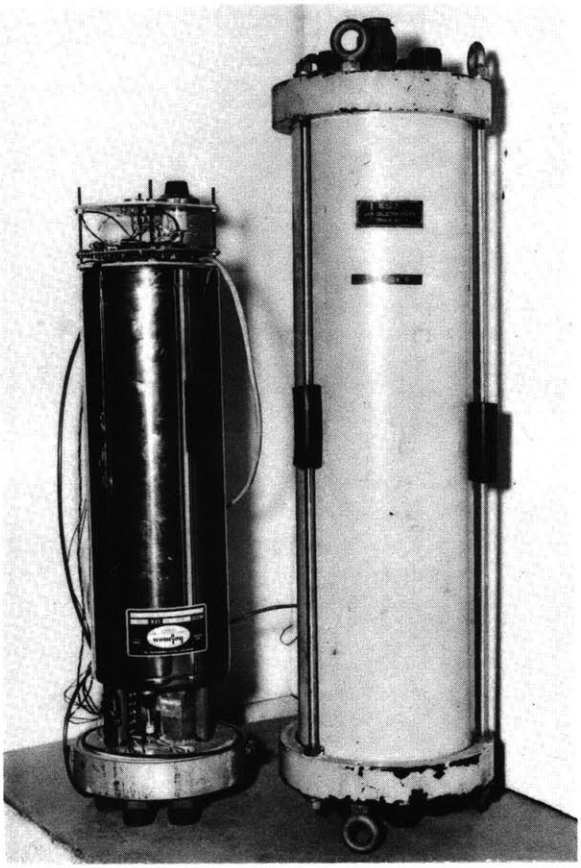

FIG. # 1-E The Bendix data collection cylinder is on the right side. The precision pressure sensor without housing is on the left. Note the large stainless steel dewar flask which insulates the temperature-controlled interior. The temperature controller is at the top and the heat sink blocks for the thermo-electric heat pumps are at the bottom.

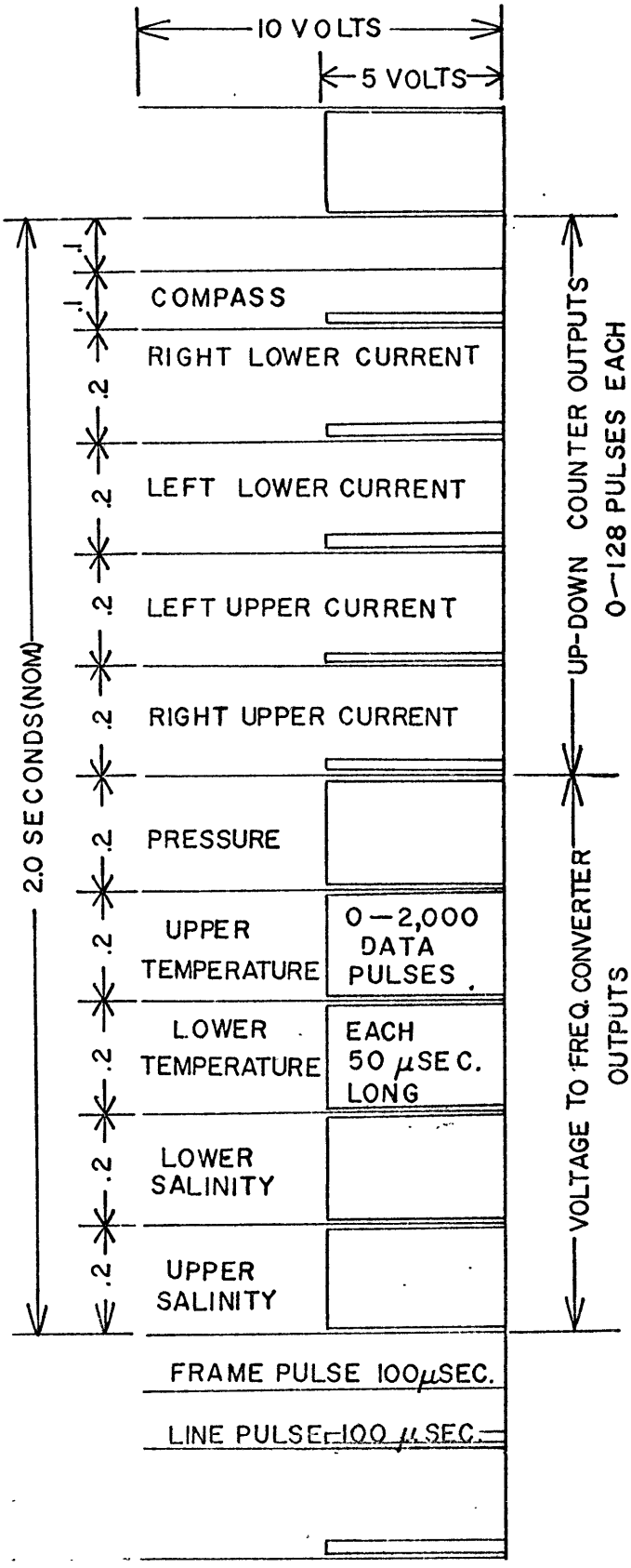

FIG. # 2-E: Nominal timing diagram for output from the Bendix DCS-100-MARK II data collection cylinder and signal driver.

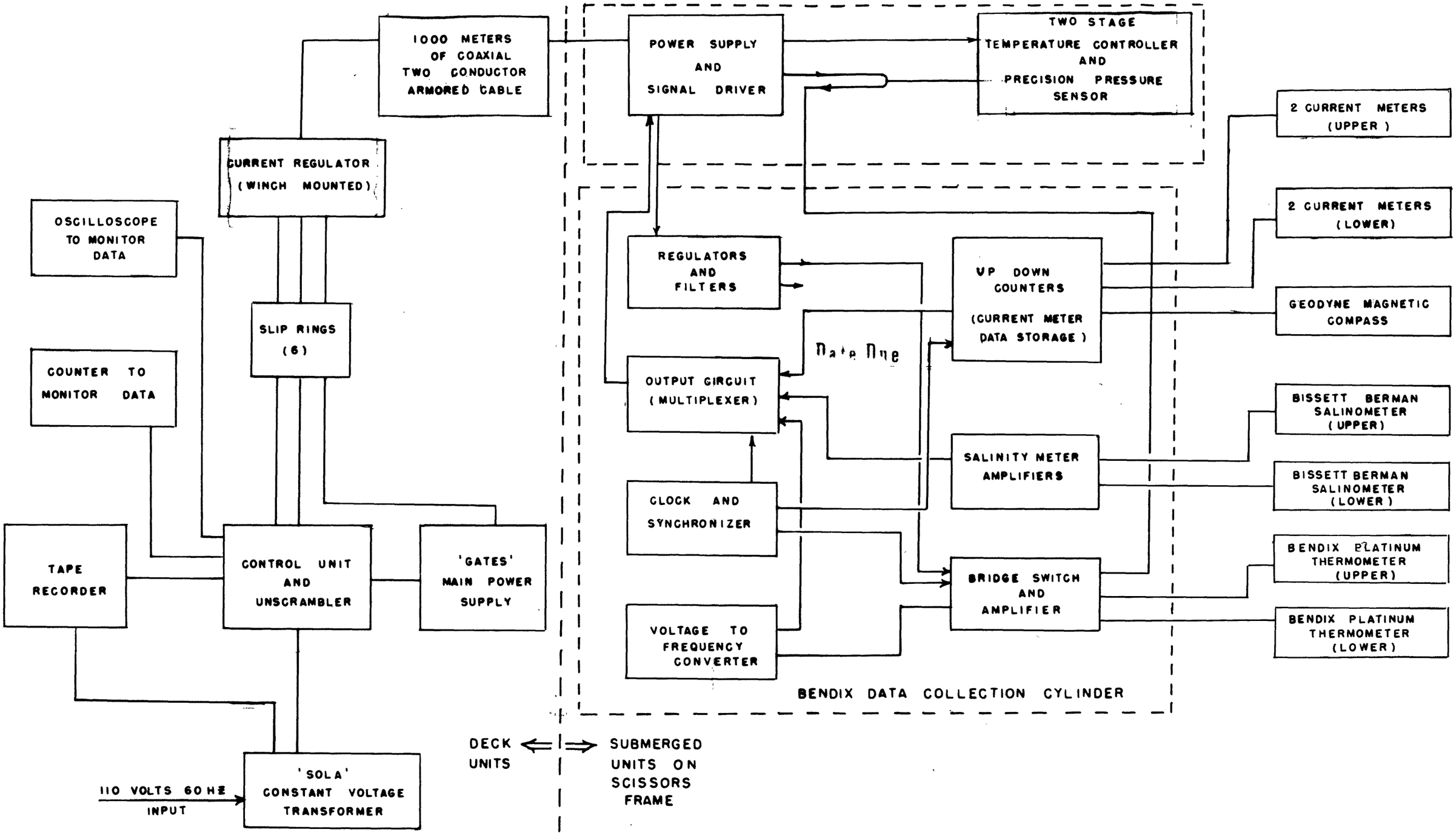

MASTER ELECTRICAL BLOCK DIAGRAM.

FIG. # 3-E

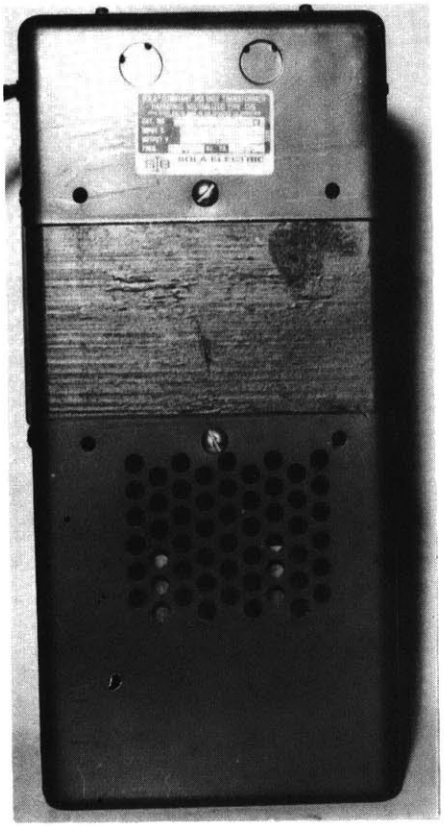

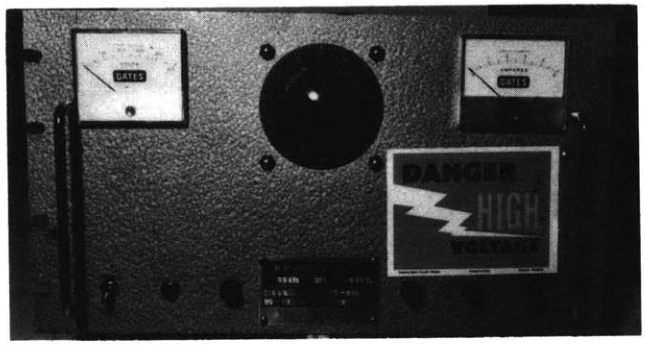

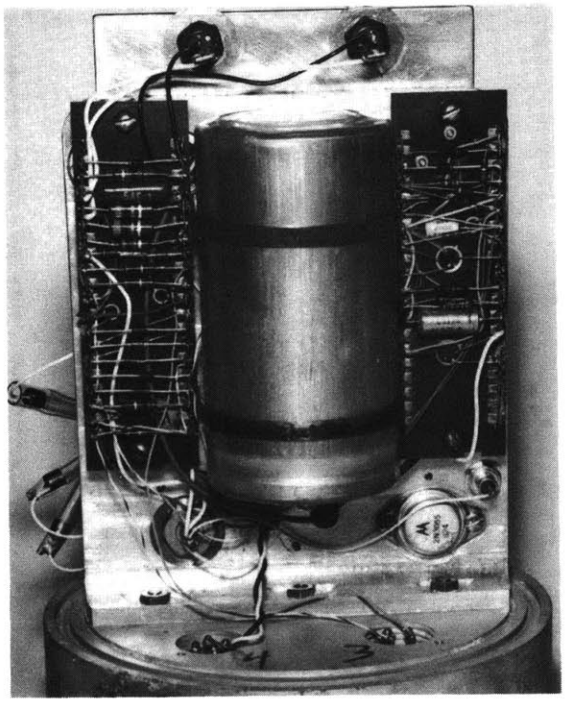

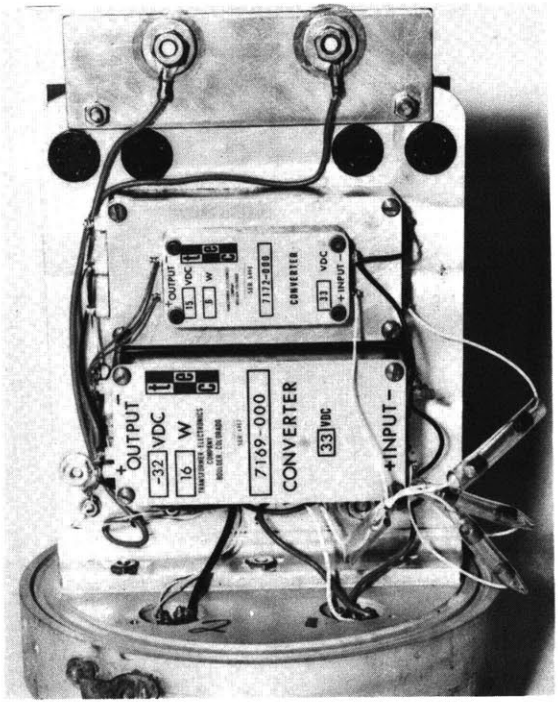

Bendix power supplies

FIG. # 4-E:

1) Sola voltage transformer (upper left)
2) Gates D.C. power supply (upper right)
3) D.C. to D.C. converters, note heat sink (lower right)
4) Filters, regulators and signal driver on heat sink (lower left).

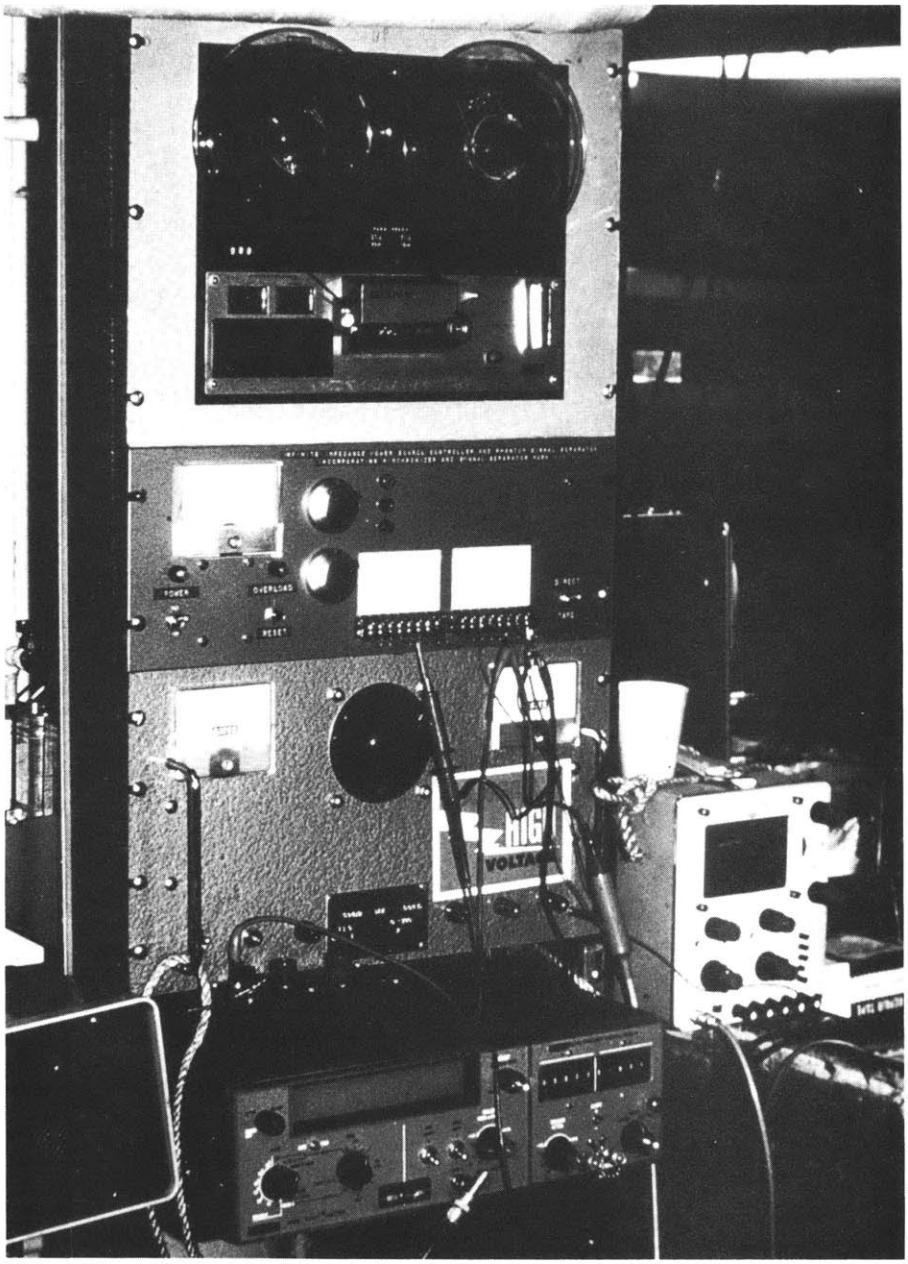

Figure 5-E: Complete deck unit including two track tape recorder, signal unscrambler, constant current master power supply and borrowed counter to monitor data.

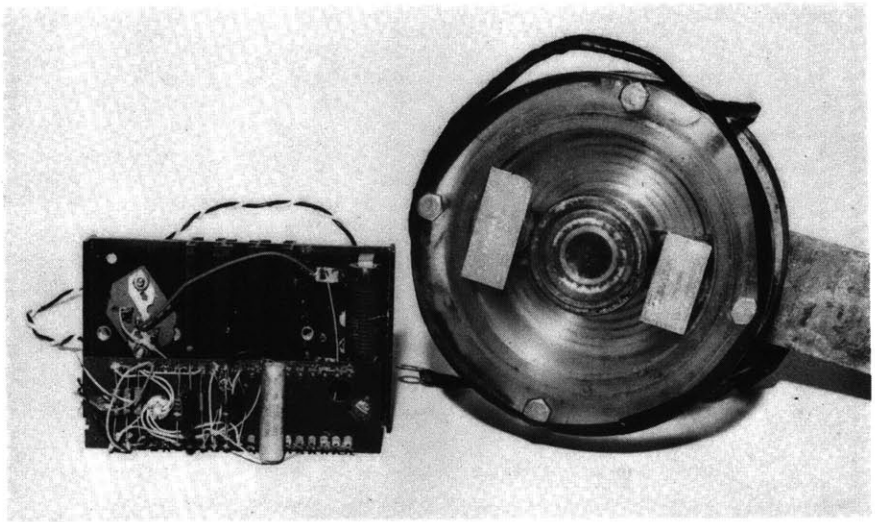

FIG. # 6-E The constant current regulator and signal separator together with this set of six slip rings rides in rotation with the winch drum. These units are enclosed in the slip ring housing seen in figure #5.

APPENDIX F

TEMPERATURE SENSORS

The temperature sensors used in the scissors experiment are matched Minco S31 Series platinum resistance thermometers. These together with their electronics were provided by Bendix Corporation as part of the SK-100 Data Collection System. These sensors are mounted in individual small brass housings which are connected by shielded cables to the data collecting cylinder (see figure # 1-F). These sensors have a time constant of about two seconds. The step response of these sensors is seen in figure # 2-F. The self heating was found to change by about .01 ±.005°C when the water velocity changed from 0 to 100 cm/sec in flume tests conducted at MIT in the Department of Earth and Planetary Sciences . In these tests no difference in self heating was observed as the angle of attack was changed from head on to right angles.

These temperature probes are extremely linear and were found to track each other to ±.010°C from 10°C to 15°C in calibration tests at MIT from 13 through 26 December 1968 in a large constant temperature bath. The temperature reference was a Hewlett Packard 2801A Quartz Thermometer with Probe S/N 709-22 which was calibrated against a Bureau of Standards reference on 5/2/68.

FIG. #1-F

Bendix platinum resistance thermometers and housings.

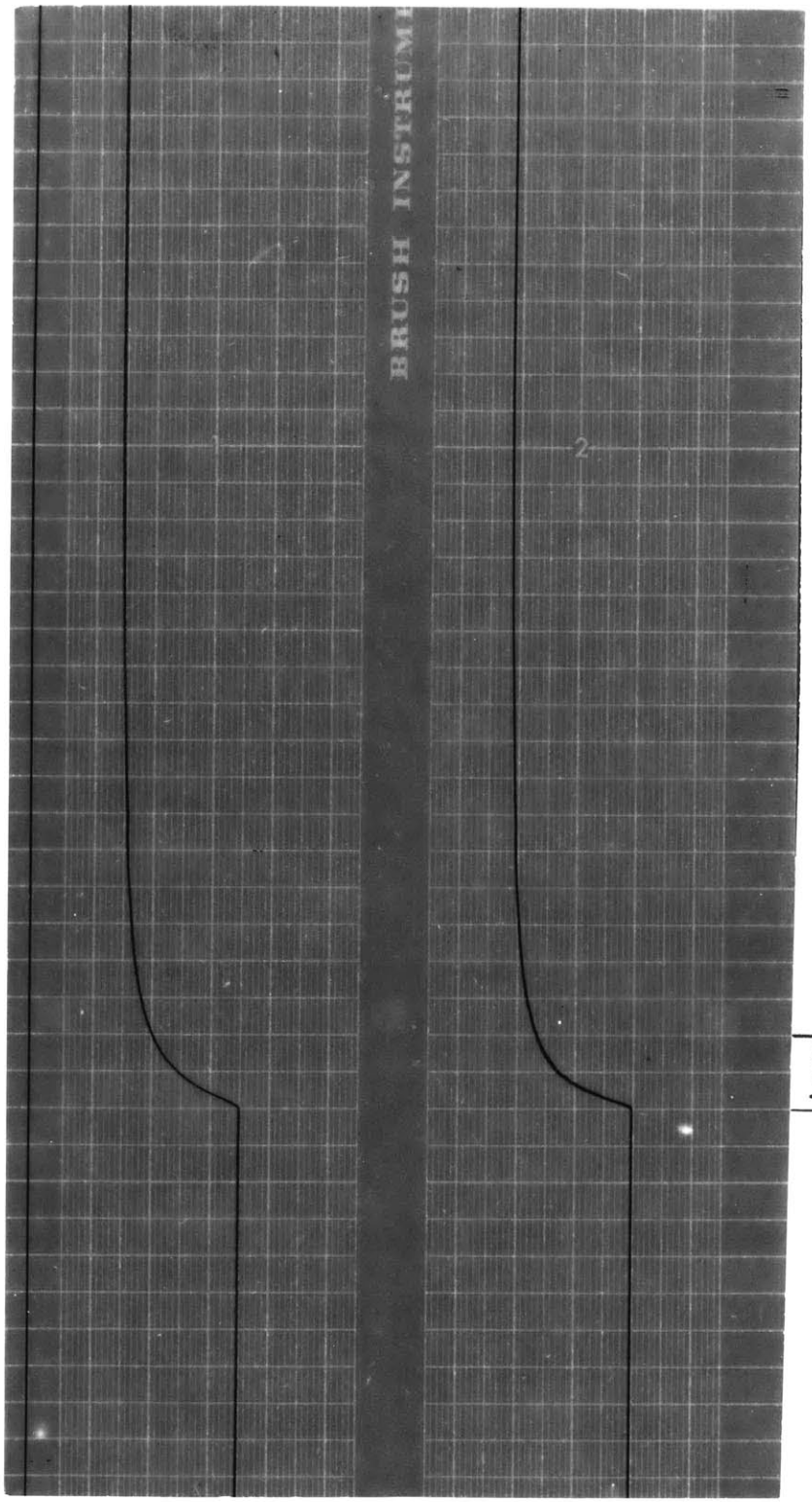

FIG. #2-F

APPENDIX G

A METHOD FOR THE INDIRECT DETECTION OF SALT FINGERS

Another possible indirect technique for finding evidence of the action of salt fingers or similar molecular processes has been suggested by the author. The different constituents of sea salt each have different molecular diffusivities. These different ions will then separate to some small extent by the fingering process. The ions which diffuse fastest will tend to follow the temperature field somewhat. A crude experiment set up in a graduated cylinder was performed at WHOI by the author, Kim Saunders and Professor Manglesdorf to test this idea. The salt solution used in both layers was filtered Sargasso Sea water. The upper layer was heated and undiluted while the lower layer was diluted with distilled water at about room temperature. The results of this experiment are shown in figure # 1-G. The final potassium to sodium ratio shows positive values in the upper layer and negative values in the lower layer as predicted above. These effects in the ocean are likely to be small for a single salt finger interface but might be measurable over many such layers since this fractionation should accumulate over some depth range large compared to a single layer thickness.

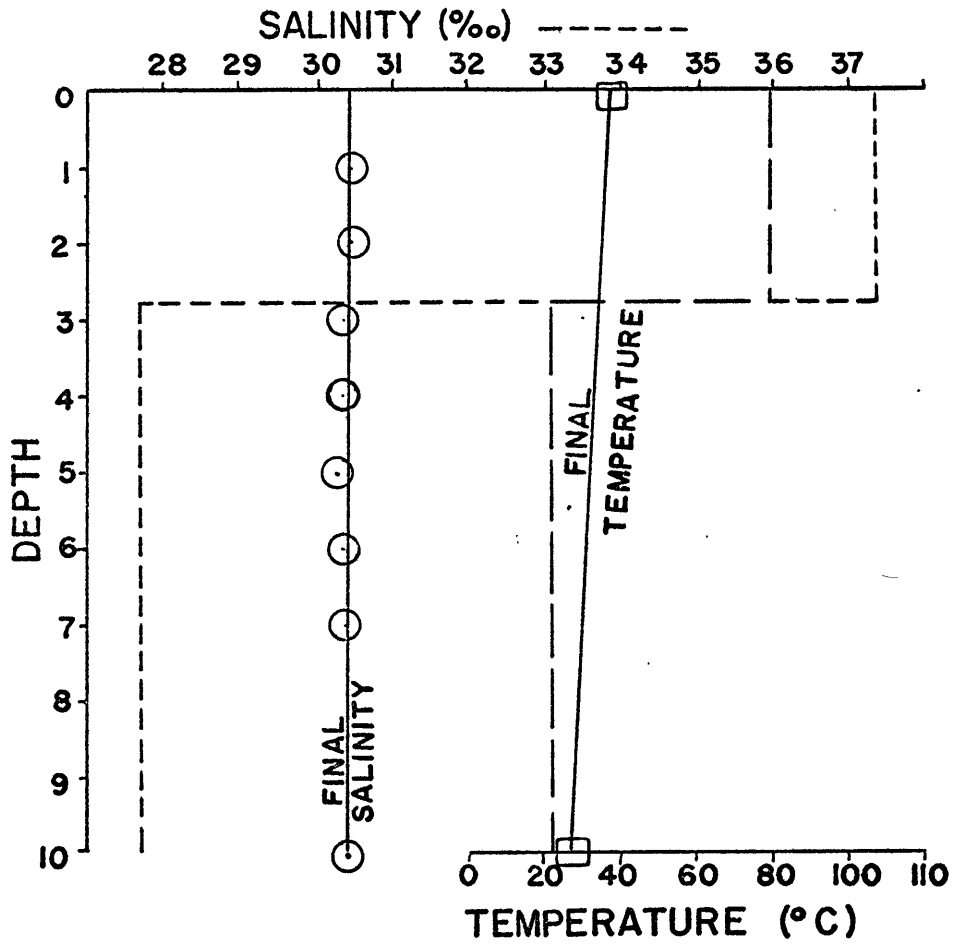

SALINITY & TEMPERATURE
vs.
DEPTH

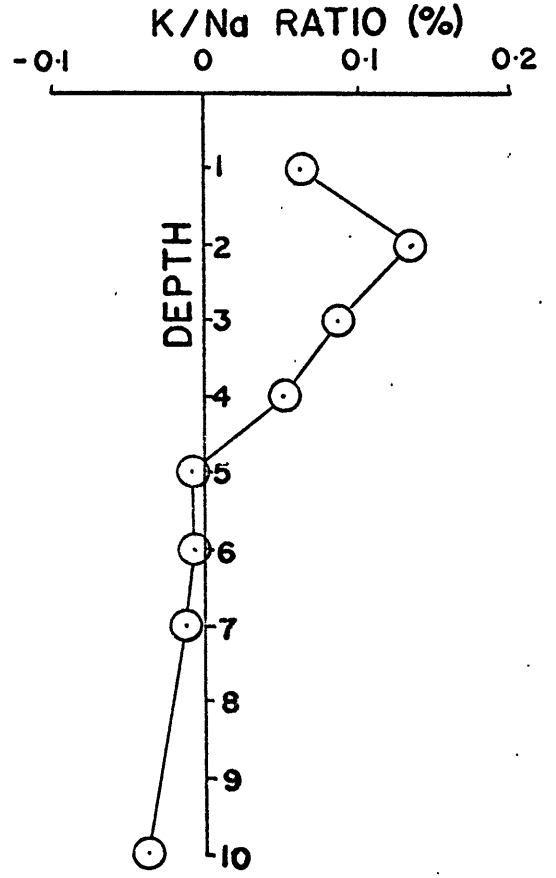

POTASSIUM/SODIUM RATIO
vs.
DEPTH

FIG. # 1-G

APPENDIX H

DIGITAL SMOOTHING FILTER

During the scissors measurements where the depth was held nominally constant most of the noise in the sensors is due to surface wave-induced motion. Least count jumps particularly in the raw salinity give rise to anomolously large salinity gradients which in turn contaminate the density gradient estimates. The current meters have a small mechanical unbalance which can give raw shear measurements a false periodic nature of period 10 counts. The temperature sensor has a time constant of about two seconds which can cause a phase lag compared to the fast depth densor. This difference in phase lag causes the temperature-depth plot of a steep temperature gradient for a single sensor oscillated vertically to scatter around the average temperature and depth in an irregular open curve much like an irregular hysterisis loop. (This effect can be seen in figure # 1-I.)

Assuming that the scissors maintains a constant average depth and that the actual temperature, salinity and current vary slowly in time and the horizontal direction, it seems desirable to average these data in some way to reduce the above effects. A running weighted average whose effect extends over several surface wave periods and yet will resolve the shortest period Doppler shifted single sheet internal wave (period $\sim$30 seconds) is required. The weighting function chosen for this running average is shown in figure # 1-H. The sum of alternate terms is equal to avoid oscillation for a string of

data with alternate least counts. Each term in the scissors time series is separated by 2 seconds so each three terms in the weighting function cover one surface wave period of approximately 6 seconds.

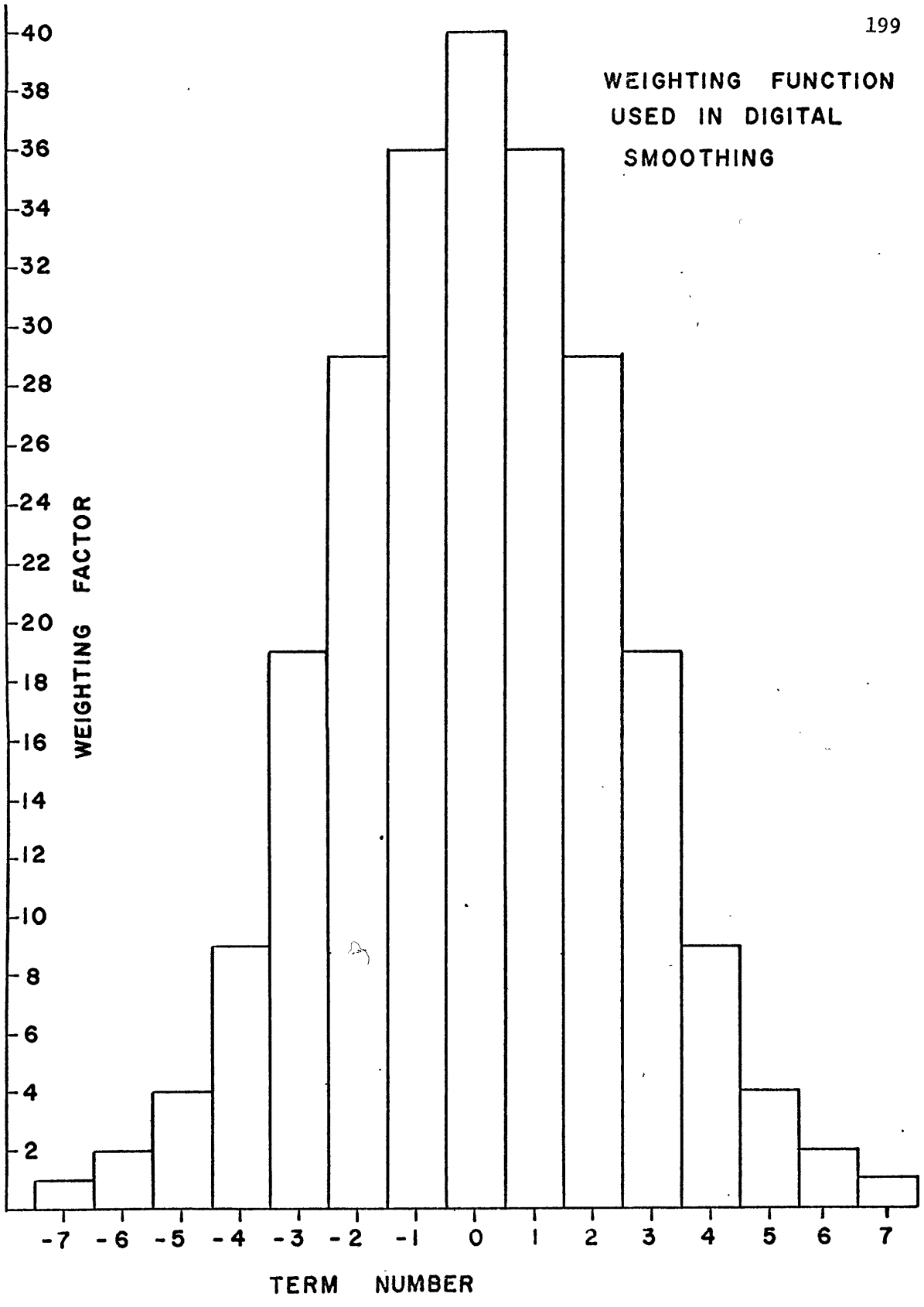
WEIGHTING FUNCTION
USED IN DIGITAL
SMOOTHING
WEIGHTING FACTOR
40
38
36
34
32
30
28
26
24
22
20
18
16
14
12
10
8
6
4
2
-7 -6 -5 -4 -3 -2 -1 0 1 2 3 4 5 6 7
TERM NUMBER

FIG. # 1-H

APPENDIX I

TIME-SERIES ANALYSIS

Examples of the raw scissors data are shown in figures #1-I and #2-I. These data were taken synchronously while the scissors was suspended from the ship so wave heave effects are quite evident. The entire shear magnitude and temperature gradient records from the fire-hose constant level were decomposed into Fourier components. A new series was reconstructed from the first 200 coefficients and sampled every minute. These sampled data are presented for both filtered and unfiltered data in figures #3-I and #4-I respectively. The filtering process is the running vector average described above and significantly reduces the average amplitude of the shear.

The coherence and phase for the above fire hose constant level data is shown for both filtered and unfiltered data (see figures #5-I and #6-I respectively). They show that the negative correlation between shear magnitude and temperature gradient discussed in chapter 3 does not occur in a single frequency band but rather is dispersed over the whole frequency range. The power spectra for the filtered and unfiltered data is presented in figures #7-I and #8-I respectively. All of the above are calculations done with 120 degrees of freedom. Other runs not present used 16 and 32 degrees of freedom but gave no substantial difference from the above result. The first 64 estimates from a power spectrum computation using 16 degrees of freedom are presented in figure #9-I. All confidence levels given are 95%.

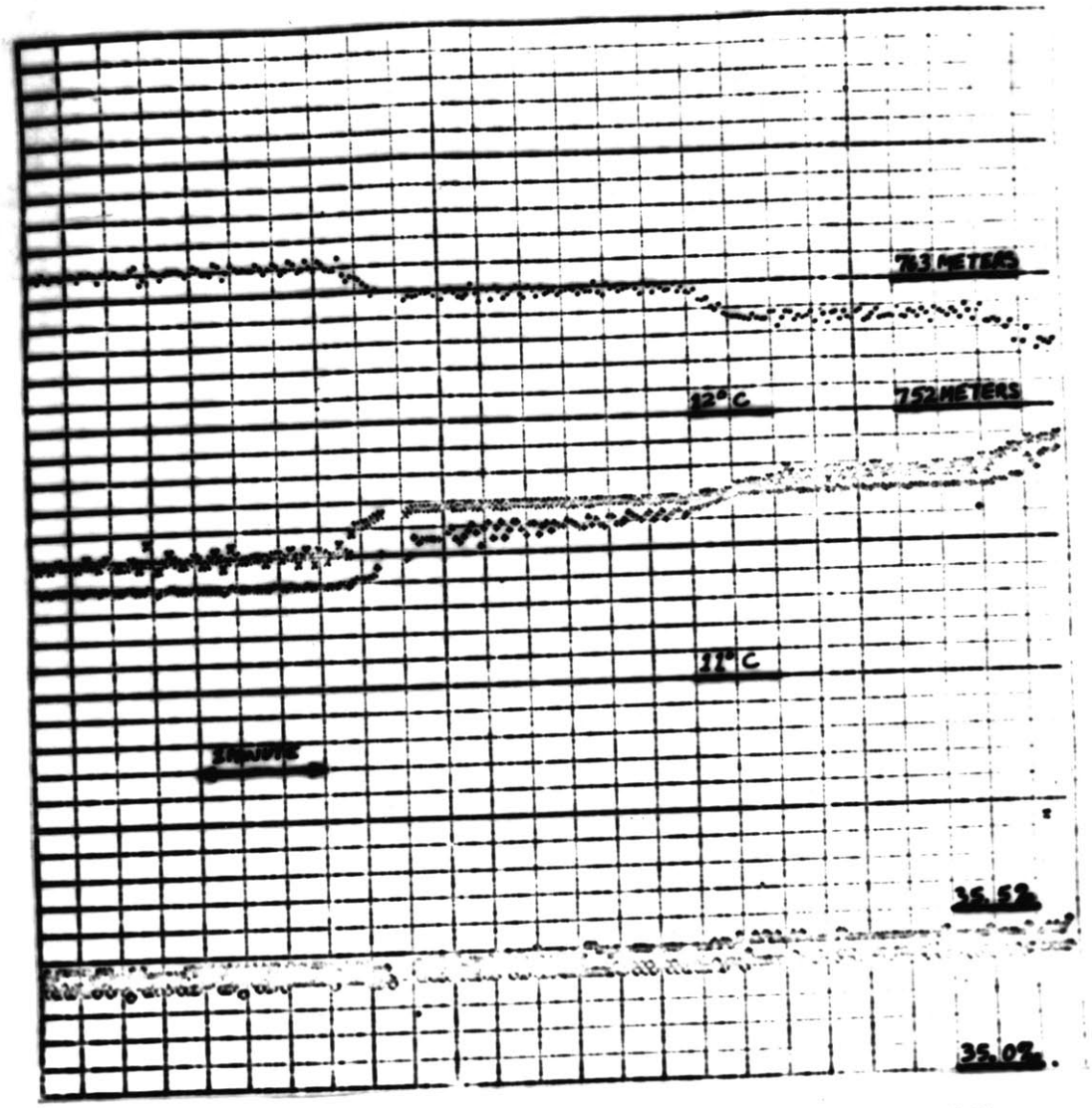

FIG. # 1-I

Raw temperature, salinity and depth plotted vs. time while scissors is raised in 3 meter steps. Note that the ship-coupled wave noise on the pressure sensor signal (·) is nearly a meter peak to peak. On the left the upper temperature sensor (x) moving vertically in a steep gradient. In the center it is raised into a well-mixed while the lower temperature sensor (+) enters the high gradient. On the right the lower sensor enters the well mixed regions. The upper salinity sensor (o) and the lower salinity sensor (•) show similar changes at lower sensitivity.

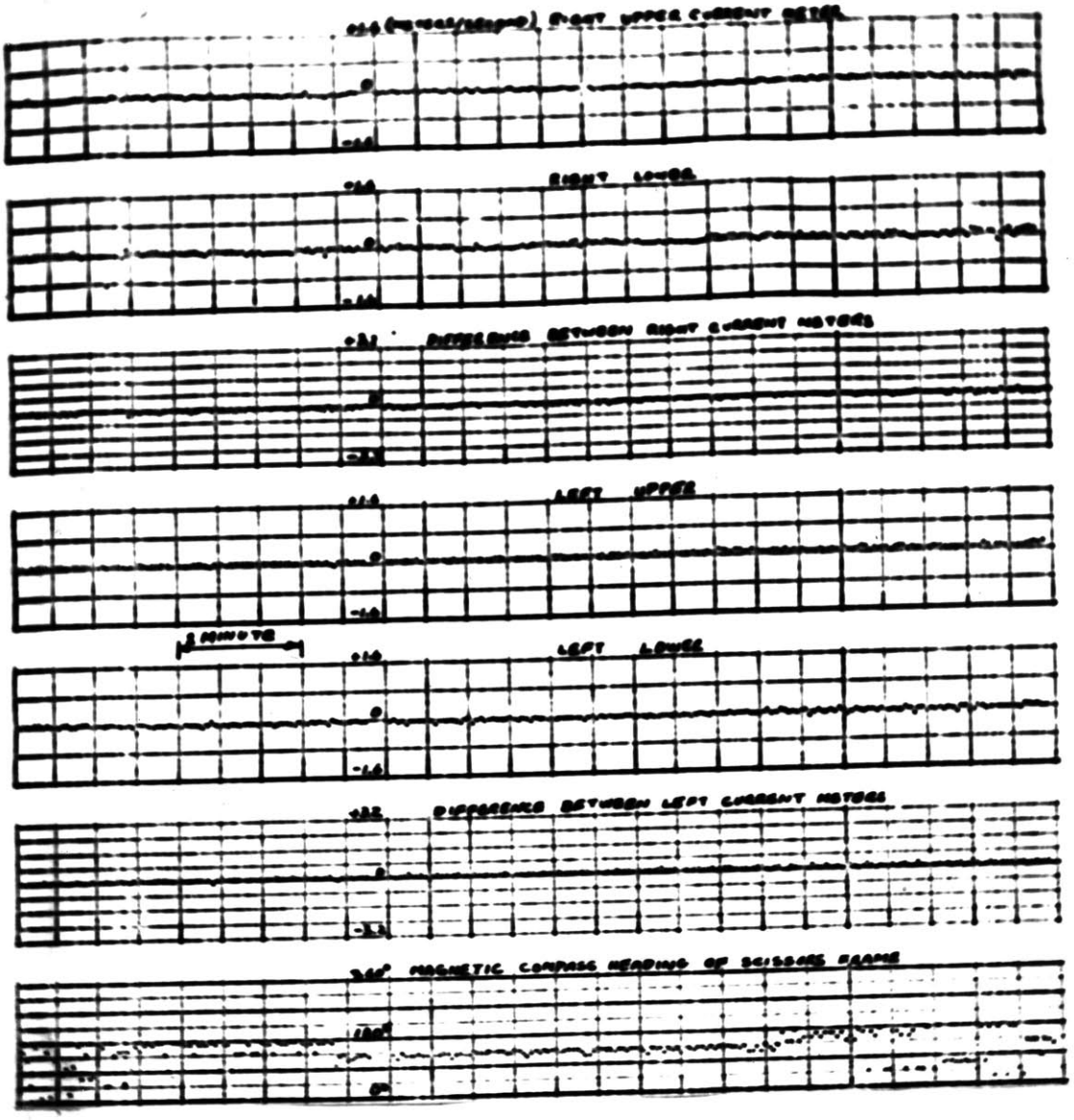

FIG. # 2-I

Raw current meter and compass data plotted vs. time. Note the erratic compass behavior. This data was taken synchronously with that in figure #5.

FIG. # 3-I

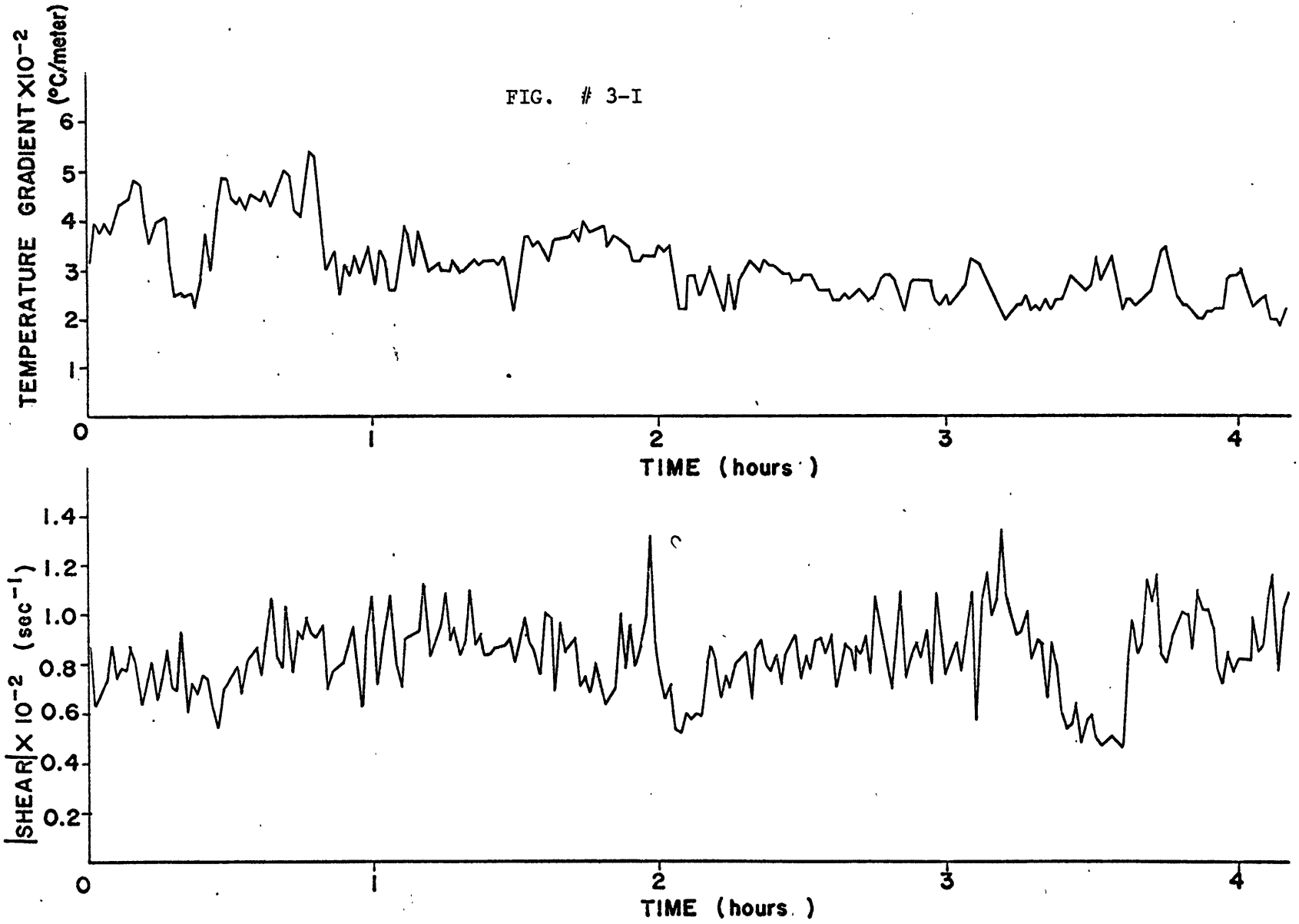
TEMPERATURE GRADIENT X10⁻² (°C/meter)
6
5
4
3
2
1
0
1
2
3
4
TIME (hours)
|SHEAR| X 10⁻² (sec⁻¹)
1.4
1.2
1.0
0.8
0.6
0.4
0.2
0
1
2
3
4
TIME (hours)

FIG. # 4-I

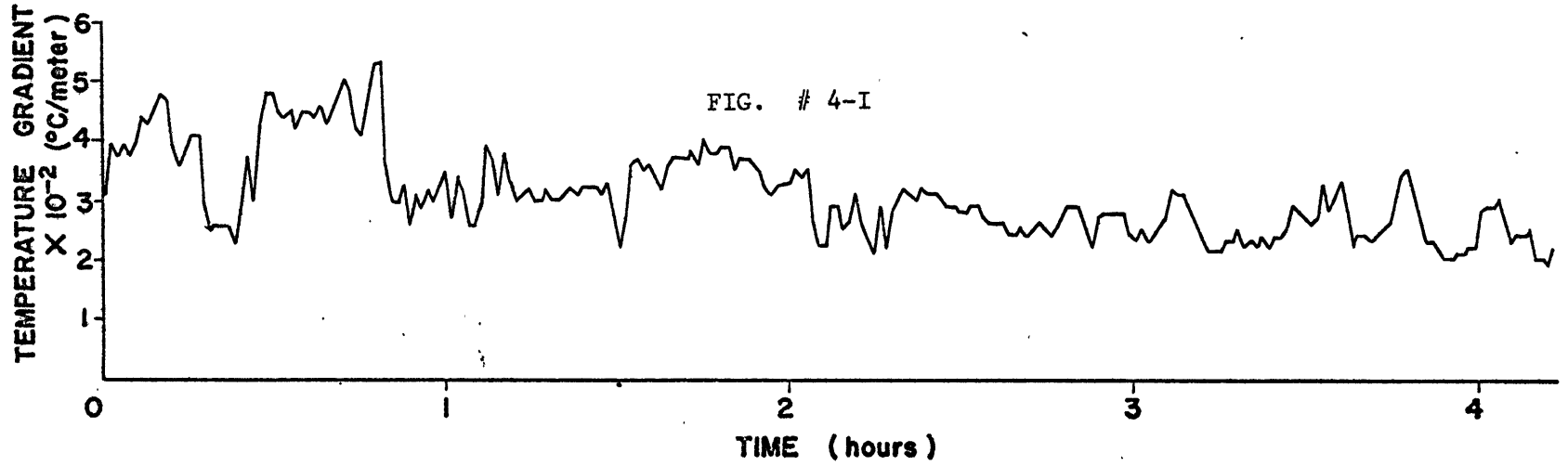
TEMPERATURE GRADIENT
X 10⁻² (°C/meter)
6
5
4
3
2
1
0
1
2
3
4
TIME (hours)

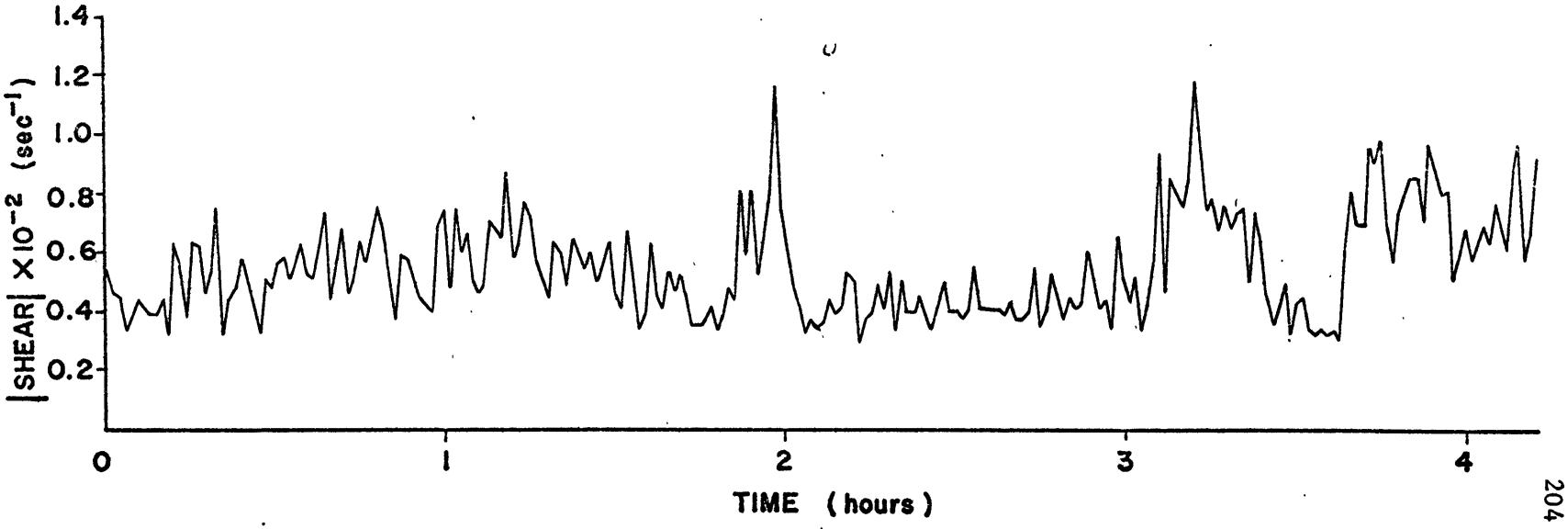
|SHEAR| X10⁻² (sec⁻¹)
1.4
1.2
1.0
0.8
0.6
0.4
0.2
0
1
2
3
4
TIME (hours)

FIG. #5-I

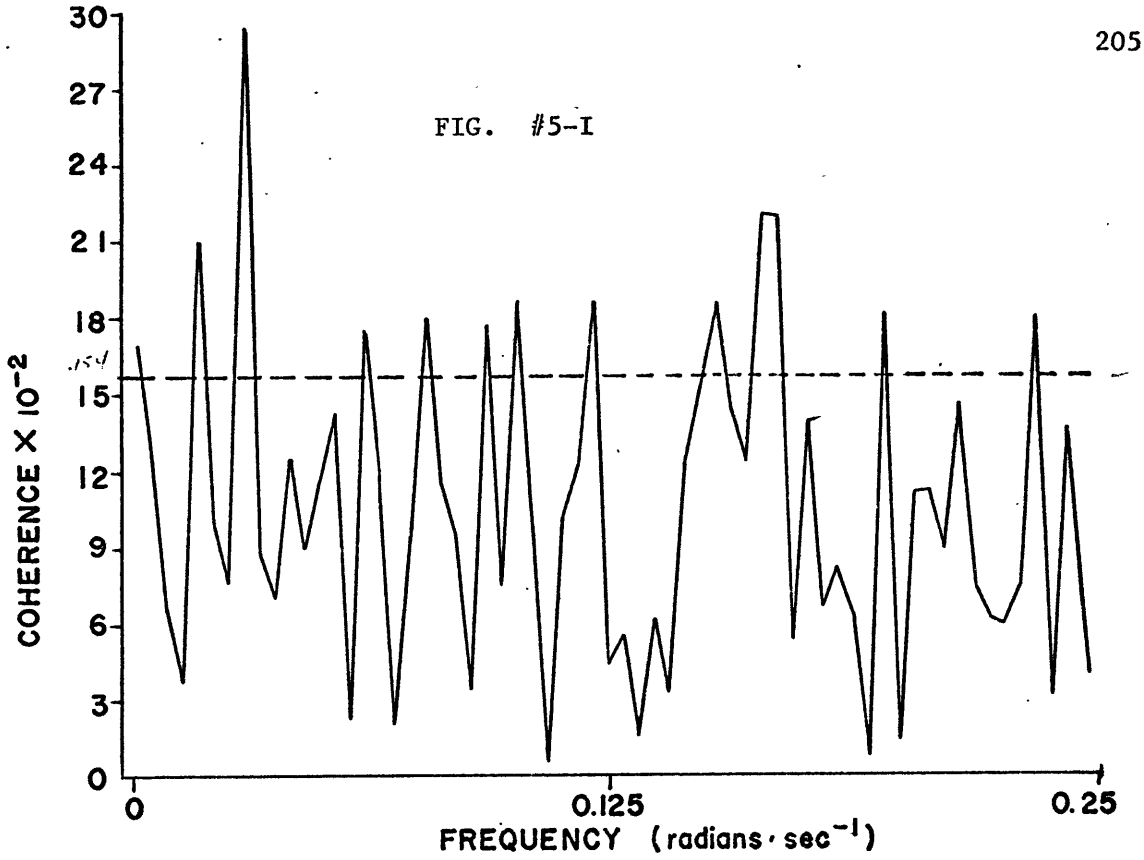
30
27
24
21
18
15
12
9
6
3
0
COHERENCE X 10^{-2}
0
0.125
0.25
FREQUENCY (radians · sec^{-1})

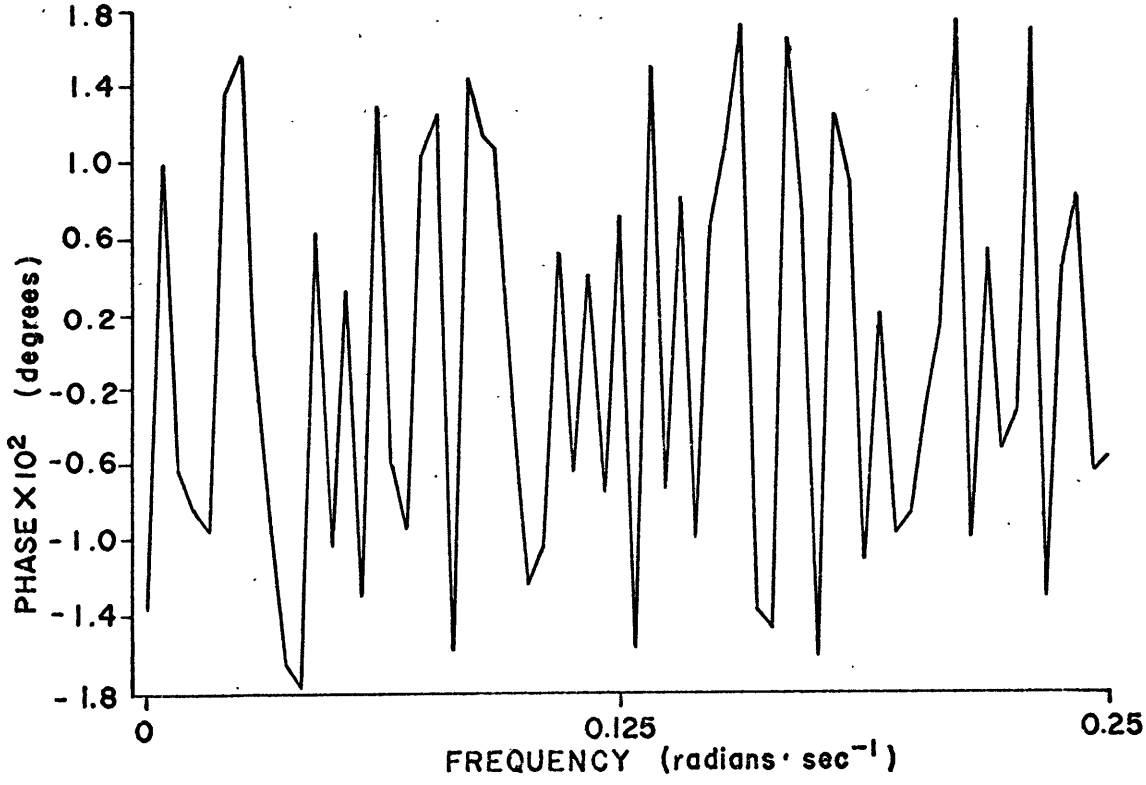
1.8
1.4
1.0
0.6
0.2
-0.2
-0.6
-1.0
-1.4
-1.8
PHASE X 10^2 (degrees)
0
0.125
0.25
FREQUENCY (radians · sec^{-1})

FIG. # 6-I

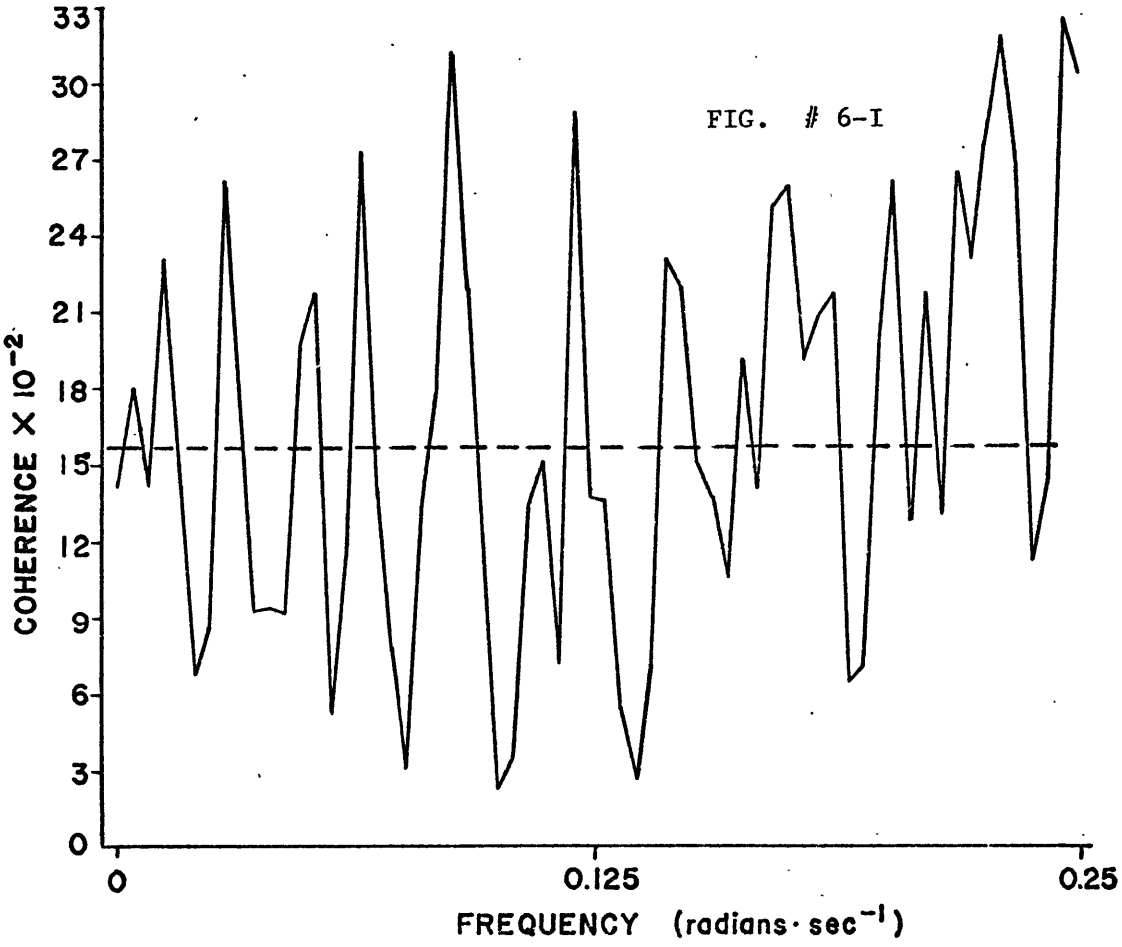
COHERENCE X 10^{-2}
33
30
27
24
21
18
15
12
9
6
3
0
0
0.125
0.25
FREQUENCY (radians · sec^{-1})

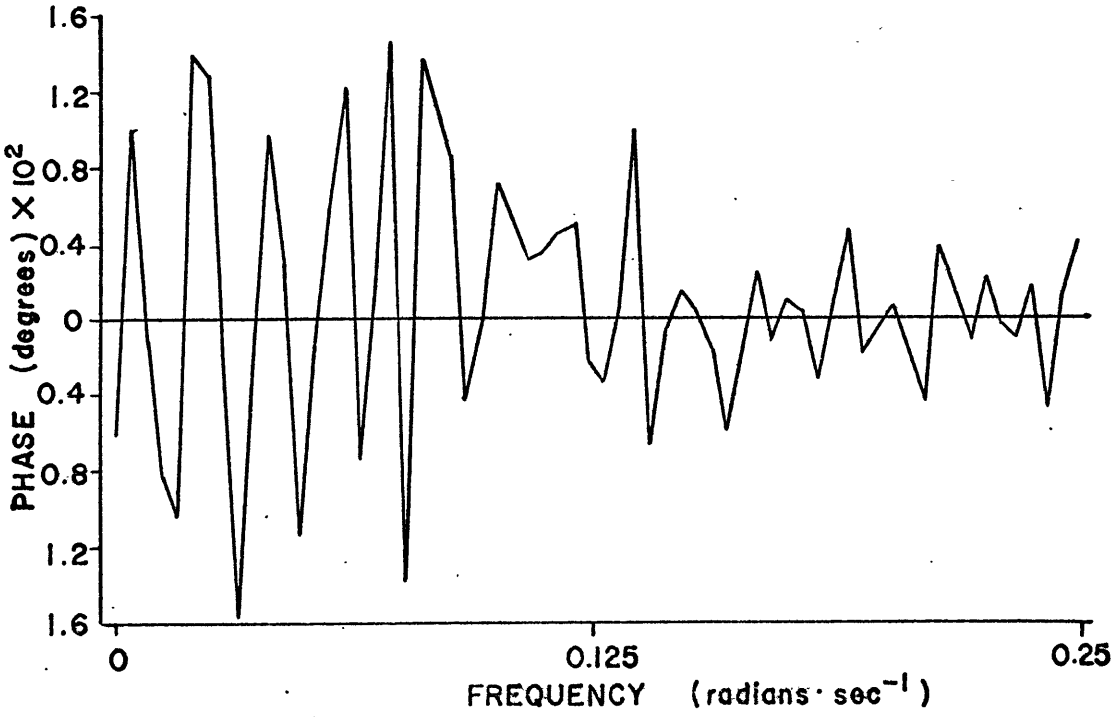
PHASE (degrees) X 10^2
1.6
1.2
0.8
0.4
0
0.4
0.8
1.2
1.6
0
0.125
0.25
FREQUENCY (radians · sec^{-1})

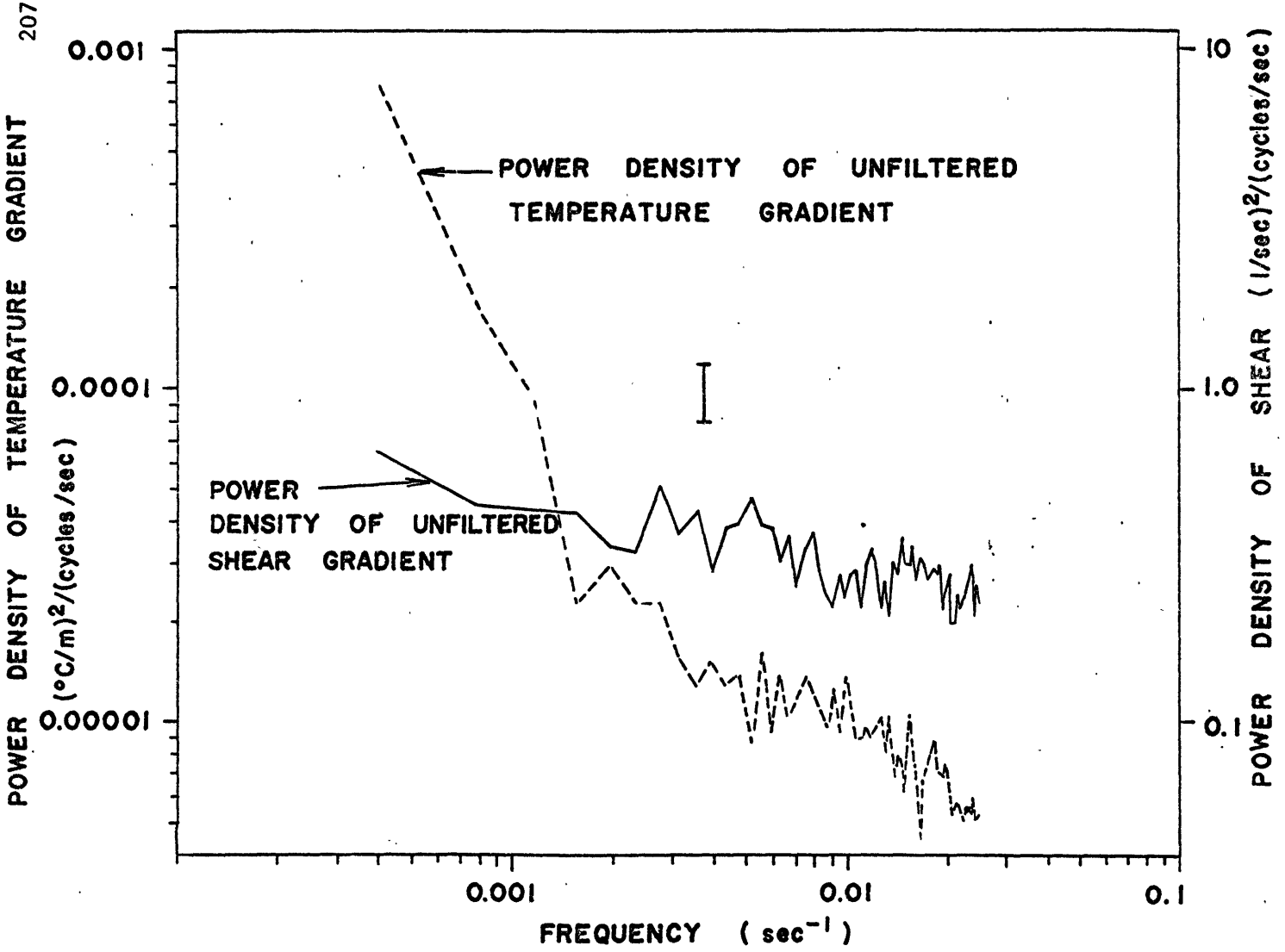
POWER DENSITY OF TEMPERATURE GRADIENT (°C/m)²/(cycles/sec)
0.001
0.0001
0.00001
POWER DENSITY OF SHEAR (1/sec)²/(cycles/sec)
10
1.0
0.1
POWER DENSITY OF UNFILTERED TEMPERATURE GRADIENT
POWER DENSITY OF UNFILTERED SHEAR GRADIENT
0.001
0.01
0.1
FREQUENCY (sec⁻¹)

FIG. # 7-I

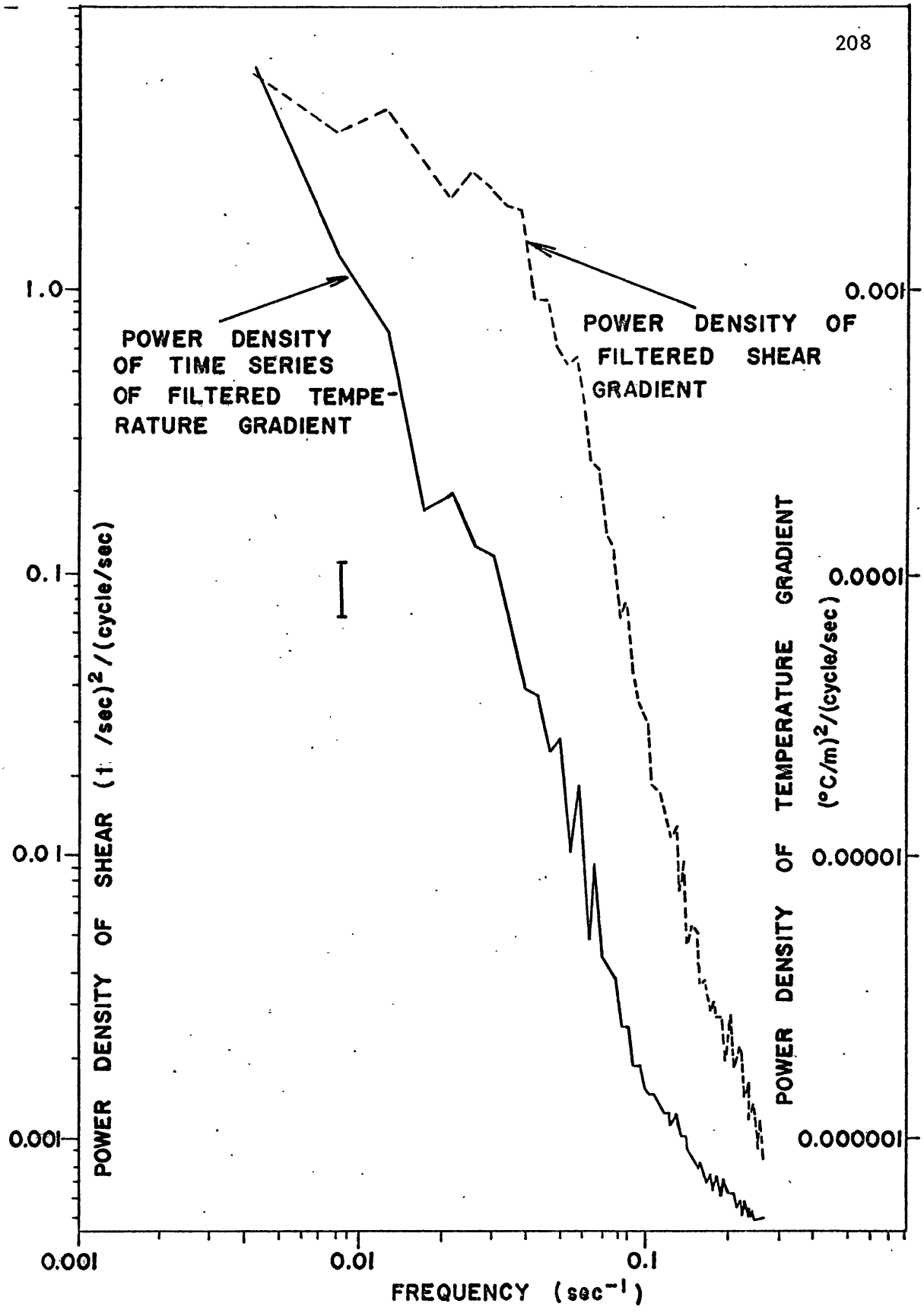
POWER DENSITY OF TIME SERIES OF FILTERED TEMPERATURE GRADIENT
POWER DENSITY OF FILTERED SHEAR GRADIENT
POWER DENSITY OF SHEAR (1/sec)²/(cycle/sec)
POWER DENSITY OF TEMPERATURE GRADIENT (°C/m)²/(cycle/sec)
FREQUENCY (sec⁻¹)
1.0
0.1
0.01
0.001
0.001
0.0001
0.00001
0.000001
0.001
0.01
0.1

FIG. # 8-I

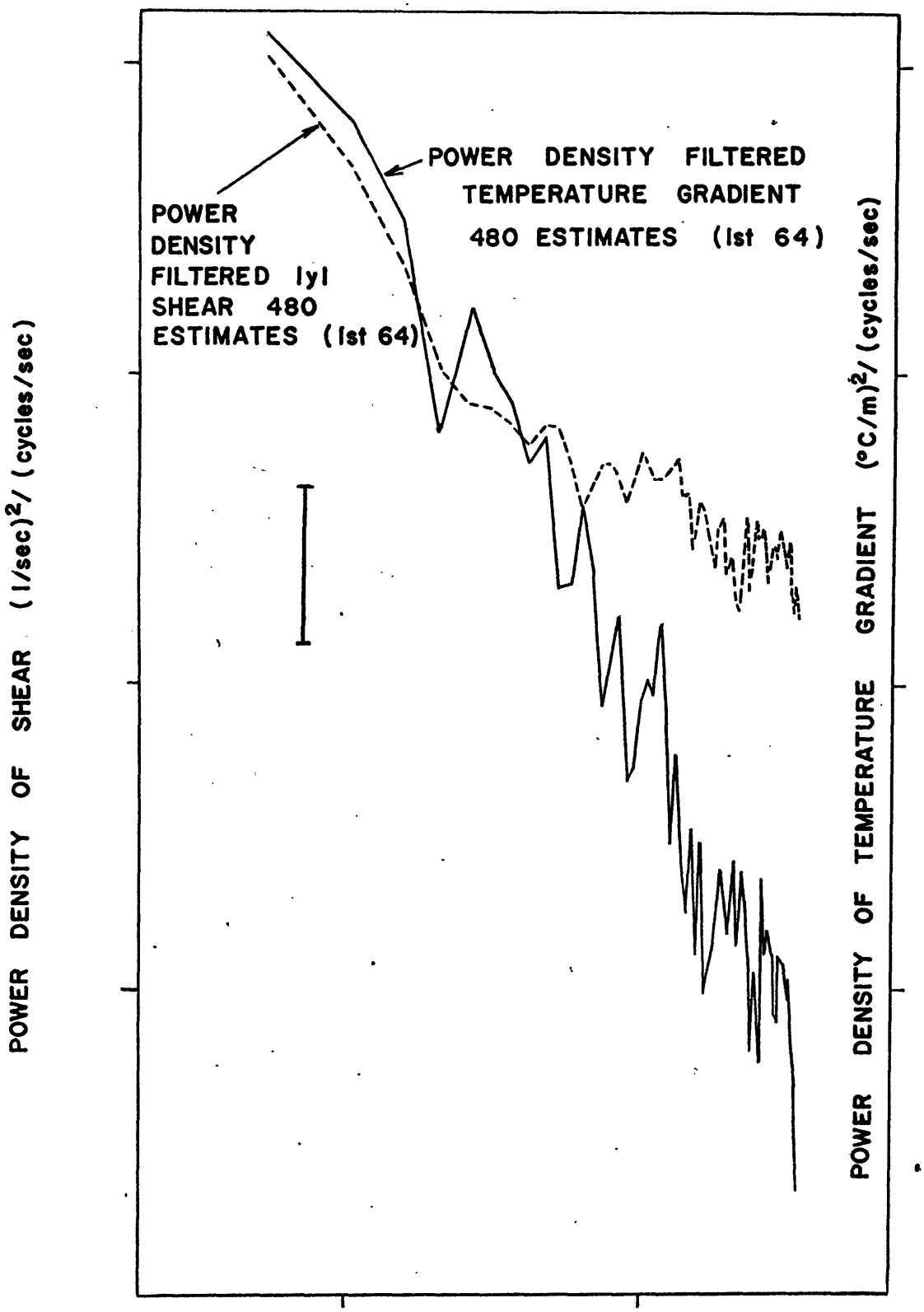
POWER DENSITY FILTERED
TEMPERATURE GRADIENT
480 ESTIMATES (1st 64)
POWER
DENSITY
FILTERED |y|
SHEAR 480
ESTIMATES (1st 64)
POWER DENSITY OF SHEAR (1/sec)²/(cycles/sec)
POWER DENSITY OF TEMPERATURE GRADIENT (°C/m)²/(cycles/sec)
FREQUENCY (sec⁻¹)

FIG. # 9-I